REPORT DOCUMENTATION PAGE

1. REPORT DATE (DD-MM-YYYY)	2. REPORT TYPE Final Technical Report	3. DATES COVERED (From - To) 01 Apr 2003 – 30 Sep 2006

4. TITLE AND SUBTITLE Numerical Simulation and Experiments of Fatigue Crack Growth in Multi-Layer Structures of MEMS and Microelectronic Devices	5a. CONTRACT NUMBER
	5b. GRANT NUMBER F49620-03-1-0152
	5c. PROGRAM ELEMENT NUMBER
6. AUTHOR(S) Dr. Thomas H. Siegmund	5d. PROJECT NUMBER
	5e. TASK NUMBER
	5f. WORK UNIT NUMBER

7. PERFORMING ORGANIZATION NAME(S) AND ADDRESS(ES) Purdue University Mechanical Engineering Building Room 308 585 Purdue Mall West Lafayette IN 47907-2088	8. PERFORMING ORGANIZATION REPORT NUMBER

9. SPONSORING/MONITORING AGENCY NAME(S) AND ADDRESS(ES) Air Force Office of Scientific Research (AFOSR) 875 N. Arlington St., Rm. 3112 Arlington, VA 22203 Dr Byung Lip Lee/NA	10. SPONSOR/MONITOR'S ACRONYM(S) AFOSR
	11. SPONSORING/MONITORING AGENCY REPORT NUMBER N/A

12. DISTRIBUTION AVAILABILITY STATEMENT

DISTRIBUTION A: Approved for public release. Distribution is unlimited.   AFRL-SR-AR-TR-07-0093

13. SUPPLEMENTARY NOTES

Numerical simulation and experiments on the toughness and fatigue crack growth resistance of MEMS relevant thin film structures are reported. Structures consisting of metal films (aluminum, 0.1 to 2.0 um thickness) confined between elastic substrates (semiconductor wafers) are considered. The study is concerned with the influence of the thickness of the metal film on the fatigue failure response. Numerical simulations of fatigue crack growth are conducted by use of cohesive zone models. Both, a damage mechanics based model as well as a model based on dislocation mechanics are employed. To enable these computations, a strain gradient plasticity model is developed. It is demonstrated that cohesive zone models of fatigue enable to analysis of fatigue failure to cases where the Paris Law is no longer applicable. The influence of geometric constraint (thin film confinement, presence of interfaces), mechanical constrain (T-stress), size, and strain gradients on fatigue crack growth are demonstrated.

15. SUBJECT TERMS

16. SECURITY CLASSIFICATION OF:			17. LIMITATION OF ABSTRACT	18. NUMBER OF PAGES	19a. NAME OF RESPONSIBLE PERSON
a. REPORT Unclassified	b. ABSTRACT Unclassified	c. THIS PAGE Unclassified	Unclassified	287	19b. TELEPONE NUMBER (Include area code) (703)

Standard Form 298 (Rev. 8-98)
Prescribed by ANSI-Std Z39-18

Numerical Simulation and Experiments of Fatigue Crack Growth in Multi-Layer Structures of MEMS and Microelectronic Devices

Thomas Siegmund
School of Mechanical Engineering
Purdue University
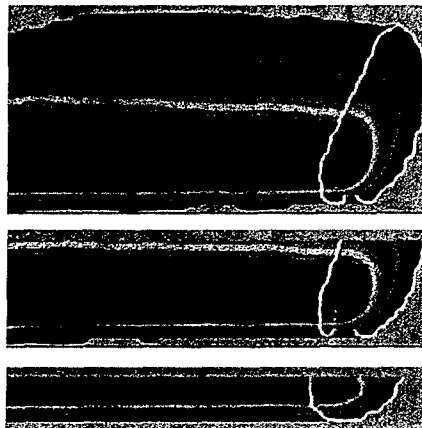
Final Report

December 2006

20070323317

TABLE OF CONTENTS

EXECUTIVE SUMMARY

Numerical simulation and experiments on the toughness and fatigue crack growth resistance of MEMS relevant thin film structures are reported. Structures consisting of metal films (aluminum, 0.1 to 2.0 μm thickness) confined between elastic substrates (semiconductor wafers) are considered. The study is concerned with the influence of the thickness of the metal film on the fatigue failure response. Numerical simulations of fatigue crack growth are conducted by use of cohesive zone models. Both, a damage mechanics based model as well as a model based on dislocation mechanics are employed. To enable these computations, a strain gradient plasticity model is developed. It is demonstrated that cohesive zone models of fatigue enable to analysis of fatigue failure in cases where the Paris Law is no longer applicable. The influence of geometric constraint (thin film confinement, presence of interfaces), mechanical constraint (T-stress), size, and strain gradients on fatigue crack growth are demonstrated. Numerical studies predict that increased constraint and smaller size will accelerate fatigue failure due to changes in plastic deformation. Strain gradients significantly affect the process. Measurements of toughness and fatigue crack growth resistance for the model material system are reported. New test protocols for the commonly used 4 point bend delamination test are developed such that both cracks can be propagated and the number of test data obtained is doubled. The novel approach is also essential for fatigue crack growth. While crack growth resistance was rather independent of the thickness of and fatigue crack growth rates were found to be dependent of film thickness. The dependence of the failure behavior on film thickness arises primarily due to enhanced crack path deflection for decreasing film thickness. Material separation in fracture and fatigue is characterized through a cohesive zone law. The model captures the Paris-law type response obtained in experiments, and also predicts that for thinner films the tendency to crack. Damage tolerant design requires accurate data on residual strength and fatigue crack growth resistance. Both quantities, however, depend on constraint and size of the structure considered. While this has been accounted for in residual strength analysis in the past, the present work provides enabling technologies to solve this problem for fatigue. With the conventional approach to fatigue crack growth, the transferability of data from lab to field, or between specimens and structures is not ensured. Thus, coefficients in the Paris law need to be determined experimentally for each level of constraint or each size of interest. It is, however, not ensured that even a large set of experiments will be able to capture all possible load scenarios. The cohesive zone model approach is provided here as alternative. Once cohesive zone parameters are determined, the dependence of fatigue crack growth on constraint and size emerges as the natural outcome of the analysis without the need to further model modifications.

PUBLICATIONS

Refereed Journal Publications

1. B. Wang, T. Siegmund, "Size effects in fatigue crack growth," Modeling and Simulation in Material Science and Engineering, 14 (2006) 775-787.

2. S. Brinckmann, T. Siegmund, Y. Huang, "A dislocation mechanics based strain gradient plasticity model," International Journal of Plasticity, 22 (2006) 1586-1609.

3. B. Wang, T. Siegmund, "Simulation of fatigue crack growth at plastically mismatched bi-material interfaces", International Journal of Plasticity, 22 (2006) 1586-1609.

4. B. Wang, T. Siegmund, "Numerical simulation of constraint effects in fatigue crack growth," International Journal of Fatigue, 27 (2005) 1328-1334.

5. B. Wang, T. Siegmund, "A numerical analysis of constraint effects in fatigue crack growth by use of an irreversible cohesive zone model," International Journal of Fracture, 132 (2005) 175-196.

6. T. Siegmund, "A numerical study of transient fatigue crack growth by use of an irreversible cohesive zone model," International Journal of Fatigue, 26 (2004) 929-939.

Refereed Journal Publications in Progress

1. S. Brinckmann, T. Siegmund, "On the influence of strain gradients on fatigue crack propagation predictions," International Journal of Solids and Structures, submitted.

2. S. Brinckmann, T. Siegmund, A cohesive surface model based on the stress caused by dislocations, to be submitted.

3. B. Wang, T. Siegmund, "An enhanced four point bend delamination test," Microelectronics Reliability, to be submitted.

4. B. Wang, S, Brinckmann, T. Siegmund, "Experiments and Numerical Simulation of Fracture and Fatigue in Multilayer Thin Film Structures," Engineering Fracture Mechanics, to be submitted.

Conference Publications and Presentations

1. S. Brinckmann, T. Siegmund, "Fatigue crack growth simulations with length scale dependent material laws " Proceedings of the 2006 International Fatigue Congress, Johnson S, Newman J., Jr, Saxena, A., eds, Atlanta, GA, May, 2006.

2. S. Brinckmann, T. Siegmund, "Damage evolution in cohesive surfaces based on the dislocation accumulation in the surrounding material," 2006 World Congress on Computational Mechanics, Los Angeles, CA, July, 2006.

3. J. Han, T. Siegmund, "Computational theory of delamination wear," Proceedings of the 2006 International Fatigue Congress, Johnson S, Newman J., Jr, Saxena, A., eds, Atlanta, GA, May, 2006.

4. T. Siegmund, "Modeling fatigue crack growth with irreversible cohesive zone models," The 43rd Annual Technical Meeting of the Society of Engineering Science August 13-16, 2006 University Park Pennsylvania.

5. S. Brinckmann, T. Siegmund, "Fatigue crack growth in metals: a strain gradient simulation," Proceedings of the 2006 International Mechanical Engineering Congress and Exposition, The American Society of Mechanical Engineers, Chicago, IL, IMECE2006-13678.

6. B. Wang, T. Siegmund "Numerical simulations of constraint and size effects in fatigue crack growth, " Proceedings of the 11th International Congress on Fracture (ICF 11), Turin, Italy, A. Carpinteri Ed., (2005), Paper No: 3975.

7. S. Brinckmann, T. Siegmund, "Modeling fatigue crack growth with ABAQUS," 2005 ABAQUS Fracture Review Team Meeting, Providence, RI, (2005).

8. S. Brinckmann, T. Siegmund, "Modeling fatigue crack growth with ABAQUS," 2005 ABAQUS Midwest User Group Meeting, West Lafayette, IN, (2005).

9. B. Wang, T. Siegmund ,"Simulation of fatigue crack growth at bi-material interfaces," Proceedings of the 2004 IMECE, ASME, Los Angeles, CA, CD-proceedings, (2004) Paper No: IMECE2004-60956.

10. B. Wang, T. Siegmund, "Numerical simulation of constraint effects in fatigue crack growth," International Conference on Fatigue Damage of Structural Materials V, Sept. 19-24, 2004, Hyannis, MA, USA.

1. INTRODUCTION

Under the cyclic loading and small-scale yielding condition, the Paris equation based on the theory of Linear Elastic Fracture Mechanics (LEFM) is commonly used to describe Fatigue Crack Growth (FCG). The Paris law provides the relationship between the applied stress intensity factor range, $\Delta K = K_{max} - K_{min}$, and FCG rate, da/dN (Paris et al., 1961) as:

$$\frac{da}{dN} = C(\Delta K)^m \qquad (1.1)$$

The parameters C and m are obtained by fitting the experimental data of regime B of FCG data as schematically depicted in Figure 1.1. The Paris law assumes that FCG is independent of planar specimen geometry such that exchange and comparison of data obtained from a variety of specimen configurations and loading conditions should be possible. This feature allows the transferability of FCG data from one specimen dimension to another and is based on the concept of similitude implying that cracks of different lengths subjected to the same nominal ΔK will advance by equal increments of crack extension per cycle. However, there are situations where the concept of similitude is violated. When FCG at small scales is considered the validity of equation (1.1) is lost since the monotonic and cyclic plastic zones interact with geometric features. Consider a geometry with an elastic plastic layer sandwiched between two elastic substrates. Then, under monotonic loading, the plastic zone size at the crack tip based on Irwin's estimation for plain strain provides one reference length

$$r_{pl} = \frac{1}{3\pi}\left(\frac{K}{\sigma_y}\right)^2 = \frac{1}{3\pi(1-v^2)}\frac{EG}{(\sigma_y)^2} \qquad (1.2)$$

6

Here, the relationship between the stress intensity factor K and strain energy release rate G is $K = \left[EG / \left(1 - v^2 \right) \right]^{\frac{1}{2}}$, and E and v are the elastic constants, and σ_y the yield strength of metal thin film. In the case of cyclic loading, the cyclic plastic zone size Δr_{pl} can be used as the second reference length. Based on the analysis of Rice (1967), the cyclic plastic zone develops upon unloading and reloading. The solution for the size of the cyclic plastic zone is obtained by replacing K or G by ΔK or ΔG and σ_y by $2\sigma_y$ in equation (1.2) as

$$\Delta r_{pl} = \frac{1}{3\pi} \left(\frac{\Delta K}{2\sigma_y} \right)^2 = \frac{1}{3\pi \left(1 - v^2 \right)} \frac{E \left(\Delta G \right)}{\left(2\sigma_y \right)^2} \tag{1.3}$$

For example, an aluminum thin film of 1μm sandwiched between two elastic substrates is considered here. For such thin aluminum films, the room temperature yield strength is in the range of 75 to 200MPa, and the elastic constants are E=70GPa and v=0.3. Figure 1.2 indicates that both monotonic and cyclic plastic zone sizes can be the same magnitude as or larger than the thickness of the aluminum film. Thus, the plastic deformation at the crack tip can not be freely developed due to the considerable constraint effects. It is the hypothesis of the present work that in cases of confinement of plastic zones, the FCG rate is changed, and that then the Paris law and its transferability is no longer valid. the constants C and m as determined on one specimen geometry can be no longer used to predict FCG rates in other specimen with different dimensions. We further hypotheses that a cohesive zone model approach can be used to overcome this problem and can provide transferable solutions to FCG regardless of constraint and size. We further aim to verify such theoretical assumptions through experiments on a relavant model material system. in

Considering the limitation of the Paris equation, several alternative methods have been proposed to describe FCG, including

1) The cyclic J-integral: Dowling and Begley (1976) and Dowling (1977) used the cyclic J-integral, ΔJ, to characterize the FCG under elastic-plastic conditions by a similar power law as equation (1.1). This method is, however, not applicable

7

under non-proportional and reverse loading conditions since the material descriptions based on the deformation theory of plasticity do not hold. Moreover, J-integral was questioned even when it was used to characterize the crack growth resistance under monotonic loading (Siegmund & Brocks, 2000).

2) Another alternative approach for characterizing FCG under elastic-plastic conditions is based on the geometric correlations between the critical cyclic crack tip opening displacement, $\Delta CTOD_c$ and crack extension, Δa (Laird, 1967; Pelloux, 1970; Neumann, 1974). Considering FCG at small scales, the application of this approach will fail since the $\Delta CTOD_c$ is not a material parameter and will depend on the mechanical constraint due to the metal thin film, the stiffness mismatch across the interface or mod mixty.

3) Based on the concept of cumulative damage at the crack tip, the process zone models use a volume element at the crack tip which endures constant cyclic strain amplitude until a critical damage state is reached, then the crack advances. The limitation for this approach is to assume the validity of the Manson-Coffin law and Miner's linear damage rule and the process zone equals the cyclic plastic zone (Davidson and Lankford, 1992). Also it is difficult to use this approach for the FCG along interfaces.

4) Node release techniques in the context of the Finite Element Method (FEM) were also used to study the FCG under cyclic loading by providing more detailed information of the continuum deformation at the crack tip. The problems such as crack closure and crack surface friction were investigated using FEM (Newman, 1981; Fleck, 1986; Sehitoglu, et al., 1996; Wu and Ellyin, 1996). Node release models still assume an infinite strength, and do not contain any arguments regarding the energy required to form new surface.

5) Several investigators (see e.g. Pippan and Riemelmoser (1998)) applied the Dugdale model to calculate plastic zone sizes and crack tip opening displacements. Based on these results FCG rates were then related to the cyclic crack tip opening displacements. While this method was quite successful, the Dugdale model requires several restrictive assumptions regarding the shape and

8

stress distribution in the plastic zone. It also lumps bulk yielding and material separation processes into a single process zone.

To overcome the limitations and disadvantages of the LFEM based Paris equation and the limitations of the above listed alternative approaches for the characterization of FCG, the Cohesive Zone Model (CZM) was employed. The basic concept of CZM was proposed by Barenblatt (1962). In a CZM the material separation process is described by a softening constitutive equation connecting the crack surface tractions and material separation across the crack. Thus, in the CZM the softening traction-separation law removes the complexity of stress singularity at the crack tip. The material separation process can be viewed as a result of progressive material deterioration in the cohesive zone and the interaction with the surrounding continuum. Two cohesive constitutive parameters, cohesive strength and cohesive energy per unit area, are used to describe the underlying material separation process. Another advantage of CZM is a broad range of different physical processes of material separation can be incorporated within a single numerical method. Moreover, the CZM can be easily employed in the numerical analysis through FEM. To use the CZM approach in FEM, the cohesive elements surrounded by continuum elements were implemented to introduce the cohesive surface for the material model investigated. Since the CZM approach has many advantages to characterize the physical material separation processes, it has been widely applied to a number of studies on fracture and crack propagation under monotonic or dynamic loading conditions in homogeneous materials, in composites and at interfaces (e.g., Camacho and Ortiz, 1996; Carranza and Haber, 1998; Chaboche et al., 1997; Chandra et al., 2002; Geubelle and Baylor, 1998; Hattiangadi and Siegmund, 2004; Hutchinson and Evans, 2000; Lane et al., 2000a; Li and Chandra, 2003; Li and Siegmund, 2002, 2004; Lin et al., 1997; Mohammed and Liechti, 2000; Needleman, 1987, 1990a, 1990b, 1997, 2000; Siegmund and Needleman, 1997; Siegmund et al., 1997; Suo and Hutchinson, 1990; Tvergaard, 1990, 1997; Tvergaard and Hutchinson 1992, 1994, 1996a, 1996b; Varias et al., 1990; Wei and Hutchinson, 1997, 1999; Xu and Needleman, 1994, 1996a, 1996b; Yang et al., 2001; Zhang et al., 2002).

Recently, several attempts to establish the CZM approach to fatigue have been reported. For example, Foulk et al. (1998) simulated the interface failure under cyclic loading by adding an unloading condition to a softening CZM. Unloading and subsequent reloading follow the same path, and consequently the traction-separation behavior stabilizes without further progress in material separation. de-Andrés et al. (1999) also developed the CZM model by adding an unloading condition and a cycle dependent damage variable. This model was successful to predict FCG under large scale yielding conditions but would shake down for small scale yielding or elastic deformation. Nguyen et al. (2001) investigated FCG rates under constant amplitude loading as well as overloads by using a CZM based on irreversible unload-load relations. There, the introduction of unloading-reloading hysteresis in the cohesive law avoids shakedown and allows for steady crack growth. Similarly, Yang et al. (2001) developed a FCG model based on a modified line spring model including the damage evolution for a brittle polymer in combination with the maximum principal stress criterion for crack advance. Yang et al. (2004) developed a fatigue CZM which can incorporate the damage into the cohesive law to account for the gradual loss of stiffness and strength of solder materials under cyclic loading. The damage evolution law was assumed to be a function of accumulated plastic strain. Maiti and Geubelle (2005) proposed a cohesive failure model to simulate fatigue crack propagation in polymeric materials subjected to mode I cyclic loading. The fatigue evolution law has been combined into the cohesive zone model and defined to describe the irreversible degradation process during each reloading cycle. Although the CZM approach has been used to study the constraint effects in the multi-layer structures (e.g., Tvergaard and Hutchinson, 1994; Lin et al., 1997; Lane et al., 2000a), these studies were limited to fracture problems under the monotonic loading, and FCG problems and constraint were not considered..

In this work the irreversible cohesive zone model originally proposed by Roe and Siegmund (2001, 2003) and Siegmund (2004) is used. This model has successfully been used by these authors to simulate FCG in elastic material systems based on an irreversible cohesive zone law which includes a cyclic damage evolution rule for the cohesive strength. The cohesive zone parameters will depend on the accumulated damage by

introduce a cyclic damage variable into the traction-separation law. This model can be used to simulate the crack nucleation and subsequent fatigue crack propagation under cyclic loads since it allows computations of the failure behavior simultaneously account for sub-critical damage accumulation. Especially, this approach allows one to capture constraint effects in fatigue because energy dissipation due to cyclic material separation at the crack tip and due to the cyclic plastic deformation in the ductile layer is accounted for independently. Subsequently, we develop a novel cohesive zone model in which material separation cyclic

The work described in this report can be divided into two parts, numerical simulation and experimental studies. Numerical simulations were conducted to study complex fatigue problems as they relate to MEMS and integrated circuit multi-layer structures. Specifically, following studies were performed: First we analyze constraint effects in FCG (Wang and Siegmund, 2005a,b) as they relate to in-plane geometry and T-stresses, then consider FCG at interfaces between two mismatched elastic-plastic solids (see Wang and Siegmund, 2006a). Subsequently, we investigate structural size effects in FCG (Wang and Siegmund, 2006b), and finally investigate the effects of strain gradients in plasticity in their influence on FCG. Also, a novel CZM for FCG simulations is presented. The experimental work includes the development of a modified 4-point bend delamination test methodology, fracture toughness test and fatigue crack growth test on MEMS relevant test structures.

The novel analysis methods will especially benefit the development of reliable microdevices. Micro-Electro-Mechanical Systems (MEMS) and microelectronic devices containing multi-layer structures are widely used in recent applications of modern technologies such as inertial sensing, signal conditioning, switching and biomedicine. To advance promising MEMS devices into field applications and to increase the yield and reliability of integrated circuit interconnect structures, systematic studies of failure mechanism are needed. The multi-layer structures of interest here correspond to configurations where a metal film is sandwiched between two elastic substrates, see e.g. the "bonding rim" of the MEMS device shown in Fig. 1.3. As the device length scales and associated film thickness decrease, the crack growth behavior under monotonic and

11

cyclic loading becomes more complex. Specifically, as the characteristic dimensions of stress and strain fields become of size similar to the thickness of the thin film, the processes at the crack tip start to be influenced by the interaction with the surrounding elastic substrates and, consequently, it is to be expected that fatigue crack growth (FCG) rates are influenced by the constraint and size effects.
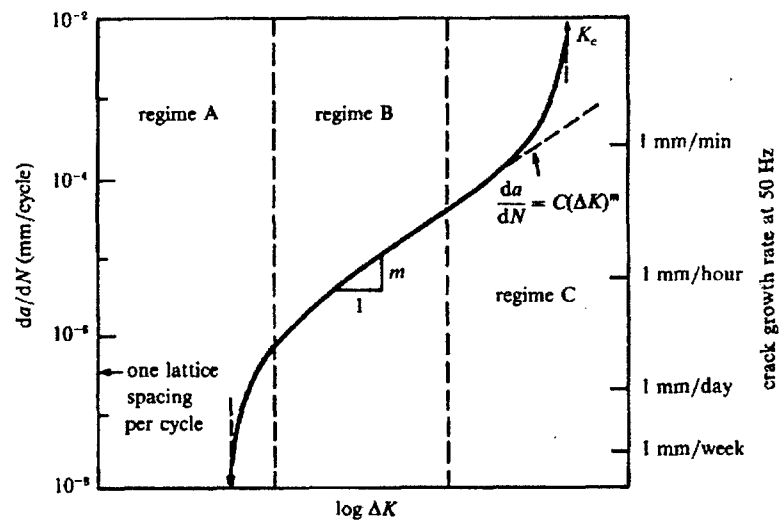
Figure 1.1 Schematic illustration of the different regimes of stable fatigue crack propagation described by Paris law (Suresh, 1998)
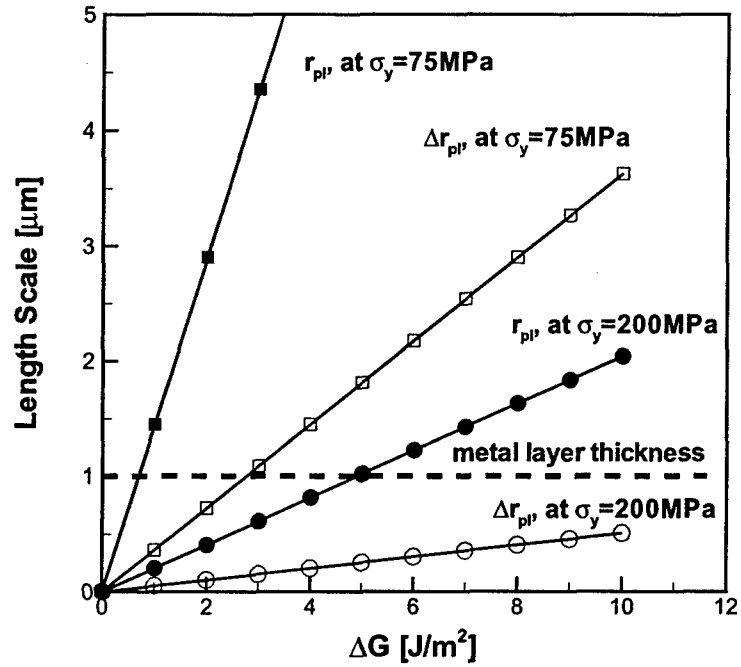
Figure 1.2: Length scales associated with FCG in dependence on the applied energy
release rate range. Yield strength data are for aluminum films thickness, $h = 1\mu m$.

Top Wafer

MEMS Switch
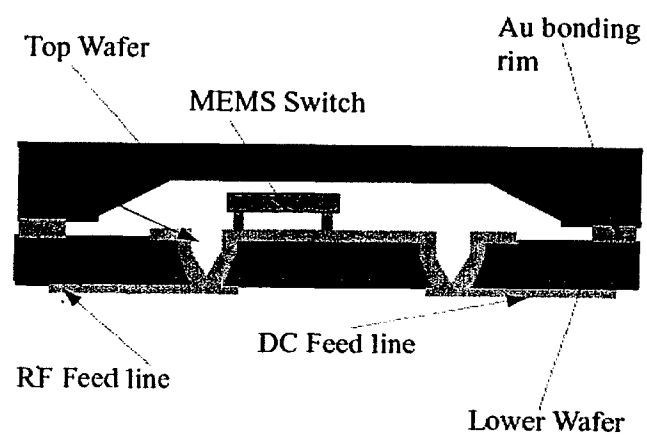
Au bonding rim

DC Feed line

RF Feed line

Lower Wafer

Figure 1.3: Schematic of one typical MEMS device with multi-layer structures.

LIST OF REFERENCE

Barenblatt, G.I., 1962, "The Mathematical Theory of Equilibrium Cracks in Brittle Fracture," *Advances in Applied Mech. Academic Press*, New York. Vol. 7, 55-129.

Camacho, G.T., and Ortiz, M., 1996, "Computational Modeling of Impact Damage in Brittle Materials," *International Journal of Solids and Structures*, Vol. 33, pp. 2899-2938.

Carranza, F.L., and Haber, R.B., 1998, "A Numerical Study of Integranular Fracture and Oxygen Embrittlement in an Elastic-Viscoplastic Solid," *Journal of the Mechanics and Physics of Solids*, Vol. 47, pp. 27-58.

Chaboche, J.L., Girard, R., and Levasseur, P., 1997, "On the Interface Debonding Models," *International Journal of Damage Mechanics*, Vol. 6, pp. 220-257.

Chandra, N., Li, H., Shet, C., and Ghonem, H., 2002, "Some Issues in the Application of Cohesive Zone Models for Metal-Ceramic Interfaces," *International Journal of Solids and Structures*, Vol. 39, pp. 2827-2855.

Davidson, D.L., Lankford J., 1992, "Fatigue crack growth in metals and alloys: mechanisms and micromechanics," *International of Materials Reviews*, Vol. 37, pp. 45–76.

de-Andrés, A., Pérez, J.L., and Ortiz, M., 1999, "Elastoplastic Finite Element Analysis of Three-Dimensional Fatigue Crack Growth in Aluminum Shafts Subjected to Axial Loading," *International Journal of Solids and Structures*, Vol. 36, pp. 2231-2258.

Dowling, N.E., Begley, J.A., 1976, "Fatigue crack growth during gross plasticity and the J-integral," *ASTM STP*, Vol. 590, pp. 82–103.

Dowling, N.E., 1977, Performance of metal-foil strain-gauges during large cyclic strains," *Experimental Mechanics*, Vol. 17 (5), pp. 193-197.

E647-91, 1991, "Standard Test Method for Measurement of Fatigue Crack Growth Rates," *Annual Book of ASTM standards*.

Fleck, N.A., 1986, "Finite element analysis of plasticity-induced crack closure under plane strain conditions," *Engineering of Fracture Mechanics*, Vol. 25, pp. 441–449.

Foulk III, J.W., Allen, D.H., Helms, K.L.E., 1998, "A Model for Predicting the Damage and Environmental Degradation Life of SCS-6/Timetal21S[0]4 Metal Matrix Composite," *Mechanics of Materials*, Vol. 29, pp. 53-68.

Geubelle, P.H., and Baylor, J.S., 1998, "Impact-Induced Delamination of Composites: A 2D Simulation," *Composites part B*, Vol. 29B, pp. 589-602.

Hattiangadi, A., Siegmund, T., 2004, "A thermomechanical cohesive zone model for bridged delamination cracks,"*Journal of the Mechanics and Physics of Solids*, Vol. 52(3), pp. 533-566.

Hutchinson, J.W., and Evans, A.G., 2000, "Mechanics of materials: top-down approaches to fracture," *Acta Materialia*, Vol. 48, pp. 125-135.

Laird, C., 1967, "The influence of metallurgical structure on the mechanisms of fatigue crack propagation," *ASTM STP* Vol. 415, pp. 131–68.

Lane, M., Dauskardt, R.H., Vainchtein, A., and Gao, H. 2000a, "Plasticity contributions to interface adhesion in thin-film interconnect structures," *Journal of Materials Research*, Vol. 15, pp. 2758-2769.

Lane, M., Dauskardt, R.H., Krishna, N., Hashim, I., 2000b, "Adhesion and reliability of copper interconnects with Ta and TaN barrier layers," *Journal of Materials Reviews*, Vol. 15(1), pp. 203-211.

Li, N., Chandra, N., 2003, "Analysis of crack growth and crack-tip plasticity in ductile materials using cohesive zone models," *International Journal of Plasticity*, Vol. 19(6), pp. 849-882.

Li, W., Siegmund, T., 2002, "An analysis of crack growth in thin-sheet metal via a cohesive zone model," *Engineering Fracture Mechanics*, Vol. 69(18), pp.2073-209.

Li, W., Siegmund, T., 2004, "An analysis of the indentation test to determine the interface toughness in a weakly bonded thin film coating – substrate system," *Acta Materialia*, Vol. 52(10), pp. 2989-2999.

Lin, G., Kim, Y.J., Cornec, A., Schwalbe, K.H., 1997, "Fracture toughness of a constrained metal layer," *Computational Materials Science*, Vol. 9, pp. 36-47.

Maiti, S., Geubelle, P.H., 2005, "A cohesive model for fatigue failure of polymers," *Engineering of Fracture Mechanics*. Vol. 72, pp. 691-708.

Mohammed, I., and Liechti, K.M., 2000, "Cohesive Zone Modeling of Crack Nucleation at Bimaterial Corners," *Journal of the Mechanics and Physics of Solids*, Vol. 48, pp. 735-764.

Needleman, A. 1987, "A Continuum Model for Void Nucleation by Inclusion Debonding," *Journal of Applied Mechanics*, Vol. 54, pp. 525-531.

Needleman, A., 1990a, "An Analysis of tensile decohesion along an interface," *Journal of the Mechanics and Physics of Solids*, Vol. 38, pp. 289-324.

Needleman, A., 1990b, "An Analysis of Decohesion Along an Imperfect Interface," *International Journal of Fracture*, Vol. 42, pp. 21-40.

Needleman, A., 1997, "Numerical Modeling of Crack Growth under Dynamic Loading Conditions," *Computational Mechanics*, Vol. 19, pp. 463-469.

Needleman, A., 2000, "Computational Mechanics at the Mesoscale," *Acta Materialia*, Vol. 48, pp. 105-124.

Neumann, P., 1974, "The geometry of slip processes at a propagating fatigue crack—II," *Acta Metallurgica et Materialia*, Vol. 22, pp. 21167–78.

Newman, J.C., 1981, "A crack-closure model for predicting fatigue crack growth under aircraft spectrum loading," *ASTM STP*, Vol. 748:53–84.

Nguyen O., Repetto, E.A., Ortiz, M., Radovitzky R.A., 2001, "A cohesive zone model of fatigue crack growth," *International Journal of Fracture*, Vol., 110, pp. 351-369.

Paris, P.C., Gomez M.P., Anderson W.P., 1961, "A rational analytic theory of fatigue," *The Trend in Engineering*, Vol. 13, pp. 9–14.

Pelloux, R.M.N., 1970, "Crack extension by alternating shear," *Engineering of Fracture Mechanics*, Vol. 1, pp. 697–704.

Pippan, R., Riemelmoser, F.O., 1998, "Fatigue of bimaterials. Investigation of the plastic mismatch in case of cracks perpendicular to the interface," *Computational Materials Science*, Vol. 13, pp. 108-116.

Rice, J.R., 1967. "Mechanics of crack tip deformation and extension by fatigue," *ASTM STP*, Vol. 415, pp. 247–309.

Roe, K.L. and Siegmund, T., 2001, "Simulation of interface fatigue crack growth via a fracture process zone model. Computational Fluids and Solid Mechanics," *Proceedings of the 1st MIT Conference on Computational Fluids and Solid Mechanics, Boston, K.J. Bathe, Ed., Elsevier*, pp. 435-437.

Roe, K.L. and Siegmund, T., 2003, "An irreversible cohesive zone model for interface fatigue crack growth simulation," *Engineering Fracture Mechanics*, Vol.70, pp. 209-232.

Sehitoglu, H., Gall, K., Garcia, A.M., 1996, "Recent advances in fatigue crack growth modeling," *International Journal of Fracture*, Vol. 80, pp.165–192.

Siegmund, T., 2004, "A numerical study of transient fatigue crack growth by use of an irreversible cohesive zone model," *International Journal of Fatigue*, Vol. 26, pp.929-939.

Siegmund, T., Brocks, W., 2000, "A numerical study on the correlation between the work of separation and the dissipation rate in ductile fracture," *Engineering Fracture Mechanics* Vol. 67, pp. 139-154.

Siegmund, T. and Needleman, A., 1997, "A Numerical Studies of Dynamic Crack Growth in Elastic-plastic Solids," *International Journal of Solids and Structures*, Vol. 34, No. 7, pp. 769-787.

Siegmund, T., Fleck, N.A., Needleman, A., 1997, "Dynamic crack growth across an interface," *International Journal of Fracture*, Vol. 85, pp. 381-402.

Suo, Z., and Hutchinson, J.W., 1990, "Interface Crack between Two Elastic Layers," *International Journal of Fracture*, Vol. 43, pp. 1-18.

Suresh, S., 1998, *Fatigue of Materials*. Cambridge University Press.

Tvergaard, V., 1990, "Effect of Fibre Debonding in a Wisker-Reinforced Metal," *Materials Science and Engineering*, Vol. A125, pp.203-213.

Tvergaard, V., and Hutchinson, J.W., 1992, "The Relation Between Crack Growth Resistance and Fracture Process Parameters in Elastic-Plastic Solids," *Journal of the Mechanics and Physics of Solids*, Vol. 40, pp. 1377-1397.

Tvergaard, V., and Hutchinson, J.W., 1994, "Effect of T-Stress on Mode I Crack Growth Resistance in a Ductile Solid," *International Journal of Solids and Structures*, Vol. 31, pp. 823-833.

Tvergaard, V., and Hutchinson, J.W., 1996a, "On the Toughness of Ductile Adhesive Joints," *Journal of the Mechanics and Physics of Solids*, Vol. 44, pp. 789-800.

Tvergaard, V., and Hutchinson, J.W., 1996b, "Effect of Strain-Dependent Cohesive Zone Model on Predictions of Crack Growth Resistance," *International Journal of Solids and Structures*, Vol. 33, pp. 3297-3308.

Tvergaard, V., 1997, "Relations Between Crack Growth Resistance and Fracture Process Parameters Under Large Scale Yielding", *Nonlinear Analysis of Fracture, J.R. Willis Ed., Kluwer Academic Publishers*, pp. 93-104.

Varias, A.G., O'Dowd, N.P., Asaro, A.J., and Shih, C.F., 1990, "Failure of Bimaterial Interfaces," *Materials Science and Engineering*, Vol. A126, pp. 65-93.

Wei, Y., and Hutchinson, J.W., 1997, "Nonlinear Delamination Mechanics for Thin Films," *Journal of the Mechanics and Physics of Solids*, Vol. 45, pp. 1137-1159.

Wei, Y., and Hutchinson, J.W., 1999, "Models of interface Separation Accompanied by Plastic Dissipation at Multiple Scales," *International Journal of Fracture*, Vol. 95, pp. 1-17.

Wu, J., Ellyin, F., 1996, "A study of fatigue crack closure by elastic–plastic finite element analysis for constant amplitude loading," *International Journal of Fracture*, Vol. 82, pp. 43–65.

Xu, X.-P., and Needleman, A., 1994, "Numerical Simulation of Fast Crack Growth in Brittle Solids," *Journal of the Mechanics and Physics of Solids*, Vol. 42, pp. 1397-1434.

Xu, X.-P., and Needleman A., 1996a, "Numerical Simulations of Dynamic Crack Growth Along an Interface," *International Journal of Fracture*, Vol. 74, pp. 289-324.

Xu, X.-P., and Needleman, A., 1996b, "Numerical Simulations of Dynamic Interfacial Crack Growth Allowing for Crack Growth Away from the Bond Line," *International Journal of Fracture*, Vol. 74, pp. 253-275.

Yang, B., Mall, S. and Ravi-Chandar, K., 2001, "A Cohesive Zone Model for Fatigue Crack Growth in Quasibrittle Materials," *International Journal of Solids and Structures*, Vol. 38, No. 22-23, pp. 3927-3944.

Yang, Q.D., Shim, D.J., Spearing, S.M., 2004, "A cohesive zone model for low cycle fatigue life prediction of solder joints," *Microelectronic Engineering*. Vol. 75, pp. 85-95.

Zhang, P., Klein, P., Huang, Y., Gao, H., and Wu, P.D., 2002, "Numerical Simulation of Cohesive Fracture by the Virtual-Internal-Bond Model," *Computer Modeling in Engineering and Sciences*, Vol. 3, No.2, pp. 263-278.

2. COHESIVE ZONE MODEL

2.1 Cohesive Zone Model Formulation

In the cohesive zone model approach potential crack surfaces are considered as internal surfaces. In the finite element formulation, the mechanical equilibrium equations include the contribution of the cohesive zone as integral over internal surfaces S_{int} as shown in Figure 2.1. The principle of virtual work is written as:

$$\int_V \mathbf{s}{:}\delta\mathbf{F} \, dV - \int_{S_{int}} \mathbf{T_{CZ}} \cdot \delta\mathbf{\Delta} \, dS = \int_{S_{ext}} \mathbf{T_e} \cdot \delta\mathbf{u} \, dS \qquad (2.1)$$

with the nominal stress tensor $\mathbf{s}=\mathbf{F}^{-1}\det(\mathbf{F})\sigma$ the Cauchy stress σ the deformation gradient $\mathbf{F}$ and the displacement vector $\mathbf{u}$. Traction vectors are related to σ by $\mathbf{T}=\mathbf{n}\,\sigma$, with $\mathbf{n}$ being the surface normal. $\mathbf{T_e}$ is the traction vector on the external surface of the body. On the internal surfaces S_{int}, the cohesive zone tractions $\mathbf{T_{CZ}}$ and the material separation $\mathbf{\Delta}$ characterize the state of the cohesive zone. The cohesive zone model provides the constitutive relationship characterizing the contribution of the internal surfaces. Cohesive tractions possess normal and tangential components $\mathbf{T_{CZ}} = T_n\mathbf{n} + T_t\mathbf{t}$. Material separation $\mathbf{\Delta} = \Delta_n\mathbf{n} + \Delta_t\mathbf{t}$ is computed from the displacements $\mathbf{u}^+$ and $\mathbf{u}^-$ on corresponding locations on opposing internal surfaces, $+$ and $-$.

Based on the cohesive surface model of Xu and Needleman (1994), the potential is given by

$$\phi = \phi_n + \phi_n \exp\left(-\frac{\Delta_n}{\delta_n}\right)\left[\left(1 - r + \frac{\Delta_n}{\delta_n}\right)\frac{1-q}{r-1} - \left(q + \frac{r-q}{r-1}\frac{\Delta_n}{\delta_n}\right)\exp\left(-\frac{\Delta_t^2}{\delta_t^2}\right)\right] \quad (2.1)$$

23

where material parameters q and r govern the coupling between the normal and tangential response. Abdul-Baqi and Van der Giessen (2001) give a detailed description and investigation of these parameters.

Under monotonic loading the constitutive relationship for the cohesive zone is derived from the above potential function by $T = \partial\phi / \partial\Delta$ and can be written in a form such that tractions T_{CZ} are given as explicit functions of separation Δ, e.g. Needleman (1990) :

$$T_n = \sigma_{max,0}\, e \exp\left(-\frac{\Delta_n}{\delta_0}\right)\left\{\frac{\Delta_n}{\delta_0}\exp\left(-\frac{\Delta_t^2}{\delta_0^2}\right)+(1.0-q)\frac{\Delta_n}{\delta_0}\left[1.0-\exp\left(-\frac{\Delta_t^2}{\delta_0^2}\right)\right]\right\}$$

$$T_t = 2\sigma_{max,0}\, e\, q\,\frac{\Delta_t}{\delta_0}\left(1.0+\frac{\Delta_n}{\delta_0}\right)\exp\left(-\frac{\Delta_n}{\delta_0}\right)\exp\left(-\frac{\Delta_t^2}{\delta_0^2}\right)$$

(2.2)

The cohesive zone parameters in equation (2.2) are the initial cohesive strength $\sigma_{max,0}$ and the cohesive length δ_0, and $e = \exp(1)$. The cohesive energy under monotonic loading is

$$\phi_0 = \sigma_{max,0}\delta_0 e$$

(2.3)

For mode I material separation, equation (2.1) can be simplified to

$$\phi = \phi_n + \phi_n \exp\left(-\frac{\Delta_n}{\delta_n}\right)\left(1+\frac{\Delta_n}{\delta_n}\right)$$

(2.4)

and equation (2.2) to

$$T_n = \sigma_{max,0}e\left(\frac{\Delta_n}{\delta_0}\right)\exp\left(-\frac{\Delta_n}{\delta_0}\right)\ .$$

(2.5)

2.2 Damage Evolution Law

In the case of simulation of cyclic loading and fatigue crack growth the model describes the processes of material separation by a hysteretic constitutive relationship between the cyclically varying tractions and displacement jumps across an interface. Such a model then describes the work spent in the creation of a fatigue fracture surface.

For cyclic loading, the irreversible CZM accounts for the progressive degradation of the cohesive strength during cycling. A cyclic damage variable D_c is introduced. The current value of the damage variable is the ratio between the damaged cohesive zone surface area A_D and the initial undamaged cohesive zone surface area A_0 so that $D_c = A_D / A_0$, e.g. Lemaitre (1996). The constitutive relation for the CZM accounting for D_c is then given by replacing the cohesive zone tractions by the effective cohesive tractions. Consequently, the initial cohesive strength $\sigma_{max,0}$ in equation (2.2) can then be substituted by the current cohesive strength σ_{max} defined as

$$\sigma_{max} = \sigma_{max,0} \left(1 - D_c\right) \tag{2.6}$$

To obtain the current state of damage, a description of the evolution of damage is needed in the form of $\dot{D}_c = \dot{D}_c \left(\mathbf{T}_{CZ}, \Delta, D_c\right)$. An evolution equation for D_c - in line with the characteristics of continuum damage evolution laws - is based on the following properties:

- Damage accumulation starts if a deformation measure, accumulated or current, is greater than a critical magnitude.

- There exists an endurance limit which is a stress level below which cyclic loading can proceed infinitely without failure.

- The increment of damage is related to the increment of absolute value of deformation as weighted by the ratio of current load level relative to strength.

Based on these three requirements the evolution for $\dot{D}_c$, was introduced by Roe and Siegmund (2001, 2003) as:

$$\dot{D}_c = \frac{|\dot{\Delta}|}{\delta_\Sigma} \left[\frac{\overline{T}}{\sigma_{max}} - \frac{\sigma_f}{\sigma_{max,0}} \right] H\left(\overline{\Delta} - \delta_0\right) \quad \text{and} \quad \dot{D}_c \geq 0 \tag{2.7}$$

with H designating the Heaviside function and $\overline{\Delta}$ an accumulated effective material separation. The effective separation Δ and its increment, $\dot{\Delta}$ are defined as $\Delta = \sqrt{\Delta_n^2 + \Delta_t^2}$ and $\dot{\Delta} = (\Delta^t - \Delta^{t-\Delta t})/\Delta t$. The accumulated effective separation is $\overline{\Delta} = \int \dot{\Delta} \, dt$. The effective traction $\overline{T}$ is defined as $\overline{T} = \sqrt{T_n^2 + T_t^2 / (2 e q^2)}$ such that equal

25

weight is given to both traction components. For mode I loading, equation (2.6) can be described by:

$$\dot{D}_c = \frac{|\dot{\Delta}_n|}{\delta_\Sigma}\left[\frac{T_n}{\sigma_{max}} - \frac{\sigma_f}{\sigma_{max,0}}\right]H\left(\Delta_{n,acc} - \delta_0\right) \quad \text{if} \quad \dot{D}_c \geq 0 \qquad \Delta_{n,acc} = \int_t |\dot{\Delta}_n| dt \quad (2.8)$$

Two cohesive zone material parameters are introduced to characterize the cyclic degradation behavior. The cohesive zone endurance limit σ_f is the highest traction or range of traction that can be repeated indefinitely without failure of the cohesive zone. As a consequence no damage accumulation occurs if the cohesive traction normalized by the current cohesive strength is less than the ratio between the cohesive zone endurance limit and the initial cohesive strength. The second parameter, the accumulated cohesive length δ_Σ, normalizes the increment of material separation, and therefore determines the magnitude of the damage increment that occurs at a given state of load. This value of this parameter determines the number of cycles to failure at a load level just above the endurance limit, i.e. it provides the location of the "knee" in an S-N diagram. Furthermore, in equation (2.6) a threshold for damage accumulation is introduced below which no damage accumulation occurs. Both theoretical considerations, Lemaitre (1996), as well as experimental data from high resolution damage measurements, e.g. Gerberich et al. (1998), indicate the necessity to account for this threshold. The threshold to initiation of damage accumulation is overcome if the accumulated effective material separation $\overline{\Delta}$ is greater than a critical value of material separation. Here, the threshold was chosen to be equal to the cohesive length δ_0. Once the threshold is overcome the magnitude of the increment of damage is proportional to the normalized increment of separation $|\dot{\Delta}|/\delta_\Sigma$ weighted by a normalized measure of current traction reduced by the normalized endurance limit.

A CZM based on equation 2.7 is used throughout the main part of this study, however, in Chapter 8 a novel cohesive zone model is developed based on the mechanics of dislocations. That CZM interestingly provides similar features as the CZM defined in equation 2.7.

2.3 Unloading/Reloading

Even with the introduction of the cohesive strength degradation unloading can still occur along a path with increasing traction following equation (2.2). Such a load path is unreasonable for a damageable solid, and thus separate unloading and reloading paths are defined for both normal and tangential material separation. For normal separation unloading is assumed to occur to the origin of the traction-separation function. The unloading-reloading condition for normal separation is given by:

$$T_n = T_{n,\max} + \left(\frac{T_{n,\max}}{\Delta_{n,\max}}\right)(\Delta_n - \Delta_{n,\max}) \qquad (2.9)$$

In equation (2.6), $\Delta_{n,\max}$ is the maximum value of normal separation that has been reached for a specific cohesive zone location. $T_{n,\max}$ is the normal traction corresponding to $\Delta_{n,\max}$ and is computed from equation (2.2) with $\sigma_{\max,0}$ replaced by $\sigma_{\max}$. Consequently, the cohesive zone model by itself does not introduce a residual separation across a crack after a load-unload cycle in mode I loading. Crack closure and crack surface contact only arises as a result of the plastic deformation in the continuum surrounding the cohesive zone. For crack growth along the interface between the two solids crack growth is mixed mode, and the unloading-reloading behavior in the tangential direction is also of concern. In mode II loading of a crack it is known that roughness induced crack closure can be significant, Tong et al. (1995). Interaction of crack surfaces arising as a result of the cohesive zone only needs thus be modeled. Residual material separation after a completed load-unload cycle is introduced. Unloading in tangential direction occurs with the current stiffness of the cohesive zone at $\Delta_t = 0$, i.e. $\partial T_t / \partial \Delta_t = \sqrt{2e}\tau_{\max}/\delta_0$. The unloading-reloading condition for tangential separation is then given by:

$$T_t = T_{t,\max} + \sqrt{2e}\left(\frac{\tau_{\max}}{\delta_0}\right)(\Delta_t - \Delta_{t,\max}) \qquad (2.10)$$

In equation (2.10), $\Delta_{t,\max}$ is the maximum value of tangential separation that has been reached for a specific cohesive zone location. $T_{t,\max}$ is the tangential traction corresponding to $\Delta_{t,\max}$ and is computed from equation (2.2) with $\sigma_{\max,0}$ replaced by $\sigma_{\max}$.

A crack surface contact model is formulated in the context of the cohesive zone model. The traction-overclosure relationship equation follows a modification of equation (2.2) such that a high penalty stiffness is prescribed for the case of $\Delta_n < 0$:

$$T_n = K\left(\frac{\Delta_n}{\delta_0}\right)\exp\left(-\frac{\Delta_n}{\delta_0}\right) \tag{2.11}$$

Here, simulations were performed with $K = 30\sigma_{\max,0}e$. In contact, the cohesive tractions are less than zero and no damage accumulation occurs.

The irreversible CZM was implemented for the commercial finite element code ABAQUS by use of the UEL subroutine feature. The damage variable was defined on averaged variables per element (Roe and Siegmund, 2003). The location of the current crack tip is defined by the condition $D_c = 1.0$, and the crack growth is denoted by Δa.
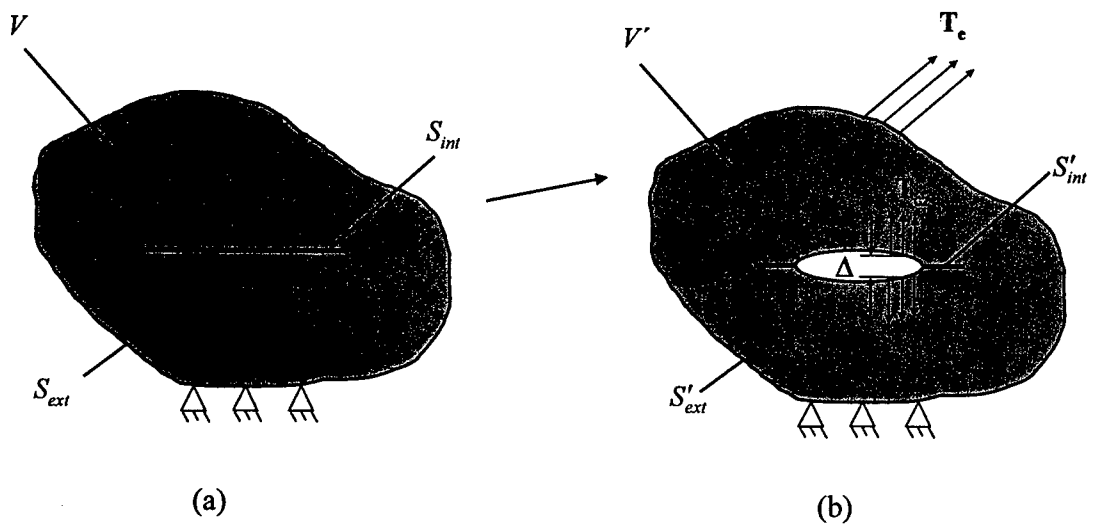
Figure 2.1: Schematic drawing of conceptual frame work of cohesive zone model, (a) Undeformed configuration, (b) Deformed configuration.

LIST OF REFERENCE

Abdul-Baqi, A. and Van der Giessen, 2001, "Indentation-induced Interface Delamination of a Strong Film on a Ductile Substrate", Thin Solid Films, Vol. 381, pp. 143-154.

Gerberich, W.W., Harvey, S.E., Kramer, D.E., Hoehn, J.W., 1998, "Low and high cycle fatigue—a continuum supported by AFM observations", *Acta Mater.*, Vol. 46, pp. 5007-5021.

Lemaitre, J., 1996, "A Course on Damage Mechanics", *Springer-Verlag, Berlin.*

Needleman ,A., 1990, "An analysis of decohesion along an imperfect interface", *Int. J. Fract.* Vol. 42, pp. 21-40.

Roe, K.L., Siegmund, T., 2001, "Simulation of interface fatigue crack growth via a fracture process zone model", *Proc. 1st M.I.T. Conf Comp Fluids Solid Mech*, Boston, MA, K.J. Bathe, ed., Elsevier, pp. 435-437.

Roe, K.L., Siegmund, T., 2003, "An irreversible cohesive zone model for interface fatigue crack growth simulation", *Eng. Fract. Mech.* Vol. 70, pp. 209-232.

Tong, J., Yates, R., Brown, M.W., 1995, "A model for sliding mode crack closure part I: Theory for pure mode II loading", *Eng. Fract. Mech.* Vol. 52, pp. 599-611.

Xu, X.P., Needleman, A., 1994, "Numerical Simulations of Fast Crack Growth in Brittle Solids", *J. Mech. Phys. Solids*, Vol. 42, pp. 1397-1434.

3. CONSTRAINT EFFECTS IN FATIGUE CRACK GROWTH

The analysis of constraint effects in FCG in multilayer structures is discussed. The constraint effects due to the different metal layer thickness and *T*-stress are of concern. A modified boundary layer model is used in simulations of FCG along the centerline crack of the metal layer sandwiched between two elastic substrates. FCG is computed for a series of values of metal layer thickness and *T*-stress under constant and variable amplitude loading conditions. The results of the computations demonstrate that certain combinations of load magnitude, layer thickness and material properties results in significantly constraint effects in FCG. The influence of these constraint effects on FCG rates and on crack closure processes is determined. The evolutions of the traction-separation law, the accumulated and current plastic zones, as well as the stress fields during the crack propagation are discussed. The FCG resistance and crack closure levels are determined as the function of *T*-stress for the different metal layer thicknesses. The results indicate that overloads under consideration of positive *T*-stresses tend to reduce the amount of crack retardation while negative *T*-stresses of the same magnitude increase crack retardation.

3.1. Introduction

Thin film multi-layer structures are widely used in many applications of technological importance. The multi-layer structures of interest here are those where a metallic layer is sandwiched between two elastic substrates. In the use of such structures

crack growth along the metallic thin film and along the interfaces to the substrate is of concern (Varias *et al.*, 1991; Evans and Hutchinson, 1995; Dauskardt *et al.*, 1998). As the film thickness decreases, the crack growth behavior under monotonic and cyclic loading becomes increasingly complex. One of the important issues to be considered in this context is that of the influence of constraint. As the thickness of individual layers in the structure is decreased, the monotonic and cyclic plastic zones present at a crack tip start to interact with the surrounding elastic substrates. Then the conventional FCG analysis methodologies based on the assumption of small-scale yielding loose their validity. From a practical perspective, the constants in the Paris equation (Paris *et al.*, 1961) will depend on the film thickness such that the transferability of FCG data among specimens with the different layer thicknesses is lost. Consequently, to enable the design of fatigue resistant multi-layer structures at small scales, a new approach for FCG analysis is needed.

Only few experimental studies on FCG in metal-ceramic multilayer structures have been reported. McNaney *et al.* (1996) studied FCG and fracture toughness behavior of a metal/ceramic sandwich geometry based on the Al/Al$_2$O$_3$ system. For the values of metal layer thickness considered no effect of constraint on the FCG rate was observed, while the energy absorption per loading cycles was observed to be dependent on the layer thickness. Also, FCG was considerable faster in the multilayer specimens when compared to pure Al samples. More recently, Kruzic, *et al.* (2004) carried out another experimentally study using samples with smaller values of metal layer thickness. There, for the near threshold regime a decrease in FCG rate was observed for decreasing values of the metal layer thickness. For larger values of applied load, the crack growth resistance again was observed as essentially independent of the metal layer thickness.

Past investigations of crack growth in multilayer material systems have demonstrated that the constraint effects arising in fracture of such specimens can be investigated well by use of the so-called Cohesive Zone Model (CZM) approach. The CZM concept uses a constitutive equation connecting the crack surface tractions and material separation across the crack, see Dugdale (1960), Barenblatt (1962), and Needleman (1990). A review on the application of the CZM approach to studies of crack growth under monotonic loading can be found in Hutchinson and Evans (2000).

Specifically, applications of the CZM approach to studies of crack growth in multi-layer structures under monotonic loading were presented in Tvergaard and Hutchinson (1994, 1996), Lin et al. (1997), Lane et al. (2000). There, the crack growth behavior of a crack lying along one of the interfaces of a thin ductile layer joining two elastic solids was computed. It was demonstrated that the interaction of the plastic zone with the elastic substrates significantly alters the energy dissipation processes during crack growth. These constraint effects on the ductile layer can significantly influence the apparent fracture toughness of the material system.

For the numerical simulations of FCG under cyclic loading, irreversible cohesive zone laws describing material separation under cyclic loading were recently developed. These models are promising to studies of FCG in the range of loads where the Paris law is traditionally applied. de-Andrés et al. (1999) added unloading conditions to a traction-separation law used in monotonic loading in conjunction with a cycle dependent damage variable to study FCG under large scale yielding. Similarly, Desphande et al. (2002) used such a traction-separation law in combination with discrete dislocation plasticity and determined both threshold values and powers in the Paris equation. Nguyen et al. (2001) developed a CZM based on irreversible unload-load relations. The model was applied to study FCG in macroscopic aluminum specimens. Constant amplitude loading as well as the effects of overloads on FCG rates were investigated. A similar idea was applied in Yang et al. (2001) together with a maximum principal stress criterion to study FCG in a brittle polymer. Roe and Siegmund (2001, 2003) and Siegmund (2004) simulated FCG at interfaces using an irreversible cohesive zone model which includes a cyclic damage evolution rule for the cohesive strength.

In addition to the constraint effects imposed by the elastic substrate, the type of loading imposes another type of constraint effects. This influence is discussed by the concept of T-stress. Based on the asymptotic expansion solution of Williams (1957), the stress field around the crack tip can be expressed as

$$\sigma_{ij} = \frac{K_I}{\sqrt{2\pi r}} f_{ij}^I(\theta) + \frac{K_{II}}{\sqrt{2\pi r}} f_{ij}^{II}(\theta) + T\delta_{1i}\delta_{1j} + O(r^{1/2}) \tag{3.1}$$

where σ_{ij} denotes the stress tensor, K_I and K_{II} are the modes I and II stress intensity factors, respectively. The parameter T is the nonsingular elastic stress contribution and $f_{ij}(\theta)$ are angular functions. Several investigations were conducted in the past to determine the dependence of crack closure, and thus the effective stress intensity factor, on the specimen geometry or the applied stress state (Fleck, 1986; McClung, 1994; Solanki, et al., 2004; Roychowdhury and Dodds, 2004). Thereby it is convenient to characterize the applied load by a two-parameter description using a combination of stress intensity factor, K and the T-stress. Specific levels of T-stress then describe the influence of certain specimen geometries, or the biaxiality ratio of the loading condition. Studies of the effect of the T-stress were almost exclusively related to constant amplitude loading cases and overloads were rarely considered (Sadananda, et al., 1999). Here, we are interested in a study that sheds light on the combined effects of T-stress and metal layer thickness on constant and variable amplitude FCG.

The CZM approach allows one to capture constraint effects in fatigue because energy dissipation due to cyclic material separation at the crack tip and due to the cyclic plastic deformation in the metal layer is accounted for independently. Computations are performed by using a modified boundary layer approach under the condition that the plastic deformation is confined to a metal film of thickness considerably smaller than all other dimensions of the structure. Results of FCG simulations along the centerline of the constraint metal layer were performed.

3.2 Model Description

3.2.1 The Irreversible Cohesive Zone Model

The irreversible cohesive zone model introduced in Chapter 2 is used here to characterize material separation under cyclic mode I loading. For the purpose of the present simulations, the cohesive energy is assumed as $\phi_0 = 20$ J/m^2 except for the noted

places. In all computations except the parametric study the initial cohesive strength, $\sigma_{max,0}$, is chosen to be $E_s/100$, with E_s the Young's modulus of the surrounding solids. The values of $\sigma_f/\sigma_{max,0} = 0.25$ and $\delta_\Sigma/\delta_0 = 4$ are selected for the computations.

3.2.2 Material Properties

The material properties of elastic substrate is described by Young's modulus, E_s and Poisson's ratio, ν_s. The°elastic properties of the elastic-plastic layer are designated by E_l and ν_l. In all of the calculations, the metal layer and the adjoining elastic substrates are taken to have identical isotropic elastic properties, i.e. $E_s = E_l = 100$ GPa and $\nu_s = \nu_l = 0.34$. The elastic-plastic layer is characterized by a linear kinematic hardening model with constant hardening modulus, E_T. The yield strength used in the simulations was $\sigma_Y/E_l = 0.0025$ and the hardening modulus is assumed as $E_s/20$. Then, for all computations except for the parametric study and specific noted places the ratio between initial cohesive strength and yield strength is $\sigma_{max,0}/\sigma_y = 4$.

The combination the cohesive zone properties with those of the adjacent solid can be used to obtain a reference plastic zone size, $r_{pl,0}$:

$$r_{pl,0} = \frac{1}{3\pi\left(1-\nu^2\right)} \frac{E\phi_0}{\sigma_Y^2} \tag{3.3}$$

The ratio of the current active plastic zone size at $t = 0.5$ to the reference plastic zone size is then obtained by substituting the cohesive energy in equation (3.3) with the load range ΔG.

3.2.3 Finite Element Model

The crack is assumed to propagate along the center of the metal layer of height, $2h_l$, sandwiched between two elastic substrates. Only mode I crack propagation is thus of concern. The geometry of the problem addressed is shown in Figure 3.1.

In the simulations of FCG a modified boundary layer approach is used. Following mode I asymptotic crack tip solutions for linear elastic materials, loading is provided by describing time, t, varying displacements $u_x(t)$, $u_y(t)$ on the outer boundary as:

$$u_x(t) = K_I(t)\sqrt{\frac{r}{2\pi}}\frac{1+v}{E}\cos\frac{\theta}{2}(3-4v-\cos\theta) + T(t)\frac{1-v^2}{E}r\cos\theta$$

$$u_y(t) = K_I(t)\sqrt{\frac{r}{2\pi}}\frac{1+v}{E}\sin\frac{\theta}{2}(3-4v-\cos\theta) - T(t)\frac{v(1+v)}{E}r\sin\theta$$

(3.4)

where $r = \sqrt{x^2+y^2}$ and $\theta = \tan^{-1}(y/x)$ are polar coordinates of points on the remote outer boundary. $K_I(t)$ and $T(t)$ represent the mode I stress intensity factor and T-stress, respectively. Simulations are conducted for $K_I(t) = \Delta K(0.5 - 0.5\cos 2\pi t)$, i.e. a load ratio of $R=0.0$ and an amplitude of ΔK. The range of the stress intensity factor ΔK is related to the range of the energy release rate ΔG as

$$\Delta K = \sqrt{\frac{E\Delta G}{(1-v^2)}}$$

(3.5)

The T-stress varies in phase with K as $T(t) = T_{max}(0.5 - 0.5\cos 2\pi t)$. Due to the nature of symmetry for the model under mode-I loading, only half of the model is considered. Figure 3.2(a) displays the global finite element mesh. The element arrangement near the crack tip is shown in Figure 3.2(b). The initial crack tip is located at point O. At the crack tip, there is a highly refined mesh region with length L. The length of one square element in this uniformly meshed region is denoted by l. Most of the computations were carried out for dimensions $r = 10000l$ and $L = 110l$. The smallest element size l is selected as $2.5\delta_0$. The ratio of element size l to cohesive length δ_0 was used as a measure of mesh refinement since all length parameters in the study are normalized with this quantity. Aspects of the mesh refinement are further discussed in the next section.

In the finite element model, four nodes plain strain elements are used. A row of cohesive zone elements was placed along the symmetry line of the model from the initial crack tip to the outer boundary. These elements use nodes on the line of symmetry as two of their nodes. The second pair of nodes of the cohesive zone elements is those in common with the adjacent solid elements. The typical finite element mesh consists of 3892 solid elements and 123 cohesive zone elements.

3.3 Results and Discussions

3.3.1 Geometry Constraint Effects in FCG

Firstly, constraint effects in FCG in dependence on different metal layer thicknesses are considered. FCG is computed for a series of values of metal layer thickness under constant and variable amplitude loading conditions (T=0).

3.3.1.1 Constant Amplitude Loading

The first set of results presented was obtained from cyclic loading under constant amplitude loading with $R = 0.0$. The dependence of the crack growth rate on the load magnitude, the metal layer thickness, and on the cohesive strength is investigated. Special attention is paid to determine the presence of eventual crack closure events.

At first, the fatigue crack behavior in dependence of the applied load level is predicted. Figure 3.3 shows a log-log plot of the predicted normalized FCG rates, $\mathrm{d}(a/\delta_0)/\mathrm{d}N$, in dependence of the normalized applied energy release rate range, $\Delta G/\phi_0$, for two cases: (a) a system with a metal interlayer of size $h_l/\delta_0 = 10$ between two elastic substrates, and (b) a system where the interface is located between two ductile substrates, $h_l/\delta_0 \to \infty$. Thus these two cases compare FCG in a geometry without constraint to that with considerable constraint. In the given range of $\Delta G/\phi_0$ a close to linear dependence of $\log[\mathrm{d}(a/\delta_0)/\mathrm{d}N]$ on $\log(\Delta G/\phi_0)$ is predicted in both cases such that it would be

reasonable to describe the outcome of the computation by use of the Paris-law, $d(a/\delta_0)/dN = C(\Delta G)^m$. The present computations predict $m \approx 2$. At low load levels for both cases the same values of crack growth rate are predicted for both cases. However, when $\Delta G/\phi_0$ is larger than about 0.1, different crack growth rates are obtained. The constraint layer geometry exhibits higher FCG rate than the unconstraint layer system. Figure 3.4 depicts the increase in FCG rate of the system $h_l/\delta_0 = 10$ over that for $h_l/\delta_0 \to \infty$, as $\{[d(a/\delta_0)/dN]_{h_l/\delta_0=10} - [d(a/\delta_0)/dN]_{h_l/\delta_0\to\infty}\}/[d(a/\delta_0)/dN]_{h_l/\delta_0\to\infty}$ in dependence of the applied load range, $\Delta G/\phi_0$. Again, it is shown that for low levels of load, $\Delta G/\phi_0 < 0.1$, the two systems show identical crack growth rates. For higher values of $\Delta G/\phi_0$ the simulations produced a nearly linear dependence of the increase in FCG rate for $h_l/\delta_0 = 10$ over that for $h_l/\delta_0 \to \infty$. For $\Delta G/\phi_0 = 0.35$, the increase in the FCG rate for $h_l/\delta_0 = 10$ over that for $h_l/\delta_0 \to \infty$ is around 42%.

Next, simulations were carried out to determine the dependence of the FCG rate on the layer thickness, h_l/δ_0. The results were obtained from simulations with $\Delta G/\phi_0 = 0.25$, $R=0$ and $\sigma_{max,0}/\sigma_Y = 4$. Figure 3.5(a) depicts the predicted increase in steady state FCG rate for various values of h_l/δ_0 over that for $h_l/\delta_0 \to \infty$ as $\{[d(a/\delta_0)/dN]_{h_l/\delta_0} - [d(a/\delta_0)/dN]_{h_l/\delta_0\to\infty}\}/[d(a/\delta_0)/dN]_{h_l/\delta_0\to\infty}$ in dependence of the layer height, h_l/δ_0. For the material parameters and the loading considered, a metal layer of height $h_l/\delta_0 > 120$ is needed such that constraint effects vanish, and the predicted FCG rate for the multi-layer geometry equals that of a model with elastic-plastic material properties everywhere. As the height of the metal layer is decreased, the FCG rate then increases. The maximum increase in FCG rate over that for $h_l/\delta_0 \to \infty$ is found to be 0.2. This value is reached for metal layer thickness of $h_l/\delta_0 \leq 10$. Beyond this value of layer height a further decrease in h_l/δ_0 has virtually no effects on the FCG rate. FCG rates predicted for the system consisting of two elastic substrates joined by the cohesive zone without the elastic-plastic layer, $h_l/\delta_0 = 0$, show the same values as those of

$h_l / \delta_0 = 10$. Figure 3.5(b) depicts the peak values in normal tractions reached during steady state FCG. As the cohesive zone formulation allows for the evolution of the cohesive strength, constraint not only affects the amount of plastic deformation but also the cohesive parameter evolution. If the layer thickness is small, high values of normal tractions develop but diminish as the height of the metal layer increases.

The cyclic traction-separation response at the location $\Delta a = 125 \delta_0$ for $h_l / \delta_0 = 10$ and $h_l / \delta_0 \to \infty$ are given in Figure 3.6(a) and 3.6(b), respectively. Damage accumulation due to cyclic loading degrades the cohesive strength leading to a continuous change in the traction-separation path, including a reduction in the stiffness of the loading/unloading path. As the traction values as well as the unloading/reloading stiffness decrease, the cohesive zone finally looses in load carrying capacity and material failure occurs. Comparison of Figure 3.6(a) and Figure 3.6(b) shows the higher values of traction and separation predicted for the case of $h_l / \delta_0 = 10$. In view of equation (2.5), these two effects are responsible for higher rates of damage accumulation and subsequently for the higher FCG rate. Furthermore, we want to focus attention on the traction values at $\Delta_n = 0$. For $h_l / \delta_0 \to \infty$, negative values of traction are predicted for $\Delta_n < 0$. This behavior indicates contact of the opposing crack faces, i.e. crack closure. For $h_l / \delta_0 = 10$, no negative values of traction are predicted indicating the absence of crack closure.

A more conventional depiction of crack closure employs the predicted crack opening profiles and opening stresses at the crack tip. Figure 3.7(a) depicts the predicted crack opening profiles, Δ_n / δ_0, obtained at the minimum load in the fatigue cycle for the system $h_l / \delta_0 = 10$ and $h_l / \delta_0 \to \infty$. Data are presented for a growing fatigue crack at the end of the 29th load cycle. The corresponding normalized crack extension, $\Delta a / \delta_0$, is equal to 82.5 for the case $h_l / \delta_0 = 10$ and 62.5 for the case $h_l / \delta_0 \to \infty$, respectively. For $h_l / \delta_0 \to \infty$ pronounced crack closure is present. The location of the closure zone with respect to the distribution of the damage variable, D_c, can be assessed by comparing the

crack opening profiles of Figure 3.7(a) to the corresponding distribution of D_c shown in Figure 3.7(b). Crack closure occurs at locations corresponding to values $D_c = 1$ and $D_c = 0.32$. For the present choice of parameters, for $D_c > 0.32$ the cohesive strength has already dropped to a value less than $3\sigma_y$. For such values of cohesive strength little or no plastic deformation is present in the solid adjacent to the cohesive zone. The area of crack closure is thus located in the wake of the location of maximum rate of plastic deformation which occurs at locations with $D_c < 0.25$ with a cohesive strength larger than $3\sigma_y$. In a situation of high mechanical constraint, $h_l / \delta_0 = 10$, the crack is predicted to remain open even under minimum load. Figure 3.8 gives the crack opening stress, σ_{22}, obtained at the several different time instances. The points 1 and 5 represent the maximum load points, 2 and 4 represent intermediate load points at $t=0.25$ and $t=0.75$, respectively, and 3 represents the minimum load. For the maximum and intermediate load points, the constraint layer system obtains a higher opening stress level which is responsible for the higher FCG rate. For the minimum load point, the negative opening stress values indicate the crack closure characteristic for the system with no constraint effects. Contact pressures predicted will depend on the specifics of the contact law employed.

The results on the damage distribution presented in Figure 3.7(b) provide an indication of the resolution of the active cohesive zone relative to the element size, l. In general, the length of the active cohesive zone depends in on the cohesive energy, the cohesive strength, the properties of the background continuum, and also on the mechanical constraint. Furthermore, in the cyclic loading case the length of the active cohesive zone depends on the load level and the load history. For the results of Figure 3.7(b) with $\Delta G / \phi_0 = 0.15$ it can be seen that the active cohesive zone is of length approximately $90\,\delta_0$ or $36\,l$. Even for calculations with the lowest level of loading considered in the present study, $\Delta G / \phi_0 = 0.05$, the active cohesive zone is of length approximately $40\,\delta_0$ or $16\,l$. The mesh density is therefore sufficiently refined such that the active cohesive zone spans multiple elements.

In Figure 3.9(a) the FCG resistance, $dN/d(a/\delta_0)$ is depicted independence of the normalized interface strength, $\sigma_{max,0}/\sigma_Y$, for several values of the different thickness of the metal layer. The results are obtained under a constant ratio of load range to initial cohesive energy, $\Delta G/\phi_0 = 0.25$. The results demonstrate that increased values of interface strength, $\sigma_{max,0}/\sigma_Y$, will increase the FCG resistance as will the increase in the metal layer thickness, h_t/δ_0. The rate of increase of FCG resistance with $\sigma_{max,0}/\sigma_Y$ depends on h_t/δ_0. For all values of h_t/δ_0 the FCG resistance depends linearly on $\sigma_{max,0}/\sigma_Y$ if $\sigma_{max,0}/\sigma_Y < 3.5$. For high values of $\sigma_{max,0}/\sigma_Y$ the dependence of the FCG resistance on the cohesive strength is linear in the absence of plastic deformation, but nonlinear of plastic deformation occurs in the background material. For $h_t/\delta_0 = 0$, i.e. in the absence of plasticity, the FCG resistance depends linearly on $\sigma_{max,0}/\sigma_Y$ even for large values of the interface strength. For all other values of h_t/δ_0 a strong increase in FCG resistance occurs once the normalized interface strength exceeds $\sigma_{max,0}/\sigma_Y = 4$. For such values of cohesive strength, plasticity starts to contribute significantly to the energy dissipation at the crack tip. Figure 3.9(b) depicts the maximum normal traction values computed for $h_t/\delta_0 = 60$. In general, the ratio between the maximum traction value developing and the yield strength increases. In the range of $\sigma_{max,0}/\sigma_Y < 4$, i.e. when plasticity plays no or only a minor role in the crack tip processes, the dependence of $\max(T_n)/\sigma_Y$ is stronger than for higher values of $\sigma_{max,0}/\sigma_Y$.

Contour plots of the equivalent plastic strain obtained for constant amplitude loading condition for three different values of metal layer thickness, $h_t/\delta_0 \to \infty$, 30 and 15, respectively, are given in Figure 3.10. Contour plots are obtained for $\Delta a/\delta_0 = 135$ under the condition of $\Delta G/\phi_0 = 0.125$, $\sigma_{max,0}/\sigma_Y = 4$ at $t=0.5$. The active plastic zone is depicted by the white contour line. In Fig. 10a, in the absence of constraint the plastic zone is fully developed. The accumulated plastic zone behind the current crack tip possesses nearly constant height. The height of the active plastic zone, as defined by the

contour of $\dot{\bar{\varepsilon}}_{pl} = 1 \times 10^{-4}$, and the height of accumulated plastic zone, as defined by $\dot{\bar{\varepsilon}}_{pl} = 0.005$, is $0.125 \times r_{pl,0}$. The size of the constraint plastic zone scales with the prediction of equation (3.3) of the cohesive energy is substituted by ΔG. For $h_l / \delta_0 = 30$ or 15, Figure 3.10(b) and 3.10(c), the plastic zone is constraint such that the value of most intense plastic deformation borders the interface between the metal layer and the elastic substrate. As the layer thickness is decreased the shape of the active plastic zone starts to spread slightly in the horizontal direction. The size of the active plastic zone at the interface between substrate and metal film is approximately equal to $2 \times h_l$.

3.3.1.2 Variable Amplitude Loading

Results presented in this section describe simulations conducted under consideration of a single overload. Initially, a constant amplitude loading of magnitude $\Delta G / \phi_0 = 0.15$ was applied. Then, in cycle $N=25$ an overload with magnitude $\Delta G / \phi_0 = 0.45$ was applied. Subsequently, loading is continued with the original constant amplitude. The remaining model and parameters used are identical to those for the constant amplitude loading cases.

The results of predicted normalized crack extension, $\Delta a / \delta_0$, vs. the cycle number, N are plotted in Figure 3.11. The results of normalized FCG rate, $d(a/\delta_0)/dN$, vs. the crack extension $\Delta a / \delta_0$ are plotted in Figure 3.12. In the absence of constraint, $h_l / \delta_0 \rightarrow \infty$, the overload first results in an instantaneous crack extension at the application of the overload, followed by a significant crack retardation. Such a response to an overload is well-known in fatigue of metals, Suresh (1998). As the crack retardation after the overload is considerably more significant than the crack jump at the overload a permanent lag in the crack extension results.

The overload behavior changes significantly as the plastic deformation is constraint and finally is absent. For all values of h_l / δ_0 an instantaneous crack advance was found at

the instance of the overload, with similar crack growth rates in the overload cycle, Figure 3.12. The constraint effects provided by decreasing values of h_l / δ_0, however, determine the crack growth behavior following the overload cycle.

In the absence of plastic deformation, $h_l / \delta_0 = 0$, or for only small values of the height of the metal layer, the overload causes an instantaneous crack advance and a temporarily increased crack growth rate in the cycles following the overload, Figure 3.12. For intermediate values of the height of the ductile layer, $20 < h_l < 60$, the crack growth behavior is found to be a combination of the two limiting cases $h_l / \delta_0 \to \infty$ and $h_l / \delta_0 \to 0$. The overloads result in a sequence of crack acceleration-deceleration-acceleration segments with the final behavior depending on the metal layer height. For the present simulations the crack acceleration events dominate over the deceleration events such that for all simulations with a constraint metal layer an additional permanent crack advance over the constant amplitude cases is predicted, see Figure 3.11.

The response to the overload is the result of two competing processes, the plastic deformation and the evolution of damage in the cohesive zone. To document the competition between these two processes during an overload event the evolution of the plastic zones and of the traction separation response is needed. Figure 3.13 depicts size of the active plastic zone size, $r_{pl} / r_{pl,0}$, present at a given value of crack extension, $\Delta a / \delta_0$. For $h_l / \delta_0 \to \infty$ the extension of the active plastic zone is measured as the maximum diameter of the active plastic zone, i.e. along a line of angle 68° to the crack growth direction. For $h_l / \delta_0 = 15$ the maximum extension of the active plastic zone is present at the metal layer-substrate interface. The definitions use to measure the plastic zone sizes are depicted in Figure 3.10. For the four locations identified in Figs. 13, the normalized traction-separation curves are plotted in Figure 3.14. The material element at location (1) failed before the overload, at location (2) during the overload cycle and at locations (3) and (4) after the overload.

Before the overload at N=25, the size of the active plastic zone scales with $\Delta G / \phi_0$ for $h_l / \delta_0 \to \infty$. For $h_l / \delta_0 = 10$ the size of the active plastic zone is given by the

geometry of the problem and equal twice the height of the metal layer. At the overload, an increased amount of plastic deformation is induced. For $h_l / \delta_0 \to \infty$ the plastic zone size nearly reaches the value of $r_{pl,0}$, an increase in size by a factor of six. For $h_l / \delta_0 = 10$ the increase in the plastic zone size at the overload is less. Here, r_{pl} only increased by a factor of 1.4.

For $h_l / \delta_0 \to \infty$ the plastic deformation induced at the overload spreads for a significant distance along the crack growth direction. Then, at locations where failure occurs at $N>25$ (after the overload) no active plastic zone develops as the crack tip passes through. Only as the crack has grown an additional distance of $\Delta a / \delta_0 = 75$, equivalent to 37 load cycles after the overload, plastic deformation is again observed. Finally, after 65 cycles passed the overload or at an additional crack extension of $\Delta a / \delta_0 = 175$ past the overload, the size of the plastic zone returns to its initial size.

For $h_l / \delta_0 = 10$ the plastic deformation induced at the overload spreads a comparatively short distance along the crack growth direction. Consequently, the segment of crack growth without an active plastic zone developing is short. As the crack has grown a distance of $\Delta a / \delta_0 = 33$, equivalent to 10 load cycles after the overload, plastic deformation is again observed at the same magnitude as before the overload.

The material separation process – including the development of crack closure – is subsequently assessed by investigating the traction-separation curves depicted in Figure 3.14.

For $h_l / \delta_0 \to \infty$, the traction-separation response at location (1), Figure 3.13(a), is essentially the same as the one depicted in Figure 3.6(a), albeit the difference in load magnitude. The peak traction value is $T_n / \sigma_{max,0} = 0.57$, and thus only slightly larger than $2\sigma_Y$. At the material point failing during the overload, (2) in Figure 3.13(a), the increased applied load magnitude at the overload manifests itself primary in a large displacement jump excursion. For a material point located in front of the crack tip at $N=25$, but located within the zone in which damage actually accumulates, the overload affects the traction level significantly. At this location and at $N=25$ the peak traction

value reached is approximately $T_n / \sigma_{max,0} = 0.68$. Such a large value of cohesive traction allows for the development of a significant amount of plastic deformation to be induced, Figure 3.13. Consequently, a significant amount of crack closure is induced. The level of crack closure pressure at location (3) is significantly above that predicted for the steady state crack growth regime, location (1) and (4). The enhanced crack closure is responsible for the reduction in crack growth and supersedes all accelerating effects due to the increased damage accumulation rate. The residual effects of this plastic zone at overload are so significant that as the crack tip passes through location (3), no active plastic zone is present then. Past the overload, the traction values at (3) are lower than those for location (1) and (2) due to the additional damage induced in the overload cycle. Material points remote from the crack tip at N=25, location (4) in Figure 3.14(a), are only little affected by the overload.

For $h_l / \delta_0 = 10$ the sequence of the traction-separation response at locations (1) to (4) is similar to that described for $h_l / \delta_0 \rightarrow \infty$, except for the evolution at locations near the crack tip at N=25. At that location, (3) in Figure 3.13(b), the increase in peak traction during the overload cycle is considerably more significant with the peak traction reaching $T_n / \sigma_{max,0}$=0.83. At this value of peak traction the material separation enters the softening branch during the overload cycle. However, since plastic deformation is inhibited due to the presence of the elastic substrates, these large traction values do not lead to a significant amount of plastic deformation. Instead, the damage evolution is accelerated. No crack closure is observed in the traction-separation response for $h_l / \delta_0 = 10$, not even at location (3). Thus, a retardation of crack growth does not occur.

3.3.2 Constraint Effects in FCG due to T-stress

Constraint effects in FCG due to T-stress is considered. The combined effects of T-stress and the different metal layer thicknesses on FCG are computed under constant and variable amplitude loading conditions.

3.3.2.1 Constant Amplitude Loading

For the case of constant amplitude loading the description of results focuses on the steady state crack growth behavior in its dependence on the prescribed T-stress and the metal layer thickness.

Figure 3.15 depicts a summary of the FCG resistance, $dN/d(a/\delta_0)$, computed for the normalized applied energy release rate range of $\Delta G/\phi_0 = 0.25$. The parameter FCG-resistance, $dN/d(a/\delta_0)$, is used in this study in place of the more common measure of FCG-rate, $d(a/\delta_0)/dN$. This parameter provides for a better presentation of the influence of plasticity on the crack growth behavior, and allows the present results to be connected to previous studies of crack growth conducted with cohesive zone models (Tvergaard and Hutchinson, 1992). For the case of a model where plastic deformation occurs in the absence of elastic substrates ($h/\delta_0 \rightarrow \infty$), the computations predict a minimum value in FCG resistance at small positive values of the applied T-stress. For negative T-stress values the FCG resistance rises significantly, while for positive values of the T-stress a smaller increase in FCG resistance is observed. As the plastic deformation becomes constrained due to the presence of elastic substrates adjacent to the central metal layer the dependence of the FCG behavior on the T-stress is reduced. The strongest reduction in FCG resistance is predicted for $T_{max}/\sigma_Y = -1.0$. Furthermore, the minimum value of FCG resistance is no longer predicted for small values of positive T-stress, but rather for small negative values of T-stress. As the metal layer height becomes small compared to the cohesive zone length ($h/\delta_0 = 0$ in the limit of two elastic substrates bonded to each other) the T-stress effect on FCG resistance finally completely vanishes and for $h/\delta_0 = 0$ the FCG resistance $dN/d(a/\delta_0)$ is virtually independent of the T-stress.

Insight into the material separation process can be obtained from steady state regime traction-separation curves obtained for several values of T-stress. Such results are shown in Figure 3.16 for computations with $h_l/\delta_0 \rightarrow \infty$ and $T_{max}/\sigma_Y = -1.0, 0.0, +1.0$, respectively. The results clearly show that the T-stress influences the material separation

response. In the present model, crack closure is present as over closure of the cohesive surfaces and the related predicted negative normal tractions in the contact regime of the cohesive constitutive relationship. Furthermore, the maximum value of tractions predicted is no longer a predetermined value and develops in dependence of the applied constraint (Wang and Siegmund, 2005). When comparing the traction-separation curves in Figure 3.16(a) to (c), the traction separation curve computed for $T_{\max} / \sigma_Y = -1.0$ clearly shows the largest negative traction values, but also the lowest maximum traction values. For $T_{\max} / \sigma_Y = 0.0$ and +1.0, respectively, the maximum traction values are considerably larger, but levels of contact tractions are also reduced, with the computation $T_{\max} / \sigma_Y = +1.0$ resulting in a larger amount of crack closure than for $T_{\max} / \sigma_Y = 0.0$.

To summarize the characteristics of the computed traction-separation curves we define the cohesive opening traction $T_{n,op}$ and the amplitude of cohesive tractions $T_{n,a}$ following the notation in Figure 3.16(c). While the ratio of the stress intensity factor at opening relative to the maximum stress intensity factor $K_{op} / K_{\max}$ is used to describe crack closure levels, here the crack closure level is described by the ratio of $T_{n,op} / T_{n,\max}$, see Figure 3.17(a). In computations with unobstructed plastic zone, crack closure is found to be maximum at negative and positive T-stress, and of minimum level at around $T_{\max} / \sigma_Y = 0.0$. The level of crack closure is reduced with increase on the constraint provided by the elastic substrates. Furthermore, for small metal layer heights, a minimum in the ratio is found for negative T-stress values. Since the actual value of $T_{n,op}$ is sensitive to the contact formulation, we also provide a characterization of the cohesive zone response in terms of $T_{n,op} / \sigma_{\max,0}$ and $T_{n,a} / \sigma_{\max,0}$, see Figure 3.17(b). In this description the contact conditions relative to the cohesive strength parameters do not skew the results. Again, for $h / \delta_0 \to \infty$ the largest amount of contact tractions, $T_{n,op} / \sigma_{\max,0}$, is present when compared to the models with constraint plastic deformation. Negative T-stresses result in the larger contact tractions than positive T-stresses with a minimum in the contact traction at T-stresses close to zero. The T-stress has a smaller

effect on the maximum value of the opening tractions, $T_{n,max}/\sigma_{max,0}$. These values depend more strongly on the value of h/δ_0 than on T_{max}/σ_Y. In both Figure 3.17(a) and (b) it is shown that in the absence of plastic deformation, $h/\delta_0 = 0$, virtually no crack closure occurs.

3.3.2.2 Variable Amplitude Loading

Results presented in this section describe simulations conducted under consideration of a single overload. A constant amplitude loading of magnitude $\Delta G_{base}/\phi_0 = 0.15$ was applied initially, an overload of magnitude $\Delta G_{OL}/\phi_0 = 0.45$ is considered in cycle N=25, with a subsequent return to the original constant amplitude. For positive T-stresses, computations were conducted with $T_{max}/\sigma_Y = 0.5$ during the constant amplitude loading part and with $T_{max}/\sigma_Y = 0.5\sqrt{3} = 0.5\sqrt{\Delta G_{OL}/\Delta G_{base}}$ during the overload cycle. For negative T-stresses computations used $T_{max}/\sigma_Y = -0.5$ during the constant amplitude loading part and $T_{max}/\sigma_Y = -0.5\sqrt{3}$ in the overload cycle. The predicted overload effect for cases of positive and negative T-stresses and $h/\delta_0 \rightarrow \infty$ and 60, respectively, are documented in Figure 3.18, and compared to results of the corresponding zero T-stress cases. In the case of zero T-stress, Figure 3.18(a), the effect of the constraint provided by the presence of the elastic substrates increases not only the crack growth rate, but also reduces the retardation effect of the overload. If a positive T-stress is considered, the overload cycle reduces the retardation effect of the overload, both for the unconstrained, $h/\delta_0 \rightarrow \infty$, as well as constrained geometry, $h/\delta_0 = 60$. However, it appears that the number of cycles needed for a return to the steady state crack growth is somewhat larger in the case of the positive imposed T-stress. If a negative T-stress is considered, Figure 3.18(b), the overload cycle imposes a significantly increased retardation for the unconstrained geometry, $h/\delta_0 \rightarrow \infty$. For the constrained geometry, $h/\delta_0 = 60$, crack retardation was found to be similar to the computation in which zero or the negative T-stress considered.

To further clarify the nonlinear effects of overloads a numerical study was conducted in which overloads in K or T only were considered in comparison to the combined overload in K and T as discussed above. Figure 3.19 depicts the results of this investigation. Overloads in T only with constant amplitude loading in K did not result in any significant change in the crack growth history compared to the constant amplitude loading case. An overload in K, with T constant during the overload cycle, results in an overload response that is initially similar to that of the combined K and T overload case, but with a significantly smaller number of cycles needed to a return to the initial crack growth rate.

3.4. Conclusions

Numerical simulations of constraint effects in FCG are investigated by used of the irreversible cohesive zone model. Two types of constraint are considered. Incremental computations of crack growth along a centerline crack of the metal layer sandwiched between two elastic substrates were carried out under the constant and variable amplitude loading conditions for different levels of T-stress. Based on the preceding computations and discussions, the following conclusions can be drawn.

3.4.1 Constraint Effects in FCG

The results of predicted FCG rates under constant amplitude loading at different load ranges indicated that, in an intermediate load range of $0.05 < \Delta G / \phi_0 < 0.3$, a Paris law can be used to describe the dependence of the predicted FCG rates on the applied energy release rate range. The present irreversible cohesive zone model leads to a similar prediction as the model proposed in Nyugen $et\ al.$ (2001). For $\Delta G / \phi_0 < 0.1$, the same values of FCG rates were predicted for the geometries without constraint where the plastic zone can freely develop and the geometries where a constraint is imposed due to the presence of an elastic substrate. For $\Delta G / \phi_0 > 0.1$, the geometry where the metal is

constrained between the elastic substrates exhibits higher FCG rates than the unconstraint layer system.

FCG rates in dependence of the layer thickness were calculated. When the layer thickness satisfied $h_l / \delta_0 > 120$, the predicted FCG rate was not affected by constraint effects, and equal to that of a model with elastic-plastic material properties everywhere. As the layer thickness decreased, the FCG rates increased and became the function of the layer thickness until $h_l / \delta_0 \leq 10$. For such small layer thickness, the FCG rates were no longer the function of the layer thickness, and equal to that of a model with elastic material properties everywhere.

The evolution of the traction-separation law was investigated in dependence of the layer thickness. Higher values of traction and separation are predicted for the thinnest metal layer. These higher traction and separation values are responsible for higher rates of damage accumulation and subsequently for the higher FCG rate.

Under constant amplitude loading, the predicted crack opening profiles and opening stresses indicated that crack closure is present only in the absence the elastic substrates. In a situation of high mechanical constraint, however, no crack closure was observed and the crack remained fully open even at minimum load. A reduction of crack closure with constraint was also observed by Roychowdhury and Dodds (2003) when comparing FCG simulations under various T-stress levels.

The dependence of the FCG resistance on the cohesive strength was determined. For $\sigma_{max,0} / \sigma_Y < 3.5$ the dependence of the FCG resistance remains linear, while for larger values of $\sigma_{max,0} / \sigma_Y$ a strong nonlinear increase of the FCG resistance was predicted. The larger FCG resistance was due to the significant plasticity contribution for high values of cohesive strength. Also, as the metal layer thickness was increased the nonlinearity of the dependence of FCG rate on σ_{max} strongly increased. The maximum values of cohesive tractions during material separation depend on the level of plasticity and constraint present. When $\sigma_{max,0} / \sigma_Y < 3.5$, the dependence of $max(T_n)/\sigma_Y$ on $\sigma_{max,0} / \sigma_Y$ is stronger than for higher values of $\sigma_{max,0} / \sigma_Y$ which corresponds to the large plasticity contributions to the FCG resistance. The predicted dependence of the FCG

50

resistance on cohesive strength somewhat resembles the results on the steady state fracture toughness in a ductile solid under monotonic loading, Tvergaard and Hutchinson (1992). There too, the crack growth resistance increased dramatically as the ratio $\sigma_{max,0}/\sigma_Y$ is increased. Under cyclic loading conditions FCG is present even at high values cohesive strength, $\sigma_{max,0}/\sigma_Y$ up to six, while for such values of cohesive strength crack growth under monotonic loading would not occur.

Under variable amplitude loading, single overload effects on FCG were captured. In the absence of constraint, the overload resulted in a well known crack retardation effect. On the other hand, in the absence of plastic deformation, the overload caused an instantaneous crack advance and temporarily increased crack growth rates. A similar response to overloads was observed in crack bridging ceramics, Gilbert and Ritchie (1998) and recently analyzed in Siegmund (2004). For intermediate values of the metal layer thickness, the crack growth behavior was found in a sequence of crack acceleration-deceleration-acceleration. Whether a permanent lag or permanent retardation in crack length developed due to the overload depends on the metal layer thickness.

Comparisons of the accumulated plastic zones among the systems with different metal layer thickness indicated that the plastic zone was distorted in thin layers due to impinging with the elastic substrates under constant amplitude loading. The application of single overload caused the active plastic zone to grow in size significantly. The increased active plastic zone size of constraint system was smaller than that of unconstraint system. The response to the overload was the result of two competing processes, the plastic deformation and the evolution of damage in the cohesive zone. Generally, when the single overload was applied, it increased the traction level significantly which resulted in the increased damage accumulation rate, i.e, the FCG rate was increased. At the same time, the overload increased the amount of plastic deformation. The overall overload response of either increased or decreased FCG rate depends on the constraint level. For low constraint level such as $h_l/\delta_0 \to \infty$, crack closure and the large amount of plastic deformation was significant and superseded all accelerating effects due to the increased damage accumulation rate and resulted in the

overall response of decreased FCG rate. For high constraint level such as $h_t / \delta_0 = 10$, the level of plastic deformation is small due to the surrounding substrates. This results in the small amount of crack closure such that the damage evolution was accelerated and overall response was an increased FCG rate.

3.4.2 Constraint Effects in FCG due to T-stress

Past investigations have contributed the change in FCG resistance with T-stress to the changes in crack closure e.g. Roychowdhury and Dodds (2004). A similar dependence of crack closure on T_{max} / σ_Y was found as the present study. In the present approach, both crack closure levels and the plastic deformation changed as the level of T-stress was changed. This is especially important since the interaction between the constraint provided by the T-stress and the geometry of the sample is non-linear in nature. Both effects were accounted for in the prediction of FCG in dependence of T-stress and the metal layer thickness.

Under constant amplitude loading, the present results indicated that a negative T-stress resulted in larger FCG resistance than a positive T-stress for the model with $h_t / \delta_0 \to \infty$. The lowest FCG resistance was obtained for small positive T-stress values. As the plastic deformation became constrained due to the decreasing metal layer thickness and the adjacent elastic substrate, the dependence of the FCG resistance on T-stress was reduced. The T-stress values which resulted in the smallest FCG resistance changed from small positive values to small negative values. When $h_t / \delta_0 = 0$, the FCG resistance finally was independent on the T-stress values. For the model with $h_t / \delta_0 \to \infty$, the higher FCG resistance can be explained by the largest negative traction values and the lowest maximum traction values under $T_{max} / \sigma_Y = -1.0$. For $T_{max} / \sigma_Y = 0.0$ and $+1.0$, the negative contact traction values were reduced and the maximum traction values were considerably larger.

Computations for the model with $h_t / \delta_0 \to \infty$ indicate crack closure was found to be higher at negative T-stress than one at positive T-stress. The minimum level of crack

closure was obtained around $T_{max} / \sigma_Y = 0.0$. The crack closure level was reduced with increasing in constraint due to decreasing layer thickness. It was shown that in the absence of plastic deformation, $h_l / \delta_0 = 0$, no crack closure occurred and the T-stress effect disappears.

An approach in which FCG is the outcome of the simulation is especially useful in the analysis of overload cases. The present study found that overloads under consideration of positive T-stresses tend to reduce the amount of crack retardation both for the unconstrained, $h_l / \delta_0 \rightarrow \infty$, and constrained geometry, $h_l / \delta_0 = 60$. For negative T-stresses of the same magnitude, the overload resulted in a significantly increased retardation for the unconstrained geometry, $h_l / \delta_0 \rightarrow \infty$. For the constrained geometry, $h_l / \delta_0 = 60$, crack retardation which was similar to one under zero or positive T-stress was obtained. The numerical simulation scheme provides the opportunity to study the effects of overloads in the K and T component of the applied loading independently. Compared to the constant amplitude loading, overloads in T-stress only were shown not to introduce any alteration to the computed FCG.
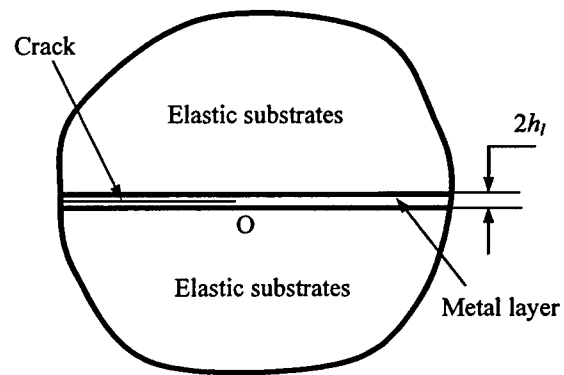
Figure 3.1: Schematic of a model geometry considered: a metal layer constraint by two elastic substrates.

$$u(t) = K_I(t) f(r,\theta) + T(t) f(r,\theta)$$

(a)

(b)
O   L
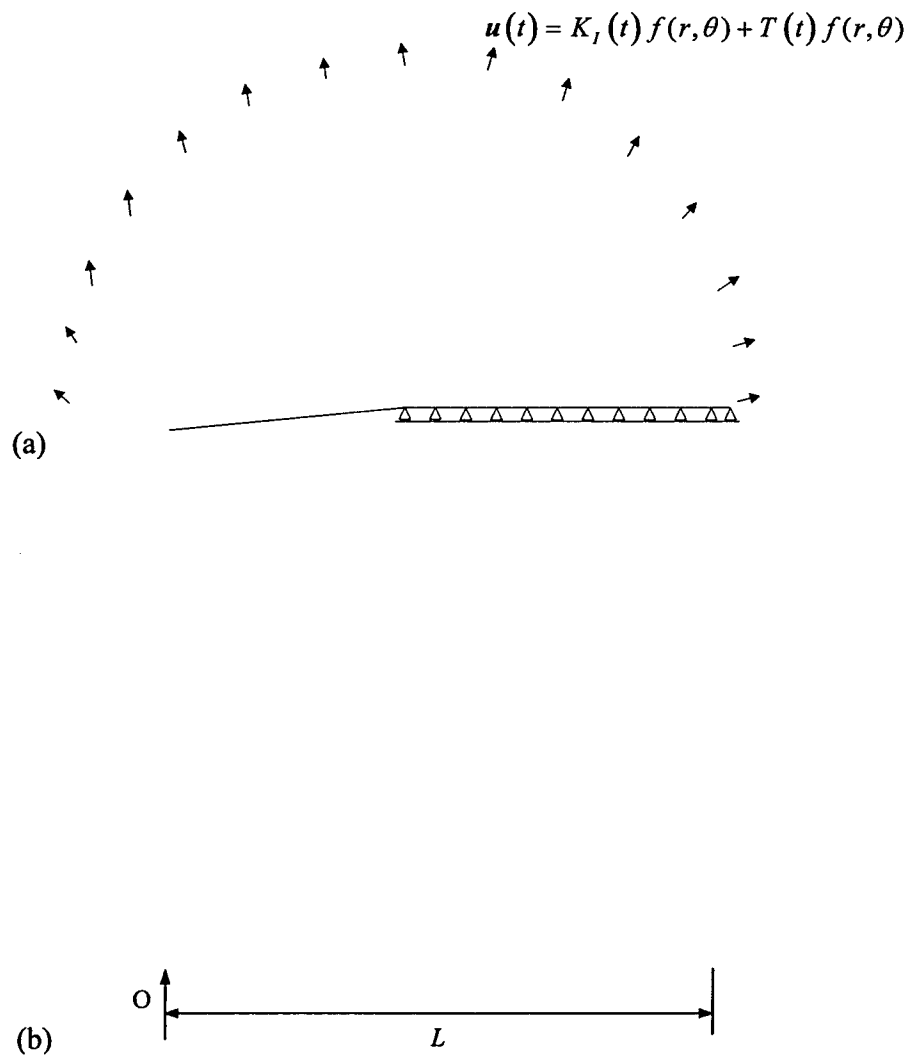
Figure 3.2: Finite element mesh for the modified boundary layer formulation approach.
(a) Global mesh. (b) Refined mesh near the crack tip.
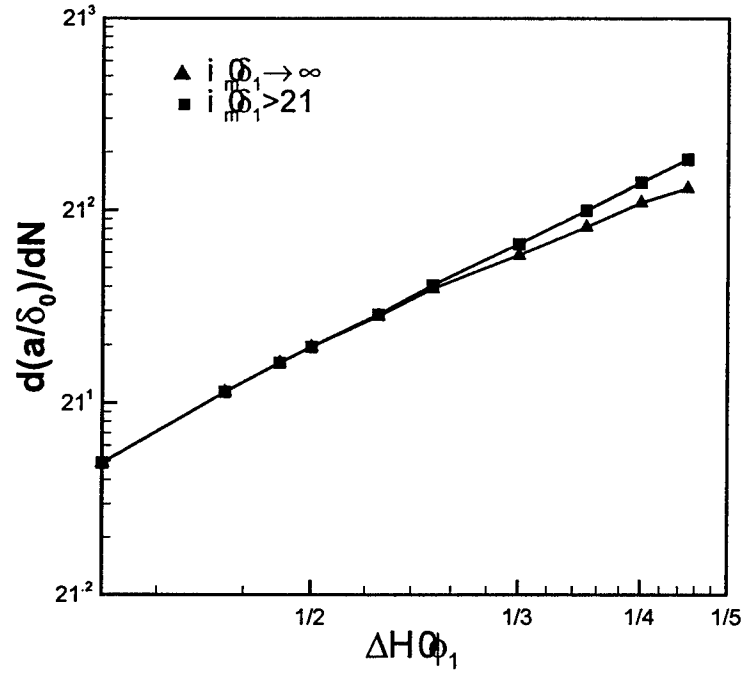
Figure 3.3 : Predicted dependence of the normalized fatigue crack growth rate, da/dN

on the normalized applied energy release rate range, $\Delta G/\phi_0$ under constant

amplitude loading: $h_i/\delta_0 \to \infty$ (▲) and $h_i/\delta_0 = 10$ (■).
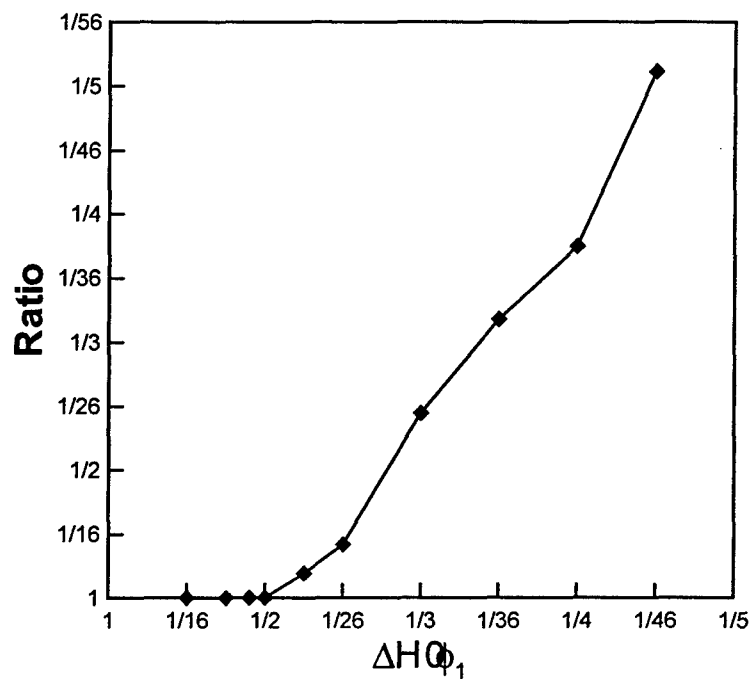
Figure 3.4 : Increase in FCG rate for the constraint geometry relative to the unconstraint geometry, $\{[\mathrm{d}(a/\delta_0)/\mathrm{d}N]_{h_l/\delta_0=10} - [\mathrm{d}(a/\delta_0)/\mathrm{d}N]_{h_l/\delta_0\to\infty}\}/[\mathrm{d}(a/\delta_0)/\mathrm{d}N]_{h_l/\delta_0\to\infty}$, vs. the normalized applied energy release rate range, $\Delta G/\phi_0$, under constant amplitude loading.
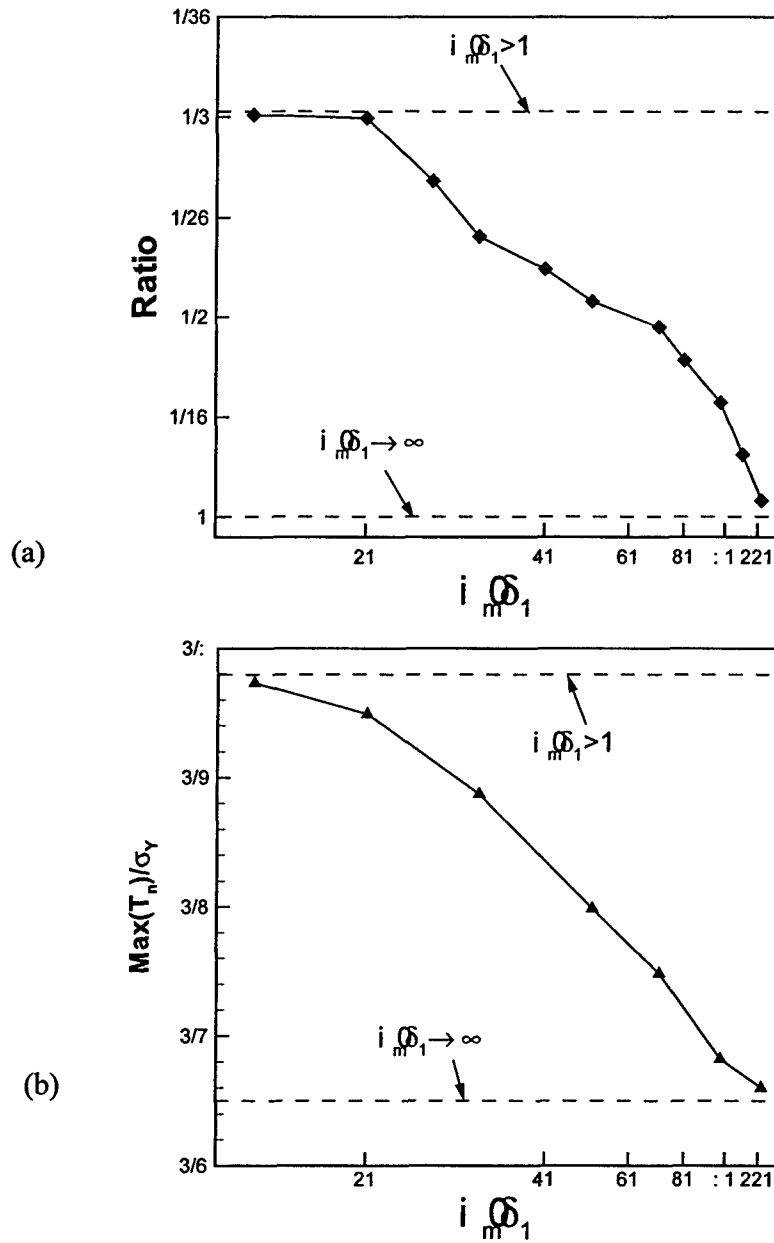
Figure 3.5 : (a) FCG rate for the constraint geometry relative to the unconstraint geometry, $\{[d(a/\delta_0)/dN]_{h_l/\delta_0} - [d(a/\delta_0)/dN]_{h_l/\delta_0 \to \infty}\}/[d(a/\delta_0)/dN]_{h_l/\delta_0 \to \infty}$, vs. the metal layer height, h_l/δ_0, and (b) maximum values of cohesive traction during steady state growth vs. the metal layer height, h_l/δ_0. Constant amplitude loading with $\Delta G/\phi_0 = 0.25$.
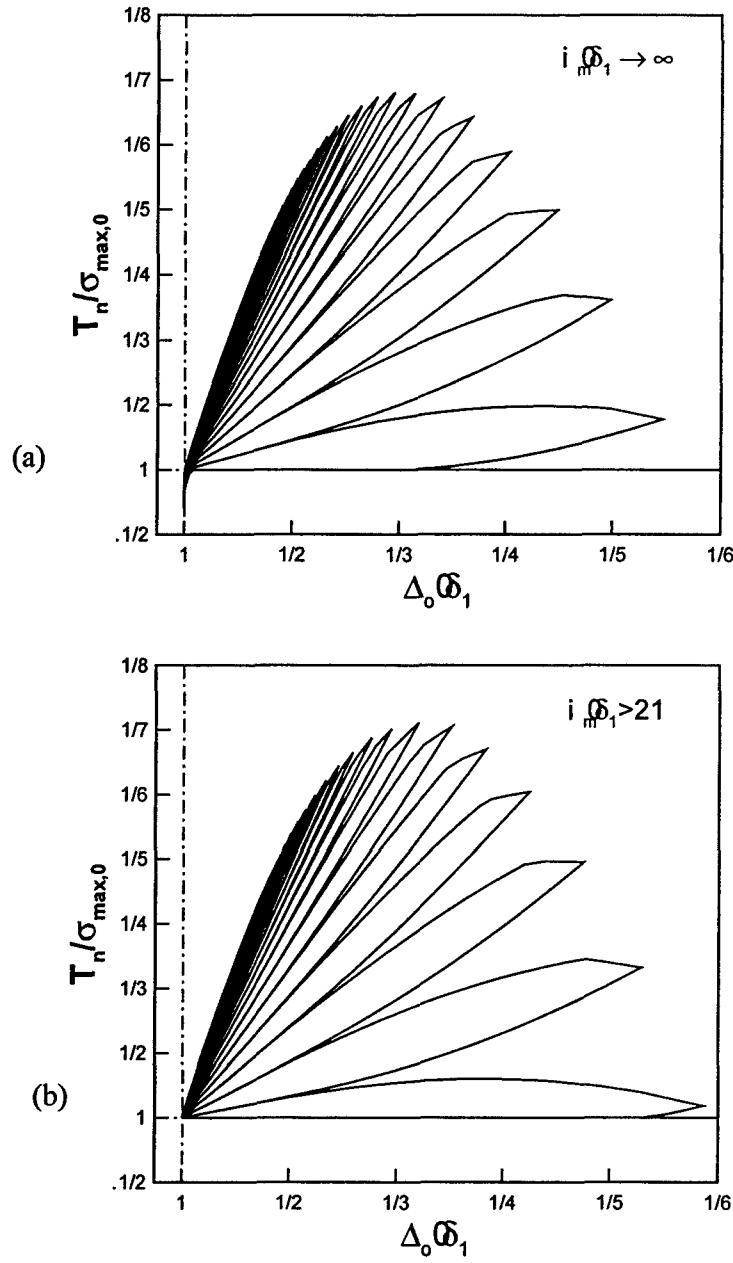
Figure 3.6 : Predicted normalized traction-separation behavior under constant amplitude

loading. (a) $h_i / \delta_0 \rightarrow \infty$. (b) $h_i / \delta_0 = 10$. Constant amplitude loading with
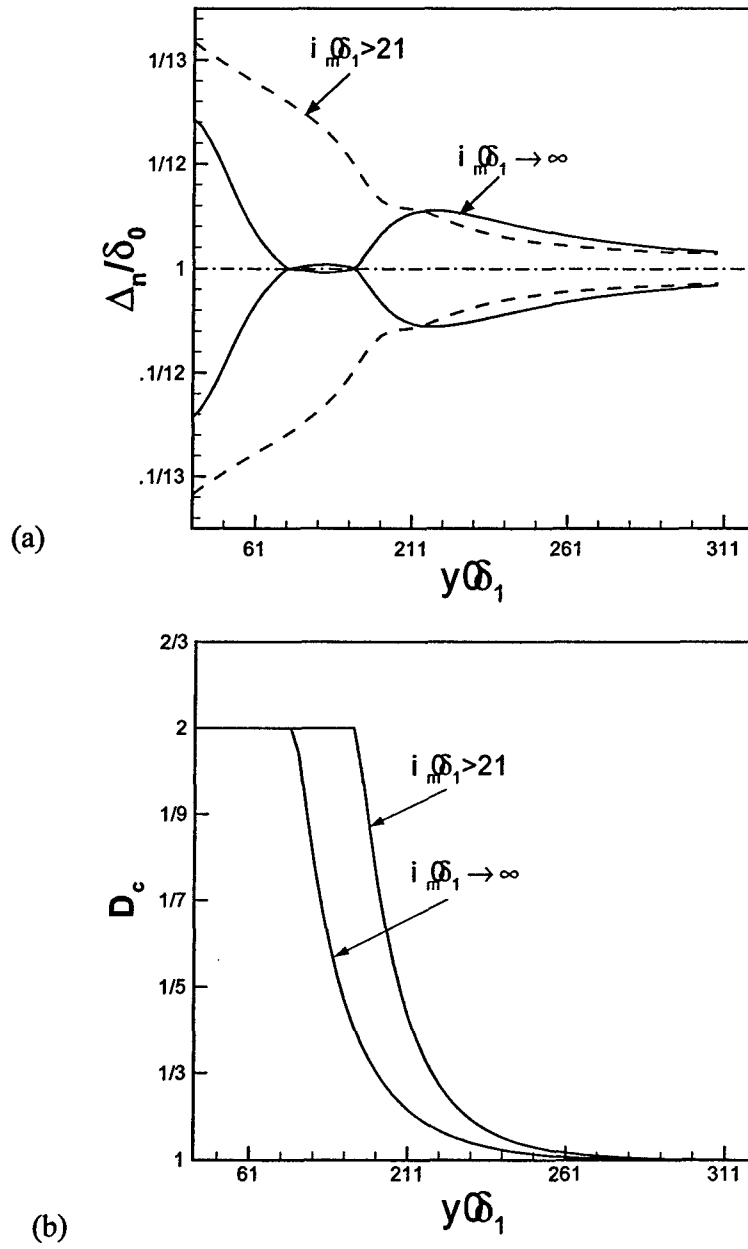
$\Delta G / \phi_0 = 0.15$.

Figure 3.7 : (a) Crack opening profiles and (b) damage distribution under constant amplitude loading at $\Delta G = 0$ for $h_i / \delta_0 \rightarrow \infty$ (—) and $h_i / \delta_0 = 10$ (---). Constant amplitude loading with $\Delta G / \phi_0 = 0.15$.
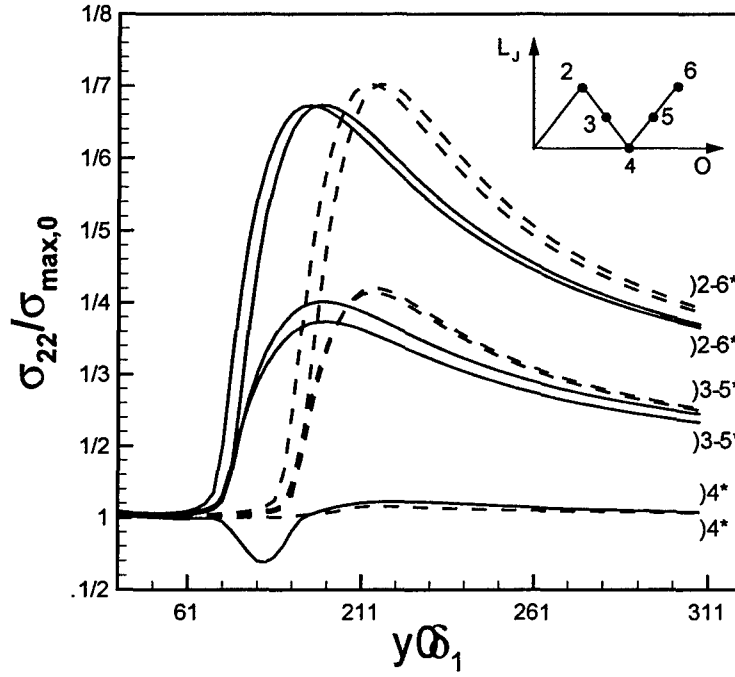
Figure 3.8: Traction distribution along the cohesive zone for several load levels for two ductile substrates, $h_t / \delta_0 \to \infty$ (—) and $h_t / \delta_0 = 10$ (---). Constant amplitude loading with $\Delta G / \phi_0 = 0.15$.
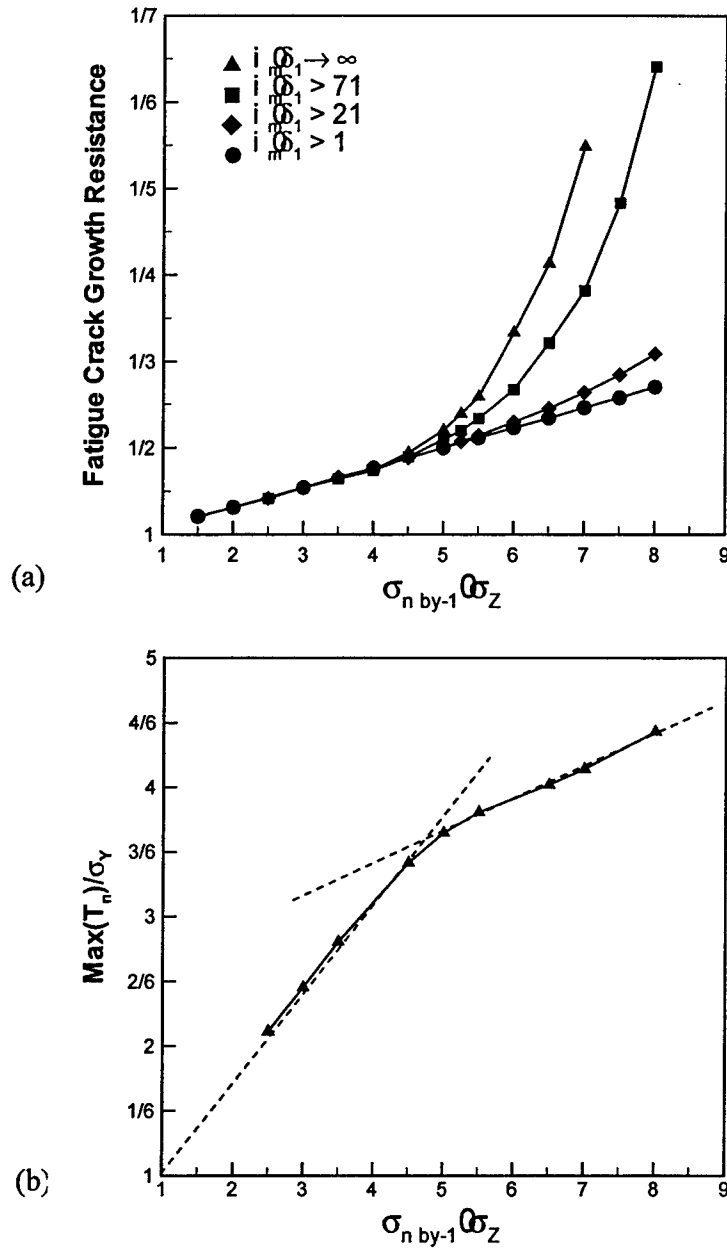
Figure 3.9: (a) Predicted fatigue crack growth resistance vs. the normalized interface strength and (b) the maximum traction value developing vs. the normalized interface strength. Constant amplitude loading for $h_l / \delta_0 \to \infty$ ($\blacktriangle$), $h_l / \delta_0 = 60$ ($\blacksquare$), $h_l / \delta_0 = 10$ ($\blacklozenge$) and $h_l / \delta_0 = 0$ ($\bullet$), all data are for steady state growth. Constant amplitude loading with $\Delta G / \phi_0 = 0.25$.
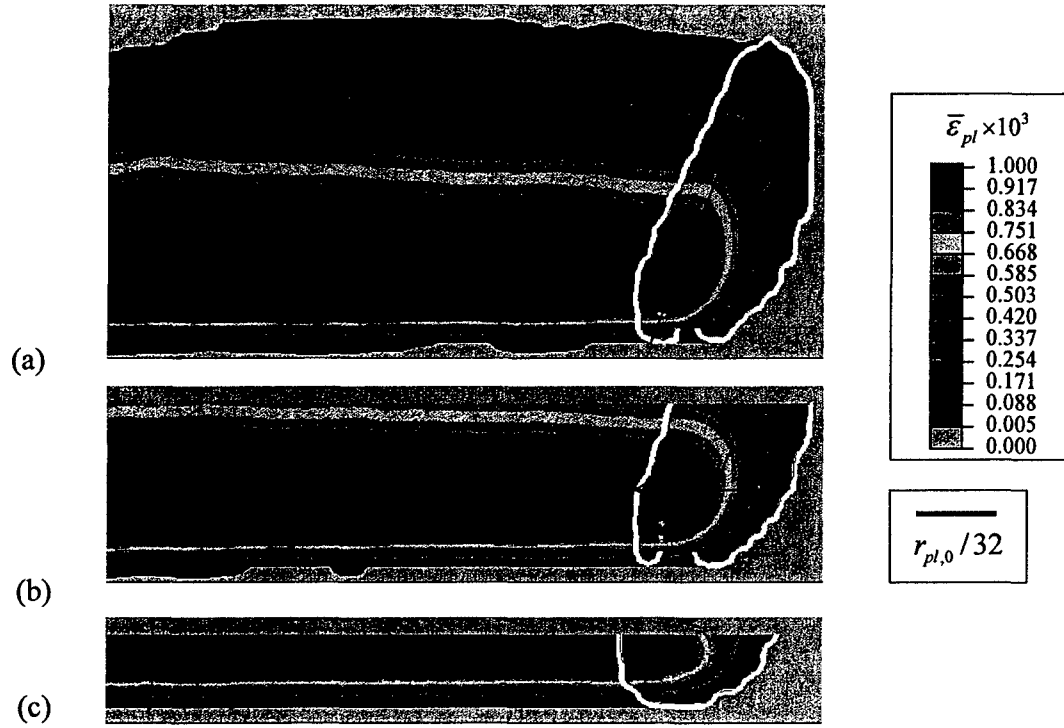
Figure 3.10: Contour plots of equivalent plastic strain under the constant amplitude loading condition for the different layer thickness. (a) $h_l / \delta_0 \rightarrow \infty$; (b) $h_l / \delta_0 = 30$; (c) $h_l / \delta_0 = 15$. (Crack extension $\Delta a / \delta_0 = 135$). The white contour line represents the active plastic zone at the maximum loading point. Constant amplitude loading with $\Delta G / \phi_0 = 0.125$.
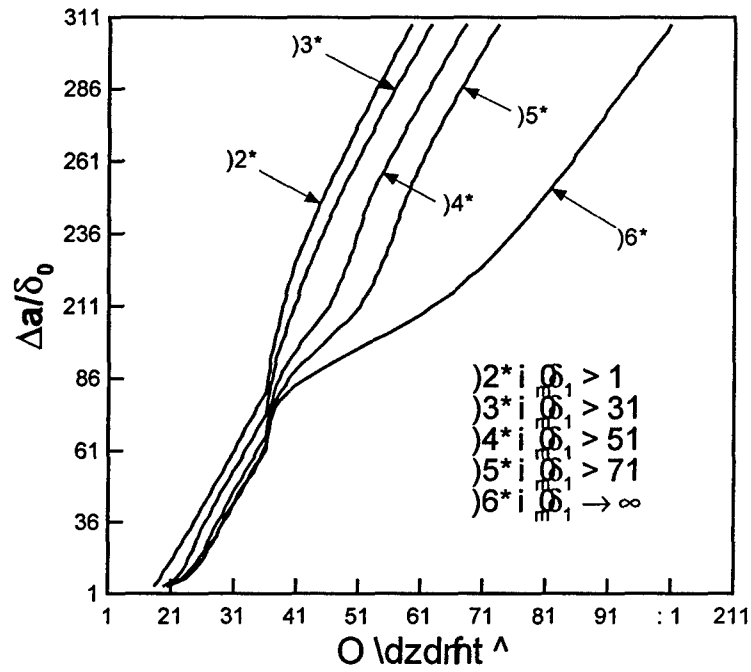
Figure 3.11: Predicted crack extension, $\Delta a / \delta_0$, vs. cycle number, N, for the load
sequence including an overload at N=25 for different values of the normalized layer
thickness, h_l / δ_0. Constant amplitude loading with $\Delta G / \phi_0 = 0.15$ and overload with
$\Delta G / \phi_0 = 0.45$.

64
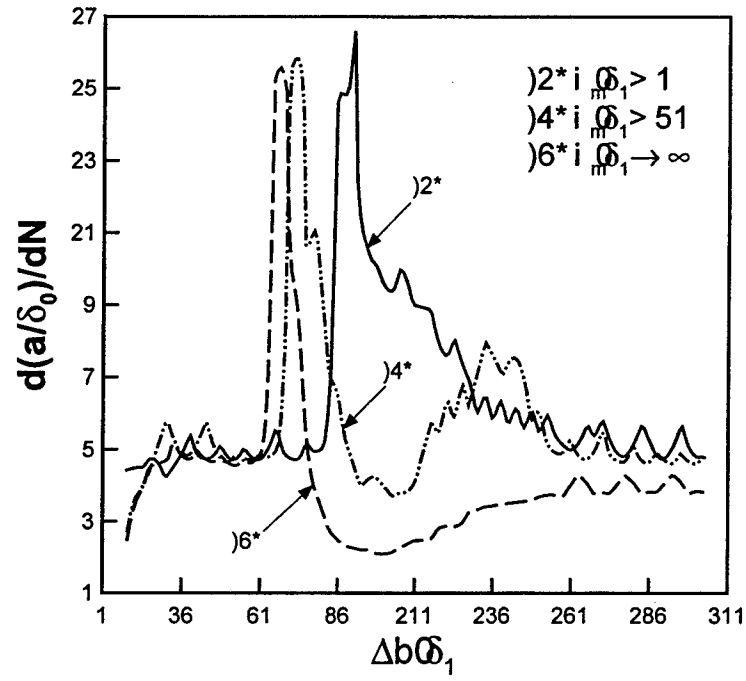
Figure 3.12: Predicted fatigue crack growth rates, da/dN, vs. normalized crack extension $\Delta a/\delta_0$ for the load sequence including an overload at $N=25$ for different values of the normalized layer thickness, h_l/δ_0.
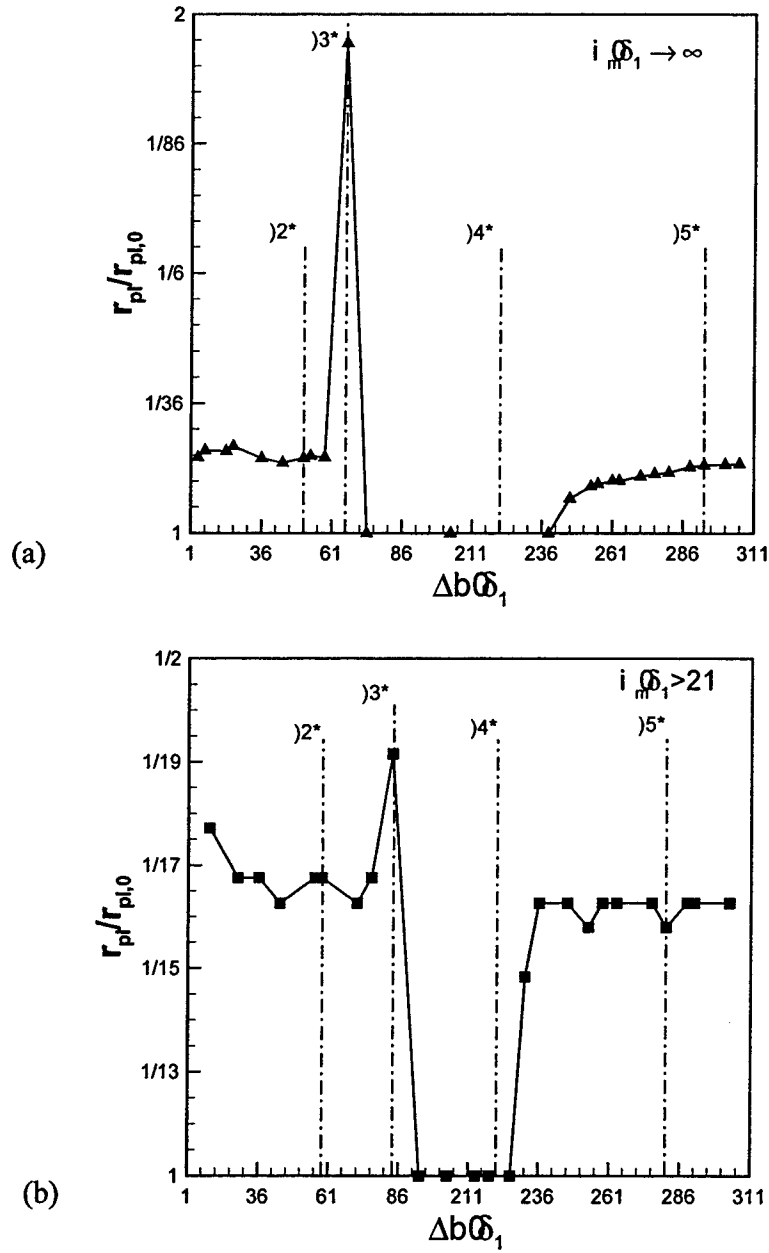
Figure 3.13: Size of the active cyclic plastic zone size in dependence of the crack tip location for the load sequence including an overload at N=25. (a) $h_l / \delta_0 \rightarrow \infty$. (b) $h_l / \delta_0 = 10$.
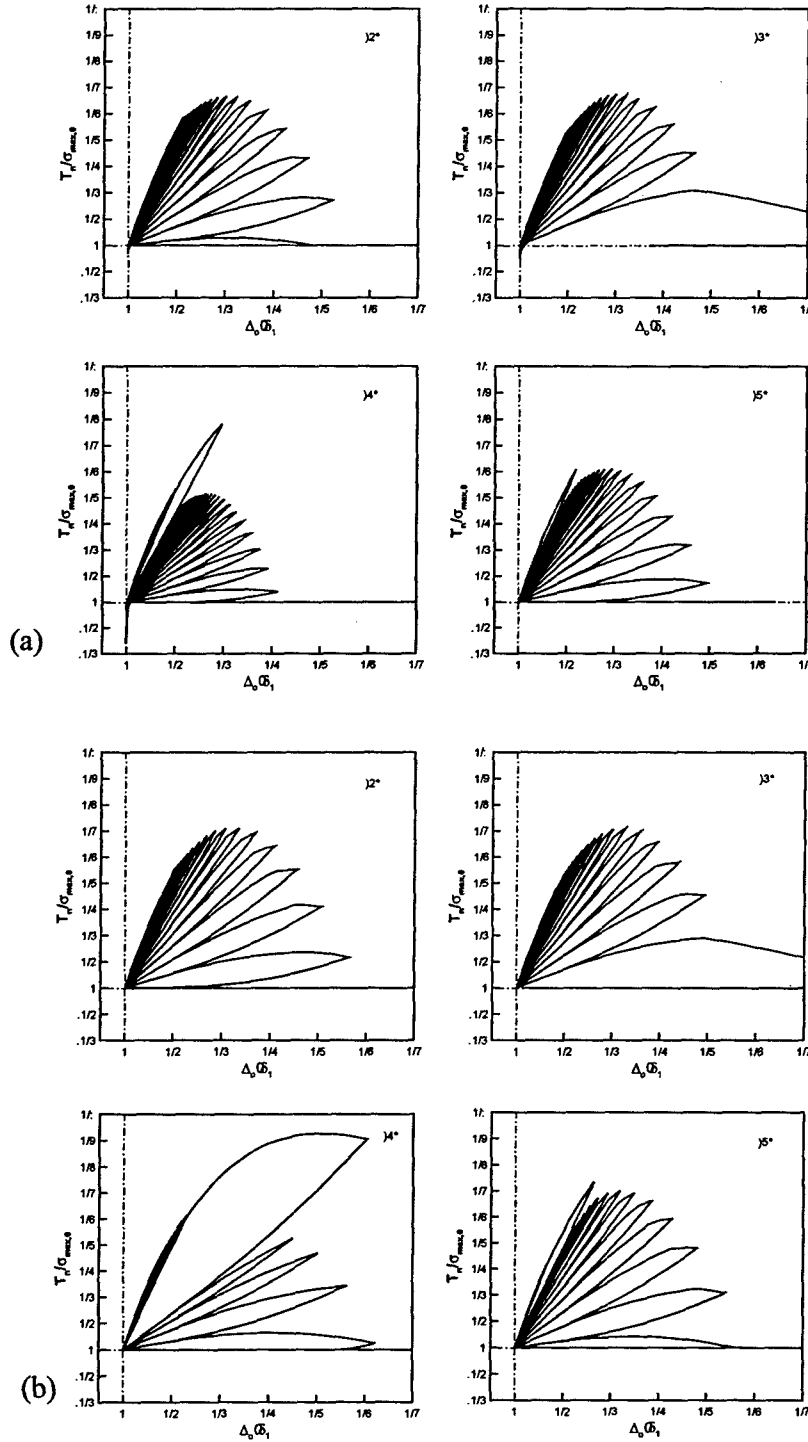
Figure 3.14: Normalized traction-separation curves for the load sequence including an overload at $N=25$, for the positions of (1), (2), (3) and (4) of Figure 3.13. (a) $h_l / \delta_0 \rightarrow \infty$.

(b) $h_l / \delta_0 = 10$.
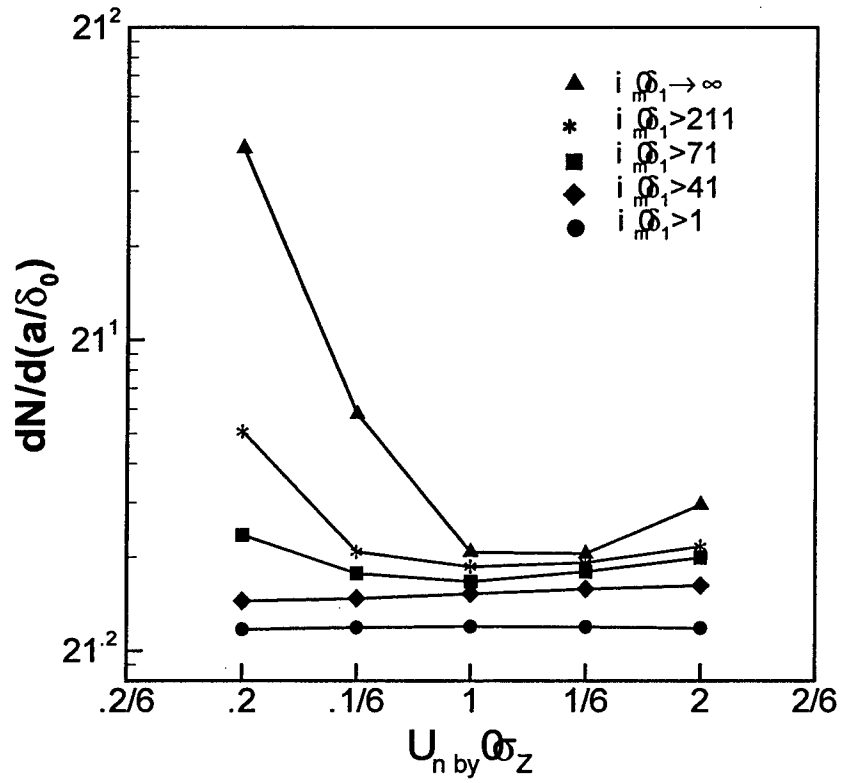
Figure 3.15: Predicted dependence of the normalized fatigue crack growth resistance $\mathrm{d}N/\mathrm{d}(a/\delta_0)$ in constant amplitude loading on the normalized T-stress, T_{max}/σ_Y for several values of the normalized metal layer height, h_l/δ_0.
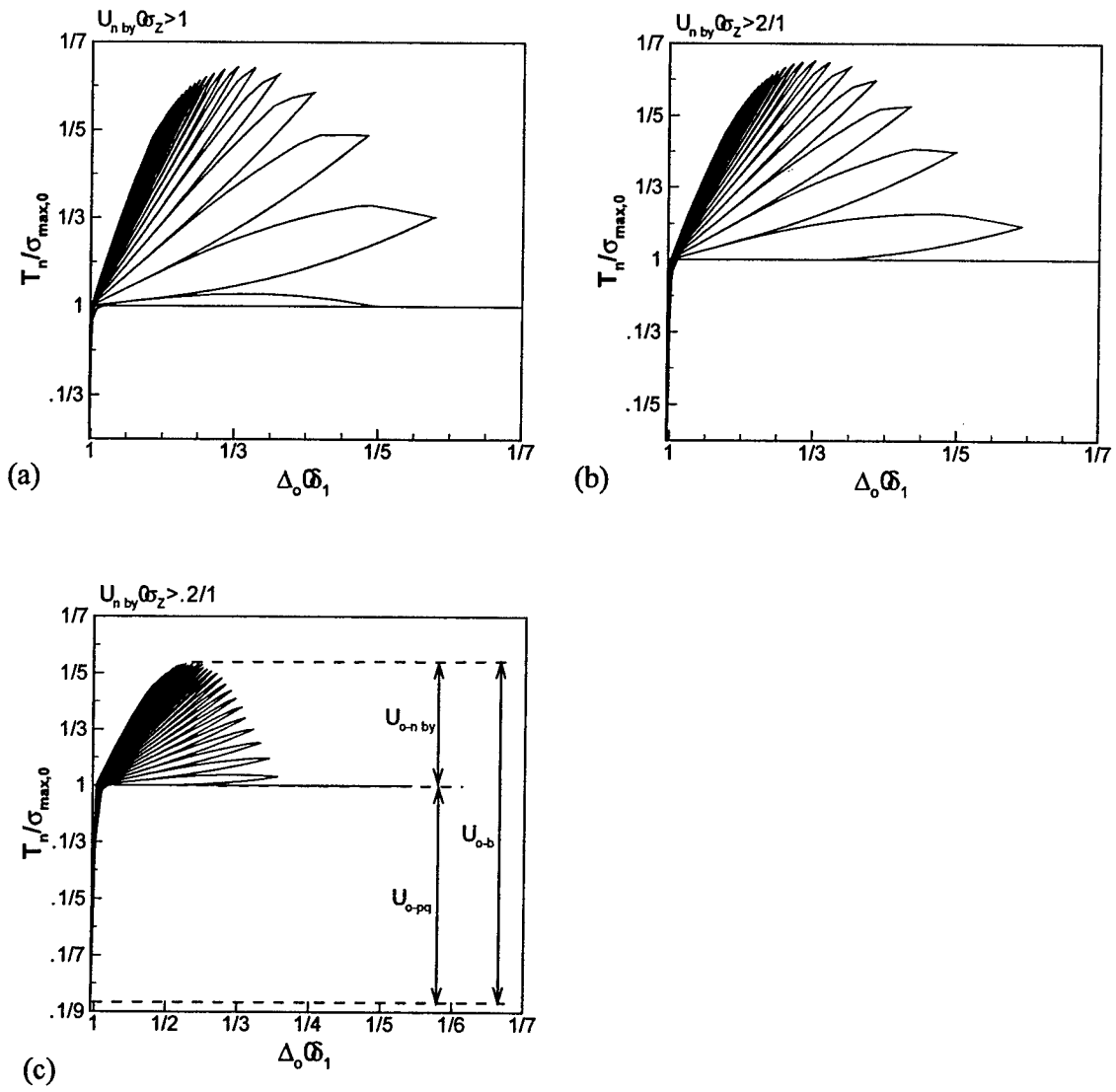
(a)

$U_{n\,by}\,\sigma_Z > 1$

$T_n/\sigma_{max,0}$ vs $\Delta_o\,\sigma_1$

1/7, 1/5, 1/3, 1, .1/3

1, 1/3, 1/5, 1/7

(b)

$U_{n\,by}\,\sigma_Z > 2/1$

$T_n/\sigma_{max,0}$ vs $\Delta_o\,\sigma_1$

1/7, 1/5, 1/3, 1, .1/3, .1/5

1, 1/3, 1/5, 1/7

(c)

$U_{n\,by}\,\sigma_Z > .2/1$

$T_n/\sigma_{max,0}$ vs $\Delta_o\,\sigma_1$

1/7, 1/5, 1/3, 1, .1/3, .1/5, .1/7, .1/9

1, 1/2, 1/3, 1/4, 1/5, 1/6, 1/7

$U_{o\text{-}n\,by}$, $U_{o\text{-}b}$, $U_{o\text{-}pq}$

Figure 3.16: Traction-separation response for a model with $h_l/\delta_0 \to \infty$ and (a) $T_{max}/\sigma_Y = 0.0$; (b) $T_{max}/\sigma_Y = +1.0$, (c) $T_{max}/\sigma_Y = -1.0$.

69
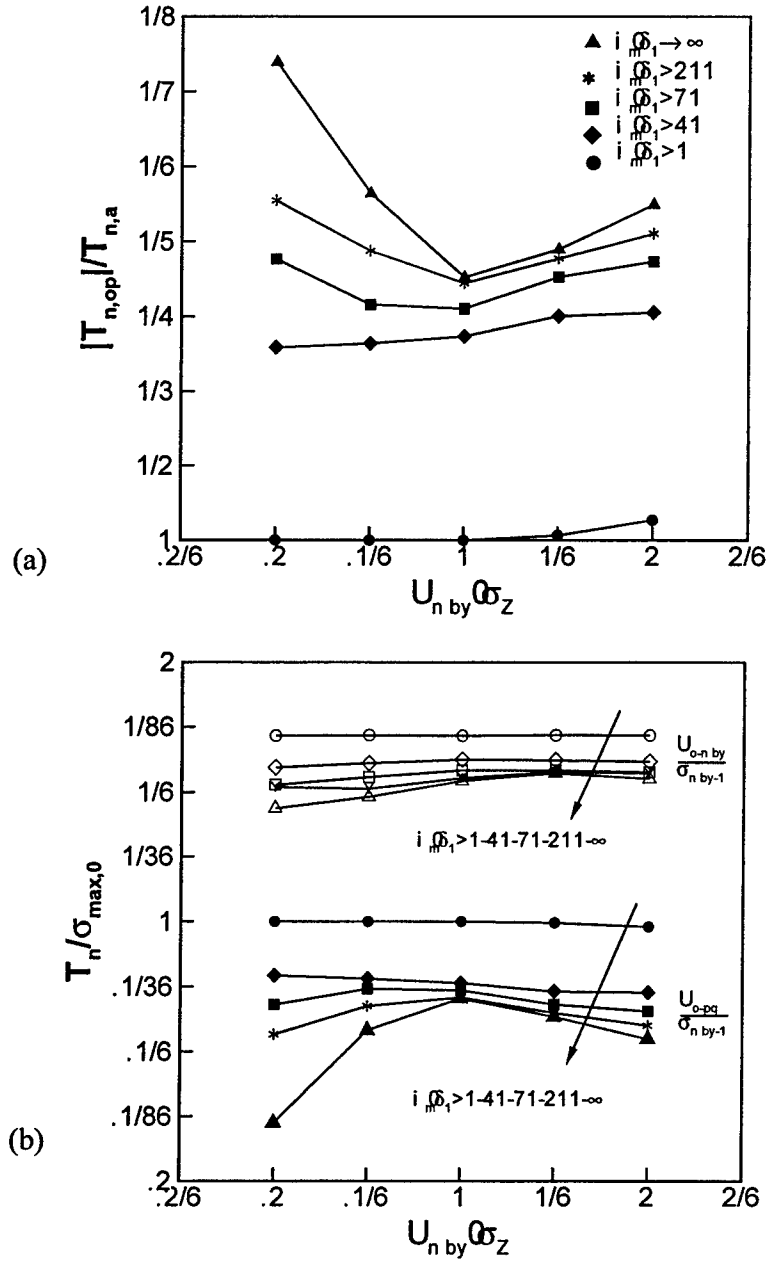
Figure 3.17 : (a) Predicted cohesive zone opening levels, $T_{n,op}/T_{n,\max}$ in dependence of $T_{\max}/\sigma_Y$; (b) Predicted maximum values of contact traction, $T_{n,op}/\sigma_{\max,0}$, and maximum crack opening traction, $T_{n,\max}/\sigma_{\max,0}$ in dependence of $T_{\max}/\sigma_Y$.
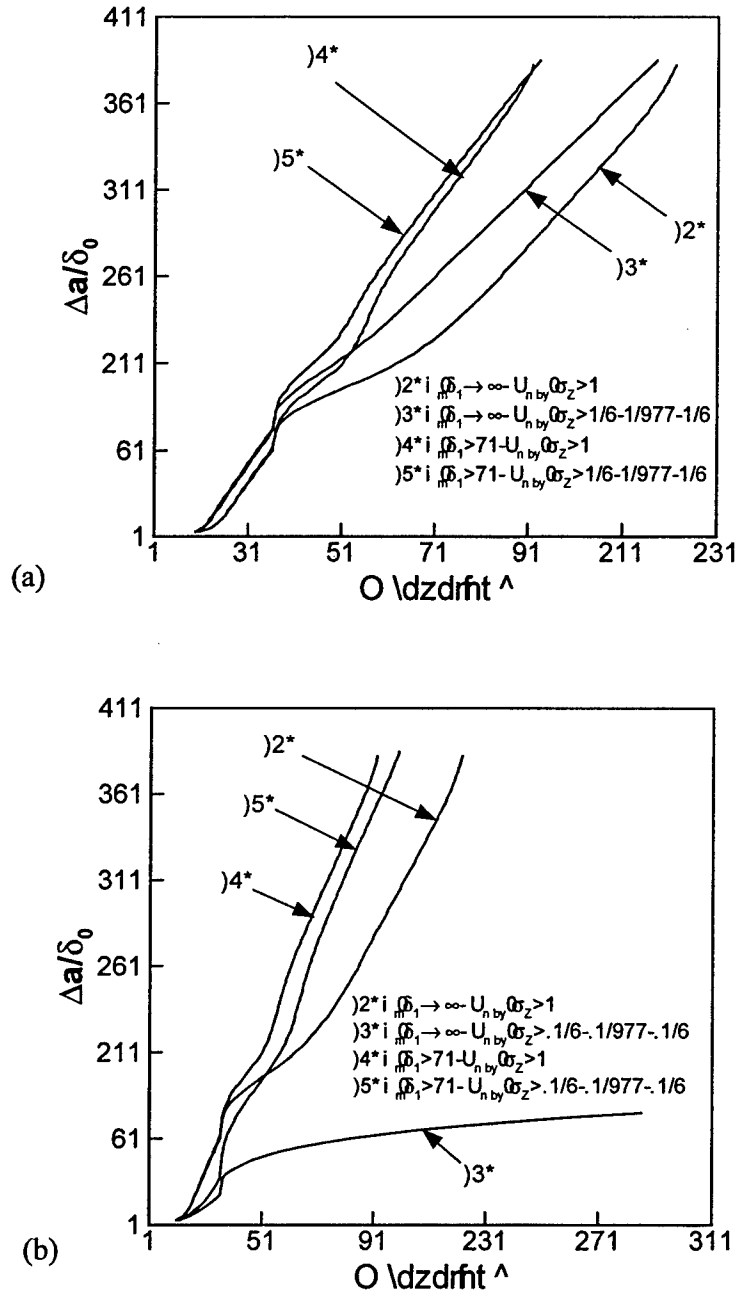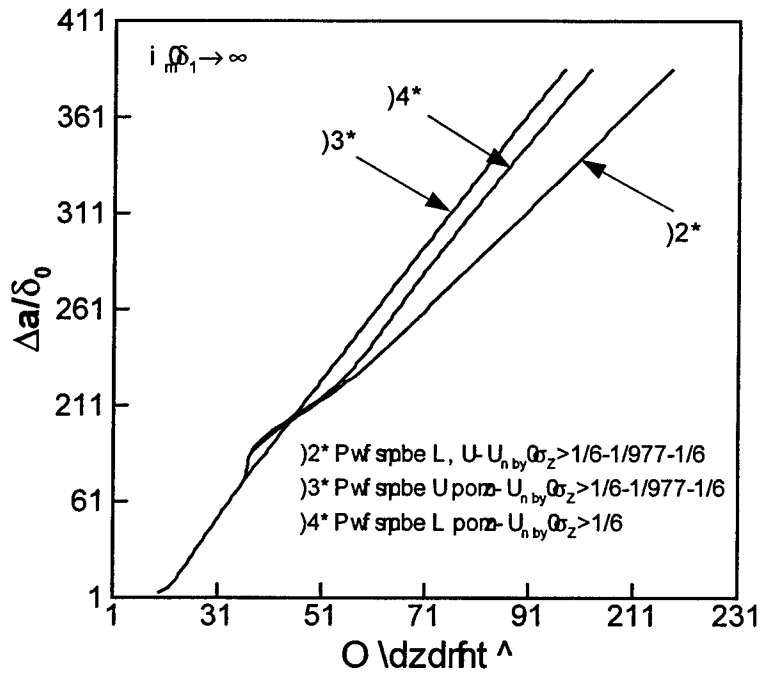
(a)

(b)

Figure 3.18: Predicted crack extension, $\Delta a / \delta_0$, vs. cycle number, N, for a load sequence including an overload at $N=25$ for $h_l / \delta_0 \to \infty$ and $h_l / \delta_0 = 60$; (a) $T_{max} / \sigma_Y = 0.0$ and

positive T-stresses, (b) $T_{max} / \sigma_Y = 0.0$ and negative T-stresses.

Figure 3.19: Predicted crack extension, $\Delta a / \delta_0$, vs. cycle number, N, for a load sequence including an overload at N=25 for $h_l / \delta_0 \to \infty$ and three overload scenarios: overload in K and T, in K only, and in T only, respectively.

LIST OF REFERENCES

Barenblatt, G.I., 1962, "The Mathematical Theory of Equilibrium Cracks in Brittle Fracture", *Advances in Applied Mechanics*. Academic Press, New York. Vol. 7, pp. 55-129.

Cannon, R.M., Dalgleish, B.J., Dauskardt, R.H., OH, T.S., and Ritchie, R.O., 1991, "Cyclic fatigue-crack propagation along ceramic/metal interfaces", *Acta Metallurgica et Materialia*, Vol. 39, 2145-2156.

Dauskardt, R.H., Lane, M., Ma, Q., and Krishna, N., 1998, "Adhesion and debonding of multi-layer thin film structures", *Engineering Fracture* Mechanics, Vol. 61, pp. 141-162.

Deshpande, V.S., Needleman, A., and Van der Giessen, E., 2002, "Discrete dislocation modeling of fatigue crack propagation", *Acta Materialia*, Vol. 50, pp. 831-846.

Dugdale, D.S., 1960, "Yielding of steel sheets containing slits", *Journal of the Mechanics and Physics of Solids*, Vol. 8, pp. 100-104.

de- Andrés, A. Pérez, J.L., and Ortiz, M., 1999, "Elastroplastic finite element analysis of three-dimensional fatigue crack growth in aluminum shafts subjected to axial loading", *International Journal of Solids and Structures*, Vol. 36, pp. 2231-2258.

Evans, A.G., and Hutchinson, J.W., 1995, "The thermomechanical integrity of thin films and multilayers", *Acta Metallurgica et Materialia*, Vol. 43, pp. 2507-2530.\

Fleck, N.A., 1986, "Finite element analysis of plasticity induced crack-closure under plane strain conditions", *Eng Fract Mech*, Vol. 25, pp. 441-449.

Gilbert, C.J., and Ritchie, R.O., 1998, "Transient fatigue crack behavior in a monolithic silicon nitride ceramic", *Engineering Fracture Mechanics*, Vol. 60, pp. 303-313.

Hutchinson, J.W., and Evans, A.G., 2000, "Mechanics of materials: top-down approaches to fracture", *Acta Materialia*, Vol. 48, pp. 125-135.

Kruzic, J.J., McNaney, J.M., Cannon, R.M., and Ritchie, R.O., 2004, "Effects of plastic constraint on the cyclic and static fatigue behavior of metal/ceramic layered structures", *Mechanics of Materials*, Vol. 36, pp. 57-72.

Lane, M., Dauskardt, R.H., Vainchtein, A., and Gao, H., 2000, "Plasticity contributions to interface adhesion in thin-film interconnect structures", *Journal of Materials Research*, Vol. 15, pp. 2758-2769.

Lemaitre, J., 1996, *A Course on Damage Mechanics*. Springer-Verlag, Berlin.

Lin, G., Kim, Y.J., Cornec, A. and Schwalbe, K.H., 1997, "Fracture toughness of a constrained metal layer", *Computational Materials Science*, Vol. 9, pp. 36-47.

McClung, R.C., 1994, "Finite element analysis of specimen geometry on fatigue crack closure", *Fatigue Fract Eng Mater Struct*, Vo. 17, pp. 861-872.

McNaney, J.M., Cannon, R.M., and Ritchie, R.O., 1996, "Fracture and fatigue-crack growth along aluminum-alumina interfaces", *Acta Materialia*, Vol. 12, pp. 4713-4728.

Needleman, A., 1990, "An analysis of decohesion along an imperfect interface", *International Journal of Fracture*, Vol. 42, pp. 21-40.

Nguyen, O., Repetto, E.A., Ortiz, M., and Radovitzky, R.A., 2001, "A cohesive model of fatigue crack growth", *International Journal of Fracture*, Vol. 110, pp. 351-369.

Paris, P.C., Gomez, M.P., and Anderson, W.P., 1961, "A rational analytic theory of fatigue", *The Trend in Engineering*, Vol. 13, pp. 9-14.

Stüwe, H.-P., and Pippan, R., 1992, "On the energy balance of fatigue crack growth", *Computers & Structures*, Vol. 44, pp. 13-17.

Roe, K.L. and Siegmund, T., 2001, "Simulation of interface fatigue crack growth via a fracture process zone model", *Computational Fluids and Solid Mechanics, Proceedings of the 1ˢᵗ MIT Conference on Computational Fluids and Solid Mechanics*, Boston, K.J. Bathe, Ed., Elsevier, pp. 435-437.

Roe, K.L. and Siegmund, T., 2003, "An irreversible cohesive zone model for interface fatigue crack growth simulation", *Engineering Fracture Mechanics*, Vol. 70, pp. 209-232.

Roychowdhury, S. and Dodds, R.H., 2003, "A numerical investigation of 3-D small-scale yielding fatigue crack growth", *Engineering Fracture Mechanics*, Vol. 70, pp. 2363-2383.

Roychowdhury, S., and Dodds, R.H., 2004, "Effect of T-stress on fatigue crack closure in 3D-small-scale yielding", *Int J Solids Struct*, Vol. 41, pp. 2581-2606.

Siegmund, T., 2004, "A numerical study of transient fatigue crack growth by use of an irreversible cohesive zone model", *International Journal of Fatigue*, Vol. 9, pp. 929-939.

Sadananda, K, Vasudevan, A.K., Holtz, R.L., and Lee, EU, 1999, "Analysis of overload effects and related phenomena", *Int J Fatigue*, Vol. 21, pp. S233-S246.

Solanki, K, Daniewicz, S.R., and Newman, Jr J.C., "Finite element analysis of plasticity-induced fatigue crack closure: an overview", *Eng Fract Mech*, Vol. 71, pp. 149-171.

Suresh, S., 1998, *Fatigue of Materials*. Cambridge University Press.

Tvergaard, V. and Hutchinson, J.W., 1992, "The relation between crack growth resistance and fracture process parameters in elastic-plastic solids", *Journal of the Mechanics and Physics of Solids*, Vol. 40, pp. 1377-1397.

Tvergaard, V. and Hutchinson, J.W., 1993, "The influence of plasticity on mixed mode interface toughness", *Journal of the Mechanics and Physics of Solids*, Vol. 41, pp. 1119-1135.

Tvergaard, V. and Hutchinson, J.W., 1994, "Toughness of an interface along a thin ductile layer joining elastic solids", *Philosophical Magazine* A70, pp. 641-656.

Tvergaard, V. and Hutchinson, J.W., 1996, "On the toughness of ductile adhesive joints", *Journal of the Mechanics and Physics of Solids*, Vol. 44, pp. 789-800.

Varias, A.G., Suo, Z., and Shin, C.F., 1991, "Ductile failure of a constrained metal foil", *Journal of the Mechanics and Physics of Solids*, Vol. 39, pp. 963-986.

Wang, B., and Siegmund, T., 2005, "Numerical analysis of constraint effects in fatigue crack growth by use of an irreversible cohesive zone model", *Int J Fract*, Vol. 132, pp.175-196.

Williams, M.L., 1957, "On the stress distribution at the base of a stationary crack", *J. Appl. Mech., Trans. ASME*, Vol. 24 (1), pp. 109–114.

Yang, B., Mall, S., and Ravi-Chandar, K., 2001, "A cohesive zone model for fatigue crack growth in quasibrittle materials", *International Journal of Solids and Structures*, Vol .38, pp. 3927-3944.

4. FATIGUE CRACK GROWTH AT PLASTICALLY MISMATCHED BI-MATERIAL INTERFACES

A study of FCG in a system with an interface between two elastic-plastic solids of different yield strength is conducted. The FCG analysis is emplored by the irreversible cohesive zone model. FCG is considered to occur along the direction perpendicular to the interface and along the interface. Crack growth rate acceleration, deceleration or arrest, as well as crack bifurcation at the interface are predicted in dependence of the plastic property mismatch of the two solids and the interface properties. The outcome of the simulations is in very good agreement with trends of published experimental data.

4.1. Introduction

The computational analysis of FCG behavior for a crack growing perpendicular to and potentially deflecting into a bi-material interface is studied. The interface separates two materials or phases, one of low yield strength (soft) and one of high yield strength (hard). Several experimental studies on FCG for such situations have been reported, *e.g.* in Suresh *et al.* (1992), Sugimura *et al.* (1995a, b), Milan and Bowen (2003), Pippan *et al.* (2000), Jiang *et al.* (2003) and Fu *et al.* (2003). In summary, from these studies the following main observations can be deduced: (1) FCG rates are constant in each of the phase except in a domain close to the interface with (2) a retardation of FCG as a crack grows from a low yield strength material to a high yield strength material; or (3) an acceleration of FCG as the crack grows from the high yield strength material into the low

77

yield strength material; and (4) a potential for deflection into the interface exists. The present type of FCG problem is of concern to both structural mechanics problems such as in welds and multilayer structures (Yeh, 1995), as well as to micromechanics problems such as in the analysis of FCG which are influenced by the microstructure of an alloy or composite (Warrier and Majumdar, 1997). In either case it is of interest to understand the interaction between plastic deformation and crack advance, including crack bifurcation at the interface.

As the crack approaches the interface small scale yielding conditions are violated and FCG cannot be described by use of the Paris law approach. In the past, several alternative analysis approaches were proposed. Elastic-plastic fracture mechanics concepts were applied to compute crack tip shielding and crack tip amplification factors in Sugimura et al. (1995) and Kim et al. (1997). Based on these factors a discussion on the crack tip driving force was then conducted. Alternatively, FCG behavior was analyzed by applying superposition of the applied stress intensity factor and a position dependent residual stress intensity factor, Milan and Bowen (2003). Crack growth rates were then obtained from employing the resulting effective stress intensity factor in the Paris law of the individual phases. Pippan and Riemelmoser (1998, 2000) applied the Dugdale model to calculate plastic zone sizes and crack tip opening displacements. Based on these results FCG rates were then related to the cyclic crack tip opening displacements. A similar approach was undertaken by Wang and Hutchinson (2001) in a study of a fatigue crack terminating at the interface between an elastic-plastic and an elastic solid. While these previous investigations clarified the interaction of the monotonic and cyclic plastic zone with the bi-material interface, they did not predict the details of the transient acceleration/deceleration events in FCG in the region close to the interface. Furthermore, only a limited analysis of conditions and the associated mechanics of crack bifurcation at the interface were presented in the past. Knesl et al. (2003) studied the influence of interface conditions in elastic systems only. The influence of plastic deformation on fatigue crack bifurcation has not been analyzed yet in detail. Experimental results of Pippan et al. (2000) indicate that interface properties alone cannot explain the bifurcation

behavior and that the plastic deformation fields need to be accounted for in detail. The present research aims to overcome these limitations.

4.2 Model Description

4.2.1 Material Model

The model investigated in the present study consists of two half spaces, a "soft", low yield strength phase V^s and a "hard", high yield strength phase V^h separated by a bi-material interface. A crack is assumed to propagate from one phase to the other in the direction perpendicular to the interface. Crack growth from the hard to the soft phase, as well as for the crack growth from the soft to the hard phase is of interest. The volumetric constitutive laws for the soft and the hard phase are those of an isotropic linear elasticity and linear kinematic hardening plasticity. Then, the yield function is given as

$$\sqrt{\tfrac{3}{2}(S-\alpha')(S-\alpha')} - \sigma_Y = 0 \tag{4.1}$$

with $S = \sigma - pI$ the deviatoric stress, $p = \tfrac{1}{3}\text{trace}(\sigma)$ the hydrostatic stress, and α' the deviatoric part of the backstress tensor α. The evolution of the backstress for the linear (Prager-Ziegler) kinematic hardening law is provided as

$$\dot{\alpha} = \frac{C}{\sigma_Y}(\sigma - \alpha)\dot{\bar{\varepsilon}}^{pl} \tag{4.2}$$

where C is the kinematic hardening modulus, and $\dot{\bar{\varepsilon}}^{pl} = \sqrt{\tfrac{2}{3}(\dot{\varepsilon}^{pl} : \dot{\varepsilon}^{pl})}$ is the equivalent plastic strain rate. Finally, the flow rule is given by:

$$\dot{\varepsilon}^{pl} = \frac{3}{2}(S-\alpha)\frac{\dot{\bar{\varepsilon}}^{pl}}{\sigma_Y} \tag{4.3}$$

4.2.2 Finite Element Model

In the finite element simulations the same modified boundary layer approach as one in chapter 3.2.3 is used. Since only mode I loading is considered, the loading is provided by the equation (3.4) with zero T-stress values. For the cyclic loading, the load ratio of R=0 and amplitude of $\Delta K = K_{max}$ which is related to the $\Delta G = G_{max}$ by equation (3.5) are used in the calculations. Due to the nature of symmetry for the model under mode-I loading, only half of the model is considered. Figure 4.1(a) displays the global finite element mesh. The element arrangement near the crack tip is shown in Figure 4.1(b). The initial crack tip is located at point O. At the crack tip, there is a highly refined mesh region with length L. The length of one square element in this region is denoted by l. The radius of the outer boundary is described by r_b. The computations were carried out for model dimensions $r_b / l = 10000$ and $L / l = 110$. The smallest element size relates to the cohesive length as $l / \delta_0 = 2.5$. Simulations are conducted under plain strain conditions. Four node solid elements with full integration are employed. A single row of cohesive zone elements was placed along the symmetry line of the model from the initial crack tip to the outer boundary. Another sequence of cohesive zone elements was placed along the bi-material interface. The distance between the initial crack tip and the interface is $L_0 / \delta_0 = 110$. The cohesive zone elements possess four nodes with linear displacement jump interpolation. Cohesive elements placed along the symmetry line use nodes on the line of symmetry as two of their nodes. The second pair of nodes of the cohesive zone elements is a pair of nodes in common with the adjacent solid elements.

The finite element mesh consists of 3892 solid elements, 123 cohesive zone elements along the symmetry axis and 44 cohesive zone elements along the interface.

4.2.3 Material Properties

Both half spaces, hard and soft, are assigned the same values of elastic properties, $E = 100$ GPa and $v = 0.34$. The two half spaces differ in their yield strength by a factor of $\sigma_Y^h / \sigma_Y^s = 2.0$. This value is motivated by the properties of the material systems in the experimental studies of Sugimura *et al.* (1995), Pippan *et al.* (2000), and Jiang *et al.* (2003) where the ratios in yield strength between hard and soft phases were 1.5, 3.7 and 1.7, respectively. In the computations the values $\sigma_Y^s = 0.0025 \times E = 250$ MPa and $\sigma_Y^h = 0.005 \times E = 500$ MPa together with a tangent modulus of $h = E/20 = 5000$ MPa were used.

For the purpose of the present simulations, the values of the cohesive length is identical for the soft and hard phase, $\delta_0 = \phi_0/(e\sigma_{max,0}) = const.$ and fixed to $\delta_0 = 7.4\ \mu$m. Figure 4.2 depicts predicted FCG rates in dependence of the ratio between initial cohesive strength and yield strength, and compares the results to those obtained in simulations with elastic material behavior only. For $\sigma_{max,0}/\sigma_y < 3.0$ the presence of plastic deformation has virtually no effect on the FCG rate. Only for $\sigma_{max,0}/\sigma_y > 3.0$ do the predicted FCG rates for the elastic-plastic analysis deviate from those obtained for the elastic solution. In order to introduce a sufficient but not overwhelming level of plastic deformation into the simulations the initial cohesive strength is taken as four times the corresponding yield strength, $\sigma_{max,0}^s = 4 \times \sigma_Y^s = 1000$ MPa and $\sigma_{max,0}^h = 4 \times \sigma_Y^h = 2000$ MPa, respectively. The initial cohesive energies for the crack path through the soft and hard phase are then $\phi_0^s = 20$ J/m^2 and $\phi_0^h = 40$ J/m^2, respectively. For the cyclic cohesive zone parameters the value of the ratio $\sigma_f/\sigma_{max,0}$ is taken to be 0.25 which is a lower bound on typical experimental values of the fatigue ratio. The value of the ratio δ_Σ/δ_0 is known to scale the number of load cycles required to fail a cohesive element (Roe and Siegmund, 2003). In order to keep the computational cost within acceptable limits the value of $\delta_\Sigma/\delta_0 = 4$ was selected for both the soft and hard phase.

For the bi-material interface, a range of cohesive zone parameters was considered. First, several computations were performed with a perfectly bonded interface such that no cohesive zone elements were introduced along the interface. Subsequently, the interface was modeled with cohesive zone elements. For the interface the cohesive zone length was identical to that for the crack paths through the adjacent solids, but the cohesive strength was varied in the range of $\sigma_{\max,0}^{\text{int}} = 1000\,\text{MPa}$ to 500 MPa. In order to keep the variation of material parameters small, the cyclic cohesive zone parameters of the interface were taken to be identical to those of the solids, $\sigma_f / \sigma_{\max,0} = 0.25$ and $\delta_\Sigma / \delta_0 = 4$.

In the presentation of the simulation results values of the energy release rate are always normalized with ϕ_0^s. Due to the differences in the cohesive zone properties assigned to the soft and hard phase, relative load magnitudes need to be considered as

$$\left(\frac{\Delta G}{\phi_0^h}\right) \Big/ \left(\frac{\Delta G}{\phi_0^s}\right) = \frac{\phi_0^s}{\phi_0^h} \tag{4.4}$$

with the present selection of the cohesive zone parameter values, $\phi_0^s / \phi_0^h = 1/2$, the hard phase experiences a relative load level of half of the soft phase. Consequently, the steady state crack growth rates in the soft phase will exceed those in the hard phase.

Three different levels of applied energy release rate range, $\Delta G / \phi_0^s = 0.15, 0.225, 0.3$ are considered. For these load levels one obtains $r_{pl}^h / \delta_0 = 19.6$, 29.4, 39.1 and $r_{pl}^s / \delta_0 = 78, 117, 156$, as well as $\Delta r_{pl}^h / \delta_0 = 5, 7, 9$ and with $\Delta r_{pl}^s / \delta_0 = 19.6, 29.4, 39.1$. It is to be noted here that $\Delta r_{pl}^s = r_{pl}^h$ since $\sigma_Y^h = 2\sigma_Y^s$.

4.3 Results and Discussions

4.3.1 Crack growth in a bi-material with a perfect interface

First, the FCG behavior of cracks propagating perpendicular to a perfectly bonded interface is investigated. Two cases are considered: (a) propagation from the hard to the soft phase, and (b) propagation from the soft to the hard phase. Figure 4.3(a) depicts the predicted normalized FCG rates, $d(a/\delta_0)/dN$, in dependence of the normalized fatigue crack extension, $\Delta a/\delta_0$, for the hard to soft case. At first, after a short transient period at crack growth initiation, FCG quickly enters a steady state growth stage in which a constant crack growth rate is present. Analysis of the data shows that $d(a/\delta_0)/dN = 15.4(\Delta G/\phi_0^s)^{1.72}$ correlates crack growth rate to loading in the hard phase. Another steady state growth stage is observed for the soft phase once the crack tip is again far from the interface. Then, the relationship $d(a/\delta_0)/dN = 44.0(\Delta G/\phi_0^s)^{1.3}$ correlates crack growth rate to loading in the steady state regime in the soft phase. The more interesting results, however, are those obtained for the transient behavior in the vicinity of the interface. Once the crack is at a critical distance from the interface, a significant increase in growth rates is predicted. This type of response is in agreement with experimental results of Pippan *et al.* (2000) and Jiang *et al.* (2003). The distance between crack tip and interface for the onset of acceleration scales well with the magnitude of r_{pl}^h, the plastic zone size in the hard phase at G_{max}, equation (4.6). A distinct maximum value in the predicted FCG rate is obtained in all cases at a very small distance beyond the interface. The maximum values of crack growth rate are significantly larger than the constant growth rates in either the hard or the soft phase, *e.g.* for the case $\Delta G/\phi_0^s = 0.3$ the peak crack growth rate is approximately 75 and 15 times large than the steady state growth rate in the hard phase and soft phase, respectively. The magnitude of the peak crack growth rate increases with increased load level. After the crack has penetrated the interface the crack growth rate drops again. The crack extension

magnitude to reach a steady state scales well with the magnitude of Δr_{pl}^s, the cyclic plastic zone size in the soft phase.

Details of the process of crack – interface interaction can be discussed in view of the predicted damage distributions and the time evolution of damage. Figure 4.3(b) depicts predicted distributions of damage in the cohesive zone as the crack moves from the hard to the soft phase for the case of $\Delta G / \phi_0^s = 0.15$. During the steady state growth regime in the hard phase the damage distribution remains self-similar as the damage front moves towards the interface. In the steady state regime in the hard phase crack growth initially occurs with a constant length of the active cohesive zone, $l_{cz} / \delta_0 = 35$. This result is typical for all steady state crack growth cases in that the length of the active cohesive zone is thus somewhat larger than the basic estimate for the monotonic plastic zone size, r_{pl}, but significantly larger than the cyclic plastic zone size, Δr_{pl}. However, before the damage in the hard phase reaches the interface, damage already occurs in the soft phase beyond the interface. A secondary damage zone is formed in which damage increases rapidly. The process of link-up between the initial crack in the hard phase and the secondary damage zone in the soft phase is the cause for the transient crack growth rate increase in the vicinity of the interface. The process occurs as the distance between the crack tip and the interface corresponds to approximately r_{pl}^h. During the link-up stage the length of the active cohesive zone is temporarily increased to a length of $l_{cz} / \delta_0 = 110$. After the link-up between the primary crack and the secondary damage zone, crack growth then progresses self-similar in the soft phase. The length of the active cohesive zone now has increased and is approximately three times as long as in the hard phase, $l_{cz} / \delta_0 = 105$.

The predicted crack growth behavior for the case of growth from the soft to the hard phase is discussed next. Figure 4.4(a) depicts the predicted normalized crack growth rates in dependence of the normalized crack extension. After the transient during crack growth initiation period, the crack growth in the soft phase rate remains nearly constant for some amount of crack extension. At $\Delta a / \delta_0 = 50$ the relationship

$d(a/\delta_0)/dN = 46(\Delta G/\phi_0^s)^{1.4}$ correlates crack growth rate to loading. These crack growth rates are very similar to those obtained for the soft phase in simulations of the hard to soft case. The steady state crack growth regime in the soft phase is less pronounced in the simulation of crack growth from soft to hard phase due to the fact that the length of the active cohesive zone in the soft phase is rather large when compared to the distance between interface and initial crack tip. Another steady state growth stage is observed for the hard phase once the crack tip is again far from the interface. Then, the relationship $d(a/\delta_0)/dN = 9.7(\Delta G/\phi_0^s)^{1.53}$ correlates crack growth rate to loading in the steady state regime in the hard phase. These crack growth rates are very similar to those predicted for the hard phase in the hard to soft case. Again, a significant transient deviation from the two steady state crack growth regimes takes place once the crack tip is in the vicinity of the interface.

As the crack tip approaches the interface the FCG rate drops strongly and reaches the minimum value as the crack tip is located at the interface. The predicted magnitude of crack retardation is dependent on the applied load level with the difference between the minimum crack growth rate at the interface and steady state growth rate in the hard material increasing with load level. The prediction of temporary crack retardation is in agreement with experimentally observed FCG retardation effects in bi-material systems, (Sugimura *et al.*, 1995; Pippan *et al.*, 2000 and Jiang *et al.*, 2003). The distance at which crack retardation sets in is well related to the magnitude of r_{pl}^s, i.e. the plastic zone size in the soft phase at G_{max}, equation (4.6). Subsequent to passing the interface the crack growth rate increases again to reach the steady state growth rate in the hard phase. The predicted distance from the interface to reach the steady state crack growth rate relates well to the cyclic plastic zone size in the hard phase, equation (4.7).

The type of interaction between crack and interface for the soft to hard case is quite different from that previously described for the hard to soft case. Figure 4.4(b) depicts predicted distributions of damage in the cohesive zone as the crack moves from the soft to the hard phase for the case of $\Delta G/\phi_0^s = 0.15$. As the crack approaches the interface via the soft phase the tip of the active cohesive zone penetrates into the hard

phase. Subsequently the speed of the cohesive zone tip is reduced considerably relative to the speed of the crack tip leading to an intermediate crack growth rate below either of the steady state growth rates.

4.3.2 Crack growth in a bi-material with imperfect interfaces

Results described in this section were obtained for computations in which crack growth along the bi-material interface is included. A range of the interface cohesive strength values was considered in order to study the crack – interface interaction in more detail.

For an initial overview of the simulation results two contour plots are presented. Figure 4.5 depicts contours of the equivalent stress for crack propagation for the hard to soft case (at $t/t_c = 80.5$) and the soft to hard case (at $t/t_c = 104.5$) for the interface strength $\sigma_{\text{max},0}^{\text{int}} = 600\,\text{MPa}$ at a load level of $\Delta G/\phi_0^s = 0.15$. For both cases, the crack is deflected into the interface. However, the predicted deformation and the stress distribution are significantly different. For crack propagation in the soft to hard case, the initial crack has reached the interface and the ligament between the initial crack tip and the interface is completely separated. The main stress concentration is found in the hard phase and located at the interface crack tips and along the interface. For the hard to soft case, a very different result is obtained. Even during interface crack growth, the initial crack has not reached the interface and an intact ligament remains between the initial crack tip and the interface. The main stress concentration is still present at the tip of the arrested initial crack and not at the location of the crack tips at the interface. The predicted "asymmetry" in the response for the two cases considered was observed experimentally by Pippan *et al.* (2000).

The details of the fatigue crack growth behavior for crack growth from the hard to soft case under consideration of the interface properties are discussed first. Computational results shown are for an applied load of $\Delta G/\phi_0^s = 0.15$. Figure 4.6

depicts predicted crack normalized extension in dependence of load cycles for values of the interface cohesive strength, $\sigma_{max,0}^{int}$, ranging between 1000 MPa and 500 MPa. Both, crack extension along the direction of the initial crack and along the interface are included in the diagram. Corresponding plots of normalized crack growth rates vs. crack extension are given in Figure 4.7(a) and 4.7(b). Figures 4.6 and 4.7 clearly demonstrate that the interface strength significantly impacts the predicted crack growth behavior. For strong interfaces, $\sigma_{max,0}^{int}$ =1000 MPa and 900 MPa, the predicted crack growth behavior is only little different from that already discussed for the perfect interface. Again, two steady state crack growth stages are predicted, with the crack growth rate in the soft phase exceeding that for the hard phase, and transient crack acceleration in the region close to the interface. A detailed comparison of the perfect interface case and the computation with $\sigma_{max,0}^{int}$ =1000 MPa and 900 MPa is included in Figure 4.7(a) and demonstrates that the steady state crack growth rates are identical for these three cases, and only a decrease in the predicted transient crack growth rate is predicted for the imperfect interfaces. As the interface strength is further reduced this response is, however, altered.

As the interface strength is reduced to $\sigma_{max,0}^{int}$ <800 MPa the computations predict that the initial crack no longer penetrates the interface. Instead, the crack growth rate is reduced as the crack tip approaches the interface, and finally the crack is virtually arrested, Figure 4.6 and 4.7(a). The distance between the arrested crack tip and the interface is larger than $r_{pl} / \delta_0 = 19.6$ at $\Delta G / \phi_0^s$ =0.15. These results are in agreement with the observation of the intact ligament between initial crack and interface as shown in Fig. 4.5(a). Concurrently with the arrest process of the initial crack the initiation of crack growth along the bi-material interface is observed, Figure 4.6 and 4.7(b). In Figure 4.7(b) to indicate the correlation between the locations of arrest of the initial crack relative to the interface crack growth, lines depicting the interface crack growth data are placed with their origin at the location of crack arrest of the initial crack. The lower the interface strength, the earlier this event occurs. Interface crack growth rates are initially large but continuously drop as the crack length increases. Initial interface crack growth rates can

exceed the steady state crack growth rates in the adjacent solid but steadily drops as the interface crack length increases.

The simulation for $\sigma_{max,0}^{int} = 800$ MPa predicts a behavior that is different from those discussed so far, Figure 4.6 and 4.7. For this case crack growth along the interface and arrest of the initial crack again are observed. The distance between the onset of crack arrest and the interface now well corresponds to $r_{pl} / \delta_0 = 19.6$ at $\Delta G / \phi_0^s = 0.15$. However, as loading processes, the ligament between the tip of the arrested crack and the interface fails, and crack growth along x-axis is resumed through a rapid transient acceleration and the subsequent steady state growth regime typical of crack growing from the hard to the soft phase. Concurrently with the re-initiation of crack growth along the x-axis, the interface crack is arrested.

Based on Figure 4.7(a) a comparison with the results of Pippan *et al.* (2000) and Sugimura *et al.* (1995) are made. The computations with the imperfect interfaces but penetrating cracks predict an increase in FCG rate of a factor of ~ 30 in good agreement with the experimental observations (~ 50) while the computations with the perfect interface significantly overestimate the increase in FCG rate. Furthermore, it is noted that the experiments of Pippan *et al.* (2000) also showed a small transient reduction in FCG rate just before the crack reaches the interface. The predicted transient acceleration is however larger than those observed in Sugimura *et al.* (1995). In agreement with the experimental studies the computations predict that the transient crack growth changes occur in the close vicinity of the interface.

The mode mixity of the material separation for the interface crack is characterized by determining $\psi = \tan^{-1}(u_t / u_n)$ at location $y / \delta_0 = 50$ for the load cycle in which damage reached $D_c = 0.5$. At the maximum load of this load cycle, $t / t_c = 105.5$ the computations predict $\psi = 4.7°$. As seem from Figure 4.5(a) during loading, tangential separation at the interface is inhibited by the remaining intact ligament. At the following minimum, $t / t_c = 106.0$, it is found that $\psi = -29.3°$. During unloading a significant amount of interaction between the upper and lower half of the model is possible again due to the remaining ligament. During unloading, this leads to only little reduction of the

material separation parallel to the interface while the material separation in the direction perpendicular to the interface is reduced significantly, finally resulting in the observed change in mode mixity.

The details of the fatigue crack growth behavior for crack growth from the soft to hard case are discussed next. Computational results shown are for an applied load of $\Delta G / \phi_0^s = 0.15$. Figure 4.8 depicts predicted crack normalized extension in dependence of load cycles for values of the interface cohesive strength, $\sigma_{max,0}^{int}$, ranging between 1000 MPa and 500 MPa. Both crack extension along the direction of the initial crack and along the interface are included in the diagram. The corresponding plots of normalized crack growth rates vs. crack extension are given in Figure 4.9(a) and 4.9(b). Figure 4.8 and 4.9 clearly demonstrate that the interface strength again significantly impacts the predicted crack growth behavior. For a strong interface, $\sigma_{max,0}^{int}$=1000 MPa, the predicted crack growth behavior is only little different than that already discussed for the perfect interface. Again, two steady state crack growth stages are predicted, with the crack growth rate in the soft phase exceeding that for the hard phase, and transient crack retardation in the region close to the interface, Figure 4.8. A detailed comparison of the perfect interface case and the computation with $\sigma_{max,0}^{int}$=1000 MPa is included in Figure 4.9(a) demonstrating that the crack growth rates for the two cases are identical in the steady state regions, but with a higher amount of crack retardation predicted for the case of $\sigma_{max,0}^{int}$=1000 MPa. As the interface strength is further reduced to 900 MPa and 800 MPa, the crack continues to penetrate the interface, and crack growth rates are not altered, except for the presence of even stronger growth retardations at the interface, Figure 4.9(a). For interface cohesive strength of 750 MPa and 700 MPa crack growth rates in the soft phase are still the same as for the perfect interface but the crack finally does no longer penetrate the interface. Arrest of the cracks at the interface is predicted, Figure 4.9(a). Finally, for even weaker interfaces, $\sigma_{max,0}^{int}$=650, 600, 500 MPa, crack deflection into the interface, and crack growth along the interface is predicted, see results for these cases in Figure 4.8 and 4.9(b). For the cases $\sigma_{max,0}^{int}$=650 and 600 MPa, the predicted growth of the

initial crack is only minimally altered and the cracks come to a halt at the interface or shortly before the interface. Interface crack growth initiation is closely associated with the crack arrest. In Figure 4.9(b) to indicate the correlation between the locations of arrest of the initial crack relative to the interface crack growth, lines depicting the interface crack growth data are placed with their origin at the location of crack arrest of the initial crack. Interface crack growth proceeds at a constant rate.

For the case of $\sigma_{max,0}^{int} = 500$ MPa, i.e. the weakest interface considered in this study, the presence of the weak interface also is predicted to alter the growth of the initial crack, i.e. to reduce the crack growth rate once the crack tip is a distance of approximately $25\delta_0$ or approximately $\Delta r_{pl}^s / \delta_0$ from the interface. The reduction in crack growth rate occurs concurrently with the initiation and growth of the interface crack. Now, the predicted crack growth rate for the interface crack shows a pronounced initial transient behavior, i.e. the initial crack growth rate is considerably larger than the subsequent steady state growth rate. Summarizing, the predicted interface crack growth rates can be characterized by $d(a/\delta_0)/dN = 4.3(\Delta G/\phi_0^s)^{0.8}$, i.e. again a Paris-type law but of considerably smaller power as found for propagation through the bulk.

Based on Figure 4.9(a) a comparison with the results of Pippan *et al.* (2000) and Sugimura *et al.* (1995) are made. The computations with the imperfect interfaces but penetrating cracks predict a decrease in FCG rate of a factor of ~ 150 in good agreement with the experimental observations while the computations with the perfect interface underestimate the decrease in FCG rate. Again, the assumption of a perfectly bonded interface leads to a less favorable agreement between simulation and experiment. In agreement with the experimental studies the computations predict that the transient crack growth changes for the soft to hard case start to occur when the crack tip is still quite remote from the interface.

The mode mixity of the material separation is again characterized by determining $\psi = \tan^{-1}(u_t/u_n)$ at location $y/\delta_0 = 50$ and the load cycle in which damage reached $D_c = 0.5$. At the maximum load of this load cycle, now $t/t_c = 76.5$, $\psi = -31.8°$. For the soft to hard case, Figure 4.5(b), tangential separation at the interface is not

inhibited. At the following minimum, $t/t_c = 77.0$, it is found that $\psi = -8.3°$. During unloading, crack closure is again present along the initial crack. Crack closure of the initial crack leads to a smaller reduction of the material separation parallel to the interface as compared to the material separation in the direction perpendicular to the interface, thereby decreasing the mode mixity.

The computational results are summarized with respect to the influence of the interface toughness on the crack deflection behavior. In Figure 4.10, the distance of the crack from the interface at crack bifurcation, λ/δ_0, is plotted in dependence of the interface cohesive energy, ϕ_0^{int}, as normalized with the cohesive energy of the phase beyond the interface, ϕ_0^P. It should be noted here that since $\sigma_{max,0} = 4\sigma_Y$ in both the soft and hard phase and $\delta_0 = const.$ the values of ϕ_0^{int}/ϕ_0^P can be directly translated into normalized cohesive strength parameters, $\sigma_{max,0}^{int}/\sigma_Y^P$.

Following the results of He and Hutchinson (1989) on crack deflection into the interfaces under monotonic loading in elastic bi-materials, crack deflection should occur only for $\phi_0^{int}/\phi_0^P < 0.2$ in elastically homogeneous materials, but is possible for significantly larger values of ϕ_0^{int}/ϕ_0^P. Subsequently, e.g. in Siegmund et al. (1997) and Arrata and Needleman (1998), it was demonstrated that plastic deformation in the phase beyond the interface will enhance the tendency for crack deflection, and also lead to interface crack growth for cases with $\phi_0^{int}/\phi_0^P > 0.2$. The earlier finding that plastic deformation enhances the tendency to crack deflection is confirmed in the present fatigue crack growth study. For the soft to hard case crack penetration into the hard phase, $\lambda/\delta_0 = 0$, occurred for $\phi_0^{int}/\phi_0^P < 0.4$. For interface strength $0.33 < \phi_0^{int}/\phi_0^P < 0.4$, crack arrest without interface crack growth is predicted. For lower values of the interface strength, $\phi_0^{int}/\phi_0^P < 0.33$, interface crack growth will occur with λ/δ_0 strongly increasing as ϕ_0^{int}/ϕ_0^P decreases further. For cracks initially growing from the hard to the soft phase crack deflection is predicted to occur at significantly increased values of

interface cohesive energy, $\phi_0^{\text{int}} / \phi_0^P < 0.95$. As the interface strength is decreased below this threshold, crack bifurcation at the interface occurs, with λ / δ_0 increasing linearly as $\phi_0^{\text{int}} / \phi_0^P$ decreases. For interfaces with $0.8 < \phi_0^{\text{int}} / \phi_0^P < 0.9$ interface crack growth occurred but as the remaining ligament between the initial crack tip and interface fails, interface crack growth will cease and crack growth into the soft phase will take place. For weaker interfaces, $\phi_0^{\text{int}} / \phi_0^P < 0.8$, interface crack growth and arrest of the initial crack is predicted here. However, it is possible that after a large number of cycles the crack might still penetrate the interface in the same way as demonstrated for the cases with $0.8 < \phi_0^{\text{int}} / \phi_0^P < 0.9$.

A detailed direct comparison with experimental data on crack bifurcation is not yet possible as experimental records do not contain detailed information on the bifurcation behavior, the asymmetric response in the bifurcation response was however also observed in the experimental study of Pippan *et al.* (2000).

4.4. Conclusions

The present study demonstrated the capability of an irreversible cohesive zone model approach to analyze FCG in a bi-material system. The model parameters were tuned such that crack growth rates in the lower yield strength material exceeded those of the higher yield strength material. This was accomplished by setting cohesive strength proportional to the yield strength. The FCG for the bi-material systems with a perfect interface and imperfect interfaces were calculated and compared. The predicted crack growth behavior was found to be in good agreement with experimental observations.

At first, FCG perpendicular to a perfectly bonded interface was investigated. The interaction between the crack and the interface was found to be strongly dependent on the position of the interfaces relative to the initial crack. Strong interaction of the crack with the interface started as the distance between crack tip and interface was approximately

equal to the monotonic plastic zone size at the maximum load level prescribed. Interaction between crack and interface ended as the crack moved beyond the interface a distance equal to the cyclic plastic zone.

When the crack propagated from the hard to the soft phase, two steady-state crack growth stages were predicted with the crack growth rate in the soft phase exceeding that for the hard phase. Crack growth was temporarily accelerated in the region close to the interface. This type of response is in agreement with experimental results of Pippan *et al.* (2000) and Jiang *et al.* (2003). The magnitude of increased crack growth rate increased with the load level. The predicted damage distribution showed that, before the crack in the hard phase reached the interface, damage already occurred in the soft phase. The process of link-up between the damage zone at the initial crack in the hard phase and the secondary damage zone in the soft case leads to the transient crack growth rate increase in the vicinity of the interface.

When the crack propagated from the soft to hard phase, two steady-state crack growth stages were also predicted with the crack growth rate in the soft phase exceeding that for the hard phase. When the crack tip approached the interface the FCG rate dropped strongly and reached the minimum value when the crack tip is located at the interface. The prediction of temporary crack retardation is in agreement with experimentally observed FCG retardation effects in bi-material systems, (Sugimura *et al.*, 1995; Pippan *et al.*, 2000 and Jiang *et al.*, 2003). The predicted level of crack growth retardation at the interface increased with the load level. The predicted damage distribution showed that, as the crack approached the interface via the soft phase, the tip of the active cohesive zone penetrated into the hard phase. Without a secondary damage zone forming beyond the interface, the speed of the active cohesive zone tip was reduced considerably as accumulation in the hard phase is shown.

Secondly, the FCG behavior for crack growth in bi-material system with an imperfect interface was investigated. Crack growth perpendicular to and along the interface was allowed. The results showed that crack acceleration, crack arrest and bifurcation were strongly dependent on the position of the phases relative to the initial crack and the interface cohesive properties.

For a crack approaching the interface from the hard phase, it was found that, for weak interface, e.g. with $\sigma_{max,0}^{int} = 600\,\text{MPa}$, crack bifurcation occurred and the initial crack arrested at least temporarily away from the interface such that an intact ligament remained between crack tip and interface. The main stress concentration was still present at the initial crack tip. The mode mixity was increased due to the remaining ligament. For strong interfaces with the strength of 1000, 900MPa, the predicted crack growth behavior was similar to that for the perfect interface except for a decrease in the predicted transient crack growth rate. As the interface strength decreased to 800MPa, crack growth along the interface and arrest of the initial crack were observed. As the loading processed, the ligament between the arrested crack tip and interface failed and the initial crack growth was resumed and penetrated into the soft phase. With the restart of the initial crack, the bifurcated interface crack was arrested. For the interface with the strength smaller than 800MPa, the initial crack was arrested. Concurrently with the arrested initial crack, the crack was bifurcated into the interface. The lower the interface strength, the earlier the bifurcation occurred. The computations with imperfect interfaces but penetrating cracks predicted an increase in FCG rate of a factor of ~30 in good agreement with the experimental observations (~50, Pippan et al., 2000 and Sugimura et al., 1995) while the computations with the perfect interface significantly overestimated the increase in FCG rate.

If the crack approached the interface from the soft phase, it was observed that for weak interface with $\sigma_{max,0}^{int} = 600\,\text{MPa}$, the initial crack was deflected into the interface and there was no ligament between the initial crack tip and interface left and the crack reached the interface completely. The main stress concentration was found at the crack tip along the interface in the hard phase. And the mod mixity was decreased due to the crack close during unloading. For strong interfaces with the strength of 1000, 900and 800MPa, the predicted crack growth behavior was similar to the case with the perfect interface except for a higher amount of crack retardation. Crack penetrated the interface and no crack bifurcation occurred. As the interface strength decreased to 750 or 700MPa, initial crack finally did no longer penetrate the interface and arrest at the interface. The crack bifurcation did not occur either. For weaker interfaces with the strength of 650, 600

and 500MPa, the initial crack arrested at the interface or a small distance before the interface. The reduction in growth rate for initial crack occurred concurrently with the initiation and growth of the interface crack. Especially, for the interface with the smallest strength of 500MPa, the growth rate of initial crack was reduced once the crack tip was a distance of approximately $\Delta r_{pl}^{s} / \delta_0$ from the interface. And the interface crack growth rate showed a larger initial value than the subsequent steady-state growth rate. The computations with imperfect interfaces but penetrating cracks predicted a decrease in FCG rate of a factor of (~ 150, Pippan *et al.*, 2000 and Sugimura *et al.*, 1995) in good agreement with the experimental observations while the computations with the perfect interface underestimated the decrease in FCG rate.
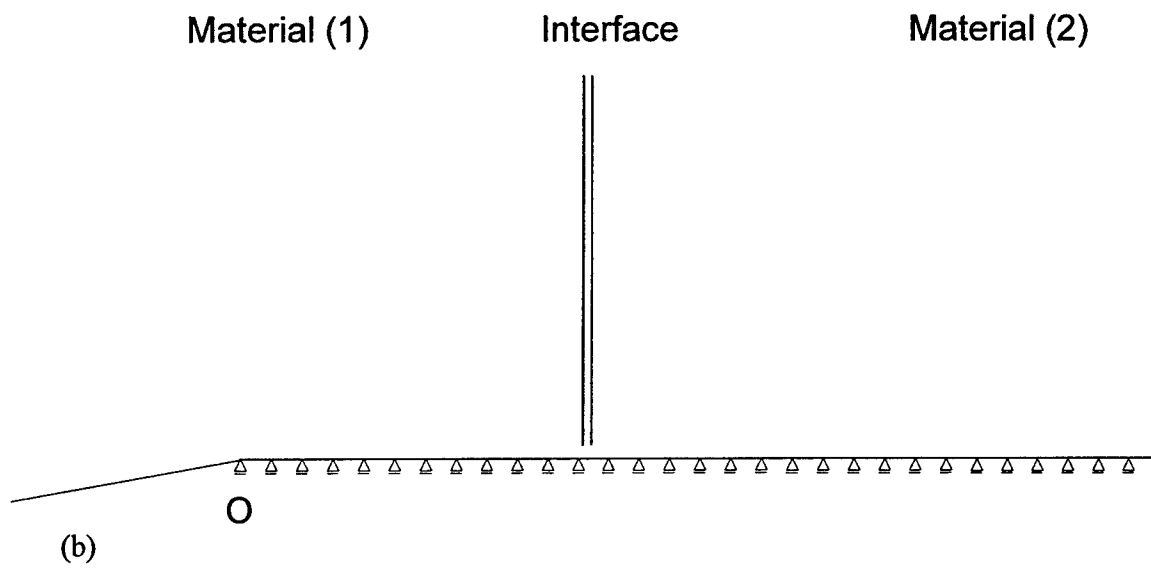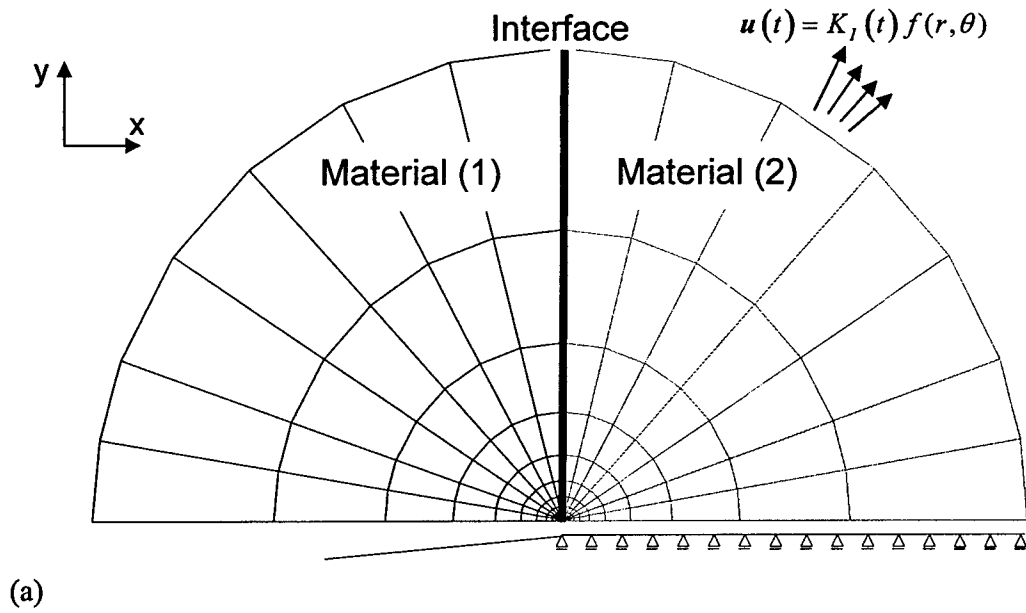
Figure 4.1: (a) A bimaterial in the modified boundary model; (b) Detail of crack tip mesh.
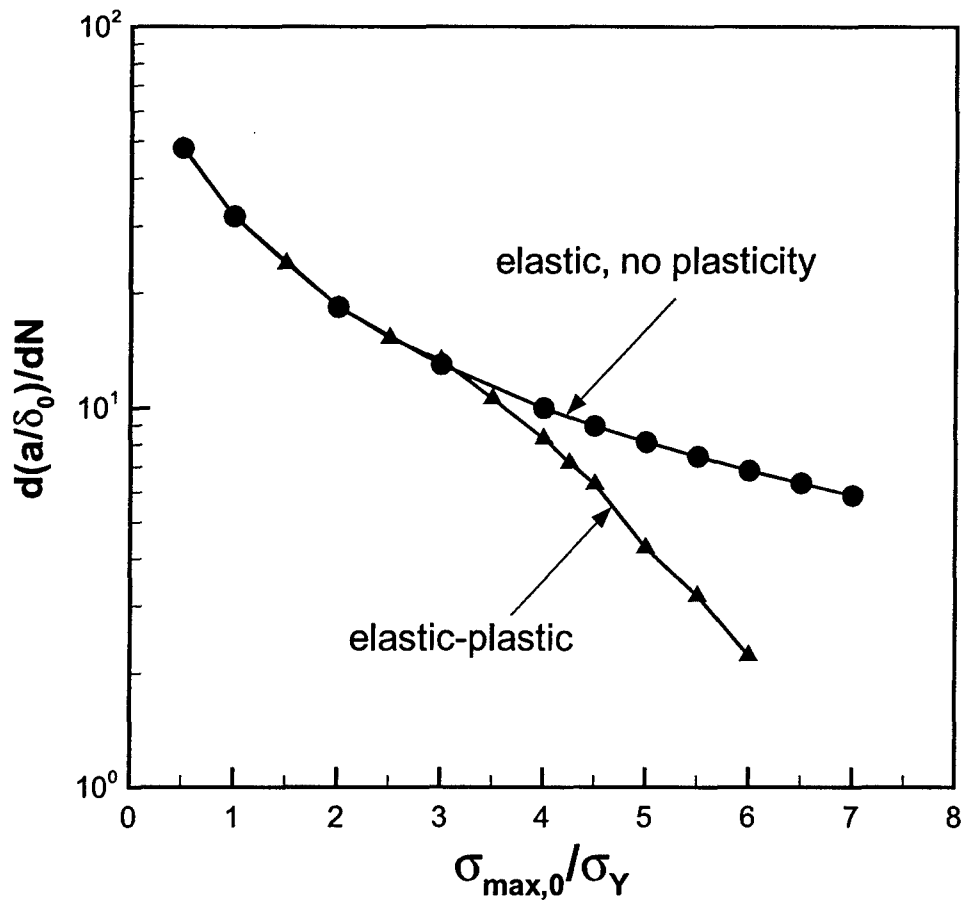
Figure 4.2: Predicted crack growth rates in homogeneous elastic-plastic solids in dependence of the ratio between initial cohesive strength and yield strength, comparison to solutions with elastic material behavior only.
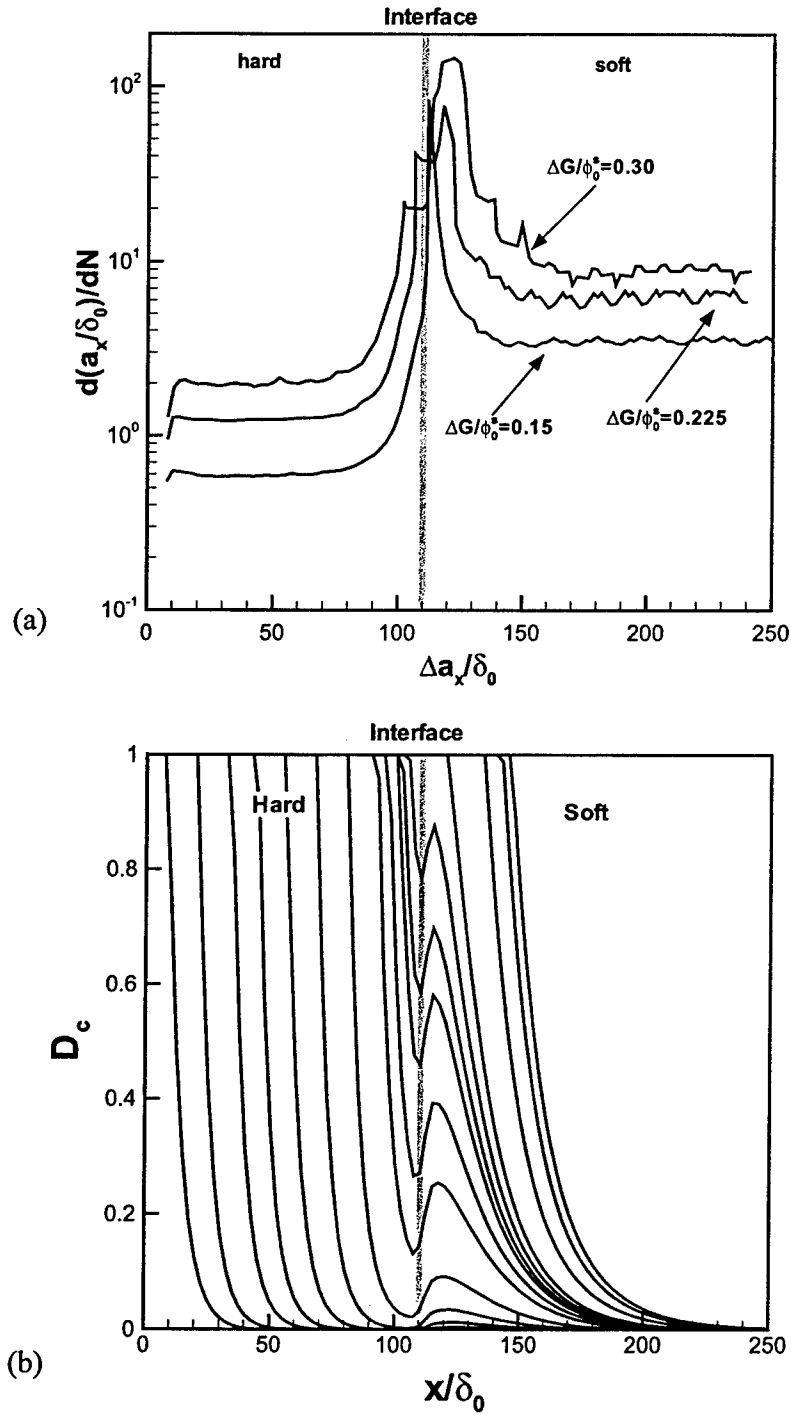
Figure 4.3: Predicted model response for crack growth across a perfectly bonded interface for the hard-soft case: (a) Crack rates in dependence of crack extension for three applied load levels; (b) Damage distribution at series of different cycles.
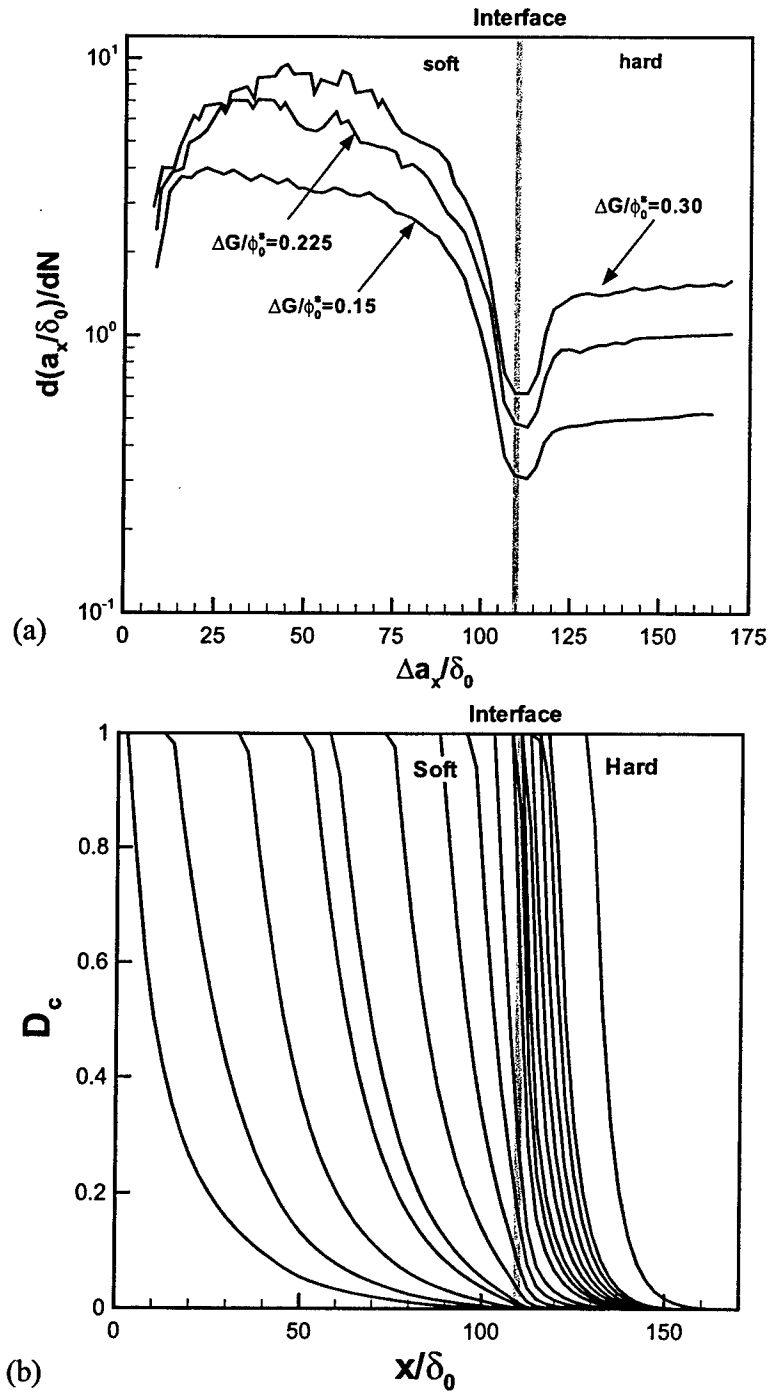
Figure 4.4: Predicted model response for crack growth across a perfectly bonded interface for the soft-hard case: (a) Crack rates in dependence of crack extension for three applied load levels; (b) Damage distribution at series of different cycles.

(a)

$110\delta_0$

(b)
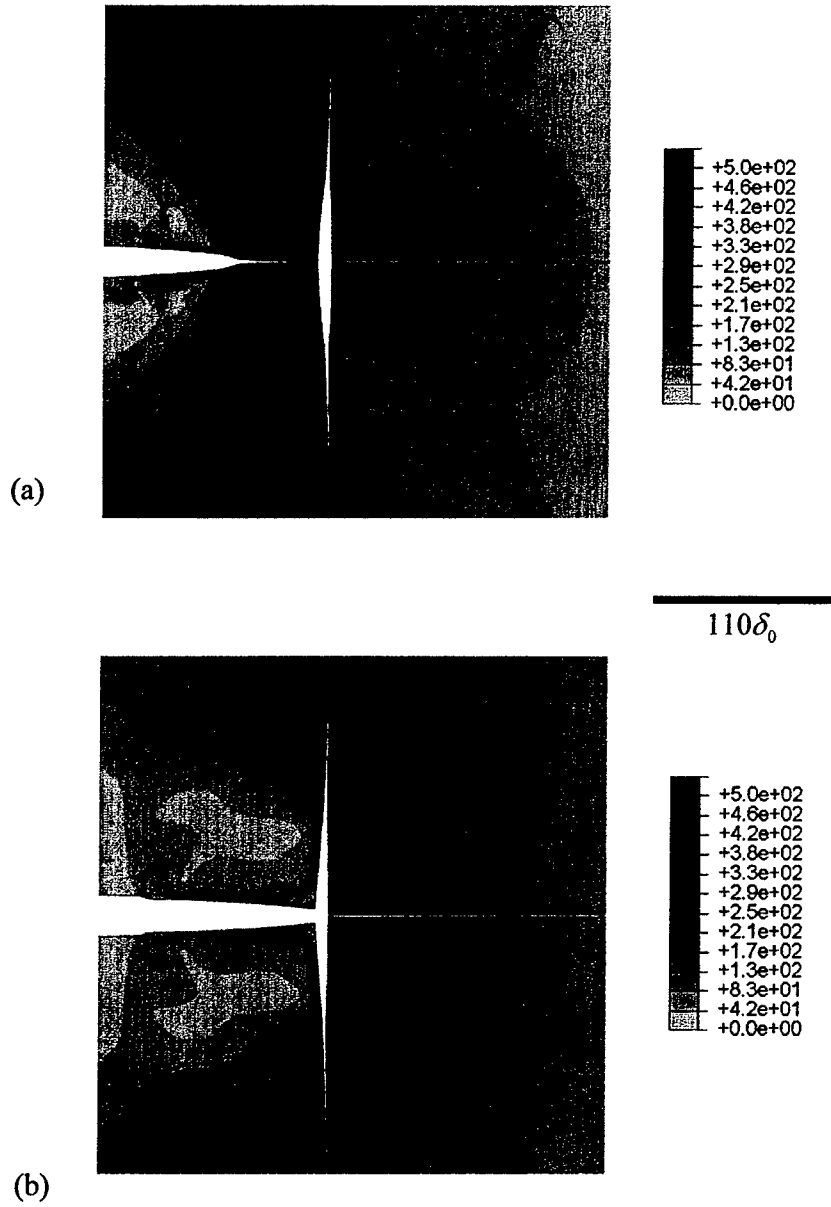
Figure 4.5: Contour plots of equivalent stress, $\sigma^{int}_{max,0} = 600\,MPa$ at a load level of $\Delta G / \phi_0^s = 0.15$: (a) Hard to soft case, $t/t_c = 104.5$; (b) Soft to hard case, $t/t_c = 80.5$. Deformation magnified $\times 10$, symmetry conditions were employed to obtain the contour plots.
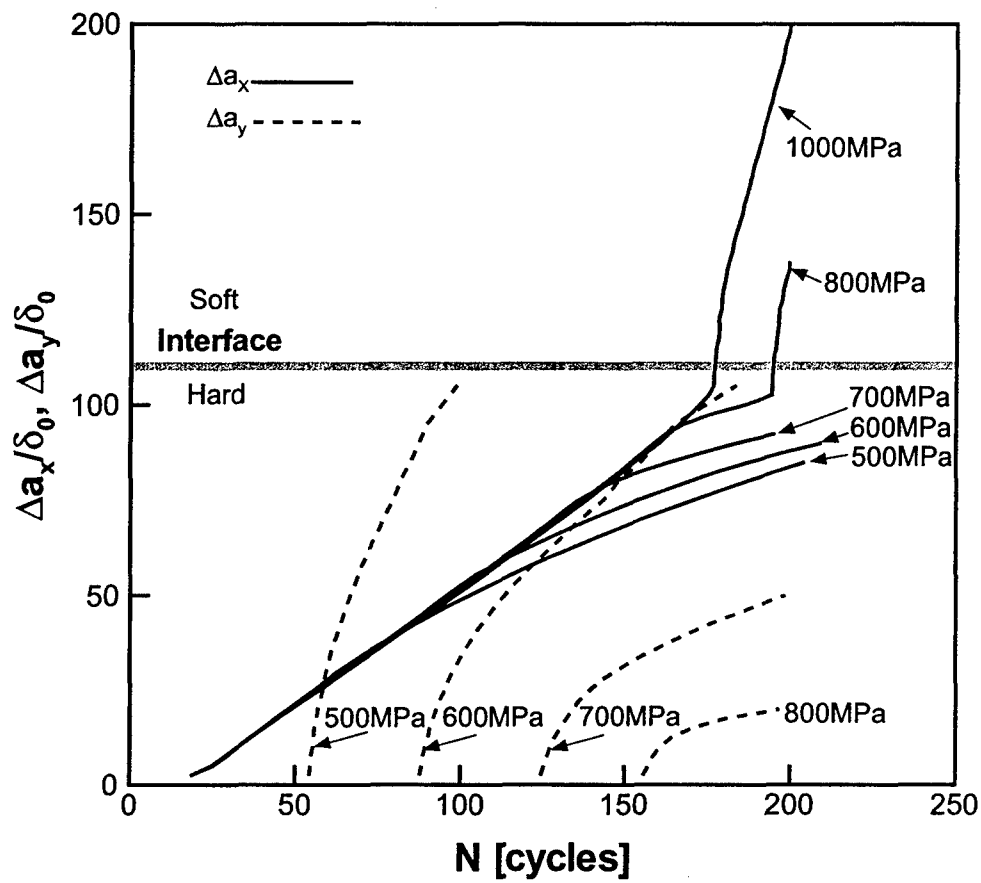
Figure 4.6: Predicted model response for the hard-soft case for several values of the initial interface cohesive strength.
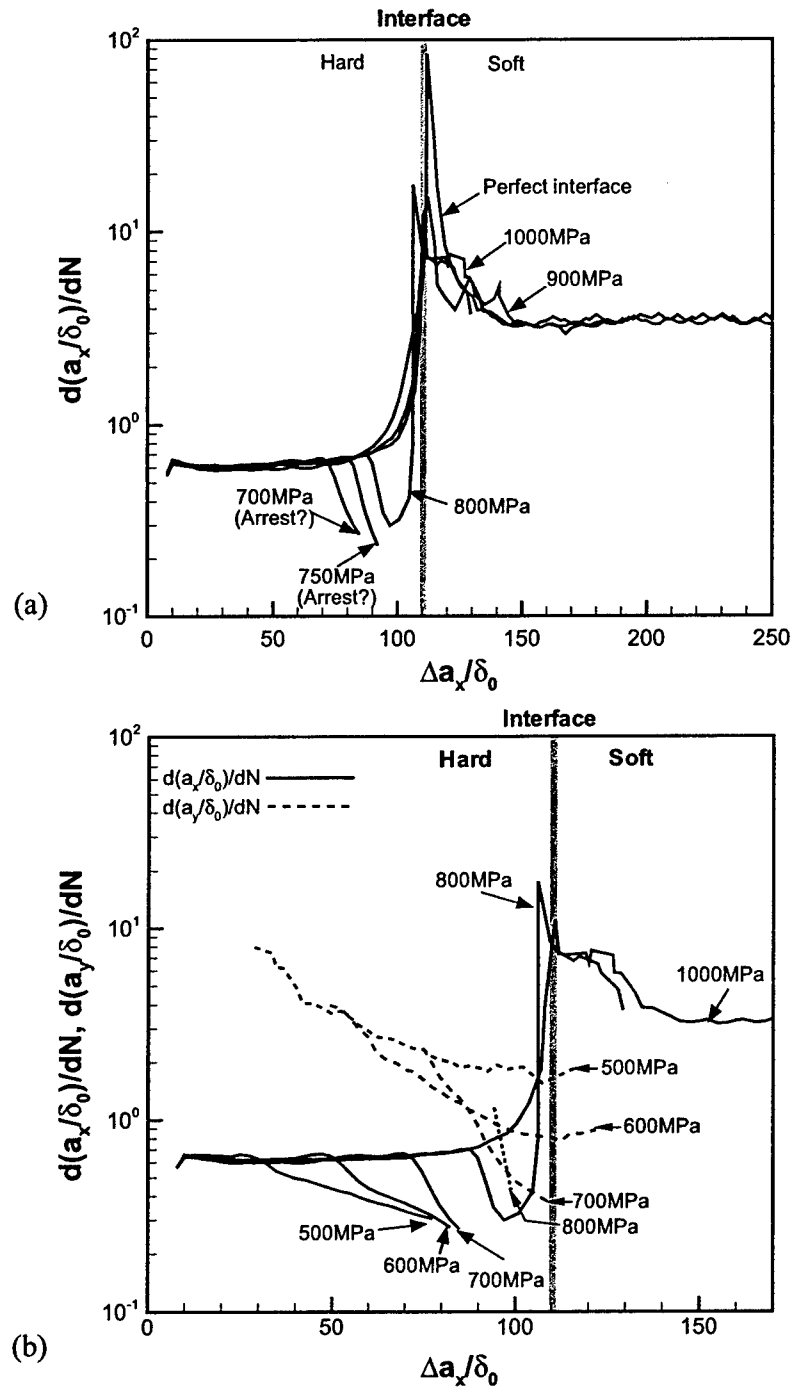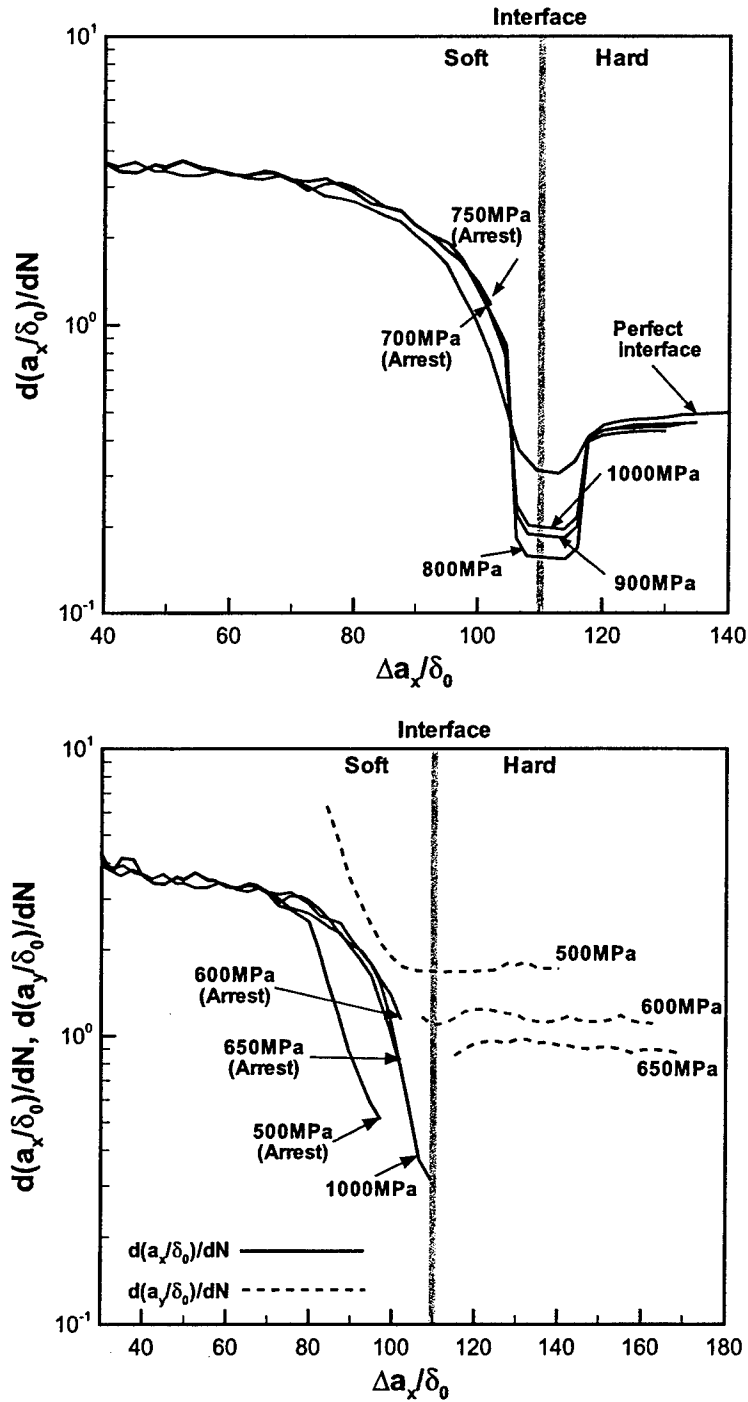
Figure 4.7: Predicted crack growth rates for the hard-soft case in dependence of crack extension for (a) several strong interfaces and comparison to a perfectly bonded interface; (b) for several weak interfaces and comparison to two strong interfaces.
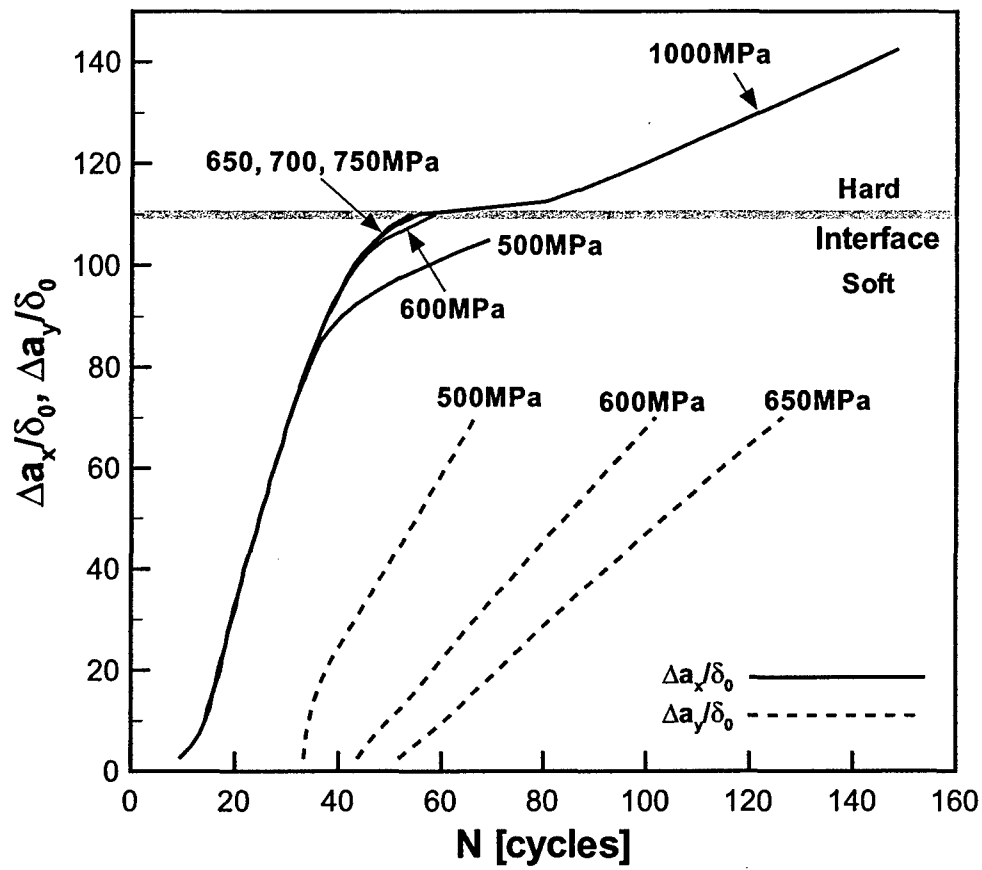
Figure 4.8: Predicted model response for the soft-hard case for several values of the initial interface cohesive strength.

Figure 4.9: Predicted crack growth rates for the soft-hard case in dependence of crack extension for (a) several strong interfaces and comparison to a perfectly bonded interface. (b) several weak interfaces and comparison to two strong interfaces.
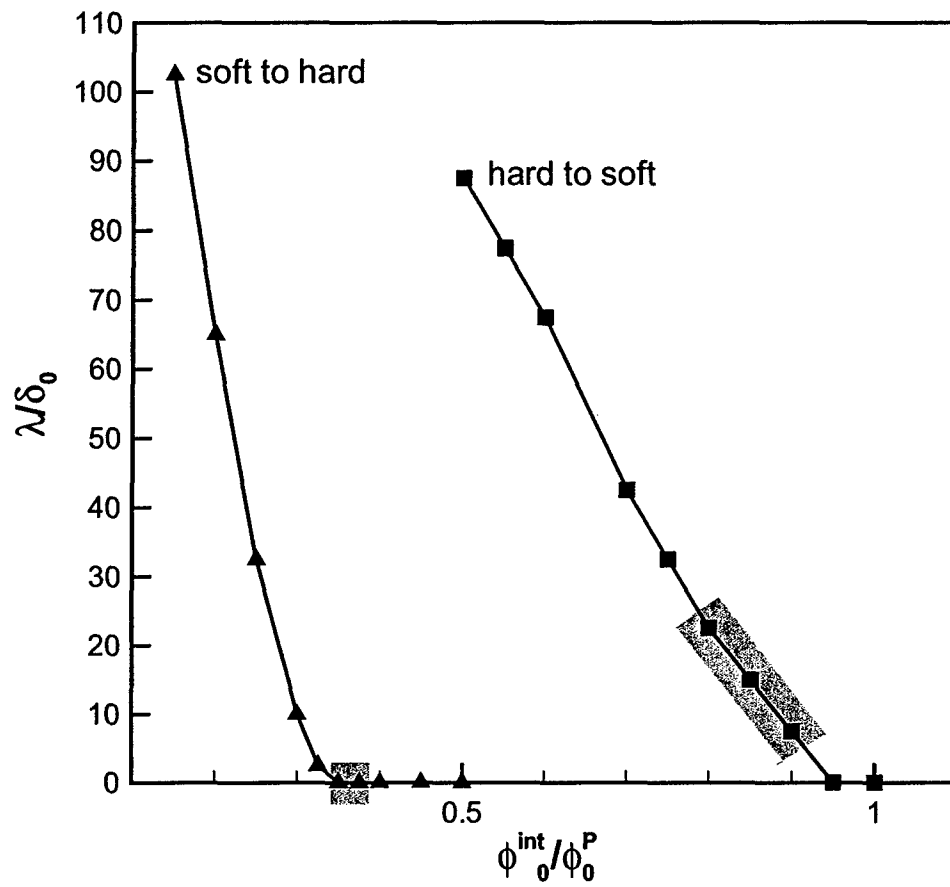
Figure 4.10: Dependence of the normalized distance of the tip of the original crack from the interface at the onset of interface crack growth, λ / δ_0, in dependence of normalized interface properties.

LIST OF REFERENCES

Arrata, J.J.M, Needleman, A., 1998, "The effect of plasticity on dynamic crack growth across an interface", Int. J. Fract, Vol. 94, pp. 383-399.

Deshpande, V.S., Needleman, A., Van der Giessen, E., 2002, "Discrete dislocation modeling of fatigue crack propagation", *Acta Mat.*, Vol. 50, pp. 831-846.

Fu, Y.H., Cui, J.G., He, H.W., 2003, "Interface toughening at Al-Cu laminate composite", *Mat. Sci. Eng.*, Vol. A355, pp. 1-6.

Gerberich, W.W., Harvey, S.E., Kramer, D.E., Hoehn, J.W., 1998, "Low and high cycle fatigue—a continuum supported by AFM observations", *Acta Mater.*, Vol. 46, pp. 5007-5021.

He, M.Y., Hutchinson, J.W., 1989, "Crack deflection at an interface between dissimilar elastic materials", Int. J. Solids Struct. 25, 1053-1067.

Jiang, F., Deng, Z.L., Zhao, K., Sun, J., 2003, "Fatigue crack propagation normal to a plasticity mismatched biomaterial interface", *Mat. Sci. Eng.*, Vol. A356, pp. 258-266.

Jiang, Y., Feng, M., Ding, F., 2005, "A reexamination of plasticity-induced crack closure in fatigue crack propagation", *Int. J. Plast.* Vol. 21, pp. 1720-1740.

Kim, A.S., Suresh, S., Shih, C.F., 1997, "Plasticity effects on fracture normal to interfaces with homogeneous and graded compositions", *Int. J. Solids Struct.*, Vol. 34, pp. 3415-3432.

Knesl, Z., Náhlík, L., Radon, J.C., 2003, "Influence of interface on fatigue threshold values in elastic bimaterials", *Comp. Mat. Sci.* Vol. 28, pp. 620-627.

Lemaitre, J., 1996, "A Course on Damage Mechanics", *Springer-Verlag, Berlin.*

Maiti, S., Geubelle, P.H., 2005, "A cohesive model for fatigue failure of polymers", *Eng. Fract. Mech.* Vol. 72, pp. 691-708.

Milan, M.T., Bowen, P., 2003, "Experimental and predicted fatigue crack growth resistance in Al2124/Al2124+35%SiC(3μm) biomaterial", *Int. J. Fatigue* Vol. 25, pp. 649-659.

Needleman ,A., 1990, "An analysis of decohesion along an imperfect interface", *Int. J. Fract.* Vol. 42, pp. 21-40.

Nguyen, O., Repetto, E.A., Ortiz, M., Radovitzky, R.A., 2001, "A cohesive model of fatigue crack growth", *Int. J. Fract.* Vol. 110, pp. 351-369.

Oskay, C., Fish, J., 2004, "Fatigue life prediction using 2-scale temporal asymptotic homogenization," *Int. J. Num. Meth. Eng.* Vol. 61, pp. 329-359.

Pippan, R., Flechsig, K., Riemelmoser, F.O., 2000, "Fatigue crack propagation behavior in the vicinity of an interface between materials with different yield stress", *Mat. Sci. Eng.* Vol. A283, pp. 225-233.

Pippan, R., Riemelmoser, F.O., 1998, "Fatigue of bimaterials. Investigation of the plastic mismatch in case of cracks perpendicular to the interface", *Comp. Mat. Sci.* Vol. 13, pp. 108-116.

Pippan, R., Riemelmoser, F.O., 2000, "The J-integral at Dugdale cracks perpendicular to interfaces of materials with dissimilar yield stresses", *Int. J. Fract.* Vol. 103, pp. 397-418.

Siegmund, T., Fleck, N.A., Needleman, A., 1997, "Dynamic crack growth across an interface", *Int. J. Fract.* Vol. 85, pp. 381-402.

Rice, J.R., 1967, ASTM STP, Vol. 415, pp. 247-309.

Roe, K.L., Siegmund, T., 2001, "Simulation of interface fatigue crack growth via a fracture process zone model", *Proc. 1st M.I.T. Conf Comp Fluids Solid Mech*, Boston, MA, K.J. Bathe, ed., Elsevier, pp. 435-437.

Roe, K.L., Siegmund, T., 2003, "An irreversible cohesive zone model for interface fatigue crack growth simulation", *Eng. Fract. Mech.* Vol. 70, pp. 209-232.

Roychowdhury, S., Dodds, Jr., R.H., 2003, "A numerical investigation of 3-D small-scale yielding fatigue crack growth", *Eng. Fract. Mech.* Vol. 70, pp. 2363-2383.

Siegmund, T., 2004, "A numerical study of transient fatigue crack growth by use of an irreversible cohesive zone model", *Int. J. Fatigue* Vol. 26, pp. 929-939.

Solanki, K., Daniewicz, S.R., Newman, Jr., J.C., 2004, "Finite element analysis of plasticity-induced fatigue crack closure: an overview", *Eng. Fract. Mech.* Vol. 71, pp. 149-171.

Sugimura, Y., Lim, P.G., Shih, C.F., Suresh, S., 1995a, "Fracture normal to a bimaterial interface: effects of plasticity on crack-tip shielding and amplification", *Acta Metall. Mater.* Vol. 43, pp. 1157-1169.

Sugimura, Y., Grodin, L., Suresh, S., 1995b, "Fatigue crack growth at arbitrary angles to bimaterial interfaces", *Scripta Metall. Mater.* Vol. 33, pp. 2007-2012.

Suresh, S., Sugimura, Y., Tschegg, E.K., 1992, "The growth of a fatigue crack approaching a perpendicularly-oriented, bimaterial interface", *Scr. Metall. Mater.* Vol. 27, pp. 1189-1194.

Tong, J., Yates, R., Brown, M.W., 1995, "A model for sliding mode crack closure part I: Theory for pure mode II loading", *Eng. Fract. Mech.* Vol. 52, pp. 599-611.

Tvergaard, V., Hutchinson, J.W., 1992, "The relationship between crack-growth resistance and fracture process parameters in elastic plastic solids", *J. Mech. Phys. Solids* Vol. 40, pp. 1377-1397.

Wang, B., Siegmund, T., 2005, "A numerical analysis of constraint effects in fatigue crack growth by use of an irreversible cohesive zone model", *Int. J. Fract.* Vol. 132, pp. 175-196.

Wang, C.H., Hutchinson, J.W., 2001, "Interactions of fatigue cracks with elastic obstacles", *Int. J. Fract.* Vol. 109, pp. 263-283.

Warrier, S.G., Majumdar, B.S., 1997, "Effects of the interface on the fatigue crack growth response of titanium matrix composites: modeling and impact on interface design", *Mat. Sci. Eng.* Vol. A237, pp. 256-267.

Yang, B., Mall, S., Ravi-Chandar, K., 2001, "A cohesive zone model for fatigue crack growth in quasibrittle materials", *Int. J. Solids Struct.* Vol. 38, pp. 3927-3944.

Yang, Q.D., Shim, D.J., Spearing, S.M., 2004, "A cohesive zone model for low cycle fatigue life prediction of solder joints", *Microelectr. Eng.* Vol. 75, pp. 85-95.

Yeh, J.R., 1995, "Fatigue crack growth in fiber-metal laminates", *Int. J. Solids Struct.* Vol. 32, pp. 2063-2075.

5. SIZE EFFECTS IN FATIGUE FAILURE

The study described in this chapter is concerned with non-statistical size effects on fatigue failure. Past studies have discussed this issue in the context of crack size dependent Paris law but retain a crack propagation type failure. In the present study, it is demonstrated that as structural size is reduced or as a crack extends, fatigue failure of cracked structures no longer occurs by crack propagation but transitions to uniform debonding. The consequences of this finding on fatigue failure and threshold conditions are studied. A fatigue cohesive zone model is applied to demonstrate this finding. It is demonstrated that in fatigue loading the evolution of the internal cohesive length scale needs to be accounted for.

5.1 Introduction

It is common practice to describe the failure of crack containing structures subjected to cyclic loads through the application of the Paris law (Paris, *et al.*, 1961). Thereby, crack advance Δa per cycle N is described by a power law of the range of the cyclic stress intensity factor ΔK. In the case of quasi-brittle materials and fatigue crack growth in specimens of different sizes h it has been proposed to introduce a size-dependent Paris law. Based on scaling theory the following size-dependent Paris law has been proposed (Bažant, 2002):

$$\frac{da}{dN}(h) = C\left[\frac{\Delta K_I}{K_{IC}(h)}\right]^m = C\left(\frac{\Delta K_I}{K_{If}}\right)^m \left(\sqrt{1+\frac{h_0}{h}}\right)^m \qquad (5.1)$$

where h_0 is a reference length and K_{If} is the fracture toughness of an infinitely large structure. Alternatively, size-dependent Paris laws based on fractal dimensions were suggested in (Spagnoli and Carpinteri, 2003 ; Spagnoli, 2005). In both approaches, the power m remains constant. Furthermore, for ductile materials a recent study (Ritchie, 2005) confirmed the prediction of size dependent power m (Barenblatt and Botvina, 1980). All these approaches retain the underlying assumption that fatigue failure occurs through the extension and propagation of a crack.

Yet, another set of studies on size effects of failure under monotonic loading has demonstrated that if the characteristic size of the structure under consideration becomes smaller than a critical, material characteristic, length scale the failure behavior will change. Failure will no longer occur through the propagation of a crack but rather through a uniform debonding of the remaining ligament. For a review of such size effects on a range of materials see (Bažant, 2004). Several studies have demonstrated that the cohesive zone failure model provides a convenient approach to study such size effects (Needleman, 1990a, b; Li and Siegmund, 2003; Gao and Ji, 2003; Elices, *et al.*, 2002). For structures of size similar to or smaller than a characteristic length scale, the stress distribution in the ligament is no longer that expected for a cracked structure, but exhibits a rather constant distribution of the crack opening stress (Needleman, 1990a, b). Then, failure is predicted to become independent of crack length or structural size, and strength becomes equal to theoretical strength (Gao and Ji, 2003). Only for structures larger than the material characteristic length does the stress distribution in the ligament remain crack tip field like, and failure depends on crack length.

In the present computational study it is explored how crack-containing structures of varying size respond to cyclic loading. An irreversible cohesive zone model is applied to conduct the numerical simulations (Roe and Siegmund, 2003). In contrast to past applications of cohesive zone models to studies of size effects, it is demonstrate that in the case of fatigue loading the material characteristic length scale is no longer constant.

where h_0 is a reference length and K_{If} is the fracture toughness of an infinitely large structure. Alternatively, size-dependent Paris laws based on fractal dimensions were suggested in (Spagnoli and Carpinteri, 2003 ; Spagnoli, 2005). In both approaches, the power m remains constant. Furthermore, for ductile materials a recent study (Ritchie, 2005) confirmed the prediction of size dependent power m (Barenblatt and Botvina, 1980). All these approaches retain the underlying assumption that fatigue failure occurs through the extension and propagation of a crack.

Yet, another set of studies on size effects of failure under monotonic loading has demonstrated that if the characteristic size of the structure under consideration becomes smaller than a critical, material characteristic, length scale the failure behavior will change. Failure will no longer occur through the propagation of a crack but rather through a uniform debonding of the remaining ligament. For a review of such size effects on a range of materials see (Bažant, 2004). Several studies have demonstrated that the cohesive zone failure model provides a convenient approach to study such size effects (Needleman, 1990a, b; Li and Siegmund, 2003; Gao and Ji, 2003; Elices, et al., 2002). For structures of size similar to or smaller than a characteristic length scale, the stress distribution in the ligament is no longer that expected for a cracked structure, but exhibits a rather constant distribution of the crack opening stress (Needleman, 1990a, b). Then, failure is predicted to become independent of crack length or structural size, and strength becomes equal to theoretical strength (Gao and Ji, 2003). Only for structures larger than the material characteristic length does the stress distribution in the ligament remain crack tip field like, and failure depends on crack length.

In the present computational study it is explored how crack-containing structures of varying size respond to cyclic loading. An irreversible cohesive zone model is applied to conduct the numerical simulations (Roe and Siegmund, 2003). In contrast to past applications of cohesive zone models to studies of size effects, it is demonstrate that in the case of fatigue loading the material characteristic length scale is no longer constant.

111

5.2 Model Description

Fatigue failure is investigated for plane strain strip specimens depicted in Figure 5.1 (Gao and Ji, 2003). The strip possesses a height of $2h_s$ and is assumed to possess a length L much larger than its height. A crack of length $a_0 = L/3$ is positioned at the centerline of the strip. A reference coordinate system (x_1, x_2) is placed at the crack tip. The specimen is loaded in cyclically varying tension by applying cyclically varying displacements $u_2(t)$ of amplitude Δu_2 and time period t_c at the locations $x_2 = \pm h_s$:

$$u_2(t) = \Delta u_2 \left[0.5 - 0.5 \cdot \cos 2\pi(t/t_c)\right] \tag{5.2}$$

For an infinite strip with a long crack, the cyclically varying energy release rate is related to the displacement through:

$$G(t) = 2h_s \left(\frac{1}{2}\sigma_{22}\varepsilon_{22}\right) = \frac{E(1-v)}{(1+v)(1-2v)} \frac{[u_2(t)]^2}{h_s} \tag{5.3}$$

The validity of equation (5.2) for the case of the present finite size geometry with $a_0 = L/3$ was verified by comparing computed values of the J-integral to predictions of equation (5.3). These results match within less than 1%. The finite element mesh used in the analysis is characterized by a constant element size in front of the crack tip along the specimen midline with elements of size $5\delta_0$. The length of the strip is $L \gg h_s$ with $L = 3740\delta_0$ chosen for the simulation. The model was constructed using four node plain strain elements. The symmetry of the strip specimen with respect to $x_2 = 0$ was considered and only a half-model with appropriate symmetry boundary conditions was analyzed numerically.

From the definition of the relationship between toughness expressed by the measure of energy release rate and stress intensity factor $G_C = \phi_0 = (K_C)^2(1-v^2)/E$ and considering $K_C = \sigma_{\max,0}\sqrt{\pi l_0^*}$, a material characteristic length scale l_0^* is introduced as combination of the cohesive zone properties with the elastic modulus E and Poisson's ratio v of the solid surrounding the cohesive zone:

$$l_0^* = \frac{\phi_0 E}{\sigma_{max,0}^2 \pi(1-v^2)} = \frac{e\delta_0 E}{\sigma_{max,0}\pi(1-v^2)} \quad . \tag{5.4}$$

Under the cyclic loading, the irreversible CZM accounts for the evolution of the cohesive properties by use of a cyclic damage variable D_c. In the present model under the consideration of cyclic loading, in addition to the cohesive strength which is the function of the damage, the material characteristic length scale calculated by equation (5.4) is also no longer a constant but dependent on damage:

$$l^* = \frac{e\delta_0 E}{\sigma_{max}\pi(1-v^2)} = \frac{l_0^*}{(1-D_c)} \tag{5.5}$$

As damage progresses the material characteristic length scale will increase. The implications of this consideration are demonstrated with the simulation results of the present study.

Simulation results discussed here were obtained for the following set of parameters. The solid is characterized as an isotropic linear elastic solid with E=100 GPa, and v=0.34. All computations, except in the parametric study, were conducted with the following material parameters for the cohesive zone: $\sigma_{max,0} = E/100$, $\sigma_f / \sigma_{max,0} = 0.25$, $\delta_\Sigma / \delta_0 = 4.0$. The endurance limit is given as $\sigma_f / \sigma_{max,0} = 0.25$ which is a lower bound on typical experimental values of the fatigue ratio. The value of the ratio δ_Σ / δ_0 is known to scale the number of load cycles required to fail a cohesive element (Roe and Siegmund, 2003). In order to keep the computational cost within acceptable limits the value of $\delta_\Sigma / \delta_0 = 4$ was selected. Combining these parameters the material characteristic length emerges is $l_0^* = 100e\delta_0 /[\pi(1-v^2)] = 97.8\delta_0$. Several different specimen dimensions were considered: (i) specimens much larger than the characteristic length scale h_s/δ_0=(900, 750) $\gg$ l_0^*/δ_0, (ii) specimen of size slightly larger than the characteristic length scale h_s/δ_0=(400, 240, 200, 150, 100) $>$ l_0^*/δ_0 , and (iii) specimen smaller than the characteristic length scale h_s/δ_0=(80, 50, 20, 10) $<$ l_0^*/δ_0 . Cyclic loading was conducted under the conditions that $\Delta G / \phi_0 = 0.2$ and $R = 0$.

5.3 Results and Discussions

First, the predicted model behavior under monotonic loading is discussed in order to provide a reference point for the further discussion. Figure 5.2 depicts the predicted normalized strength $\sigma_s / \sigma_{max,0}$ in dependence of the normalized specimen size. In line with well-known relationships between strength and size, the present model predicts strength independent of size and equal to the cohesive strength for small specimens. For larger specimens strength is predicted as dependent on size. From equation (5.3) and equation (2.3) one obtains:

$$\frac{\sigma_s}{\sigma_{max,0}} = \sqrt{\frac{(1-\nu)}{(1+\nu)(1-2\nu)} \frac{E\phi_0}{\sigma_{max,0}^2 h_s}} = \sqrt{\frac{(1-\nu)e}{(1+\nu)(1-2\nu)} \frac{E}{\sigma_{max,0}} \frac{\delta_0}{h_s}} \tag{5.6}$$

For the present model parameters the transition size ($\sigma_s = \sigma_{max,0}$) is predicted to be $h_s / \delta_0 = 420.25$. The computational results are found to approach the theoretical predictions well.

All following results refer to computations under cyclic loading. Figure 5.3 depicts the predicted normalized crack extension $\Delta a / \delta_0$ in dependence of the number of applied load cycles N. For all specimen sizes considered an initial number of cycles N_{ini} is required such that crack extension is predicted. For large specimens with size exceeding the material characteristic length h_s/δ_0=750 and 900, the incubation period is followed by a crack extension stage with a nearly constant crack growth rate. For the largest specimen h_s/δ_0=900 a maximum crack extension of $\Delta a / \delta_0$=650 was computed to occur after N=100 load cycles. Smaller specimens ($100 < h_s/\delta_0 < 750$) initially behave identical to the larger specimens with an incubation period to crack growth initiation followed by a crack growth stage. However, for these specimen sizes the crack growth rate subsequently increases substantially at a critical cycle sudden failure of the entire specimen occurs. For the third group of even smaller specimens $h_s/\delta_0 < 100$ a longer initial incubation period is predicted. Subsequently, these specimens fail without any real crack growth stage developing. The number of load cycles to crack growth initiation is

summarized in Figure 5.4(a). The number of cycles to initiation is largest for the smallest specimens and decreases with specimen size to an asymptotic and size independent value. Figure 5.4(b) summarizes the predicted initial crack growth rates, i.e. crack growth rates for a state in which the internal length scale l^* is still close to its initial value l_0^*. The crack growth rate was calculated for crack propagation close to the initial crack (from the 5th to the 6th cohesive element). No crack growth rates could be determined for specimens (delete "smaller") with $h_s / \delta_0 < 50$ as no crack growth type failure occurs. Even if these specimens contain a crack, a Paris law cannot be used here. For specimens $50 < h_s / \delta_0 < 200$ crack growth rates are predicted to be decreasing with specimen size. Such a result is in qualitative agreement with findings in experimental studies (Bažant and Xu, 1991; Bažant and Schell, 1993). For these specimens a size-dependent Paris law, e.g. equation (5.1), can be used to characterize the crack growth rate. For larger specimens $h_s / \delta_0 > 200$ the computations predict the initial crack growth rates to be independent of size. It is in this range that the classical Paris law is valid and crack growth rates determined on one specimen can be transferred to another specimen. Final failure of the specimens is characterized as the number of cycles required for given values of crack extension ($\Delta a / \delta_0 = 20, 100, 200, 700$), Figure 5.4(c). For small values of crack extension ($\Delta a / \delta_0 = 20$) the number of cycles to failure is dominated by the number of cycles to initiation, and small specimens possess the longest life-time under this criterion. For large values of crack extension ($\Delta a / \delta_0 = 100, 200, 700$) the life time no longer only depends on crack growth initiation but also on crack propagation. As a result, large specimens then allow for a larger number of cycles to failure while for small specimens (no crack growth stage) the number of cycles to failure remains unchanged. The interaction of these two mechanisms leads to the result that for intermediate size specimens the lowest number of cycles to failure is predicted. Specimens of size similar to the material characteristic length scale l_0^* are predicted to be most critical to fatigue failure.

For more details of the computations, results on specimens of size $h_s / \delta_0 = 20$, 240, 750 are discussed in the following. While previous studies have commonly used the ligament stress distribution (Gao and Ji, 2003) or the spatial traction distributions (Needleman, 1990a, b) to further investigate the size dependent failure response, here it is useful to investigate the spatial distribution of the damage variable and the crack opening displacement. Figure 5.5(a) depicts the distribution of D_c along the cohesive zone at N=15.5. For the large specimen, the condition D_c=1 is fulfilled for x_1 / δ_0 <75, and subsequently drops sharply to negligible values. The damage distribution represents a crack-type response. For the intermediate size specimen, the damage distribution at the current crack tip is similar to that of the larger specimen, but D_c is reduced less and does not reach zero for the remainder of the ligament. The damage distribution for the smallest specimen is significantly different. Damage depends little on location and for the cycle considered remains less than one. The simulations thus predict that a crack growth type failure only occurs for large structures, but small structures fail in a uniform debonding mode despite the presence of a crack. A similar response can be seen from the predicted crack opening profiles at N=15.5, Figure 5.5(b). For the large specimens $h_s / \delta_0 = 240$ and 750 the crack opening profiles are crack like, while for $h_s / \delta_0 = 20$ a uniform debonding mode is clearly present. To visualize the specimen response in more detail, Figure 5.6 depicts the contours of the normalized stress component $\sigma_{22} / \sigma_{max,0}$ on the deformed shape of the specimen. For the largest specimen, a pronounced stress concentration is present at the crack tip both initially as well as during crack propagation. The deformed shape of the specimen clearly depicts the presence of a crack. For the smallest specimen no stress concentration is present and stresses are uniform throughout the ligament. The stress level degrades with the number of cycles essentially identically for all points in front of the initial crack tip. At final failure the specimen separates uniformly into two halves. A more complex response is found for intermediate size specimen, Figure 5.6(b). Initially, a stress concentration is present at the crack tip and the deformed shape of the specimen is crack-type. However, the strength of the stress

concentration diminishes as the number of load cycles increases. Final failure is predicted through uniform debonding.

The change in failure modes can be explained through the evolution of the material characteristic length scale, equation (5.3). Figure 5.7 depicts the ratio between the current material characteristic length scale l^* and its initial value l_0^* in dependence of the number of load cycles. For the numerical evaluation of equation (5.3) the values of D_c are averages over the domain $x_1 > 0$. For the largest specimen ($h_s/\delta_0 = 750$) the ratio l^*/l_0^* hardly changes throughout the computation, max(l^*/δ_0) $= 1.5 \times l_0^*/\delta_0$, such that the specimen size remains always much larger than the current internal length scale $h_s/\delta_0 \gg l^*/\delta_0$. For the smallest specimen ($h_s/\delta_0 = 20$), the ratio l^*/l_0^* increases quite rapidly right from the onset of cyclic loading. Again the change in the characteristic length scale does not affect the failure mode since the specimen is already initially smaller than the characteristic length scale, i.e. $h_s/\delta_0 \ll l_0^*/\delta_0 \ll l^*/\delta_0$. For intermediate size specimens ($h_s/\delta_0 = 240$, 400) the change in characteristic length scale is responsible for a change in the failure mode. While these specimens are initially larger than the characteristic length scale ($h_s/\delta_0 > l_0^*/\delta_0$) this is no longer the case as cyclic loading progresses, and finally $h_s/\delta_0 < l^*/\delta_0$. The conditions $h_s = l^*$ are marked in Figure 5.7, and correspond well to the number of cycles at which the specimens of size $h_s/\delta_0 = 240$, 400 fail by uniform debonding of their remaining ligament, see Figure 5.3.

To provide an understanding of the influence of the cohesive zone parameters on the computational results, a limited parametric study was conducted. Results for computations on specimens of size $h_s/\delta_0 = 240$ are presented in Figure 5.8. It is demonstrated that changes in the accumulated cohesive length δ_Σ influence the predicted crack growth rate through changes in the incremental values of damage. Changes in the value of the accumulated cohesive length δ_Σ however do not influence the shape of the damage distribution. As a consequence the crack length at which the transition from crack propagation-type failure to uniform debond-type failure occurs remains unchanged.

117

Changes in the value of the cohesive zone endurance limit σ_f on the other hand change both the rate of damage accumulation and the shape of the damage distribution. Consequently, this value of this parameter affects both the predicted crack growth rate as well as the transition in the failure mode. For small values of σ_f the transition between failure modes will occur early, while for large values of σ_f a crack propagation type failure mode dominates.

In addition, to the determination of the failure characteristics of the specimens under cyclic loading, it is of interest to determine conditions of load for which failure is excluded, i.e. the threshold or fatigue limit conditions. In order to summarize such information for the present model a Kitagawa-type diagram is developed in which the dependence of the threshold stress $\sigma_{22} = \sigma_{th}$ on specimen size is depicted, Figure 5.9. In the context of the present model threshold conditions are reached if the maximum traction value in the cohesive zone remains below the fatigue limit σ_f. At small values of h_s a bound for the threshold stress is therefore given by $\sigma_{th} = \sigma_f$. For larger size specimens and considering the definition of the stress intensity factor (Suresh, 1998), the criterion

$$\frac{\sigma_{th}}{\sigma_f} = \left(\frac{l_0^*}{h_s} \right)^{1/2} \tag{5.7}$$

describes the size dependent threshold stress. A transition size between the two criteria ($\sigma_{th} = \sigma_f$) is then obtained as $h_s = l_0^*$. The computational results approach these predictions well.

5.4 Conclusions

The present computational study demonstrated that the type of the process of fatigue failure depended on the ratio between the size of the cracked structure under consideration and a material characteristic length scale. The fatigue cohesive zone model

employed in this study predicted such effects as the outcome of the analysis without the need to introduce any size dependent failure criteria. The model introduced the material characteristic length scale as an evolving internal variable. The absolute values of the terms "large" and "small" are dependent on the microstructure and/or the failure mechanism of the material under investigation as expressed by the material characteristic length scale.

For larger specimens with size exceeding the material characteristic length, the fatigue failure occurred through crack growth and the crack growth rate was size-independent. A Paris law approach was an appropriate approach to describe this response. For the intermediate size specimens, the failure mode changed from the crack type failure to uniform debonding. The predicted FCG rate was dependent on the specimen size and is in qualitative agreement with findings in experimental studies (Bažant and Xu, 1991; Bažant and Schell, 1993). A size-dependent Paris law can be use to characterize the crack growth rate. For the smaller specimens with size less than the material characteristic length, the failure occurred through the uniform debonding without any real crack growth. For those structures an S-N approach was appropriate. The calculation results for those specimens showed that the number of cycles to initiation was the largest for the smallest specimens and decreased with specimen size to an asymptotic and size-independent value.

Fatigue life was considered to mainly include both crack initiation and crack propagation. The fatigue life time which corresponded to a specific crack extension was predicted to be dependent on the specimen size. The results showed the small specimens possessed the longest life time due to the longer crack initiation time under the small crack extension. For larger values of crack extension, the large specimens possessed the longest life time since the crack propagation time was longer. For intermediate size specimens the lowest number of cycles to failure was predicted. It means that structures of intermediate size were most prone to fatigue failure due to the interaction between crack growth initiation and early transition to the debonding mode.

Fatigue failure under the different specimen size was studied based on the damage distribution, crack opening profiles and crack opening stresses. The comparison results showed that, for large specimens, the damage distribution and crack opening profile

represented a typical crack-type response. A pronounced stress concentration was present at the crack tip both initially and during crack growth. For the intermediate size specimen, the damage distribution at the current crack tip was similar to that of the large specimen and the damage was reduced less and remains some values for the remainder of the ligament. The corresponding crack opening stress showed that the strength of the stress concentration diminishes as the number of load cycles increased. For small size specimens, the damage had a constant value through the whole ligament. No stress concentration was present and stresses were uniform throughout the ligament. It resulted in the uniform debonding.

In the context of the fatigue cohesive zone model the material characteristic length scale was no longer a constant but increased with the accumulation of damage. For the largest size specimen, the current material characteristic length scale hardly changed throughout the computation such that the specimen size remained larger than the current internal length scale. For the smallest size specimen, the current material characteristic length scale increased quite rapidly which resulted in no effects on the failure mode since the specimen was already initially smaller than the characteristic length scale. For intermediate size specimens, the change in characteristic length scale was responsible for a change in the failure mode. In that case the initiation of failure was through crack growth but later the failure mode transition to that of uniform debonding of the ligament occurred.

A Kitagawa-type diagram was developed to determine the fatigue limit conditions under the different specimen sizes. The results indicated that, for very small size specimens, the threshold stress was close to the fatigue limit. The threshold stress decreased with increasing the specimen size. It was in good agreement with the published experimental results.
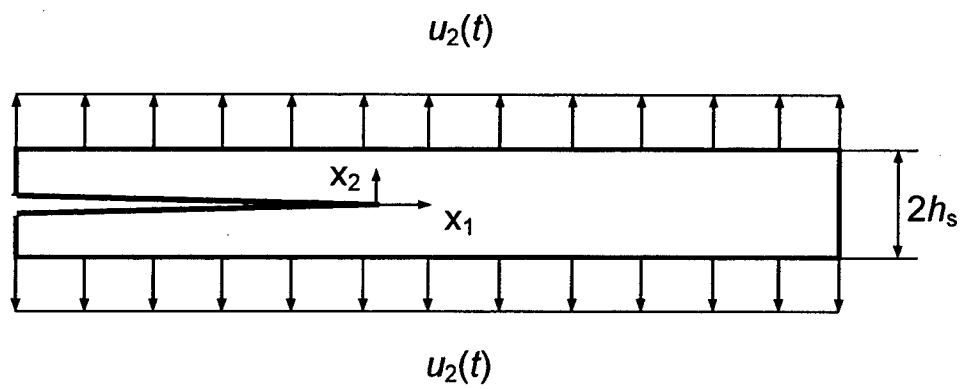
Figure 5.1: Model geometry.
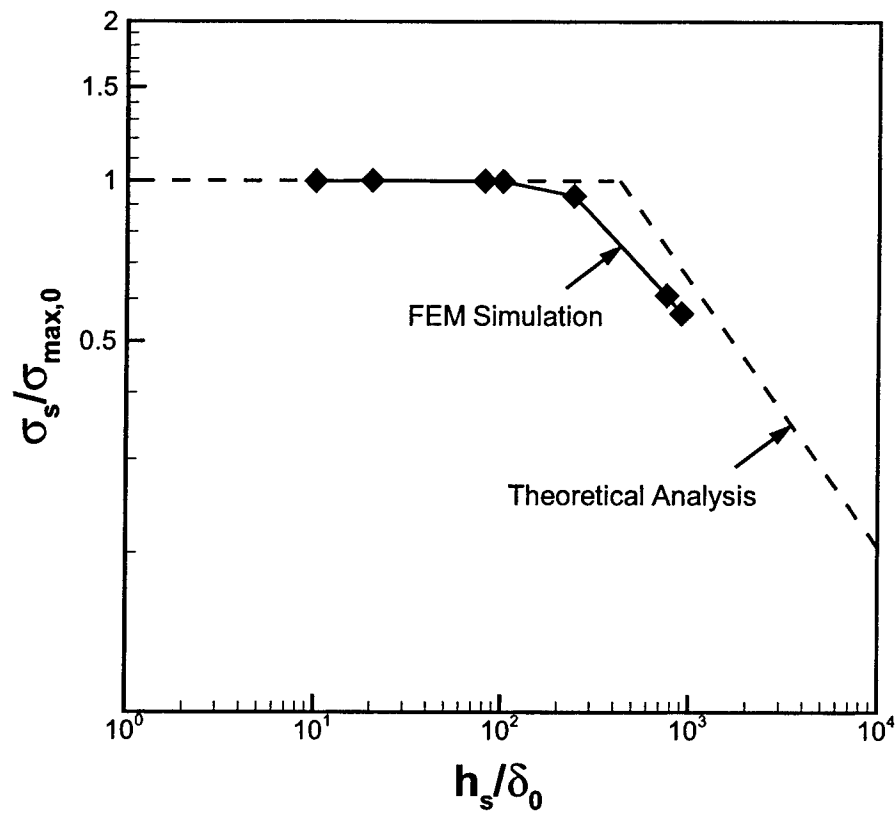
Figure 5.2: Predicted normalized strength $\sigma_s / \sigma_{max,0}$ in dependence of the specimen size h_s / δ_0 and comparison to theoretical prediction.
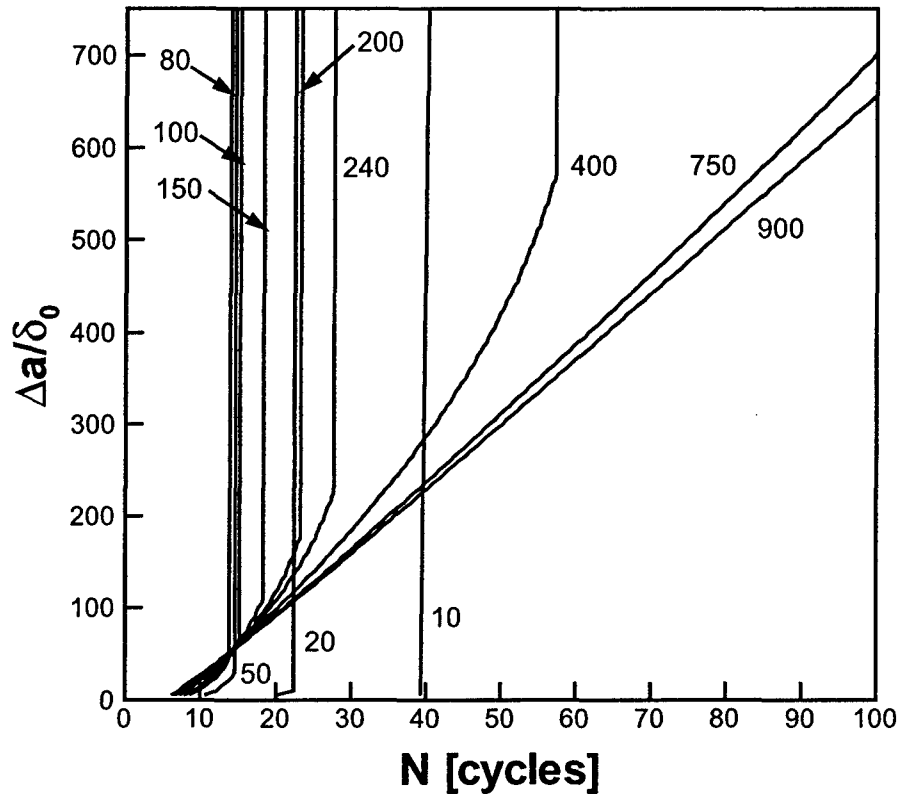
Figure 5.3: Predicted normalized crack extension in dependence of the number of applied load cycles for specimens of size $h_s / \delta_0 = 10$ to $h_s / \delta_0 = 900$.
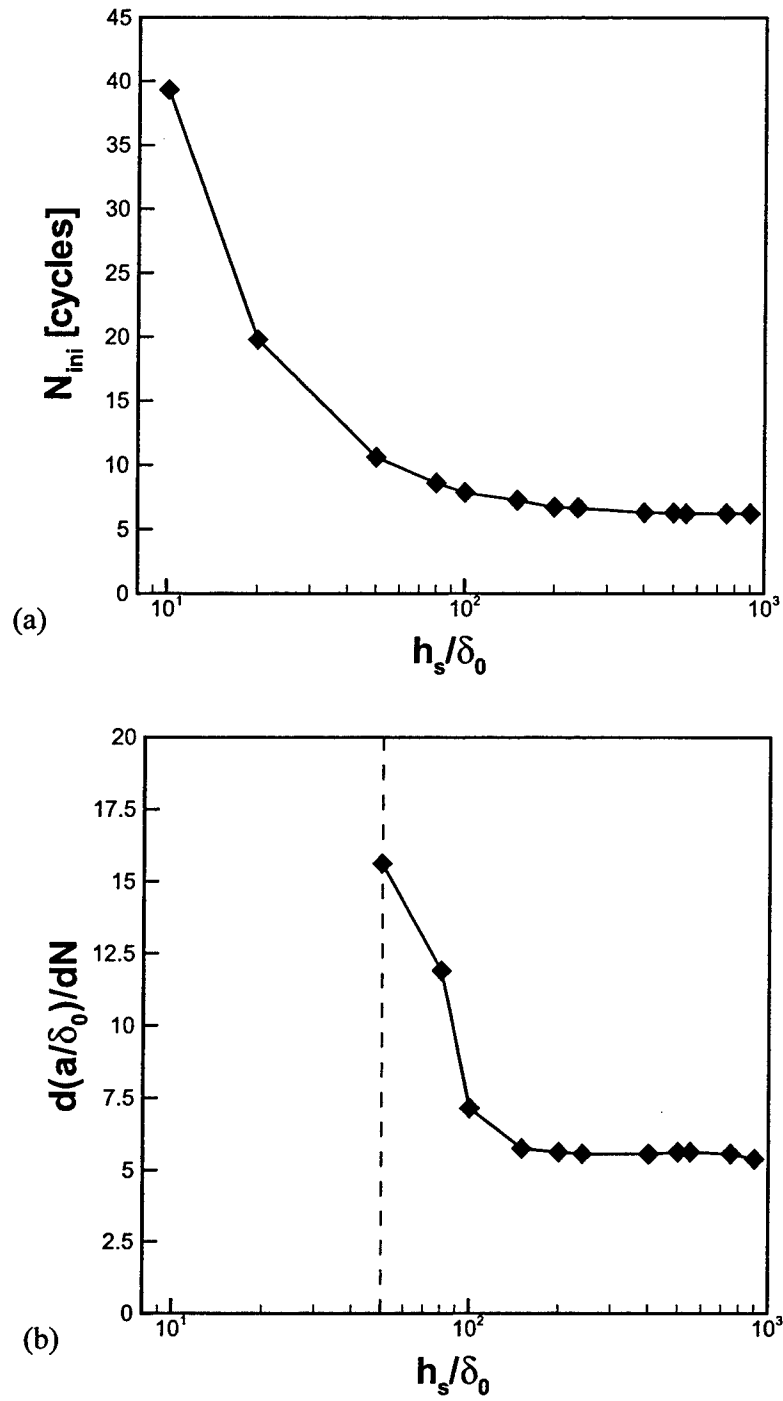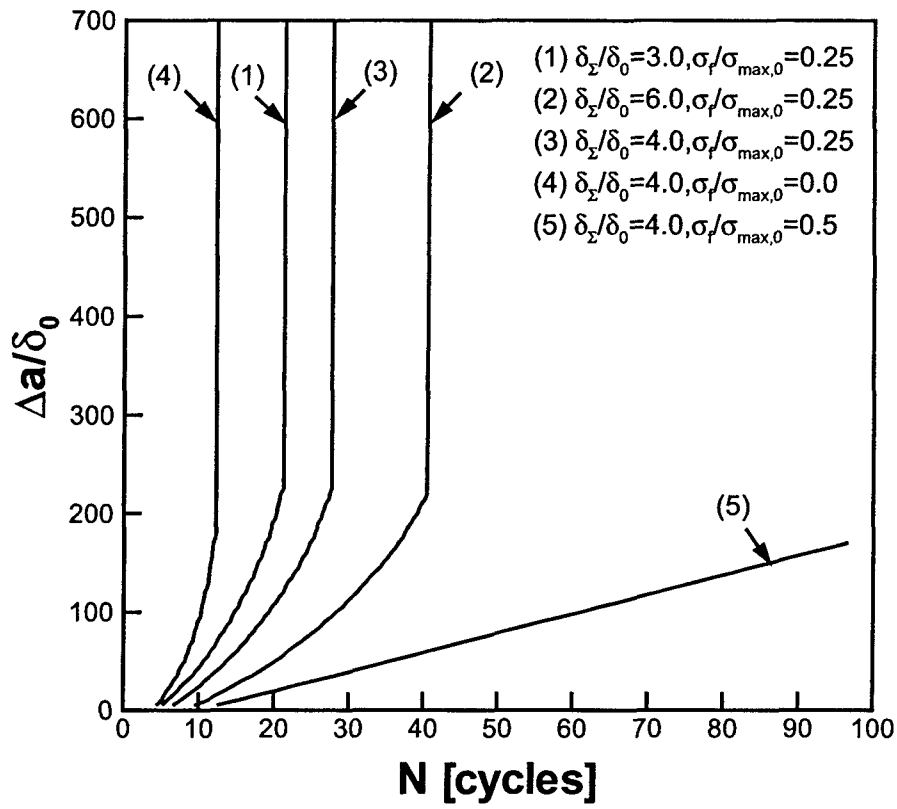
Figure 5.4: Size dependence of (a) Predicted number of cycles to crack growth initiation, (b) Crack growth rate, (c) Predicted number of cycles to crack extensions $\Delta a / \delta_0 = 20, 100, 200, 700$.

(1) $\Delta a/\delta_0$: 0 to 20
(2) $\Delta a/\delta_0$: 0 to 100
(3) $\Delta a/\delta_0$: 0 to 200
(4) $\Delta a/\delta_0$: 0 to 700

(c)
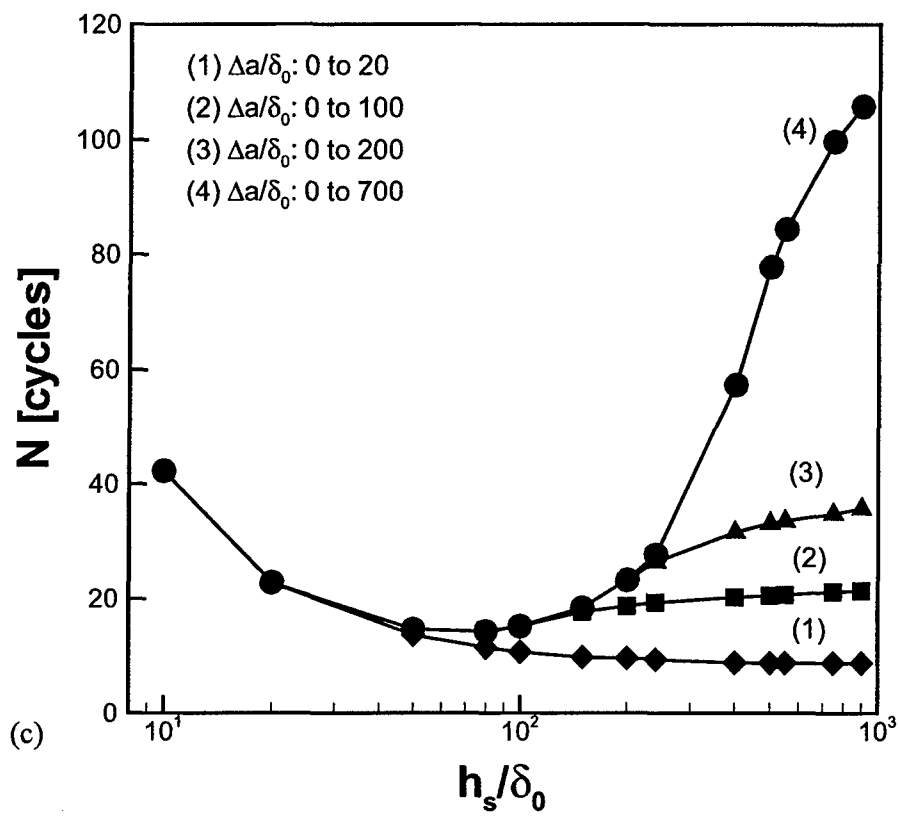
Figure 5.4: Continued
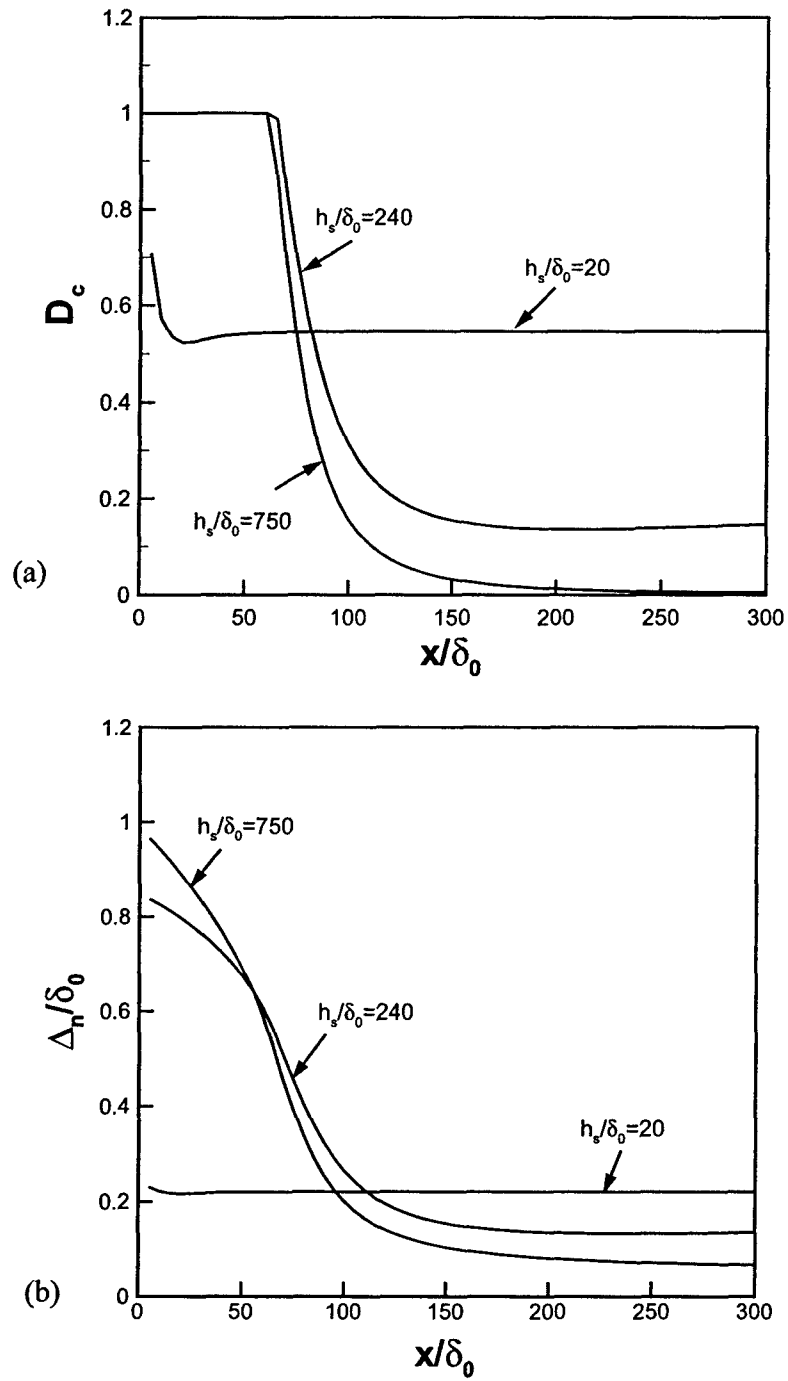
Figure 5.5: (a) Damage distribution and (b) Crack opening profile at N=15.5.

$\sigma_{22}/\sigma_{max,0}$

1.0

0.0

N=0.5

N=50.5

N=75.5
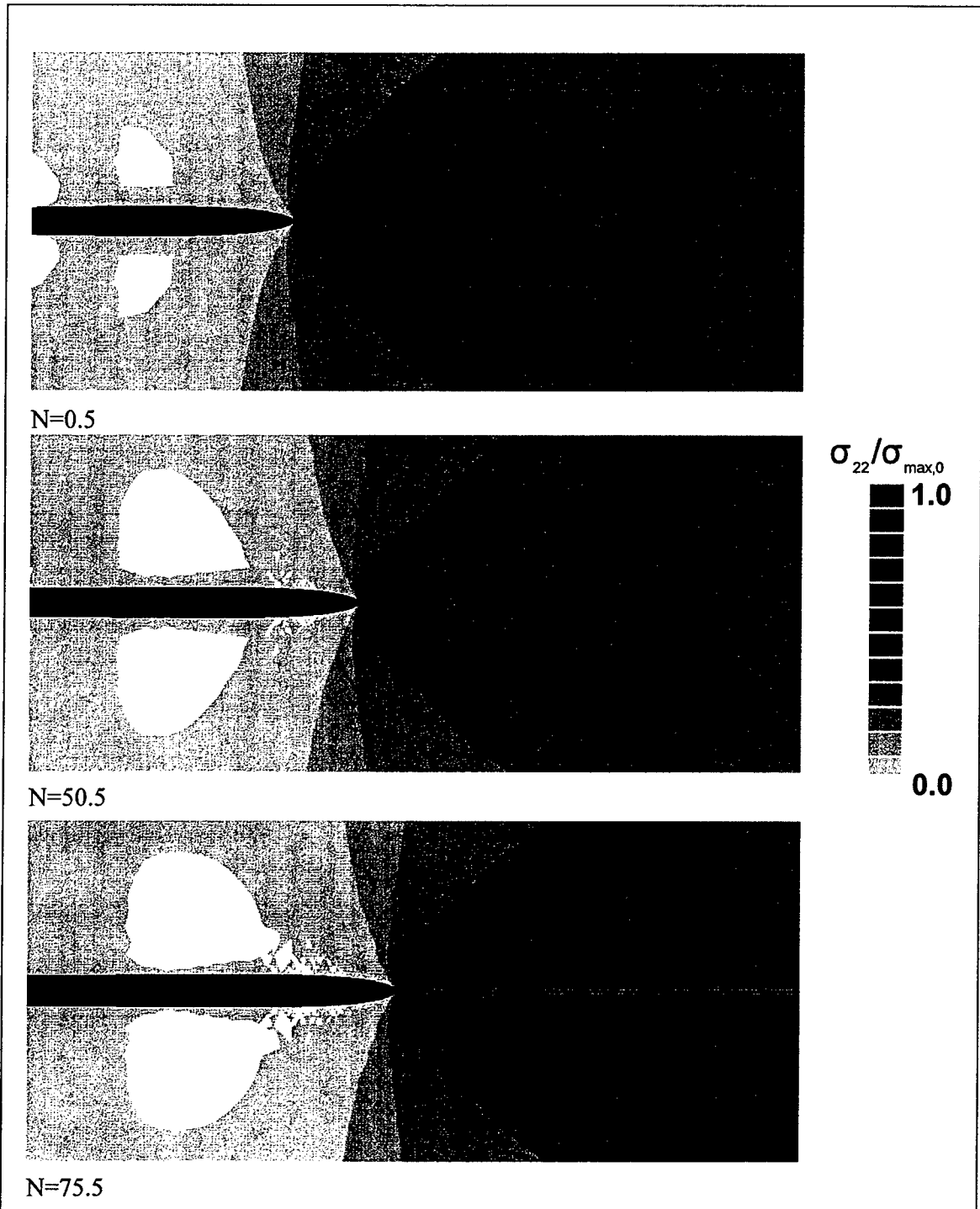
(a)

Figure 5.6: Distribution of crack opening stress, $\sigma_{22}/\sigma_{max,0}$ (displacement u_2 magnified $\times 50$): (a) $h_s/\delta_0 = 750$ (b) $h_s/\delta_0 = 240$, (c) $h_s/\delta_0 = 20$.

(b)
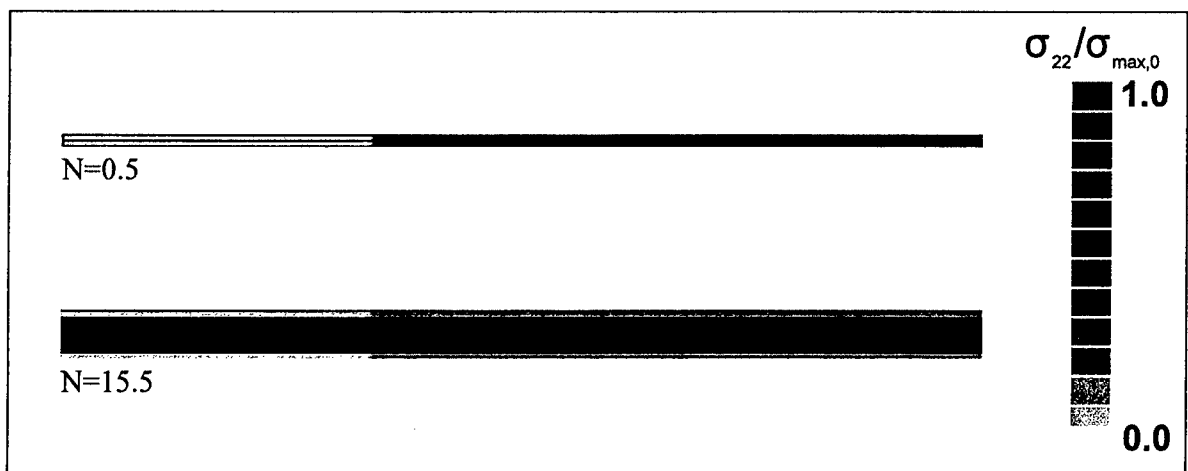
(c)

Figure 5.6: Continued
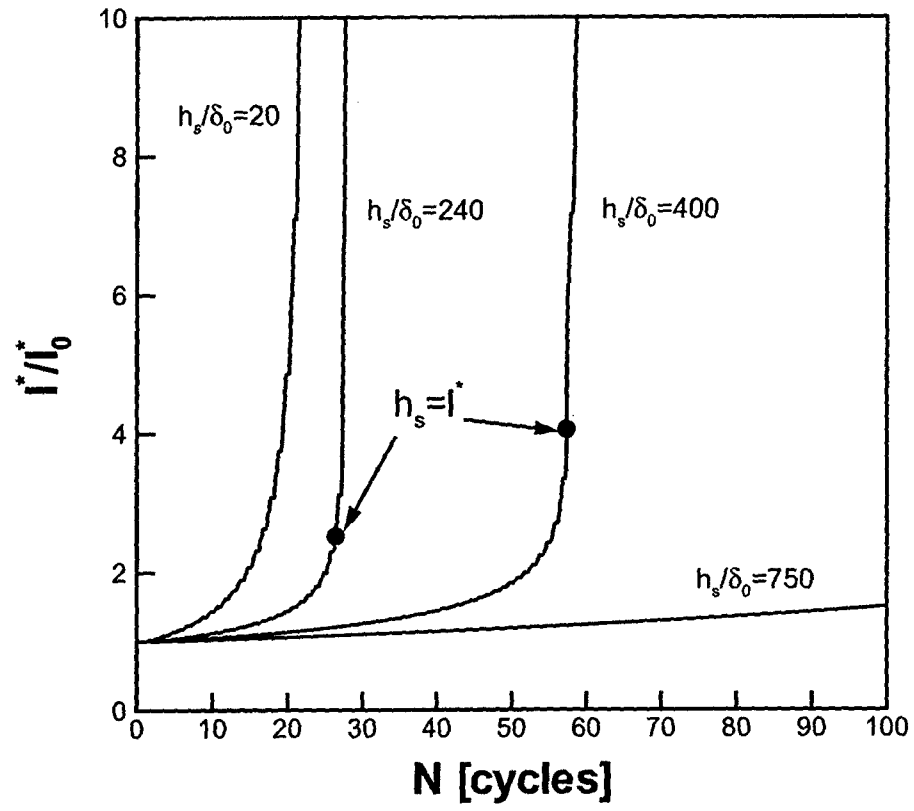
Figure 5.7: Evolution of the normalized internal material length scale l^*/l_0^* with progression of cyclic mechanical loading.

Figure 5.8: Predicted normalized crack extension in dependence of the number of applied load cycles for specimens of size $h_s / \delta_0 = 240$ and various cohesive zone parameter combinations.
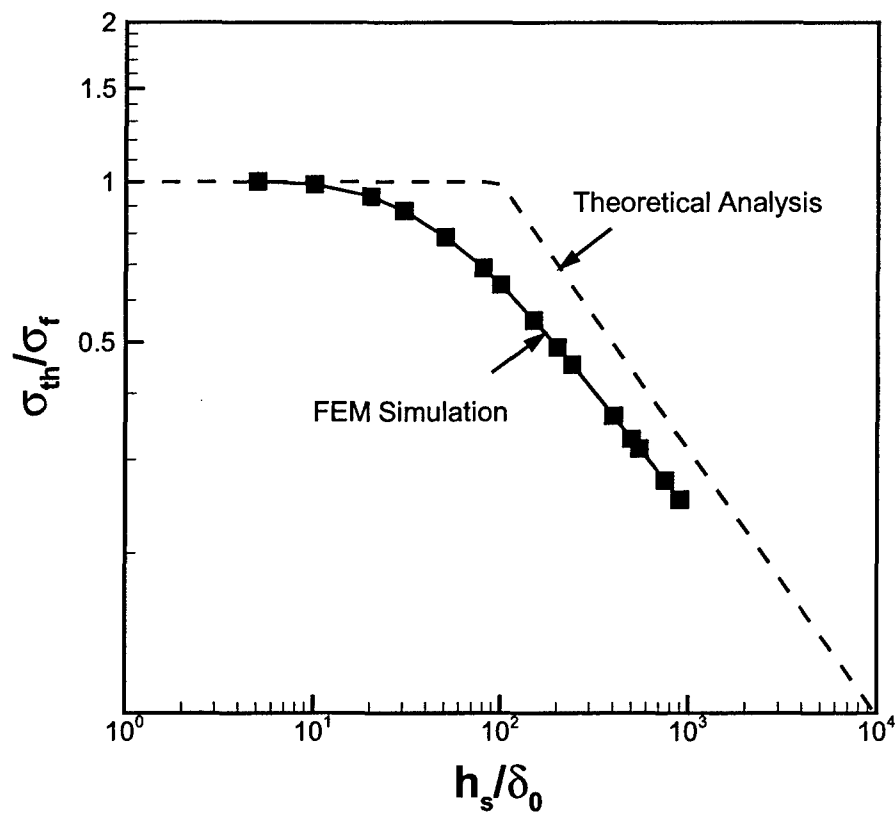
Figure 5.9: Predicted normalized strength σ_{th} / σ_f in dependence of the specimen size h_s / δ_0 and comparison to theoretical prediction.

LIST OF REFERENCES

Barenblatt G.I., Botvina L.R., 1980, "Incomplete self-similarity of fatigue in the linear range of crack growth", *Fatigue and Fracture of Engineering Materials & Structures*, Vol. 3, pp. 193-202.

Bažant Z., 2002, *"Scaling of Structural Strength"* Hermes Penton Science, London, 2nd Ed.

Bažant Z., 2004, "Scaling theory for quasibrittle structural failure", *Proc Natl Acad Sci U S A*, Vol. 101, pp. 13400-13407.

Bažant Z., Schell W.F., 1993, "Faigure Fracture of High-Strength Concrete and Size Effect", *ACI Materials Jounal*, Vol. 90, pp. 472-478.

Bažant Z., Xu K., 1991, "Size Effect in Fatigue Fracture of Concrete". *ACI Materials Jounal*, Vol. 99, pp. 390-399.

Carpinteri A., Spagnoli A., 2004, "A fractal analysis of size effect on fatigue crack growth", *International Journal of Fatigue*, Vol. 26, pp. 125-133.

Elices M., Guinea G.V., Gomez J. and Planas J., 2002, "The cohesive zone model: advantages, limitations and challenges", *Engineering Fracture Mechanics*, Vol. 69(2), pp. 137-163.

Gao H., Ji B., 2003, "Modeling fracture in nanomaterials via a virtual internal bond method", *Engineering Fracuret Mechanics*, Vol. 70, pp. 1777-1791.

Li W., Siegmund T., 2003, "An analysis of a size effect in indentation delamination of a ductile film on an elastic substrate", *Scripta Materialia*, Vol. 49(6), pp. 497-502.

Needleman A., 1990a, "An analysis of tensile decohesion along an interface", *Journal of the Mechanics and Physics of Solids*, Vol. 38(3), pp. 289-324.

Needleman, A., 1990b, "An analysis of decohesion along an imperfect interface", *International Journal of Fracture*, Vol. 42, pp. 21-40.

Paris, P.C., Gomez, M.P., and Anderson, W.P., 1961, "A rational analytic theory of fatigue", *The Trend in Engineering*, Vol. 13, pp. 9-14.

Ritchie R.O., 2005, "Incomplete self-similarity and fatigue-crack growth", *International Journal of Fracture*, Vol.132, pp. 197-203.

Roe, K.L. and Siegmund, T., 2003, "An irreversible cohesive zone model for interface fatigue crack growth simulation", *Engineering Fracture Mechanics*, Vol. 70, pp. 209-232.

Spagnoli A., 2005, "Self-similarity and fractals in the Paris range of fatigue crack growth", *Mechanics of Materials*, Vol. 37 (5), pp. 519-529.

Suresh, S., 1998, *"Fatigue of Materials"*, Cambridge University Press.

6. A DISLOCATION DENSITY BASED STRAIN GRADIENT MODEL

Strain gradients play a vital role in the prediction of size-effects in the deformation behavior of metals at the micrometer scale. At this scale the behavior of metals strongly depends on the dislocation distribution. In this paper, a dislocation density based strain gradient model is developed aiming at predictions of size-effects for structural components at this scale. For this model, the characteristic length is identified as the average distance of dislocation motion, which is deformation dependant and can be determined experimentally. The response of the model is compared to the strain gradient plasticity model of Huang et al. (2004). It is shown that the present strain gradient model, which only requires a physically measurable length-scale, can successfully predict size effects for a bar with an applied body force and for void growth.

6.1 Introduction

Recent experiments indicate that strong size effects are present in the deformation response of metals at the micro-scale. For example, [14] found an increase in plastic work hardening of copper wires during micro-torsion experiments while decreasing the diameter from 170 to $12\mu m$. Micro-indentation experiments showed an increase in hardness with a decrease in indentation depth to the micron-level, as presented by [30]. Furthermore, micro-bending experiments of [33] yield an increased hardness for thinner foils ($\sim 1\mu m$) compared to thicker once. [22] give a comprehensive review of size effects in different metallic materials and loading conditions. All these studies lead to the conclusion that there is strong experimental

evidence for a size effect "smaller is stronger".

Classical continuum plasticity models predict identical stress-strain responses for different geometrical dimensions, i.e. classical continuum answers are size independent. These self-similar predictions are consistent with experiments for large dimensions (>1mm). However, as the dimensions of the sample decrease experimental results do not agree with classical predictions. Strain gradient models predict size effects and are therefore appropriate for problems involving small dimensions. The reason for the size dependence of the strain gradient models at small dimensions is the length-scale introduced in all these models. [18] and [29] give a detailed overview of strain gradient models.

Strain gradient models can be separated into two groups. On the one hand, in first-order models (e.g. [13], [1], [22], [25], [23], [31] and [37]) the strain gradient enters only the incremental material stiffness. Therefore, no additional boundary conditions are needed for this class of models ([2]). The second group is constituted of higher-order models (e.g. [10], [14], [32], [15], [19], [20], [21], [26], [16], [38] and [9]), which include higher-order stresses as work-conjugate of the strain gradient. This increases the order of the equilibrium equations and requires additional, i.e. higher-order, boundary conditions. [18] gives a unified approach to these higher-order strain gradient models. In the present paper we introduce a first-order strain gradient model, since a first-order model is more attractive in respect to numerical efficiency and ease of implementation. [29] have pointed out that first-order strain gradient models show numerical instabilities in simulations that lack strain gradients. These instabilities were not observed in the present model.

Dislocation motion has long been known to be the reason for plasticity. Furthermore, the occurrence of specific dislocation structures is an indication of structural failure, e.g. persistent slip bands in fatigue. The new model, called dislocation density based strain gradient (DDSG) model, is based on physical materials properties only, e.g. dislocation density and their characteristics.
Strain gradient plasticity models, as discussed here, are continuum models that do not differentiate between specific slip directions. Therefore, the interaction between two dislocations is identical regardless of the orientation of the slip systems. To overcome this restriction, crystal plasticity models ([4]) or discrete dislocation models ([35]) are necessary, which describe the underlying physical mechanisms in more detail and are

135

therefore more costly.

In the next section, we will derive the model by providing relations for the total dislocation density, the density of statistically stored and geometrically necessary dislocations, and the incorporation of the dislocation densities into a continuum theory. The density of statistically stored dislocations is a function of the characteristic length l^*, which is compared to the other proposed length-scales in strain gradient plasticity. Thereafter, the application of the model is shown by three examples, which range from an analytical derivation for simple tension to a numerical simulation of void growth. The numerical implementation of the model is follows that of the conventional mechanism-based strain gradient model of [22]. We will close this paper with some conclusions.

6.2 Dislocation Density Based Strain Gradient (DDSG) Model

6.2.1. Taylor hardening and total dislocation density

The shear flow-stress of a metal depends on the dislocation density ([5]). To include this effect into a flow-rule, the shear flow-stress has to be related to the macroscopic tensile flow-stress. Here we employ

$$\sigma_{\text{Taylor}} = \sqrt{3}\tau \qquad (6.1)$$

Within a two-dimensional framework of continuum theory, the ratio of uniaxial flow stress to shear flow stress is two for the direction of maximum resolved shear stress. However, in crystalline materials the system of discrete slip planes is often not oriented such to maximize the shear stress in a particular slip direction, but is randomly oriented. Therefore, the ratio is larger than two. [22] employ the Taylor factor $M = 3.06$ ([7], [24]) in their conventional theory of mechanism based strain gradient plasticity (CMSG). However, the elastic and plastic mismatch between grains increases the local, i.e. microscopic, resolved shear stress in poly-crystalline materials. This additional stress decreases the macroscopic external stress required for plastic slip. Therefore, we choose the von Mises factor $\sqrt{3}$ here. [2] gives the shear flow-stress τ for a dislocation hardened material as

$$\tau = \alpha\mu b\sqrt{\rho_{\text{total}}} \qquad (6.2)$$

where μ is the shear modulus, b the magnitude of the Burgers vector, ρ_{total} is the total dislocation density and α a scalar coefficient between $0.2-0.4$ ([28]).

Dislocations can be divided into statistically stored dislocations (SSDs) and geometrically necessary dislocations (GNDs). The former accommodate homogeneous plastic strain (e.g. [28]). The latter are related to plastic strain gradients which arise from compatible deformation in an inhomogeneous, e.g. multi-granular, material ([5]). Generally, the composition of the total dislocation density can be written as ([28])

$$\rho_{\text{total}}^{q} = \rho_{\text{SSD}}^{q} + \rho_{\text{GND}}^{q}. \qquad (6.3)$$

where ρ_{SSD} and ρ_{GND} is the statistically stored and geometrically necessary dislocation density, respectively. The exponent q is larger than zero. For q less than one, the total dislocation density is larger than the sum of SSDs and GNDs. For values of q larger than one, the total density is smaller than the sum. Therefore, q either increases ($q<1$) the effect of both kinds of dislocation or decreases ($q>1$) such effect. [14] suggest a value of $q=2$ to match their strain gradient model to the dislocation theory. However, [11] employ a value of $q<1$ for their model. Both values of q cannot be correct at the same time. By geometrical considerations we reason for $q=1$. The average dislocation distance of both classes, i.e. SSD and GND, is the square root of the sum of statistically stored and geometrically necessary dislocation density. This average dislocation separation is the average distance of dislocation motion before the dislocation encounters another dislocation and before the first dislocation is hindered by the second. This is expressed by the Taylor law equation (6.2), in which the hardness is proportional to the inverse average dislocation spacing, i.e. inverse of the square root of the total dislocation density. Therefore, $q=1$, which leads to

$$\rho_{\text{total}} = \rho_{\text{SSD}} + \rho_{\text{GND}}. \qquad (6.4)$$

In addition to distinguish SSDs and GNDs, [36] suggested to assign different magnitudes of Burgers vectors and different α-coefficients to both classes. However, SSDs and GNDs populate the same crystalline structure of the same material. Different Burgers vectors, i.e. different atomic spacings in the crystal, are therefore

unphysical. Moreover, different α-coefficients weight the SSDs and GNDs differently although their atomic structures and interactions are identical. Here we avoid any additional factors emphasizing one dislocation density over the other in order not to introduce any fitting parameters.

6.2.2. Statistically stored dislocation density

Statistically stored dislocations (SSDs) develop during homogeneous plastic deformation. As a dislocation loop expands on its glide plane, it plastically displaces the crystal structure in the interior of the loop. Within the continuum framework, we average locally over the discrete dislocations. Infinitely long and parallel SSDs distributed uniformly in a crystal are shown schematically in Figure 6.1.

The light shaded area denotes the crystal area displaced by the array of dislocations. The dark shaded area is the one swept by one dislocation segment. The density of the SSDs is

$$\rho_{SSD} = \frac{1}{l^* d} \tag{6.5}$$

where d the average spacing of the slip planes as shown in Figure 6.1. l^* denotes the average travel distance of a dislocation segment, i.e. the radius of the dislocation loop. In principle, this length is not a materials constant but evolves during deformation or a heat treatment. As the material deforms an increasing number of dislocations populates the crystal thereby hindering the motion of other dislocations. This forest hardening decreases l^*. During annealing the dislocation structure relaxes and grains grow. Such heat treatment increases the average travel distance of dislocations. The magnitude of the length l^* in different environments and after different loading histories can be determined experimentally, as demonstrated by [27] for fatigue loading.

The plastic shear of the crystal shown in Figure 6.1 is

$$\gamma^p = \frac{b}{d} \tag{6.6}$$

where b is the magnitude of the Burgers vector. According to continuum theory the elements of the plastic strain tensor are $\varepsilon_{12}^p = \varepsilon_{21}^p = \frac{1}{2}\gamma^p$ while all other components are

zero. The equivalent plastic strain $\bar{\varepsilon}^p$ is defined as $\bar{\varepsilon}^p = \sqrt{\frac{2}{3}\varepsilon_{ij}^p\varepsilon_{ij}^p}$. This leads to

$$\bar{\varepsilon}^p = \frac{1}{\sqrt{3}}\gamma \qquad (6.7)$$

The combination of equations (6.5) and (6.7) leads to a relationship between statistically stored dislocation density the plastic deformation and two physical material lengths b and l^*.

$$\rho_{SSD} = \frac{\sqrt{3}\bar{\varepsilon}^p}{bl^*} \qquad (6.8)$$

6.2.3 Geometrically necessary dislocations density

Geometrically necessary dislocations accommodate strain gradients. As they consist of an arbitrary array of dislocations of one sign, their presence leads to local lattice curvature. Figure 6.2 shows such an array of dislocations. This geometry is also commonly used as model for low-angle grain boundaries. The density of dislocations in such an array is approximated by

$$\rho_{GND} = \frac{1}{d^2} \qquad (6.9)$$

For small angles of rotation between both sides of the lattice $\beta = \frac{b}{d}$. Furthermore, the strain gradient is defined as $\eta = \frac{\beta}{d}$. Combining these equations we derive the density of geometrically necessary dislocations, which depend only on the strain gradient and the magnitude of the Burgers vector, as also given by [22] and [28].

$$\rho_{GND} = \frac{\eta}{b} \qquad (6.10)$$

6.2.4 Magnitude of SSD, GND and critical dislocation density

[17] and [12] have experimentally determined the dislocation density in copper during fatigue. They found dislocation densities ranging from $10^{11}/m^2$ for the initial undeformed material to $10^{15}/m^2$ in highly deformed material preceding failure. By theoretical considerations we want to establish an upper boundary for the dislocation density. Based on equations (6.1) and (6.2) the maximal admissible

dislocation density ρ_{crit} corresponding to the initial flow-stress σ_{y0} is calculated as

$$\rho_{\text{crit}} = \left(\frac{1}{\sqrt{3}\alpha b} \frac{\sigma_{y0}}{\mu} \right)^2 \tag{6.11}$$

where the shear modulus $E = 77\text{GPa}$, the initial yield stress $\sigma_{y0} = 250\text{MPa}$. The empirical scalar of the Taylor hardening is taken to be $\alpha = 0.3$ and the magnitude of the Burgers vector is $b = 0.25\text{nm}$. This equation leads to a critical dislocation density of $0.5 \times 10^{15}/\text{m}^2$. In this approximation grain boundaries and precipitates are neglected. These contribute substantially to the initial flow-stress. Their strength against impinging dislocations is greater than that of a forest dislocation. Therefore, the physical critical dislocation density is much lower than the value calculated here which only serves as an upper boundary for the initial dislocation density.

In the next step we estimate the density of SSDs and GNDs with equation (6.8) and (6.10). Assuming an effective plastic strain $\varepsilon^p = 0.05$, the statistically stored dislocation density is approximately $\rho_{\text{SSD}} = 10^{14}/\text{m}^2$. Furthermore, we assume strain gradients act over dimensions on the order of $1\mu\text{m}$. Therefore, assuming a linear plastic strain gradient $\eta^p = \varepsilon^p/1\mu\text{m}$. This leads to a density of GNDs of $\rho_{\text{GND}} = 2imes10^{14}/\text{m}^2$. Both densities have an order of magnitude which agrees to the experiments by [17] and [12]. Furthermore, both densities have the same order of magnitude. These results lead us to the conclusion that SSD and GND are capable of equal contributions to the hardening due to homogeneous strain and strain gradients.

6.2.5 Flow-stress and continuum theory

In a continuation of the derivations of the previous section, the flow-stress due to dislocation hardening, i.e. Taylor hardening, can be written as

$$\sigma_{\text{Taylor}} = \sqrt{3}\alpha\mu b\sqrt{\rho_{\text{SSD}} + \rho_{\text{GND}}} \tag{6.12}$$

where the dislocation densities of SSDs and GNDs is given in equation (6.8) and (6.10), respectively. The superposition of this dislocation density dependent flow-stress σ_{Taylor} and the initial flow-stress σ_{y0} leads to the current flow-stress σ_y:

$$\sigma_y = \sigma_{y0} + \sigma_{\text{Taylor}} \tag{6.13}$$

$$= \sigma_{y0} \left(1 + \frac{\sigma_{\text{Taylor}}}{\sigma_{y0}} \right)$$

$$= \sigma_{y0} \left(1 + \sqrt{\frac{\rho_{\text{SSD}} + \rho_{\text{GND}}}{\rho_{crit}}} \right)$$

$$= \sigma_{y0} \left(1 + \frac{\sqrt{3}\alpha\mu b}{\sigma_{y0}} \sqrt{\frac{\sqrt{3}\bar{\varepsilon}^p}{bl^*} + \frac{\eta}{b}} \right)$$

where the critical dislocation density is given by equation (6.11). The flow model of equation (6.13) is incorporated into a framework similar to that of the CMSG theory, as described by [22]. There, the flow-stress is determined by a contribution from the statistically stored and geometrical necessary dislocations. The contribution from the geometrically necessary dislocations is identical to the present model while the contribution from the statistical stored dislocations differ between the CMSG and the present DDSG model. Huang et al. give a comprehensive overview of the equations and the implementation. Here, only a brief summary is given.

The total response is given by a decomposition of elastic and plastic strain:

$$\varepsilon = \varepsilon^e + \varepsilon^p \tag{6.14}$$

where the strains are given by

$$\varepsilon^e = C^{-1}\sigma \tag{6.15}$$

$$\varepsilon^p = d\varepsilon \left[\frac{\bar{\sigma}}{\sigma_y} \right]^m \tag{6.16}$$

where $\bar{\sigma}$ and m is the effective von Mises stress and the rate-sensitivity exponent, respectively. The current plastic strain ε^p is given by the time integration of the plastic strain rate ε^p. The effective plastic strain gradient is derived by [15] as

$$\eta^p = \sqrt{\frac{1}{4}\eta_{ijk}^p \eta_{ijk}^p} \tag{6.17}$$

where

$$\eta_{ijk}^p = \varepsilon_{ik,j}^p + \varepsilon_{jk,i}^p - \varepsilon_{ij,k}^p \tag{6.18}$$

Finally, equilibrium is enforced by

$$\text{div}\sigma - f = 0 \qquad \text{and} \qquad t = \sigma n \qquad (6.19)$$

6.2.6 Length-scales

Recall, classical plasticity, which inherently includes no material length-scale, cannot predict size effects. Strain gradient models extend classical plasticity models by including a length-scale and are therefore appropriate for problems involving small dimensions.

Some length-scales employed in strain gradient model are listed in descending order in the following table and compared to those relevant in the present model. However, this list does not intent to summarize all possible length-scales due to the abundance of strain gradient models at present. [3] presents an analytical and experimental determination of some length-scales employed in strain gradient models. To differentiate the types of length-scales, different keywords are used in the list above. Items starting with 'Dimension' are physically measurable dimensions and constant during deformation. Items starting with 'Size' are also physically measurable but evolve during deformation. Items starting with 'Length' are length-scales introduced into strain gradient models.

The length-scales associated with the conventional theory of mechanism-based strain gradient plasticity ([22]) $l = \sim 30\mu\text{m}$ and mechanism-based strain gradient plasticity ([15]) $l = \sim 6\mu\text{m}$ are constant during deformation. Furthermore, they are a manifolds of the Burgers vector, i.e. scaled by the square of the ratio of shear modulus and yield stress ($\sim \left(\frac{\mu}{\sigma_{y0}}\right)^2 b$) and not directly measurable by experiments. On the other hand, the length introduced in the DDSG model is in principle deformation dependent. As deformation increases the density of forest hardening dislocations increase which in turn decreases the average travel distance of the dislocations. The upper boundary of this length is the dimension of the grain and the lower boundary is the size of the dislocation core. However recall, continuum models are designed for areas where one can average over discrete dislocations.

6.3 Examples

In the following three examples are given to demonstrate the capabilities of the DDSG model and to compare its predictions to the previously established CMSG model. We assume a material with Young's modulus $E = 200\text{GPa}$, Poisson's ratio $\nu = 0.3$ and initial yield stress $\sigma_{y0} = 250\text{MPa}$. The empirical scalar of the Taylor hardening is taken to be $\alpha = 0.3$ and the magnitude of the Burgers vector is $b = 0.25\text{nm}$. The average distance of dislocation motion l^* is on the order of magnitude of a typical thin film thickness or the grain size in an ultra-fine granular material. Here, the value of the length is taken as $l^* = 2.5\mu\text{m} = 10^4 b$ and therefore constant in these examples. As already stated, in general l^* is deformation dependent and should therefore evolve. This evolution equation, however, would introduce additional materials parameters and complicate the assessment of the capabilities of the DDSG model. Thus, in order to keep the presentation of the model concise predictions of constant values of l* are given. The rate-sensitivity exponent $m = 100$ is used for numerical accuracy.

6.3.1 Uniaxial Tension

In the first example, the response to homogeneous uniaxial tension is calculated in order to compare the results obtained by the dislocation density based strain gradient model (DDSG) to those of classical plasticity. A conventional power hardening law is defined as

$$\sigma_y = \sigma_{y0}\left(1 + \frac{E}{\sigma_{y0}}\varepsilon^p\right)^n \tag{6.20}$$

where n is the hardening exponent. Recall, that no macroscopic hardening law is introduced in this strain gradient model, but that the microscopic Taylor hardening rule is used instead. However, as a component approaches a uniform stress distribution, i.e. as the influence of the strain gradient disappears, the solution derived by the DDSG should be close to that of classical isotropic-plasticity. To this end, we set the density of GNDs to zero. Therefore, according to equation (6.13) the yield stress is given by

$$\sigma_y = \sigma_{y0}\left(1 + \frac{\sqrt{3\sqrt{3}}\alpha\mu}{\sigma_{y0}}\sqrt{\frac{b}{l_*}}\sqrt{\bar{\varepsilon}^p}\right). \qquad (6.21)$$

Employing the material properties given above, the uniaxial hardening of the DDSG model is shown in Figure 6.3. The predicted behavior is close to that of a power-law hardening with n=0.1. The hardening is significantly altered by a change in thematerials length l^*. For a small length, corresponding to a dislocation hardened material and a short distance of dislocation motion, the model predicts a harder materials response than for a longer length l^*. During the deformation of the materialthe materials length decreases due to dislocation hardening. This decrease in l^* would increase the hardening and lead to stage three hardening ([6]).

6.3.2 One dimensional strain gradient example

One of the simplest examples of a deformation state with a strain gradient is that of a column experiencing a body force. The gradient in stress, due to the uniform body force, leads to a strain gradient. This example is one-dimensional and it is possible to find an analytical solution. [22] give the expressions for strain gradients, hardening and displacements for the column under gravitational force. Since only the expression for the flow-stress differs between the CMSG and DDSG model, we do not repeat the equations here but direct the reader to [22]. We solved the differential equations for the flow stress numerically.

Figure 6.4 shows the results for the DDSG model for several values of g_2/g_1. g_2 and g_1 is the volume integral of the body force and the applied force the end of the bar, respectively. As evident in the previous example, in the absence of a stress gradient the DDSG predicts a hardening which is close to that of power-law hardening. For larger strain gradients, i.e. as g_2 increases, the DDSG model predicts a stronger hardening.

For increasing stress gradients the hardening predicted by the DDSG model increases much stronger than with the CMSG model, as evident in Figure 6.5. There, the flow-stress at $\bar{\varepsilon}^p = 0.04$ is depicted as a function of the ratio of the spacial integral of the stress gradient to the homogeneous stress. For small strain gradients both models predict a similar flow stress. However, thereafter the flow-stress increases

linearly for increasing stress gradients according to the DDSG model, while the CMSG model predicts a smaller increase in the flow-stress.

Both models have an identical contribution to the flow-stress due to the strain gradient. However, the contribution due to the uniform strain differs. Due to this difference, the material hardens stronger for the DDSG model. This process leads to a higher strain gradient for the DDSG model and therefore to an increased hardening due to the strain gradient.

6.3.3 Numerical example

The final example is that of a void growth problem. As a metal containing voids is deformed, strain gradients near the void surface develop and influence void growth, coalescence and the final failure of the material. Here, a void growth problem is modeled under plane strain conditions. Initially, voids have a circular shape, and a volume fraction of 12.6% is assumed. During the simulation the unit cell of the void is subjected to uniaxial tension as shown in Figure 6.6.

Values of macroscopic stress σ_{yy} are plotted against the macroscopic strain ε_{yy} for different material models in Figure 6.6. Common to all results is the general character of the stress-strain curve. The stress initially increases rapidly and reaches the strength of the material. Afterwards, the stress decreases as the void grows and reaches zero asymptotically. The DDSG model predicts a substantial increase in strength with decreasing void size. For a void radius $r = 0.1 \mu\text{m}$ it predicts a strength which is more than twice that of classical plasticity.

The strength of the material normalized by the strength predicted by classical plasticity depending on the void radius is shown in Figure 6.7. The classical material model predicts a constant strength, i.e. independent of void size. The CMSG model and the DDSG model predict a size effect: smaller voids result in stronger materials. This size effect is significantly stronger for the DDSG model.

6.4 Conclusion

In this paper we have proposed a first-order strain gradient model. As such it does not require higher-order boundary conditions and computationally efficient. This mesoscopic model is merely based on mechanisms at the micro-scale and therefore presents a bottom-up approach.

The dislocation density based strain gradient (DDSG) model predicts size-effects under deformation for geometrical dimensions on the order of a micrometer. Moreover, the model predicts stronger size-effects than the CMSG model. This is due to the fact that the flow-stress in CMSG model is derived with the help of classical plasticity, which inherently does not predict size effects.

Unlike many strain gradient theories, the present model only assumes physically measurable materials properties like dislocation densities. The length-scale, introduced into this model, is the average distance of dislocation motion, i.e. the average radius of dislocation loops, and it can be determined experimentally. Furthermore, this length-scale is not a constant materials property but evolves during deformation, which is not employed in the present paper. Continuum models are designed for areas where one can average over discrete dislocations. Therefore, the DDSG model will not lead to satisfactory results at small length-scales. In these regions local dislocation interactions, which are not captured by DDSG, play a significant role and discrete dislocation dynamics should be used (e.g. [8]).

Dislocation densities are state variables determining the material response. These dislocations can be divided into two groups, dislocations arising from homogeneous plastic deformation, i.e. statistically stored dislocations or first-order dislocations, and dislocations arising from strain gradients, i.e. geometrically necessary dislocations or second-order dislocations. Both contribute to the hardening of the material while only the latter are the reason for the size effect predicted by the DDSG model.

Magnitude of Length	Description
$> 1mm$	Dimension of component.
$> 1\mu m$	Dimension of substructure, e.g. thin film thickness.
$1\mu m - 100\mu m$	Size of grain in poly-granular crystalline material.
$\sim 1\mu m$	Size of dislocation structures, e.g. channels in persistent slip bands in fatigue.
$\sim 1\mu m$	Length of average dislocation motion, used in the present strain gradient model.
$\sim 0.1nm$	Dimension of interatomic spacing, e.g. Burgers vector.

Table 6.1: Different keywords used to differentiate the types of length-scales.
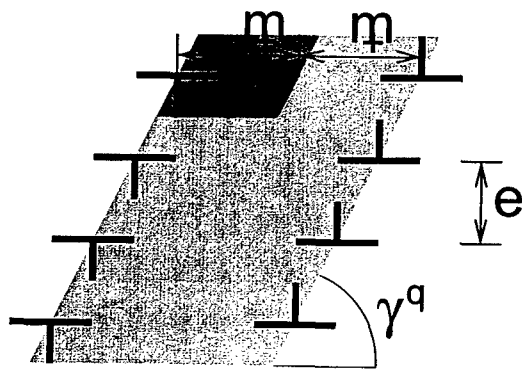
Figure 6.1: Crystal strained by statistically stored dislocations.
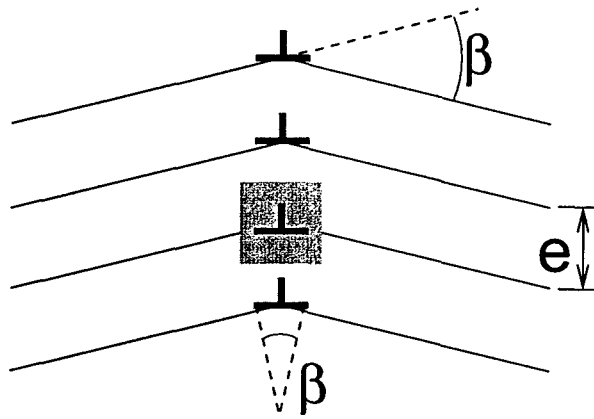
Figure 6.2: Crystal distorted by geometrically necessary dislocations.
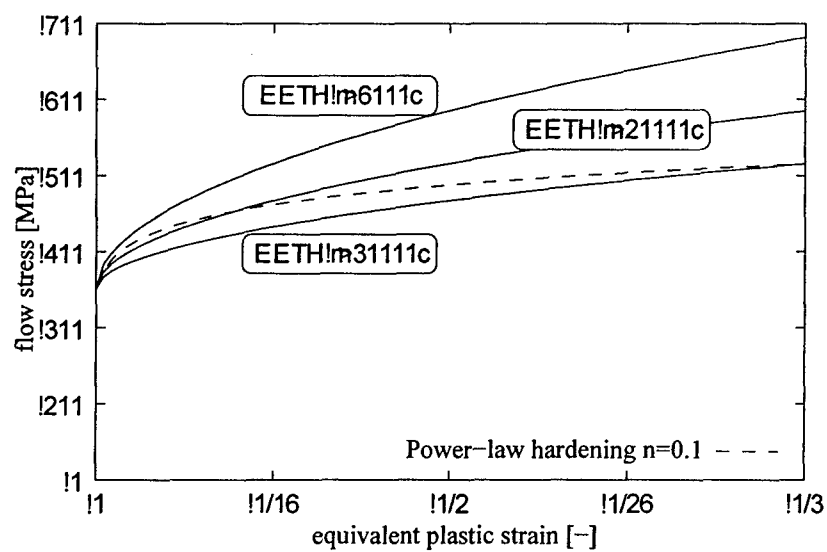
Figure 6.3: Hardening due to homogeneous tension predicted by the DDSG model for three materials length l^* compared to power-law hardening.
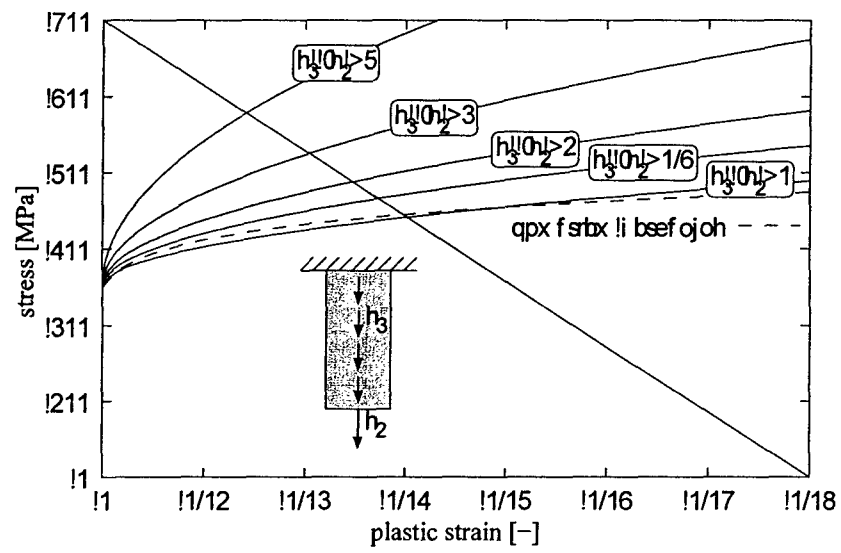
Figure 6.4: Hardening of the DDSG model with a stress gradient.
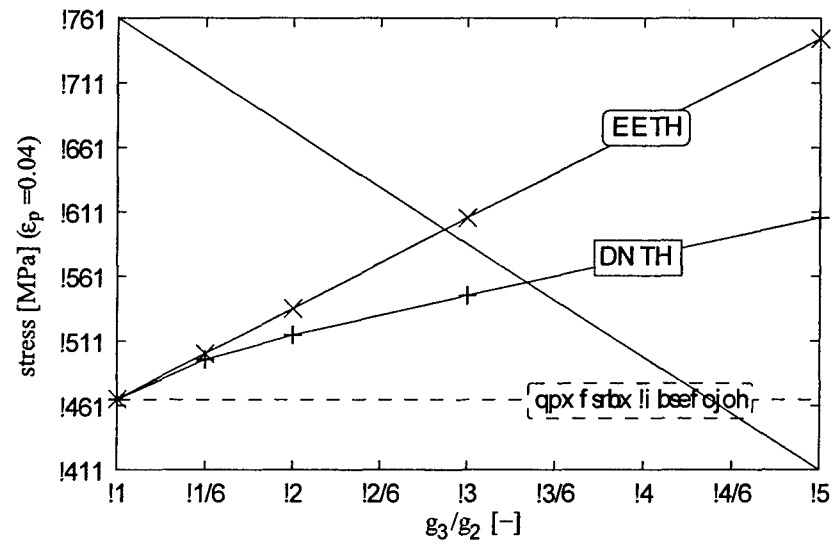
Figure 6.5: Hardening of the CMSG and DDSG model depending on the stress gradient.
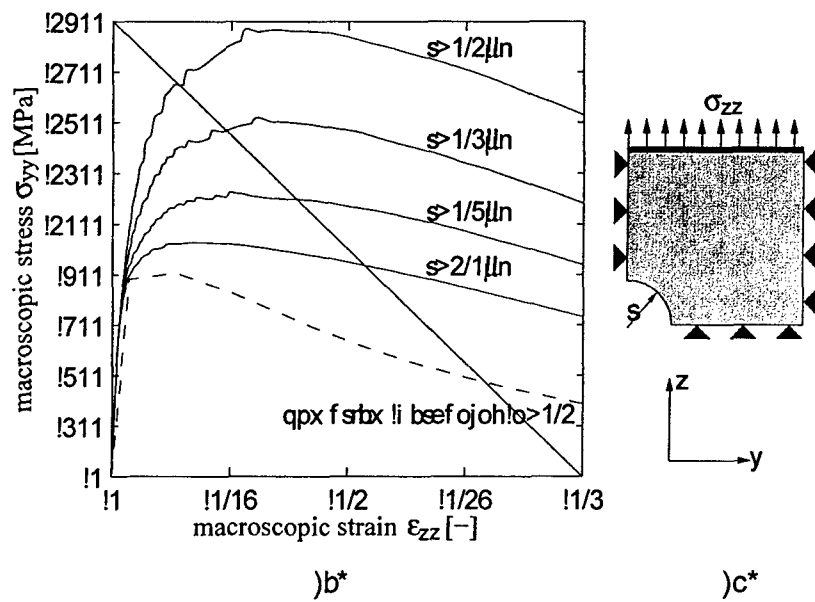
Figure 6.6: Macroscopic stress-strain curves for a material with circular hole for different material models and different void radii (a). Unit-cell of a material with voids under tension (b).
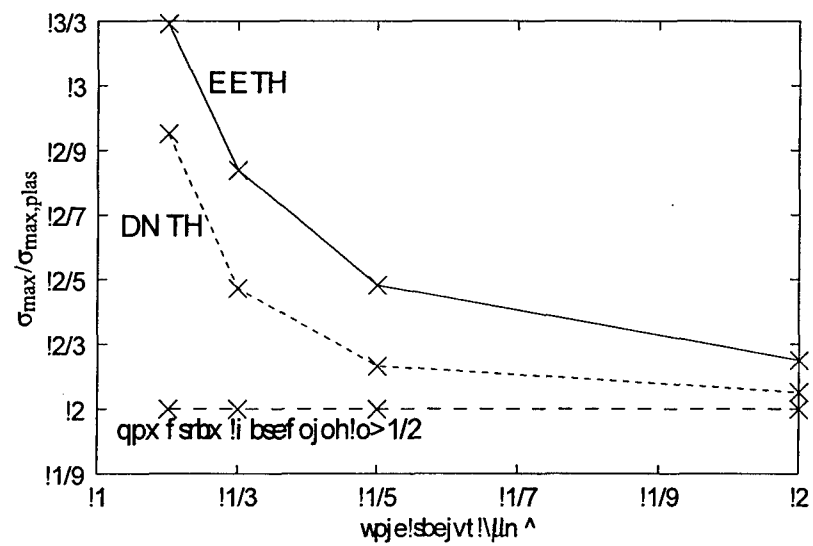
Figure 6.7: The strength of a material with voids normalized by the classical strength according to classical plasticity, CMSG and DDSG model depending on the void radius.

LIST OF REFERENCES

[1] Acharya, A., Bassani, J.L., 2000. Lattice incompatibility and a gradient theory of crystal plasticity. *J. Mech. Phys. Solids* 48, 1562-1595.

[2] Acharya, A., Tang, H., Saigal, S., Bassani, J.L., 2004. On boundary conditions and plastic strain-gradient discontinuity in lower-order gradient plasticity. *J. Mech. Phys. Solids* 52, 1793-1826.

[3] Al-Rub, R.K.A., Voyiadjis, G.Z., 2004. Analytical and experimental determination of the material intrinsic length scale of strain gradient plasticity theory from micro- and nano-indentation. *Int. J. Plasticity* 20, 1139-1182.

[4] Asaro, R.J., 1983. Micromechanics of crystals and polycrystals. *Advances in Applied Mechanics*, Hutchinson, J.W., Wu, T.Y..

[5] Ashby, M.F., 1970. The deformation of plastically non-homogeneous alloys. *Philos. Mag.* 21, 399-424.

[6] Benzerga, A.A., Bréchet, Y., Needleman, A., Van der Giessen, E., 2004. Incorporating three-dimensional mechanisms into two-dimensional dislocation dynamics. *Modelling Simul. Mater. Sci. Eng.* 12, 159-196.

[7] Bishop, K.F.W., Hill, R., 1951. A theoretical derivation of the plastic properties of a polycrystalline face-centered metal. *Philos. Mag.* 42, 1298-1307

[8] Brinckmann, S., Van der Giessen, E., 2004. A discrete dislocation dynamics study aiming at understanding fatigue crack initiation. *Mater. Sci. Eng.* A 387-389, 461-464.

[9] Clayton, J.D., McDowell, D.L., Bammann, D.J., 2004a. A multiscale gradient theory for elastovisco-plasticity of single crystals. *Int. J. Eng. Sci.* 42, 427-457.

[10] Dillon, O.W., Kratochvil, J., 1970. A strain gradient theory of plasticity. *Int. J. Solid Struct.* 6, 1513-1533.

[11] Duan, D.M., Wu, N.Q., Slaughter, W.S., Mao, S.X., 2001. Length scale effect on mechanical behavior due to strain gradient plasticity. *Mater. Sci. Eng.* A 303, 241.

[12] Essmann, U., Gösele, U., Mughrabi, H., 1981. A model of extrusions and intrusions in fatigued metals - I. Point-defect production and the growth of extrusions. *Philos. Mag.* A 44, 405-426.

[13] Fleck, N.A., Hutchinson, J.W., 1993. A phenomenological theory for strain gradient effects in plasticity. *J. Mech. Phys. Solids* 41, 1825-1857.

[14] Fleck, N.A., Muller, G.M., Ashby, M.F., Hutchinson, J.W., 1994. Strain gradient plasticity: theory and experiments. *Acta Metall. Mater.* 42, 475-487.

[15] Gao, H., Huang, Y., Nix, W.D., Hutchinson, J.W., 1999. Mechanism-based strain gradient plasticity– I. Theory. *J. Mech. Phys. Solids* 47, 1239-1263.

[16] Garikipati, K., 2003. Couple stresses in crystalline solids: origins from plastic slip gradients, dislocation core distortions, and three-body interatomic potentials. *J. Mech. Phys. Solids* 51, 1189-1214.

[17] Grosskreutz, J.C., Mughrabi, H., 1975. *Constitutive Equations in Plasticity*. Cambridge, Massachusetts: MIT Press, 301.

[18] Gudmundson, P., 2004. A unified treatment of strain gradient plasticity. *J. Mech. Phys. Solids* 52, 1379-1406.

[19] Gurtin, M.E., 2000. On the plasticity of single crystals: free energy, microforces, plastic strain gradients. *J. Mech. Phys. Solids* 48, 989-1036.

[20] Gurtin, M.E., 2002. A gradient theory of single-crystal viscoplasticity that accounts for geometrically necessary dislocations. *J. Mech. Phys. Solids* 50, 5-32.

[21] Gurtin, M.E., 2004. On a framework for small-deformation viscoplasticity: free energy, microforces, strain gradients. *Int. J. Plasticity* 19, 47-90.

[22] Huang, Y., Qu, S., Hwang, K.C., Li, M., Gao, H., 2004. A conventional theory of mechanism-based strain gradient plasticity. *Int. J. Plasticity* 20, 753-782.

[23] Hwang, K. C, Guo, Y., Jiang, H., Huang, Y., Zhuang,Z., 2004. The finite deformation theory of Taylor-based nonlocal plasticity. *Int. J. Plasticity* 20, 831-839.

[24] Kocks, U.F., 1970. The relation between polycrystal deformation and single crystal deformation. *Metal. Mater. Trans.* 1, 1121-1144.

[25] Liu, B., Huang, Y., Li, M., Hwang, K.C., Liu, C., A study of the void size effect based on the Taylor dislocation model. *Int. J. Plasticity* 21, 2107-2122.

[26] Menzel, A., Steinmann, P., 2000. On the continuum formulation of higher gradient plasticity for single and polycrystals. *J. Mech. Phys. Solids* 48, 1777-1796.

[27] Mughrabi, H., 1983. Dislocation wall and cell structures and long-range internal stresses in deformed metal crystals. *Acta Metall.* 31, 1367-1379.

[28] Mughrabi, H., 2004. On the current understanding of strain gradient plasticity. *Mater. Sci. Eng.* A 387-389, 209-213.

[29] Niordson, C.F., Hutchinson, J.W., 2003. On lower order strain gradient plasticity theories. *Euro. J. Mech. A/Solids* 22, 771-778.

[30] Nix, W.D., 1997. Elastic and plastic properties of thin films on substrates: nanoindentation techniques.. *Mater. Sci. Eng.* A 234, 37-44.

[31] Qu, S., Huang, Y., Pharr, G.M., Hwang, K.C., 2005. The indentation size effect in the spherical indentation of iridium: A study via the conventional theory of mechanism-based strain gradient plasticity. *Int. J. Plasticity* (In Press).

[32] Shu, J.Y., Fleck, N.A., 1999. Strain gradient crystal plasticity: size-dependent deformation of bicrystals. *J. Mech. Phys. Solids* 47, 297-324.

[33] Stolken, J.S., Evans A.G., 1998. A microbend test method for measuring the plasticity length scale. *Acta Mater.* 46, 5109-5115.

[34] Taylor, G.I., 1938. Plastic strain in metals. *J. Institute Metals* 62, 307-324.

[35] Van der Giessen, E., Needleman, A., 1995. Discrete dislocation plasticity: a simple planar model. *Modelling Simul. Mater. Sci. Eng.* 3, 689-735.

[36] Voyiadjis, G.Z., Abu Al-Rub, R.K., 2005. Gradient plasticity theory with a variable length scale parameter. *Int. J. Solids Struct.* 42, 3998-4029.

[37] Wallin, M., Ristinmaaw M., 2005. Deformation gradient based kinematic hardening model. *Int. J. Plasticity* 21, 2025-2050.

[38] Wen, J., Huang, Y., Hwang, K.C., Liu, C., Li, M., 2005. The modified Gurson model accounting for the void size effect. *Int. J. Plasticity* 21, 381-395.

7. STRAIN GRADIENTS AND FATIGUE CRACK PROPAGATION

Strain gradients play an important role in many engineering problems of small dimension. We investigate strain gradients in the area surrounding a growing fatigue crack tip and investigate how strain gradients and strains influence the failure behavior of an elastic-plastic material. To that end, we compare different elastic-plastic continuum models including recent length scale dependent material laws, i.e. strain gradient models, and find that the fatigue crack growth rate depends significantly on the description of the material surrounding the crack. A dislocation density based strain gradient model predicts dislocation density distributions that are similar in value and distribution to those obtained by discrete dislocation simulations. It is found that there is no straight-forward relation between strain gradient contribution to plastic hardening and crack growth rate: taking strain gradients into account leads to faster fatigue crack growth; strong strain induced hardening in the absence of strain gradients however may lead to faster crack growth than weak strain hardening while accounting for strain gradients. Moreover, we vary the thickness of a plastic layer surrounding the crack tip and constrain it by an elastic substrate. We find that an increase in the thickness of the layer non-linearly reduces the fatigue crack growth rate in layered systems.

7.1 Introduction

In metals, experiments for micro-torsion by [3], micro-bending by [4] and micro-indentation by [5] and [6] demonstrated that strain gradients play a vital role in small-sized components and in the vicinity of stress concentrations. These

observations are frequently summarized as a – so called – size effect: smaller components are harder than larger ones. In the present study we investigate the influence of two effects on fatigue crack propagation:

- Strain gradient effects as they occur at the tip of a fatigue crack.

- Constraint effects due to structural constraints,

For monotonic loading, [7], [8], [32], [30] and [33] have shown that crack tip stress fields are significantly elevated at distances on the order of the material length scale when strain gradients are taken into account. [30] reported that taking strain gradients into account in the crack growth simulation of monotonic loading lowers the steady state toughness significantly. In the present paper we investigate the influence of strain gradients on fatigue crack growth predictions. We evaluate how changes in the stress field, in crack closure and the cyclic loading influence crack growth rates.

Macroscale constitutive models, i.e. classical elasticity and classical plasticity, are not able to capture the observed gradient effects in metals, since these theories do not include an intrinsic material length scale. Therefore, we pose the hypothesis that these theories deliver poor results in fatigue crack predictions. On the micro-scale, the dislocation dynamic method give physically sound predictions for fatigue crack propagation as recently shown by [1] and [2]. However, analysis domains being modeled by this method are restricted to a few micrometers and few load cycles due to computational expense. Here, an alternative model is introduced with focus on the meso-scale. Such meso-scale plasticity models bridge the gap between classical macro-scale models and expensive micro-scale models.

Strain gradient models, i.e. meso-scale models, for elastic-plastic materials can capture gradient effects since their formulation includes strain gradients and a length scale. Most strain gradient models (e.g. [9-19]) are of second order and therefore are still computationally expensive. In second order strain gradient models, strain gradients are included as independent kinematic variables, which are work-conjugate to second order stresses. Recently, [31] established a multi-scale model for fracture with incorporates dislocation considerations in the immediate crack process zone and a strain gradient formulation outside this zone. They find that the choice of the boundary between both models plays the

dominating role in their approach.

The present study employs the dislocation density based strain gradient model of Chapter 6 [21] and the conventional mechanism-based strain gradient theory of [20]. In these models, strain gradients depend on strains and therefore do not require work-conjugate terms. The gradient terms are included into the model as contribution to the incremental material stiffness, as proposed by [22]. First order strain gradient models include only first order boundary conditions, which makes these models attractive for inclusion into finite element programs.

The fatigue crack growth simulation approach employed in this study includes two parts: a description of the material surrounding the crack, and a model which describes the subcritical separation of material at the crack tip under cyclic deformation. The latter part is modeled by cohesive surfaces, which [28] and [26] have recently extended incorporate fatigue. Fatigue is understood as a process in which material is deformed due to the applied boundary conditions and thus deformation accumulates. This deformation leads to damage which decreases the local load carrying area, leading to higher stresses in the remaining area. Finally, damage progresses such that the material fails. We reduce the cohesive strength of the material as damage accumulates. To that end, a damage evolution law is included in the cohesive surface description. Both parts of the simulation, i.e. material deformation and material separation, are coupled by their displacement and stress fields.

7.2 Problem Formulation

The dislocation density based strain gradient model (DDSG) by [21] employs considerations of statistically stored (SSD) and geometrically necessary dislocation (GND) densities. Figure 7.1 summaries the mechanics of the two classes of dislocations

In the present fatigue crack simulations, the creation of fracture surfaces is described by the cohesive surface model as described in Chapter 2. The only difference between the cohesive zone model as employed in the previous chapters and in the present chapter refers to the unloading and reloading conditions. We

neglect changes in the potential of the cohesive surface besides those arising due to damage accumulation. Specifically, if no damage accumulates the material follows the same traction-separation curve during unloading as during loading, i.e. no specific unloading behavior has been specified. We neglect changes in the cohesive potential that occur due to a change in loading direction because it is not settled which type of unloading behavior, i.e. elastic unloading (e.g. [26]) or unloading to origin (e.g. [27], [28]), is more physical.

We study the propagation of fatigue cracks in an infinitely large elastic-plastic solid, and in solids where an elastic-plastic layer is embedded in an infinitely large elastic substrate. We approximate this configuration by a symmetric plane-strain modified boundary layer models shown in Figure 7.2. We focus on two parameters which influence the fatigue crack growth prediction. Firstly, we concentrate on the influence of the material description for the elastic-plastic material. Secondly, we vary the thickness of the elastic-plastic layer. The outside model radius is $100 \mu m$. The elastic-plastic material layer has a thickness of $2h$ ranging from 0.14 to $0.72 \mu m$. The maximum amount crack extension, i.e. the length of the row of cohesive surfaces in front of the initial crack tip, is $2.1 \mu m$. This length is much smaller than the radius of the outer perimeter of the material.

We execute an incremental forward Euler time integration with the initial dislocation densities being zero. The Young's modulus is $E = 200 \text{GPa}$, the shear modulus $\mu = 77 \text{GPa}$ and the initial yield strength $\sigma_{y,0} = 250 \text{MPa}$ with isotropic hardening. The Burgers vector is $b = 0.25 \text{nm}$ and the Taylor coefficient $\alpha = 0.3$. For the dislocation density based strain gradient (DDSG) model we neglect an evolution of the material length scale and assume $l_* = 2.5 \mu m = 10000b$, which is motivated by the experimental findings of [23]. For comparison, also $l_* = 1000b$ and $l_* = 100b$ are used. In absence of a strain gradient the DDSG model with $l_* = 10000b$ predict similar hardening as the J2-Plasticity with $n = 0.1$ (see [21] for details). The length scale l_* is stain hardening related and has to be smaller than the largest dimension of the film structure, i.e. the ligament length of the plastic layer. Otherwise, dislocation loops of l^* radius are not physical. Here, SSDs are assumed to glide parallel to the layer.

The cohesive surface has an initial strength of $\sigma_{max,0} = 1\text{GPa}$, a characteristic separation $\delta_n = 3.6\text{nm}$, a characteristic fatigue separation $\delta_\Sigma = 5\delta_n$ and an endurance limit of $\sigma_f = 0.25\sigma_{max,0}$, therefore, the characteristic separation is one order of magnitude larger than the Burgers vector and three orders of magnitude smaller than the continuum material length scale. These material properties are motivated by previous studies of [1] and [26].

The maximum prescribed energy release rate is $G_{max} = 0.3\Phi_{n,0}$. The energy release rate enters the simulation through the displacement boundary conditions. These displacements are given by the singular solution for an infinitely sharp mode I crack and the magnitude of the displacements is scaled by a sinusoidal function with $R = u_{min}/u_{max} = 0.1$.

The monotonic and cyclic ([29]) plastic zone size, respectively, is estimated according to classical J2-plasticity and employing the values given above, as:

$$r_{pl} = \frac{1}{3\pi}\frac{EG_{max}}{(\sigma_{y,0})^2} = 1.08\mu\text{m}, \qquad (7.1)$$

$$\Delta r_{pl} = \frac{1}{3\pi}\frac{EG_{max}}{(2\sigma_{y,0})^2} = 0.27\mu\text{m}; \qquad (7.2)$$

Therefore both, the cyclic and monotonic plastic zone size, are much smaller than the radius of the outer perimeter of the material. This leads to the applied energy release rate being independent of the crack extension in this configuration.

All length scales employed in this study are summarized in Figure 7.3.

7.3 Results and Discussion

Initially, we describe results of simulations of fatigue crack growth for the case of the homogeneous elastic-plastic solid and investigate the influence of strain gradients. Later in this section we focus on the influence of the layer thickness h on fatigue crack growth predictions.

7.3.1 Influence of strain gradients on fatigue crack growth in an elastic-plastic solid

The crack advance according to several material models, i.e. the dislocation density based strain gradient plasticity, classical J2-Plasticity and classical plasticity are shown in Figure 7.4. For comparison results for a simulation with an isotropic elasticity ($\sigma_y = \infty$) are also included. All material models predict an initial phase of loading without crack advance since the simulations starts from a virgin-state material without preexisting dislocations or plastic strain and without initial damage in the cohesive zone. After few cycles sufficient damage has accumulated such that $D = 1$ in the first cohesive surface element. The crack now advances. After the initial cycles, the material surrounding the crack tip is deformed and damage has accumulated in the cohesive zone elements ahead of the crack tip. Therefore, these cohesive elements are already weakened and the crack can propagate faster through them than through the first few cohesive elements.

The simulations using the classical J2-Plasticity model predict the slowest crack growth. The dislocation density based strain gradient model without geometrically necessary dislocations, i.e. DDSG*, neglects strain gradients. Results for this model are nearly identical to those for the classical J2-Plasticity model, emphasizing the similarity between the DDSG* and J2-Plasticity model. The DDSG model, which includes strain gradients, predicts a significant faster crack growth rate. Similarly, the conventional mechanism based strain gradient model (CMSG) of [20] predicts higher crack growth rates when including strain gradient effects, as shown in the appendix. Both models predict similar crack growth rates, although the CMSG model, unlike the DDSG model, employs the Nye and the Taylor factor.

Summarizing, the simulations demonstrate that simulations accounting for strain gradients predict higher fatigue crack growth rates than computations neglecting strain gradients. The explanation for these central observations can be given in different ways:

- There are two dissipative mechanisms related to material deformation and material separation. Materials with a large plastic hardening due to strain gradients dissipate less energy. As the amount of

applied external energy is constant, more energy is available to create the free surfaces on either crack flank in harder materials. This in turn leads to a higher crack growth rate for models which take strain gradients into account. [30] had previously reported lower crack growth resistance for monotonic loading when strain gradients are accounted for.

- [7] and [8] report that the strain gradient model of [10] leads to higher stresses in the area ahead of the crack tip. Similarly, [30] and [32] report higher stresses ahead of the crack tip when employing the mechanism-based strain gradient plasticity theory of [12] and conventional theory of mechanism-based strain gradient model of [20], respectively. For the cyclic load case presented here, we find a similar elevation of stresses due to the additional hardening caused by the strain gradients, i.e. the attained tractions are higher if the material experiences significant plastic hardening, as shown in Figure 7.5(a). Higher tractions lead to increased damage accumulation in the cohesive surface and consequently higher fatigue crack growth rate.

- Materials with an enhanced plastic hardening due to elevated strains or strain gradients deform less in the bulk. The applied displacement is equal in the simulations for all material models. The separation of the cohesive surface, Figure 7.5(b), i.e. the difference of applied deformation and the deformation of the bulk material, is thus larger for materials which harden more. This increase in cohesive surface separation leads to enhanced damage accumulation and consequently to a higher fatigue crack growth rate. This finding is compatible with the classical understanding of fatigue crack growth, where $da/dN \sim \Delta$CTOD : the elevation in cohesive surface separation for strain gradient models leads to an increased crack opening, or blunting, as show in Figure 7.5(b).

The difference between the crack profiles at minimal (Figure 7.6) and maximal (Figure 7.5) applied load at $x = 0.5\mu$m is 3.0nm and 2.6nm for the DDSG model and DDSG*, respectively. Therefore, cyclic blunting, i.e. difference between the crack profile at minimal and maximal applied load, is larger for the strain gradient model than for the model neglecting strain gradients, leading to faster fatigue crack

growth for the DDSG model.

- It is widely acknowledged that crack closure plays an important role in fatigue crack growth ([34]). Figure 7.6 depicts the crack profiles for crack extension of $0.55\mu m$ at the minimum applied displacement $u_{applied} = u_{min}$. At the current crack tip, i.e. $D = 1$, as denoted by point '*' neither model predicts crack closure. Ahead of this location, simulations with J2-Plasticity and the DDSG* model predict crack surface contact with J2-Plasticity predicting the largest closure zone. The DDSG model ($l_* = 10000b$), however, did only lead to minor crack surface contact in the area ahead of the location $D = 1$. The crack surface contact area decreases as the influence of the strain gradient is incorporated. While, the DDSG* model predicts $0.1392\mu m$ of crack length under contact, the DDSG model predicts that $0.0078\mu m$ of crack surface experience closure. A similar decrease in contact length is found for the CMSG model, as shown in the appendix. Crack closure shields the crack tip and leads to a reduction in crack growth rate. In summary, as the influence of strain gradients are accounted for, the amount of closure decreases leading to an increase in fatigue crack growth rate.

These findings show that materials with an increased plastic hardening due to strain gradients exhibit an increased fatigue crack growth rate, if the material separation process itself is not altered by the strain gradients, as assumed in this study.

[8] found singular compressive stresses in close proximity ahead of the crack tip when employing the material model of [10]. They conclude that strain gradient theories loose their validity in this range. We find less compressive, i.e. more tensile, stresses if strain gradients are included in the simulation (Figure 7.5(a)). Similarly, [30] has found tensile stresses in their study employing a strain gradient model and cohesive surfaces. Therefore, the results reported by [8] appear to be specific to the approach taken by those authors, and not a general property of strain gradient models.

7.3.2 Influence of DDSG material length on fatigue crack growth rate

Fatigue crack growth rates for the DDSG and DDSG* model are given for three values of l_* in Figure 7.7. Both models predict that for decreasing material length scale, i.e. decreasing average distance of SSD motion, fatigue crack growth rates increase. These findings with respect to changes in length scales are consistent with the model definition. In the DDSG model the material length is associated with the strain. In the DDSG model the material length describes the average distance of SSD motion. As this distance decreases, i.e. the material hardens plastically, the crack accelerates.

The decrease in fatigue crack growth rate with increasing material length l_* is logarithmic when neglecting strain gradients. Taking strain gradients into account, i.e. in the DDSG model, leads to higher crack growth rates and a less then logarithmic decay. This difference between the DDSG and DDSG* model is stronger for larger material lengths l_*, i.e. in weakly strain hardening materials. This regime of weakly strain hardening material is more relevant than the regime of low material length scale because the corresponding J2-hardening exponents n for the latter regime are significantly higher than normally observed in experiments.

If the cohesive surface strength is uncoupled from the yield strength, simulations predict that plastic hardening leads to an increase in fatigue crack growth rate, as also reported by [27]. Experimentally determined Paris-law graphs ([34]) show that a decrease in yield strength leads to an increase in fatigue crack growth rate. Lower hardening leads to an increase in plastic deformation and in an increased fatigue crack growth rate. The results reported here cannot be directly compared to this specific experimental finding since the cohesive strength is constant in our simulation. To simulate the reported experiments, the cohesive strength would have to be coupled to the current yield strength of the material, which evolves as the solid is plastically deformed. This deformation would lead to an evolution of the cohesive strength. While such models can in principle be envisioned, they are not in the scope of the current study.

7.3.3 Dislocation density

Dislocation motion results in plastic deformation. The dislocation density determines the plastic hardening: as dislocations populate the material it becomes increasingly difficult for other dislocations to move as the former dislocations obstruct the motion of the latter. The area of dislocation motion is called (cyclic) plastic zone size and is a characteristic size of boundary value problem. If this size is restricted by geometric features such as elastic layers, the plastic zone cannot fully develop and constraint effects will be observed. Because dislocations play such an important role in the present boundary value problem we now look into the distribution of dislocations.

Figure 7.8 shows the distribution of statistically stored (SSD) and geometrically necessary dislocations (GND) according to the DDSG model ($l_* = 10000b$) after 25 cycles. The statistically stored dislocation density is maximum at the initial crack tip. As observed in Figure 7.4, initially the crack tip is immobile for a period, leading to several load cycles during which strains are maximum in the area of the initial crack tip. Therefore, many dislocations accumulate in this region. A similar distribution is observed for the geometrically necessary dislocations in the area of the initial crack tip. However, the GND density is one order of magnitude larger than that of SSDs.

In the simulations, Figure 7.4, the cracks advanced into a steady state growth regime after some initial cycles. This difference in crack growth rate is also observed in the dislocation density distribution. In Figure 7.8, both dislocation densities exhibit a almost steady state distribution once the crack leaves the area surrounding the initial crack tip disturbance. The maximum of the GND density is closer to the crack surface than that of the SSD. The GND density is one order of magnitude larger than that of SSDs. In the area in proximity of the crack the total dislocation density, i.e. sum of SSDs and GNDs, is on the same order of magnitude as $2.4e8\text{mm}^{-2}$ which was determined by [1] in discrete dislocation simulations.

Figure 7.9 depicts the change in dislocation density in the half-cycle from 15.0 to 15.5, i.e. during loading. The increase in the GND density is significantly larger than in the SSD density. Additionally, the maximum of the GND density is trailing the maximum of the SSD density. The area of maximum dislocation

168

density is inclined by 57 degrees to the crack. Discrete dislocation simulations of [1] predicted an angle of 60 degrees.

Figure 7.10 depicts the changes in dislocation densities in the half-cycle from 14.5 to 15, i.e. during unloading. Compared to the dislocation densities during loading, the area of dislocation activity is larger during unloading than during the loading half-cycle. However, the increase in SSD and GND densities are significantly smaller (roughly 40 times) during unloading than during loading. As during loading, the increase in the geometrical necessary dislocation density is significantly larger than in the statistically stored dislocation density and the domain of GND activity surrounds that of SSD activity.

The active fracture process zone, i.e. the distance between $D = 1$ and $D = 0.1$, is $0.44 \mu m$ for the specified loading and was found to be the same during unloading (see Figure 7.10) and reloading (see Figure 7.9). The crack process zone has roughly the same size as the plastic zone, see equation (7.2).

7.3.4 Confined plasticity

Now we confine the plastic zone by placing the elastic-plastic solid within an elastic substrate, i.e. we introduce a constraint effect. We concentrate on the influence of the thickness $2h$ of the plastic layer on fatigue crack growth predictions. In Figure 7.11 the steady state crack growth rate according to the DDSG model ($l_* = 10000b$) and J2-Plasticity is shown for different layer thicknesses.

An increase in the thickness of the plastic layer, i.e. a reduction in the geometric constraint on plastic deformation, leads to a slower the crack advance. The evaluation of the fatigue crack growth rate for different layer thicknesses leads to scattered points. The parameter c of the exponential function

$$\frac{da}{dN} = (\frac{da}{dN})_{0-\infty} \exp(-c^2h^2) + (\frac{da}{dN})_\infty \qquad (7.3)$$

is fitted to the calculated points. The parameter $(\frac{da}{dN})_{0-\infty}$ is determined by the crack growth rate for a layer of zero thickness and $(\frac{da}{dN})_\infty$ is the fatigue crack growth rate in an infinite thick plastic layer (see Figure 7.4). Both models predict a similar dependence of the fatigue crack growth rate on the thickness of the plastic layer.

169

Classical J2-Plasticity for all values of h predicts a lower crack growth rate than the strain gradient plasticity model.

As the thickness of the elastic-plastic layer is decreased the plastic zone is geometrically restricted. For $h = 0$ the fatigue crack growth rate approaches that of an elastic bulk material. The size-constraint is lifted for layers with thicknesses $2h$ larger than the plastic zone size $\sim 2\mu m$, which we calculated from DDSG simulations and equation (7.2). The simulations show that a higher relieve of constraint is necessary when strain gradients are accounted for, since the strain gradients act over a larger area.

7.4 Conclusion

The fatigue crack simulations described in the present study incorporate a continuum material model and a cohesive surface model. The latter is included to describe the behavior of the crack surfaces. It was shown that the choice of the material model significantly determines the fatigue crack growth predictions:

- Classical plasticity predicts the lowest crack growth rates. Strain gradient models predict faster crack growth rates because the strain gradient induced hardening leads to faster crack advance. This observation can be explained by either the maximum attained tractions in the material, the deformation of the material compared to the crack opening and the plastic energy dissipation in the material. σ_f, which were not in focus of this study.

- Accumulation of plastic strain leads to an increase in the statistical stored dislocation density, which leads to strain induced hardening. In the DDSG and DDSG* model hardening is incorporated via material length scale l_*. A decrease in the material length scale leads to an increase in fatigue crack growth rate for strain hardened material. Therefore, if the strain induced hardening increases at constant contribution from the strain gradients, i.e. the contribution of strain gradients decreases, accelerated fatigue crack growth will be observed. Concluding, hardening

irrespectively whether originating of strains or strain gradients leads to increased fatigue crack growth.

• Classical plasticity predicts significant crack closure. Strain gradient models predict less crack closure depending on the contribution to hardening due to strain gradients. The more strain gradients contribute, the less closure is observed. This enhances the classical view of closure: reduced closure reduces shielding of the crack tip and leads to an increase in fatigue crack growth rate.

• The dislocation density based strain gradient model (DDSG) predicts that the geometrically necessary dislocation (GND) density is significantly larger than the statistically stored density (SSD) in the area surrounding the crack. The maximum GND density is in close proximity to the crack while the maximum of the SSD is more distant. The total dislocation density calculated in the present study ($\sim 10^8$ mm) is on the same order of magnitude as in the dislocation dynamics simulations.

• Thinner plastic layers surrounded by elastic substrate exhibit a faster crack growth than thicker layers, since the plastic zone size is restricted in thin layers. Computations predict that constraint effects in thin film-structures persist to larger values of thickness if strain gradients are accounted for.

Our observations lead to the conclusion: strain gradients significantly influence fatigue crack predictions. Classical plasticity underestimates the fatigue crack growth rate and therefore leads to potentially unsafe fatigue life predictions.

171

Previously, in Chapter 6, following [20], we defined the flow stress for the conventional mechanism-based strain gradient plasticity theory (CMSG). Thereby, the material length scale l_k is interpreted as a scale parameter for the influence of strain gradients. [20] and [12] give the length l_k as a multiple of the Burgers vector $\sim (\mu/\sigma_{y,0})b$. [12] calculates the length as $l_1 = 2.3\mu m$. [20] employs two additional factors, i.e. Nye factor and Taylor factor, which leads to an increase in the material length l_k by the factor of 17.1 ($l_2 = 38\mu m$) compared to the length as defined by [12]. For comparison, we rewrite the DDSG model into as form similar to that of the CMSG model:

$$\sigma_y = \sigma_{y,0}\left(1 + \frac{\sqrt{3}\alpha\mu b}{\sigma_{y,0}}\sqrt{\rho_{SSD} + \rho_{GND}}\right) \qquad (7.4)$$

$$= \sigma_{y,0}\left(1 + \sqrt{\frac{\sqrt{3}l_k\bar{\varepsilon}^p}{l_*} + l_k\bar{\eta}^p}\right) \qquad (7.5)$$

where α is the Taylor coefficient and $l_k = 3\alpha^2\frac{\mu^2}{\sigma_{y,0}^2}b$ is a length scale, which is identical to the definition of [12]. Recall, the DDSG model introduces a physically measurable material length scale l_* which is associated with the strain. For the CMSG theory a hardening exponent of $n = 0.1$ is employed in the following simulations.

We conduct computations along the model outlined in the main part of this chapter. In absence of a strain gradient the CMSG theory is identical J2-Plasticity. The $CMSG_1$ model, which employs a material length scale of $l_1 = 2.3\mu m$, predicts a similar crack growth behavior as J2-Plasticity and DDSG* (see Figure 7.4). The material length scale $l_1 = 2.3\mu m$ is not large enough to provide equal contributions from strain gradients and strain to plastic hardening equation (7.4), i.e. the contributions from the plastic strain dominate. As the material length scale l_k is increased in the CMSG model the crack growth rate increases. Employing a material length scale $l_2 = 38\mu m$ the predicted crack growth is significantly faster than the predictions from classical plasticity. The DDSG model does not include the Nye or Taylor factor, but predicts a similar crack growth rate as the $CMSG_2$

model which includes additional factors. The crack opening, shown in Figure 7.13, supports the finding of the DDSG model, the contact decreases when increasing the material length scale from $2.3\mu m$ to $38\mu m$, i.e. when increasing the absolute contribution of the strain gradients. The CMSG model with a material length scale of $l_1 = 2.3\mu m$ and $l_2 = 38\mu m$ predict $0.1559\mu m$ and $0.1496\mu m$ of closed surface, respectively
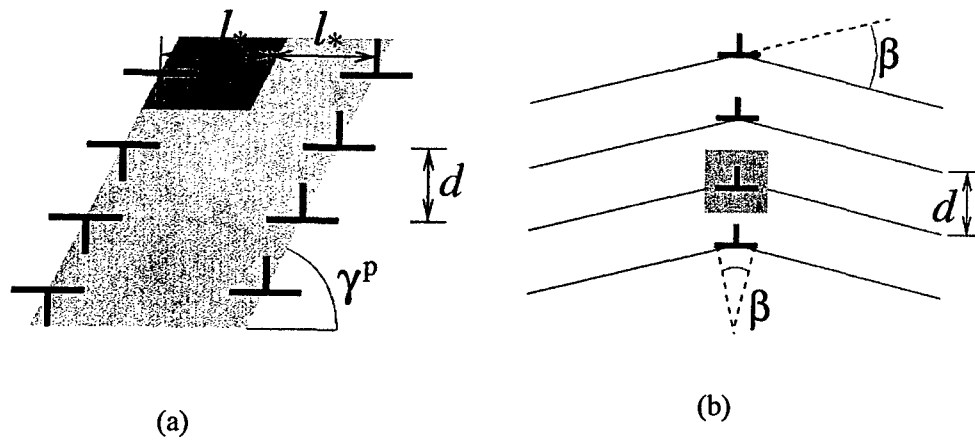
Figure 7.1: Schematic representation of statistically stored (a) and geometrically necessary dislocations (b).
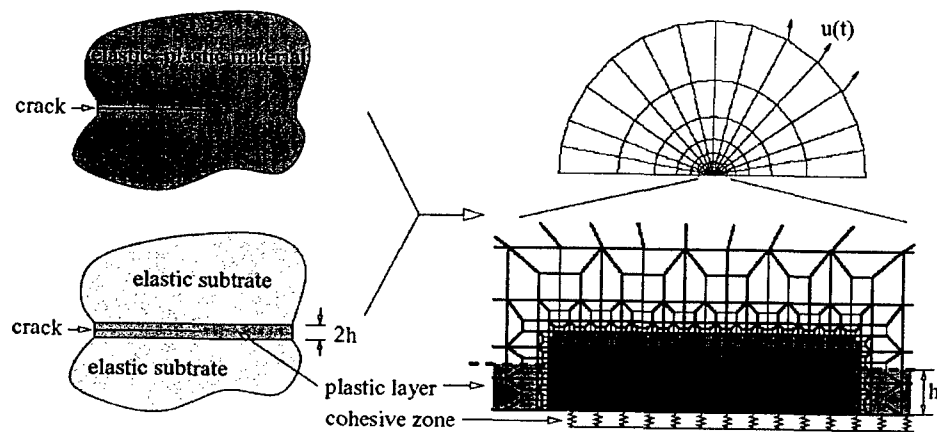
Figure 7.2: Definition of boundary value problem and definition of the plastic layer.
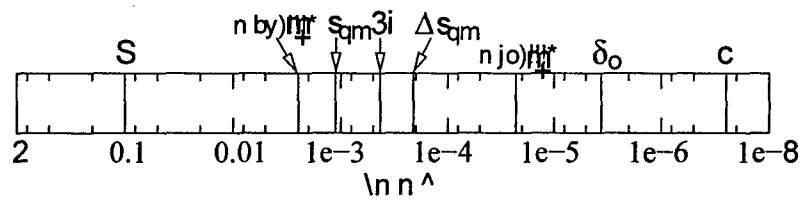
Figure 7.3: Compilation of length scales: perimeter of computational model R, monotonic plastic zone size r_{pl}, material length scale l_* of the DDSG model, average elastic-plastic layer thickness $2h$ in layered model, cyclic plastic zone size Δr_{pl}, characteristic cohesive surface opening δ_n, magnitude of Burgers vector b.

crack extension [μm]

!3/1

!2/6

!2/1

!1/6

!1

!1 !6 !21 !26 !31 !36 !41 !46 !51

dzdrfn

Elastic

DDSG
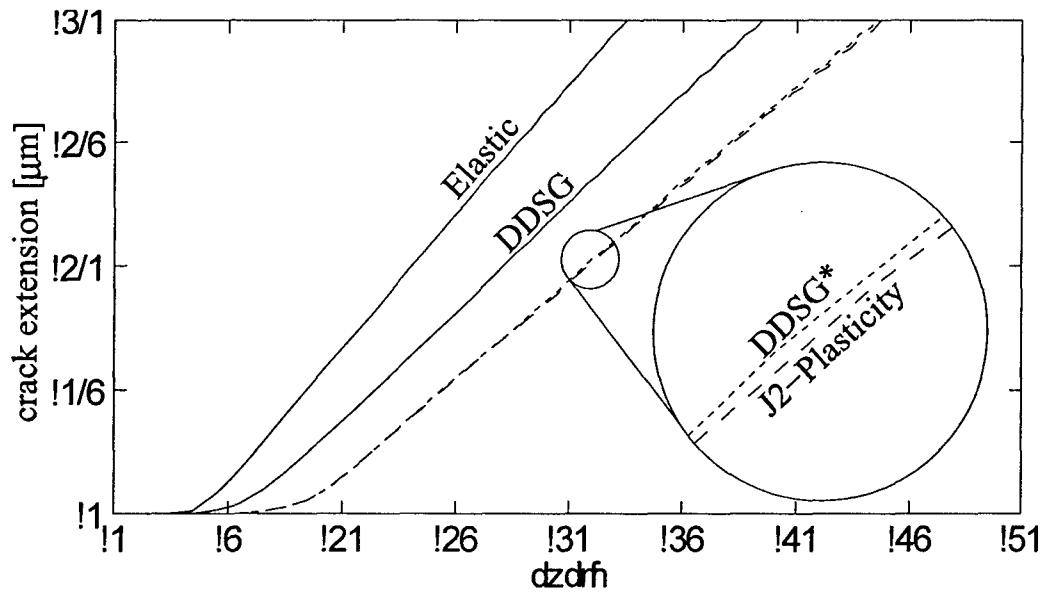
DDSG*

J2-Plasticity

Figure 7.4: Predicted fatigue crack extension in an elastic-plastic solid: dislocation density based strain gradient plasticity (DDSG) with $l_* = 10000b$, 1 mechanism-based strain gradient model with $l_1 = 2.3\mu m$ (CMSG$_1$), dislocation density based strain gradient plasticity neglecting GNDs (DDSG*), classical J2-Plasticity, and isotropic elasticity.

177
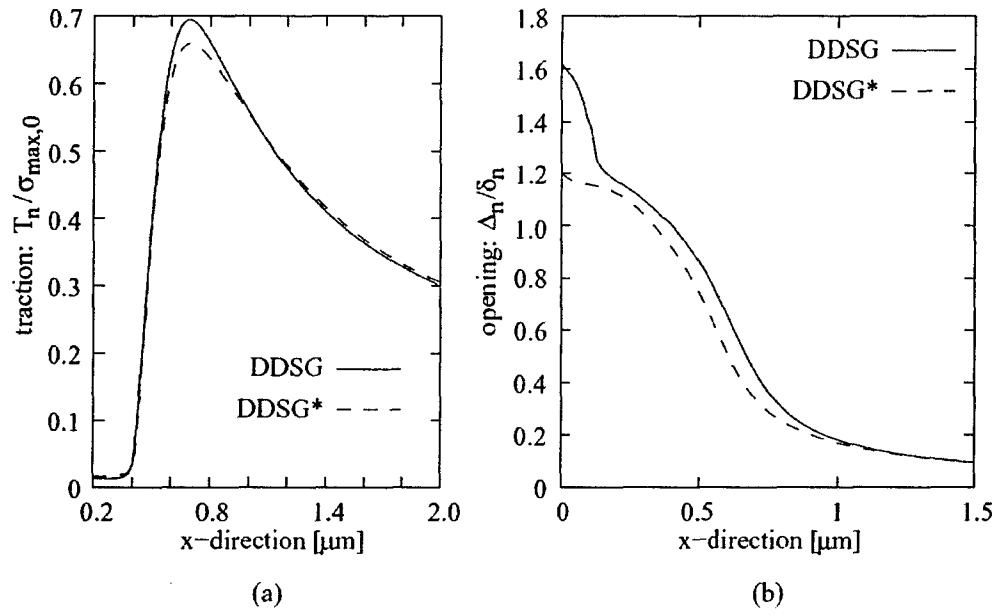
Figure 7.5: Predicted tractions (a) and predicted crack opening (b) along crack direction at maximal (after 14.5 cycles) and minimal applied load (after 15 cycles) according to the dislocation density based strain gradient plasticity (DDSG) and dislocation density based strain gradient model neglecting strain gradients (DDSG*).
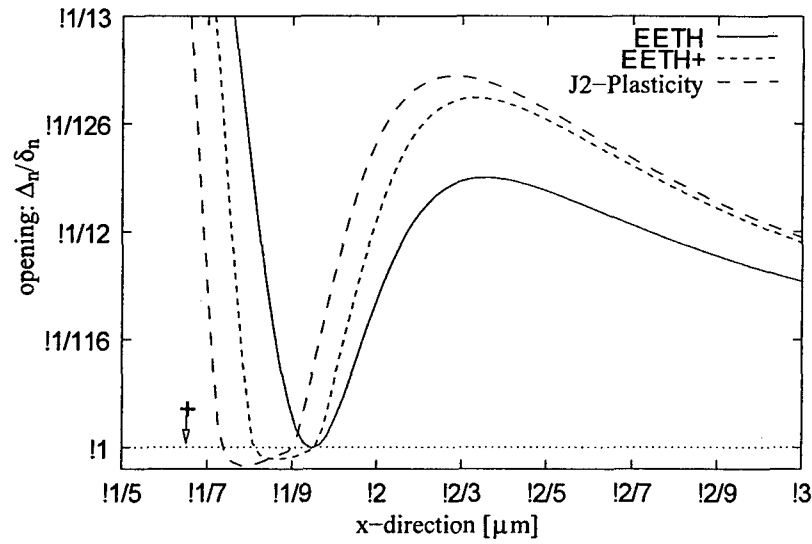
Figure 7.6: Crack closure profiles for an infinitely large material according to dislocation density based strain gradient plasticity (DDSG), dislocation density based strain gradient model neglecting strain gradients (DDSG*) rain gradient model with $l_2 = 38\mu m$ ($CMSG_2$), conventional mechanism-based strain gradient model with $l_1 = 2.3\mu m$ ($CMSG_1$) and classical J2-Plasticity. The profiles correspond to the minimum applied displacement $u_{applied} = u_{min} = 0.1u_{max}$.
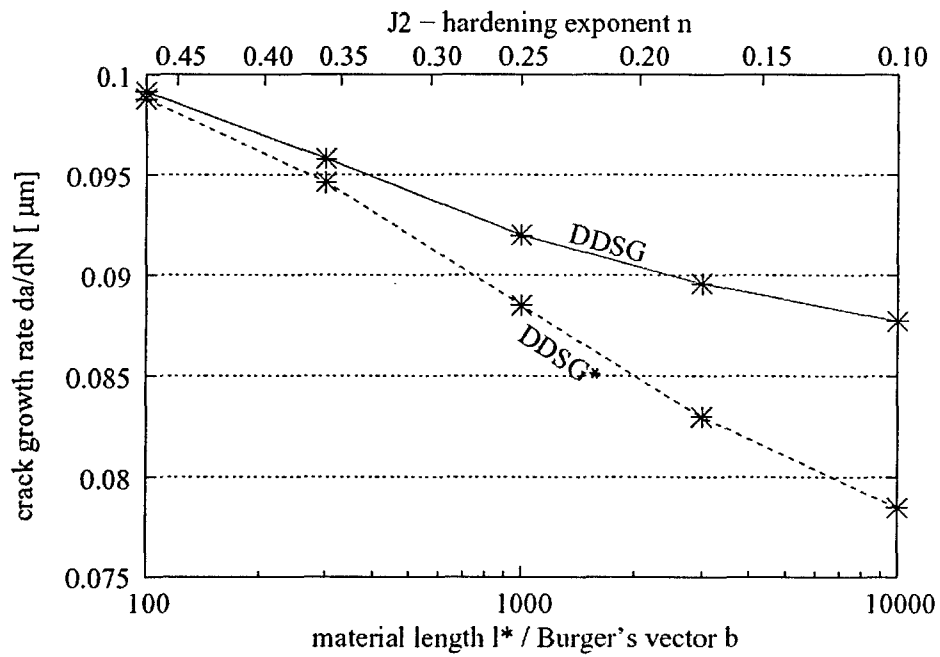
Figure 7.7: Predicted fatigue crack growth rate as a function of the material length l_* for the dislocation density based strain gradient plasticity (DDSG) and dislocation density based strain gradient plasticity neglecting GNDs (DDSG*).
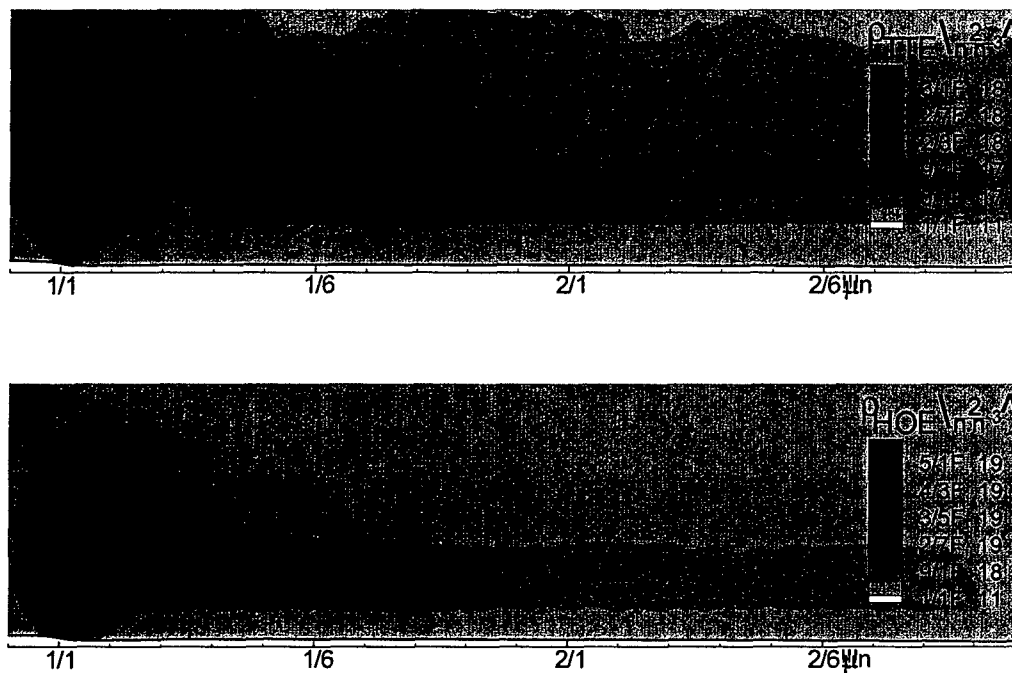
Figure 7.8:The distribution of the accumulated statistically stored (a) and geometrically necessary dislocation density after 25 cycles in the area surrounding the crack tip. The deformation is magnified by 10 .
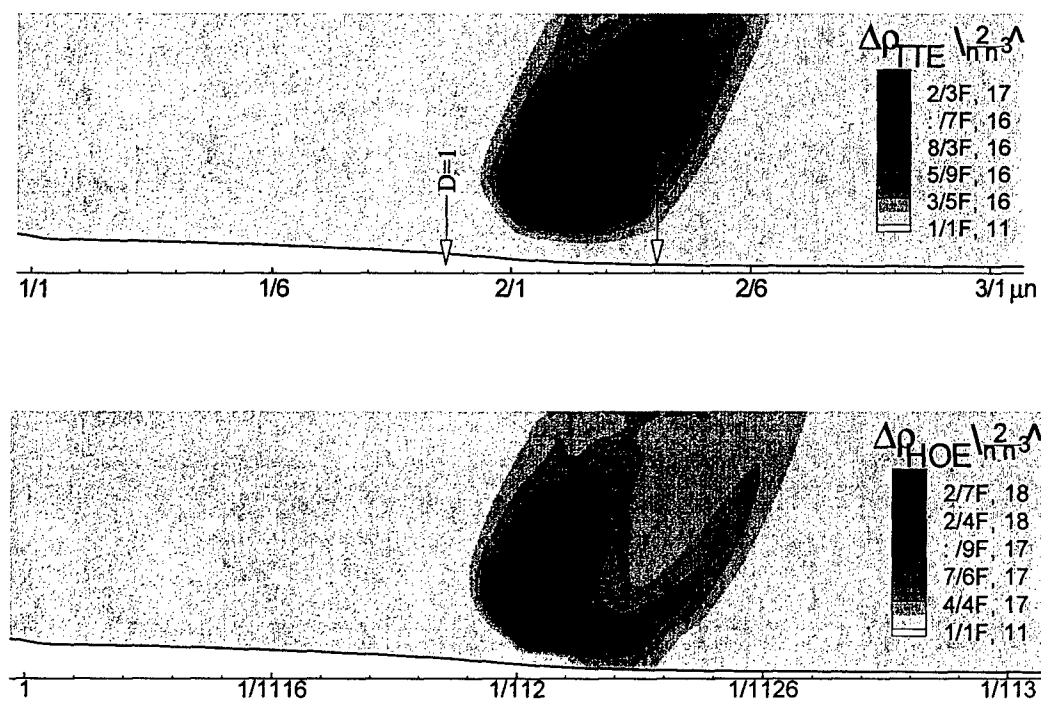
Figure 7.9:Distribution of the increase in statistically stored (a) and geometrically necessary dislocation densities (b) between cycle 15.0 and 15.5 (loading). The deformation is magnified by 10.
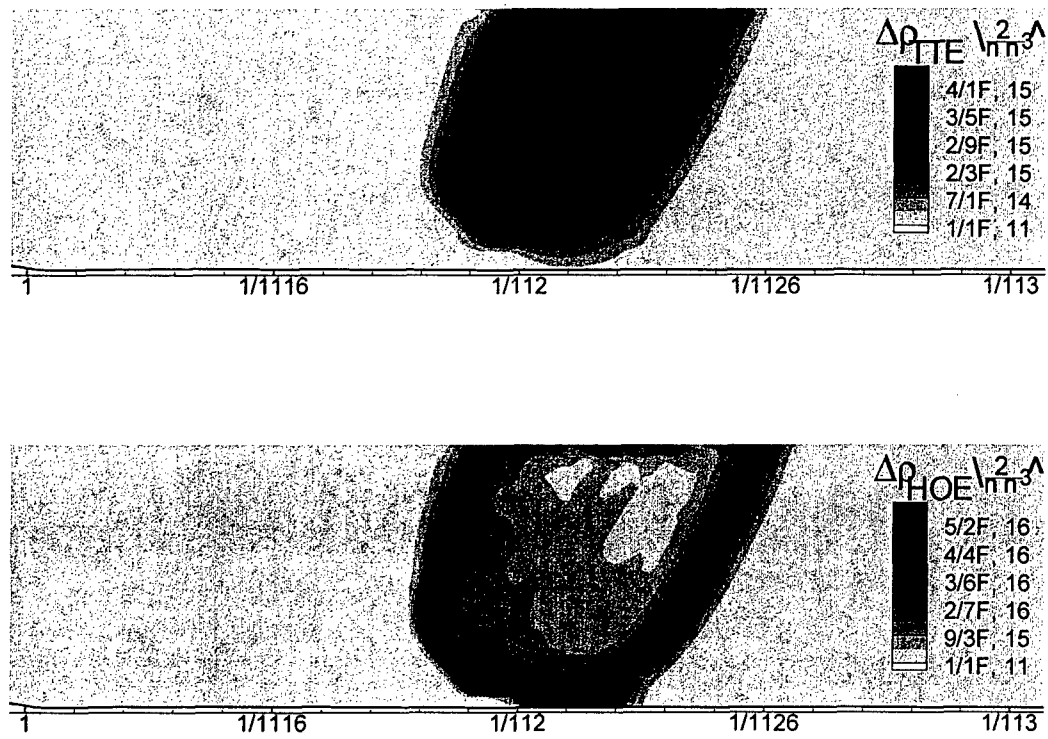
Figure 7.10: Distribution of the increase in statistically stored (a) and geometrically necessary dislocation densities (b) between cycle 14.5 and 15 (unloading). The deformation is magnified by 10.
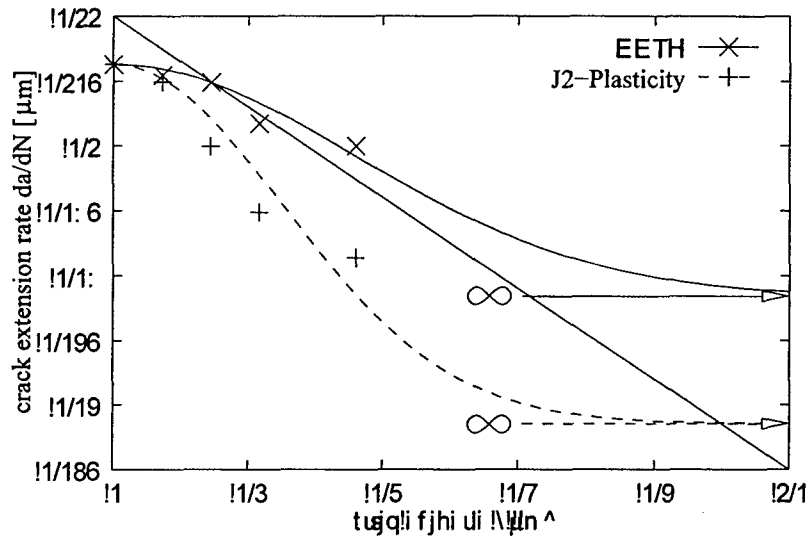
Figure 7.11: Rate of steady fatigue crack growth depending on the thickness of the plastic layer surrounded by an elastic substrate. The results are shown for the dislocation density based strain gradient model and classical J2-Plasticity.
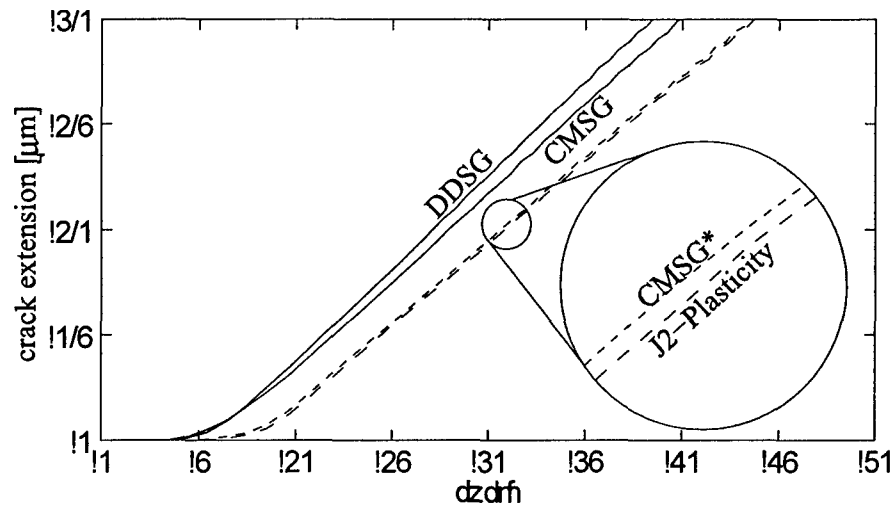
Figure 7.12: Predicted fatigue crack extension in an infinitely large material: dislocation density based strain gradient plasticity (DDSG) with $l_* = 10000b$, conventional mechanism-based strain gradient model with $l_2 = 38\mu m$ (CMSG$_2$), conventional mechanism-based strain gradient model with $l_1 = 2.3\mu m$ (CMSG$_1$), and classical J2-Plasticity.
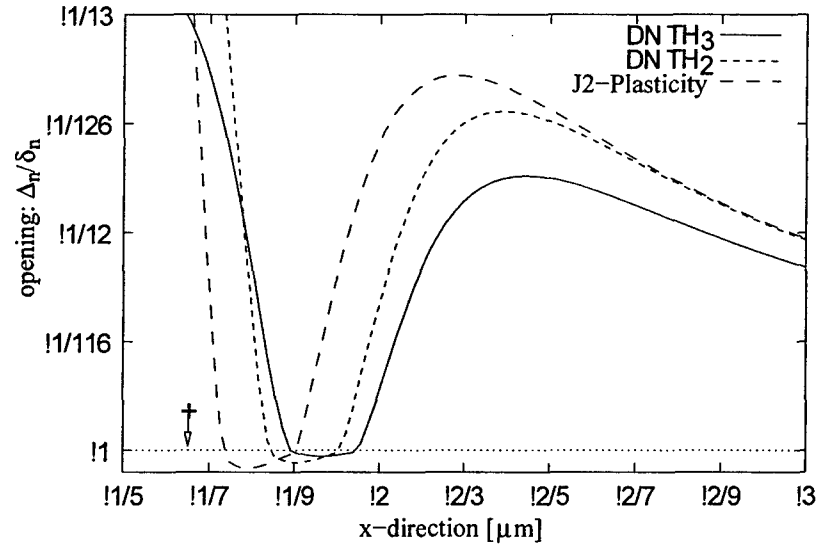
Figure 7.13: Crack closure profiles for an infinitely large material according to classical J2-Plasticity, conventional mechanism-based strain gradient model with $l_2 = 38\mu m$ ($CMSG_2$), conventional mechanism-based strain gradient model with $l_1 = 2.3\mu m$ ($CMSG_1$) and classical J2-Plasticity. The profiles correspond to the minimum applied displacement $u_{applied} = u_{min} = 0.1u_{max}$.

LIST OF REFERENCE

[1] Cleveringa, H.H.M., Van der Giessen, E., Needleman, A., 2000. A discrete dislocation analysis of mode I crack growth. *J. Mech. Phys. Solids* 48, 1133-1157.

[2] Deshpande, V.S., Needleman, A., Van der Giessen, E., 2002. Discrete dislocation modelling of fatigue crack propagation. *Acta Mater.* 50, 831-846.

[3] Fleck, N.A., Muller, G.M., Ashby, M.F., Hutchinson, J.W., 1994. Strain gradient plasticity: Theory and experiment. *Acta Metall. Mater.* 42, 475-487.

[4] Stolken, J.S., Evans A.G., 1998. A microbend test method for measuring the plasticity length scale. *Acta Mater.* 46, 5109-5115.

[5] Ma, Q., Clarke, D.R., 1994. Size dependent hardness of silver single crystals. *J. Mat. Research* 10, 853-863.

[6] Poole, W.J., Ashby, M.F., Fleck, N.A., 1996. Micro-hardness tests on annealed and work-hardened copper polycrystals. *Scr. Metal. Mater.* 34, 559-564

[7] Huang, Y., Chen, J.Y., Guo, T.F., Zhang, L., Hwang, K.C., 1999. Analytic and numerical studies on mode I and mode II fracture in elastic-plastic materials with strain gradient effects. *Int. J. Fracture* 100, 127.

[8] Chen, J.Y., Wei, Y., Huang, Y., Hutchinson, J.W., Hwang, K.C., 1999. The crack tip fields in strain gradient plasticity: the asymptotic and numerial analyes. *Eng. Fract. Mech.* 64, 625-648.

[9] Dillon, O.W., Kratochvil, J., 1970. A strain gradient theory of plasticity. *Int. J. Solid Struct.* 6, 1513-1533.

[10] Fleck, N.A., Hutchinson, J.W., 1993. A phenomenological theory for strain gradient effects in plasticity. *J. Mech. Phys. Solids* 41, 1825-1857.

[11] Shu, J.Y., Fleck, N.A., 1999. Strain gradient crystal plasticity: size-

dependent deformation of bicrystals. *J. Mech. Phys. Solids* 47, 297-324.

[12] Gao, H., Huang, Y., Nix, W.D., Hutchinson, J.W., 1999. Mechanism-based strain gradient plasticity– I. Theory. *J. Mech. Phys. Solids* 47, 1239-1263.

[13] Gurtin, M.E., 2000. On the plasticity of single crystals: free energy, microforces, plastic strain gradients. *J. Mech. Phys. Solids* 48, 989-1036.

[14] Gurtin, M.E., 2002. A gradient theory of single-crystal viscoplasticity that accounts for geometrically necessary dislocations. *J. Mech. Phys. Solids* 50, 5-32.

[15] Gurtin, M.E., 2004. On a framework for small-deformation viscoplasticity: free energy, microforces, strain gradients. *Int. J. Plasticity* 19, 47-90.

[16] Menzel, A., Steinmann, P., 2000. On the continuum formulation of higher gradient plasticity for single and polycrystals. *J. Mech. Phys. Solids* 48, 1777-1796.

[17] Garikipati, K., 2003. Couple stresses in crystalline solids: origins from plastic slip gradients, dislocation core distortions, and three-body interatomic potentials. *J. Mech. Phys. Solids* 51, 1189-1214.

[18] Wen, J., Huang, Y., Hwang, K.C., Liu, C., Li, M., 2005. The modified Gurson model accounting for the void size effect. *Int. J. Plasticity* 21, 381-395.

[19] Clayton, J.D., McDowell, D.L., Bammann, D.J., 2004. A multiscale gradient theory for elastovisco-plasticity of single crystals. Int. J. Eng. Sci. 42, 427-457.

[20] Huang, Y., Qu, S., Hwang, K.C., Li, M., Gao, H., 2004. A conventional theory of mechanism-based strain gradient plasticity. *Int. J. Plasticity* 20, 753-782.

[21] Brinckmann, S., Siegmund, T., Huang, Y., 2006. A Dislocation Density based Strain Gradient Model. *Int. J. Plasticity* 22, 1784-1797.

[22] Acharya, A., Bassani, J.L., 2000. Lattice incompability and a gradient theory of crystal plasticity. *J. Mech. Phys. Solids* 48, 1565-1595.

[23] Mughrabi, H., 1983. Dislocation wall and cell structures and long-range internal stresses in deformed metal crystals. *Acta Metall.* 31, 1367-1379.

[24] Mughrabi, H., 2004. On the current understanding of strain gradient plasticity. *Mater. Sci. Eng.* A 387-389, 209-213.

[25] Xu, X.P. and Needleman, A., 1994. Numerical simulations of fast crack growth in brittle solids. *J. Mech. Phys. Solids* 42, 1397-1434.

[26] Roe, K.L., Siegmund, T., 2003. An irreversible cohesive zone model for interface fatigue crack growth simulation. *Eng. Frac. Mech.* 70, 209-232.

[27] Wang, B., Siegmund, T., 2005. A numerical analysis of constraint effects in fatigue crack growth by use of an irreversible cohesive zone model. *Int. J. Fract.* 132, 175-196.

[28] Nguyen, O., Repetto, E.A., Ortiz, M., Radovitzky, R.A., 2001. A cohesive model of fatigue crack growth. Int. J. Fract. 110, 351-369.

[29] Rice, J.R., 1967. The Mechanics of Crack Tip Deformation and Extension by Fatigue. in Fatigue Crack Propagation, Special Technical Publication 415, ASTM 247-311.

[30] Wei, Y., Qiu, X., Hwang, K.C., 2004. Steady-state crack growth and fracture work based on the theory of mechanism-based strain gradient plasticity. *Eng. Frac. Mech.* 71, 107-125.

[31] Wei, Y., Xu, G., 2005. A multiscale model for the ductile fracture of crystalline materials. *Int. J. Plasticity* 21, 2123-2149.

[32] Qu, S., Huang, Y., Jiang, H., Liu, C., Wu, P.D., Hwang, K.C., 2004. Fracture analysis in the conventional theory of mechanism-based strain gradient (CMSG)

plasticity. *Int. J. Fract.* 129, 199-220.

[33] Radi, E., Gei, M., 2004. Mode III crack growth in linear hardening materials with strain gradient effects. *Int. J. Fract.* 130, 765-785.

[34] Suresh, S., 1998. Fatigue of Materials. Cambridge UK: Cambridge University Press, 2nd edition.

8. A COHESIVE SURFACE MODEL BASED ON THE STRESS CAUSED BY DISLOCATIONS

Strains and strain gradients in the proximity of a crack tip lead to an increase in dislocation density, which plays a vital role in the fatigue crack resistance of metallic materials. We introduce an enhancement to conventional cohesive zones, which are frequently used to simulate fracture and fatigue. This enhancement is derived from the analytical stress fields of individual dislocations. The micromechanical fatigue simulations predict an accelerated crack growth during the final stages of each loading phase. Additionally, significant crack closure is observed. The predicted dislocation densities are similar to those predicted by discrete dislocation simulations. The fatigue crack growth threshold and Paris-law are studied and compared to experimental findings. An overload prediction is discussed with respect to the production of different kinds of dislocations and fatigue crack growth retardation.

8.1 Introduction

Fatigue simulations often employ cohesive surface laws, which where initially introduced for fracture problems. Fatigue occurs at lower applied loads than monotonic fracture. To employ cohesive zone laws in fatigue we have described a damage mechanics approach in Chapter 2 (based on Roe and Siegmund, 2003) such that the crack propagates under the reduced applied loads.

It is understood that in metals dislocations play an essential role in fatigue. Discrete dislocation simulations (Cleveringa et al., 2000; Deshpande et al., 2001, 2002) revealed that dislocations play a dual role in crack propagation. On the one

hand, they shield the crack tip by their motion, reducing the stress and thereby increasing the crack growth resistance. This effect is captured by continuum models which include plasticity to limit the elastic regime. On the other hand, dislocations form clusters which trap the constituting dislocations in the proximity of the crack tip. These cluster dislocations, as any dislocation, carry a stress singularity. If sufficient dislocations are trapped, the stress at the crack tip is elevated, leading to a reduced crack resistance. The effect of cluster dislocations on crack propagation is not included in conventional models. Therefore, we introduce this effect into a cohesive surface model. The stress enhancement is based only on smaller length scale results and does not include any phenomenological laws.

Strain gradients play a vital role in fatigue crack predictions (Brinckmann and Siegmund, 2006) as they do in conventional fracture (Huang et al., 1999; Chen et al., 1999). These strain gradients together with conventional strains give rise to an accumulation of dislocations in the proximity of the crack tip.

Discrete dislocation simulations of fatigue crack propagation (Cleveringa et al., 2000; Deshpande et al., 2001, 2002) capture the physical behavior at the crack tip but are computationally costly, limiting the dimension of the analyzed structure to a few micrometers and the number of load cycles to a few tenths. However, real engineering structures are significantly larger. Therefore, we choose a continuum model to simulate fatigue crack growth. There are a number of strain gradient models (e.g. Dillon and Kratochvil, 1970; Fleck and Hutchinson, 1993; Shu and Fleck, 1999; Gao et al., 1999; Gurtin, 2000, 2002, 2004; Menzel and Steinmann, 2000; Garikipati, 2003; Wen et al., 2005; Clayton et al., 2004; Huang et al., 2004 and Brinckmann et al., 2006) which captured the effects that strain gradients play in the vicinity of a propagating fatigue crack.

Since the dislocation density based strain gradient model (Brinckmann et al., 2006) yields the density of statistically stored and geometrically necessary dislocations, we employ that model to determine crack propagation. In the present model both dislocation types, i.e. geometrically necessary and statistically stored, contribute equally to the stress enhancement.

In this chapter we present a novel approach to the simulation of fatigue crack growth in metals by the use of a cohesive zone model. This cohesive zone model accounts for the action of dislocation in material separation. Fatigue simulations are

carried out and crack growth, closure, dislocation density and overload are discussed. The study is closed by a summary and conclusions.

8.2 Material Model

To simulate fatigue crack propagation, we employ the dislocation density based strain gradient model (DDSG) by Brinckmann et al. (2006) as outlined in Chapter 6. Figure 8.1 depicts the main ideas on the dislocation model.

8.3 Cohesive Surface Model

We couple material separation and tractions across the evolving crack front, using the cohesive surface model of Xu and Needleman (1994), which is based on the Universal Binding Law of Rose et al. (1981).

Each dislocation shields the crack tip by its motion, thereby preventing elastic stress singularities due to the geometric singularity at an infinitely sharp crack tip. This dislocation motion restricts the maximal attainable stress by the plastic yield stress. However, each dislocation carries its individual stress singularity which leads to a local stress increase in the proximity of the individual dislocation. Depending on the distance of a dislocation from the crack tip, either function can dominate: if the dislocation is close, it leads to a stress increase and vice versa.

During deformation dislocations evolve; some of whom get trapped in the proximity of the crack tip. These dislocations then form clusters. We extend the cohesive surface model to include traction contributions from dislocation clusters. The total traction T across the cohesive zone is the sum of the elastic contribution which is bound by the yield stress due to dislocation shielding T_{rmds} and a contribution arising from dislocation clustering T_{dc}, as shown in Figure 8.2. The former part is calculated as the tractions across a surface using conventional continuum mechanics equations.

The stress arising from the dislocation clusters is derived from the equations for a single dislocation (Hirth and Lothe, 1968) which are superposed to account for the dislocation distribution:

$$T_{cd} = \sum_{disl} T_i = \sum_{disl} f_C f(\Theta) \frac{1}{r} = \int f_C f(\Theta) \frac{1}{r} \rho_{disl} \, dA \tag{8.1}$$

where $f_C = \frac{Gb}{2\pi(1-v)}$. G is the shear modulus, b is the Burger's vector and v Poisson's ratio. Θ is the angle between the Burger's vector of the discrete dislocation and the point of interest. Since this continuum model, i.e. strain gradient model, does not include dislocation orientations, we find $\Theta = const \rightarrow f(\Theta) = const$. r is the distance of the dislocation to the point of interest.

We express the traction in the continuum material T_{cont} as function of the distribution of the accumulated dislocation density. To this end, at failure the following equation is given:

$$T = T_{ds} + T_{dc} \overset{!}{=} \sigma_{max,0} \quad \Rightarrow \quad T_{cont} = T_{ds} = (1 - E_\sigma)\sigma_{max,0} \tag{8.2}$$

where T_{dc} is expressed as $T_{dc} = E_\sigma \sigma_{max,0}$. E_σ is a stress enhancement factor and it is calculated, following equation (8.1), as

$$E_\sigma = \frac{\int f_C f(\Theta) \frac{1}{r} \rho_{disl} \, dA}{\sum_{DD,disl} f_C f(\Theta) \frac{1}{r}} = \frac{\int \frac{1}{r} \rho_{disl} \, dA}{\sum_{DD,disl} \frac{1}{r}} \tag{8.3}$$

where the denominator is calculated from the discrete dislocation (DD) results3of Cleveringa et al. (2000) for monotonic fracture. (Monotonic fracture and fatigue require the same stress at the crack tip because the strength of the atomic-bond is a material property which does not depend on the loading condition, i.e. monotonic loading or cyclic loading.) The stress enhancement factor E_σ will take values in the interval $[0-1]$. With these equations the boundary value problems in fatigue simulations can be evaluated.

8.4 Problem Formulation

In the present work we study the propagation of fatigue cracks in an infinitely large elastic-plastic solid. We approximate this configuration by a symmetric plane-strain modified boundary layer model shown in Figure 8.3. The elastic-plastic material has a radius of $100\mu m$. The maximum crack extension, i.e. the length of the row of cohesive surface elements in front of the initial crack tip, is $6.66\mu m$. This length is much smaller than the radius of the outer perimeter of the material.

We execute an incremental forward Euler time integration. The Young's modulus is $E = 200\text{GPa}$, the shear modulus $\mu = 77\text{GPa}$. We employ isotropic hardening and the initial yield strength is $\sigma_{y,0} = 250\text{MPa}$. The Burgers vector is $b = 0.25\text{nm}$ and the Taylor coefficient $\alpha = 0.3$. We assume $l_* = 2.5\mu m = 10000b$, which is motivated by the experimental findings of (Mughrabi, 1983) and a study by Brinckmann and Siegmund (2006). $\sum_{DD,disl}\frac{1}{r} = 5831/\mu m$ was determined from the discrete dislocation distribution for monotonic loading (Cleveringa, et al., 2000). The cohesive surface has an initial strength of $\sigma_{max,0} = 10\text{GPa}$ and a characteristic separation $\delta_n = 1\text{nm}$. (See Brinckmann and Siegmund (2006) for a discussion of length scales).

In this study we employ a quasi-static numerical framework because we focus on slow moving cracks. Therefore, we will concentrate on applied energy release rates which are at or slightly above the threshold for fatigue crack propagation. At higher applied energy release rates, the crack velocity is of such magnitude that the crack tip is not slow moving and that inertia terms should be included. The maximum prescribed energy release rate is $G_{max} = 0.25\Phi_{n,0}$, where $\Phi_{n,0}$ is the initial cohesive energy, as defined above. The energy release rate enters the simulation through the displacement boundary conditions at the outer perimeter. These displacements are given by the singular solution for an infinitely sharp mode I crack and the magnitude of these displacements is scaled by a sinusoidal function with $R = u_{min}/u_{max} = 0.1$.

The plastic zone size in a solid with the given material parameters and under given loading conditions is identical to the plastic zone size in a previous study by Brinckmann and Siegmund (2006). This size is much smaller than the radius of the

outer perimeter of the elastic-plastic solid. This leads to the applied energy release rate being constant, i.e. independent of the crack extension, in this configuration.

Under the specified loading condition the maximum tractions across the cohesive surfaces are below the strength of the material $\sigma_{max,0}$ in the first load cycle. Without stress enhancement due to dislocation clusters, the tractions would never exceed the cohesive surface strength and the model would shakedown, i.e. predict an infinite fatigue life.

8.5 Results and Discussion

Firstly, we concentrate on the dislocation densities for an applied stress intensity factor range $\Delta K = 0.904 \text{MPa}\sqrt{\text{m}}$. The dislocation density distribution, shown in Figure 8.4, reveals that the density of geometrically necessary dislocations is orders of magnitude larger than that of statistically stored dislocations. Brinckmann and Siegmund (2006) reported higher densities of geometrically necessary dislocation compared to statistically stored dislocations in fatigue simulations using the Roe and Siegmund (2003) cohesive surface evolution rule. However, this study predicts significantly more localized dislocation densities. Atomic lattice curvature, i.e. crack tip blunting, leads to strain gradients and therefore geometrically necessary dislocations. The blunting at the initial crack tip leads to a high density of geometrically necessary dislocations. The crack tip blunting in the steady state regime is much lower than the blunting at the initial crack tip leading to a lower geometrically necessary dislocation density in the steady state regime.

The maximum of the statistically stored dislocations is found at some distance from the crack surface, while the maximum of geometrically necessary dislocations is at the crack surface.

Brinckmann and Siegmund (2006) reported distinct patterns for the rate in dislocation density during loading and unloading using the Roe and Siegmund (2003) cohesive surface evolution rule. No patterns were observed using the present model. The rate of statistically stored dislocation density has its maximum at a distance from the crack tip during loading and unloading and decays from that point in all

directions. The rate of geometrical necessary dislocation density is maximal at the crack tip and decays asymptotically.

The asymptotic decay of the accumulated total dislocation density, i.e. sum of statistically stored and geometrically necessary dislocations, for the fatigue simulation presented here is compared to discrete dislocation simulations for monotonic crack growth of Cleveringa, et al. (2000) in Figure 8.5.

The discrete dislocation simulation predicts significantly lower dislocation densities in the immediate proximity of the crack. In discrete dislocation simulations, dislocations experience a so-called image force which pulls the dislocations out of the solid at the crack surface. This leads to a lower dislocation density. This image force is not taken into account in the present model, which therefore predicts a higher density.

In the first cycle the crack advances significantly, as shown in Figure 8.6. In later cycles, the crack advance is slower, reaching its steady state value after 11 cycles. In the insert of Figure 8.6 two regimes of crack growth are distinguishable. During the initial duration of the loading phase (14.00 − 14.35 cycles) the crack extension remains constant. The crack advances only during the final duration of the loading phase (14.35 − 14.50 cycles). This advance is very rapidly. Once the applied energy has reached its maximum (14.50 cycles) the crack growth stops. During the last duration of the compressive phase (14.75 − 15.00 cycles) the crack advances again, as the crack surfaces get into contact. This advance however is smaller than the advance during the loading phase. When increasing the applied energy release rate the general behavior of alternating periods of crack growth and crack arrest remains the same; only the amount of crack growth during the final duration of the loading phase increases. Using discrete dislocation simulations (Deshpande, et al., 2001) report a similar accelerated crack growth during the final stage of loading while during most of the cycle the crack arrests.

After ~ 50 cycles the crack growth rate changes into a second state and the crack accelerates by a factor of two. As shown above, in the wake of the propagating crack tip a plastically hardened boundary layer remains. Brinckmann and Siegmund (2006) have shown that a strong plastically hardened material leads to faster fatigue crack growth than a material with a low plastic hardening. In the present problem, this

boundary layer stiffens the material leading to an accelerated crack growth if the effect of the boundary layer comes into effect, as observed in above figure. However, free surface forces which act on dislocations, i.e. image forces, would prevent the retention of the high number of dislocations and the plastically hardened material close to the crack surface. These free surface forces are not included in the present model. To that end, we neglect in the remainder of the discussion the domain of increased fatigue crack growth rate which occurs for long crack extensions.

The profile of the crack surfaces is shown in Figure 8.7 for the 19th cycle. During this period the crack tip had, on average, advanced $0.54\mu m$ from its initial crack tip (see Figure 8.6). The crack surfaces in the wake of the crack tip and in the proximity of the crack tip are in contact at minimum applied stress intensity factor. However, ahead of the crack tip the crack surfaces are separated. The opening increases during the first half of the cycle and subsequently decreases during the compressive phase of the applied energy release rate (AERR).

Notice the profiles at median AERR are significantly different during loading and unloading. The separation during the loading stage is smaller than at the corresponding time during unloading phase. During loading phase, even at the median AERR the crack is still closed in the wake of the crack tip. Subsequent increase in AERR leads to a significant increase in the opening. During this final phase of loading also the increase in dislocation density and the crack advance are maximal.

The steady state crack growth rates of different stress intensity factor ranges are given in a double-logarithmic plot in Figure 8.8. The simulations predict that the threshold of the stress intensity factor range is $0.89 MPa\sqrt{m}$. Below that value crack propagation is essentially zero. Stress intensity factor ranges above the threshold lead to a gradual increase in crack growth rate. The simulations predict a Paris-law exponent of 4, which agrees to the values determined for metals (Elber, 1971).

Quasi-static approach. (Tvergaard and Hutchinson, 1996) employ a special method to control nodal displacements to stabilize the simulation. Viscous damping would be another means to reach more stability. However, these methods alter the results and are therefore not used in the present study. However, this model predicts a threshold which is 5 times lower than the values determined by those experiments. Better agreement with experimental results can possibly be achieved if $\sum_{DD,dist} \frac{1}{r}$ is

based on experimental in-situ observations and not discrete dislocation simulations as in the present study. However, the predicted fatigue crack growth rate at the threshold is identical to the experimental findings.

Tvergaard and Hutchinson (1996) reported that their results are mesh-size depended. Similarly, in this study the mesh-size, i.e. the distance between the integration point and the cohesive surface, has been introduced as material-length. The singular dislocation density, shown in Figure 8.5, leads to increasing stress enhancement factors if the mesh-size is refined. An identical approach would be the introduction of a cut-off length for r in equation 8.3 on the lower end. Such a cut-off length is also employed in the discrete dislocation approach of Cleveringa, et al. (2000) and Deshpande, et al. (2001, 2002). The introduction of a length scale, either cut-off length or mesh-size, is acceptable since the proposed continuum model breaks down in areas with strong-discontinuities in the atomic structure such as the crack-tip area. ich influences significantly the crack tip zone through the geometrically necessary dislocations. Therefore, in this case the Paris-law exponent decreases. Vice versa, if the length-scale decreases, the Paris-law exponent increases. Therefore, the mesh-size can be considered a material parameter which determines the Paris-law exponent m at a distant away from the crack surface.

Figure 8.9 shows a simulation with overload. The initial part of the curve is identical to a simulation without overload. During the overload in cycle 18 the crack advances significantly. Subsequently, the crack velocity decreases substantially to a tenth of its initial velocity. Finally, the crack growth rate increases again and reaches the same final fatigue crack growth rate as without the overload. The discrete dislocation analysis for fatigue of Deshpande, et al. (2001) finds that an 8% overload leads to significant crack retardation, which supports the present findings. Furthermore, Elber (1971) reports that the retarded fatigue crack growth rates are observed for more than 200 post-overload cycles. The present study predicts this value, as the post-overload retardation is observed from the ~ 25 th to the ~ 300 th cycle.

The evolution of the traction – separation behavior of a cohesive surface in the steady state regime of the fatigue crack propagation is shown in Figure 8.10(a). Initially the behavior follows the prescribed traction – separation curve, i.e. initial stiffness, of the virgin material. The stiffness of the cohesive behavior decreases as

dislocations accumulate throughout the following cycles. Afterwards, the reduced strength of the cohesive surface is reached and the tractions decrease. Finally the stress enhancement factor reaches 1 and the traction – separation curve is constant at zero. This evolution of the traction separation curve has previously reported by Wang and Siegmund (2005) for conventional plasticity and the cohesive surface law of (Roe and Siegmund, 2003).

During the overload cycle the traction – separation follows the same envelope as during the steady state regime, as shown in Figure 8.10. However, the decrease in stiffness, i.e. the accumulation of dislocations, is significantly increased during the overload cycle. Wang and Siegmund (2005) had reported a significantly different envelope of the curve during the overload. In their model, damage accumulation is not as significantly elevated during the overload as the stress enhancement in the present model. When compared to the present study, the decreased damage accumulation in the model used by Wang and Siegmund (2005) leads to a higher stiffness and therefore higher tractions. These higher tractions lead to a larger envelope during the overload cycle. In the present model this change in envelope is not present.

Figure 8.11 shows the dislocation density distribution for the simulation with an overload cycle. The initial crack tip is at the position marked by 'A'. The current crack tip is defined as that position for which all cohesive surface elements to the left-hand side have failed, i.e. $E_\sigma = 1$. During the initial cycle the dislocation density increases locally and the crack extends. The crack reaches its steady state growth regime as the crack tip approaches 'B'. From this point the dislocation density is evenly distributed along the crack until the crack tip reaches point 'C', i.e. the end of the steady state growth regime,. As the crack tip reaches point 'D', the maximum load of the overload cycle is reached. This overload leads to an increase in the local dislocation density. The density elevation of geometrically necessary dislocations is similar to the elevation at the initial crack tip. However, the elevation of statistically stored dislocations is less than the initial elevation. It can be concluded that the overload as a stronger effect on strain gradients and therefore geometrically necessary dislocations than it has on strains and statistically stored dislocations.

The fatigue crack growth rate decreases once the crack tip has reached the point 'E' and has left the area of elevated dislocation density due to the overload.

However, the long-range interaction forces of the dislocations in the area of elevated dislocation density continue to influence the crack propagation behavior. These long-range interaction forces have decreased the strength, and therefore the stiffness according to $K \sim \sigma_{max}$, during the overload at cohesive surfaces far ahead into the material. This reduced stiffness in the cohesive surfaces leads to reduced strain gradients and therefore a reduced 'production' of new geometrically necessary dislocations along the crack. The reduced dislocation accumulation leads to the slower fatigue crack growth rate after the overload cycle.

The cohesive surfaces to the right-hand side of point 'F' were not sufficiently influenced by the overload, since they are very distant from point 'D'. Therefore they retained their initial stiffness and ability to lead to high strain gradients. These high strain gradients lead to the observed acceleration of the fatigue crack after cycles of retarded crack growth.

8.6 Conclusion

In the present study a cohesive zone evolution model for metallic materials was developed, which is based on the stress fields of dislocations. The stress caused by dislocations is combined with the stress of the continuum model to reach the theoretical strength of the material. The continuum description employs a first order strain gradient model which directly yields the statistically stored and geometrically necessary dislocation density. The characteristic material parameter due to dislocations at fracture is determined from the discrete dislocation simulations of monotonic crack propagation by Cleveringa et al. (2000).

In the present fatigue simulations, the strength of the material is assumed to be $E/20$, which is the theoretical strength of the material. Most fatigue simulations studies employ far lower material strengths (e.g. Tvergaard and Hutchinson, 1996, Deshpande, et al., 2001, 2002 and Brinckmann and Siegmund, 2006 employ $\sim E/100$). This high but physically reasonable material strength leads to small time-steps for large applied stress intensity factor ranges. Numerical stability could be achieved by the use of a dynamic approach or by under-relaxation.

The present model predicts a significant crack growth during the last period of the loading and unloading stage while during most of the cycle the crack propagation is zero. The crack advance during the loading stage is larger than that during the unloading stage. A similar crack growth behavior was reported by Deshpande, et al. (2001).

At the initial crack tip significant crack tip blunting is observed. The crack closes during the compressive stage in the wake and in the immediate proximity of the crack tip with an $R = 0.1$. Far ahead the crack tip, this study predicts no closure.

If the crack has advance for a distant longer than $1\mu m$ the model introduces an artifact. This artifact is due to the lack of including image forces of dislocations into the model. These image forces would lead to a reduction of the dislocation density. However, the present study predicts a high dislocation density which leads to accelerated crack growth if the crack extension is sufficiently long.

The statistically stored dislocation density is two orders of magnitude lower than that of geometrically necessary dislocations. The geometrically necessary dislocations reach its maximum density at the crack surface while the statistically stored dislocations reach the maximum in the proximity to the crack surface. In this study no distinct patterns in the rate of statistically stored and geometrically necessary dislocations during the loading or unloading stage were found. (The previous study of Brinckmann and Siegmund (2006) has revealed such patterns.)

The predicted crack growth rates reveal a threshold in the applied stress intensity factor range, below which no crack growth occurs. Above that threshold the model predicts a power-law crack growth rate. The power-law exponent was predicted to be 4.

Furthermore, the model predicts a significant crack advance during an overload cycle. After the overload cycle the crack is retarded and advances much slower than before the overload for roughly 280 cycles. Afterwards the crack accelerates and reaches same crack growth rate as without the overload. Experimental findings (Elber, 1971) and discrete dislocation simulations (Deshpande, et al., 2001)) support these findings. However, the discrete dislocation simulations cannot predict the post-overload behavior because the number of cycles is computationally not feasible.

Strain gradients play a far more dominant role in overload cases than strains.

During the overload the geometrically necessary dislocations, which occur due to strain gradients, increase more than the statistically stored dislocations, which occur due to strains. During the stage of retarded crack growth after the overload cycle, the reduced production of geometrically necessary dislocations leads to the slow growing fatigue crack. Finally, the fatigue crack growth rate increases again once the local GND density increases.

Concluding, it is possible to simulate fatigue crack growth using the micromechanical based cohesive surface model without phenomenological material laws or parameters. This computationally efficient model predicts local dislocation densities, power-law fatigue crack growth and overload behavior.

(a)

(b)
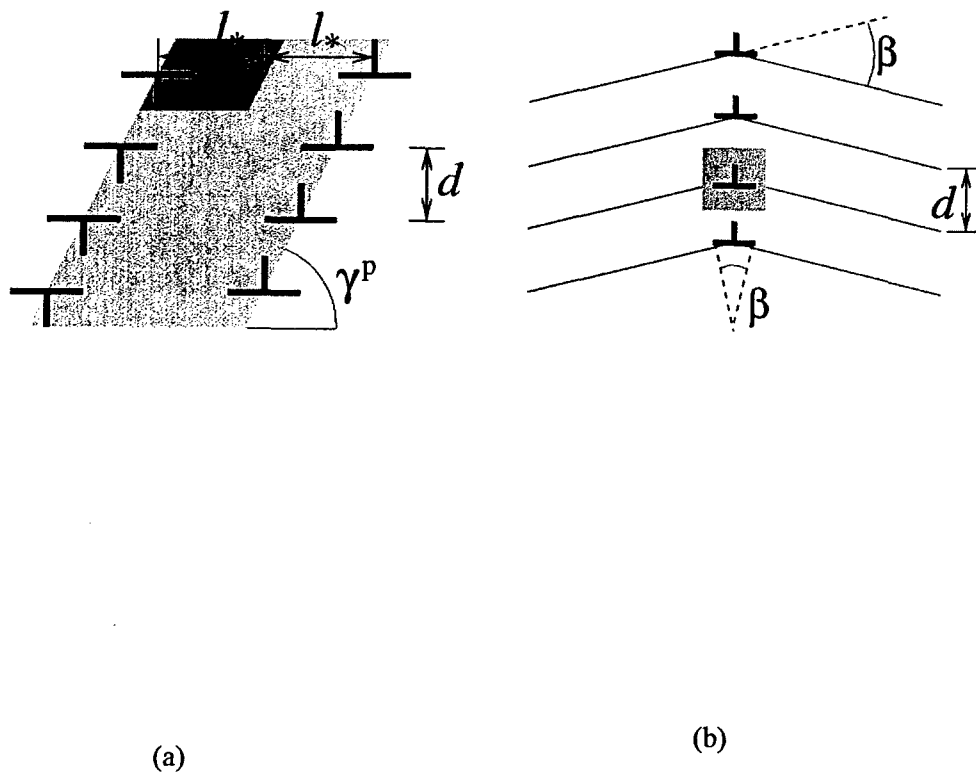
Figure 8.1: Schematic representation of statistically stored (a) and geometrically necessary dislocations (b).
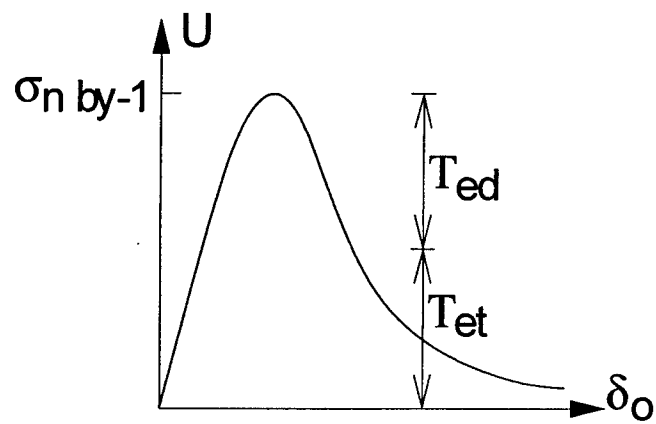
Figure 8.2: Traction across the cohesive surface as sum of the elastic contribution which is bound by the yield stress due to dislocation shielding (ds) and the contribution due to dislocation clustering (dc).

crack

elastic-plastic material

u(t)
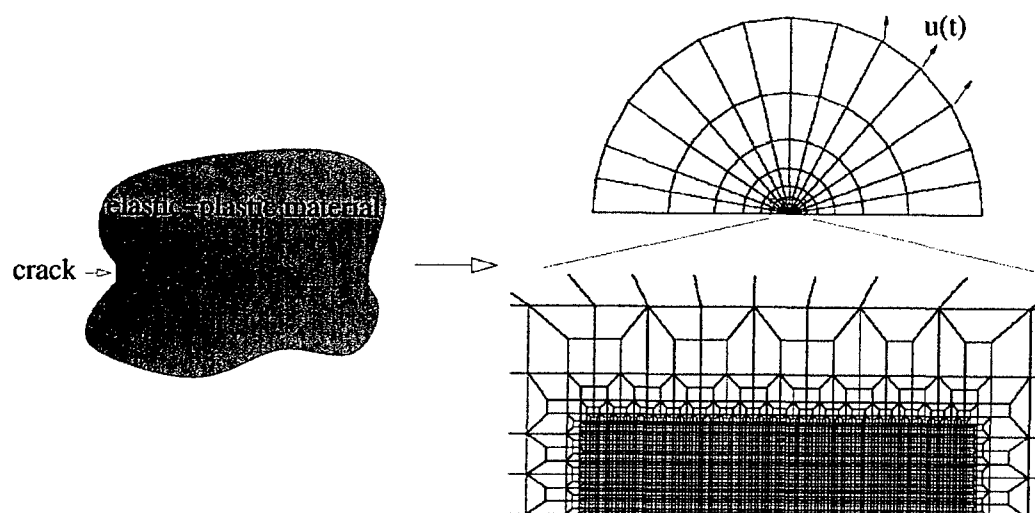
Figure 8.3: Computational system.
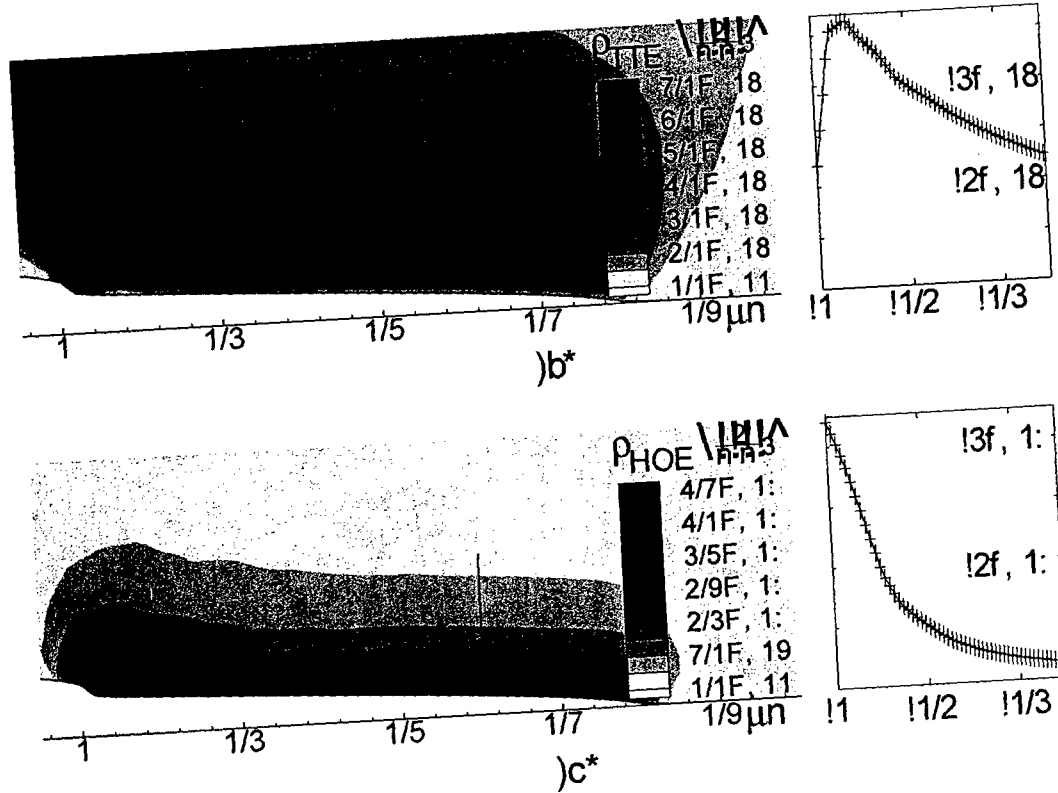
Figure 8.4: Dislocation density distribution of statistically stored dislocations (a) and geometrically necessary dislocations (b) after 18.5 cycles at an applied stress intensity factor range $\Delta K = 0.904 \mathrm{MPa}\sqrt{m}$. On the right-hand side the dislocation distribution along $x = 0.5\mu$m is shown in the undeformed configuration.
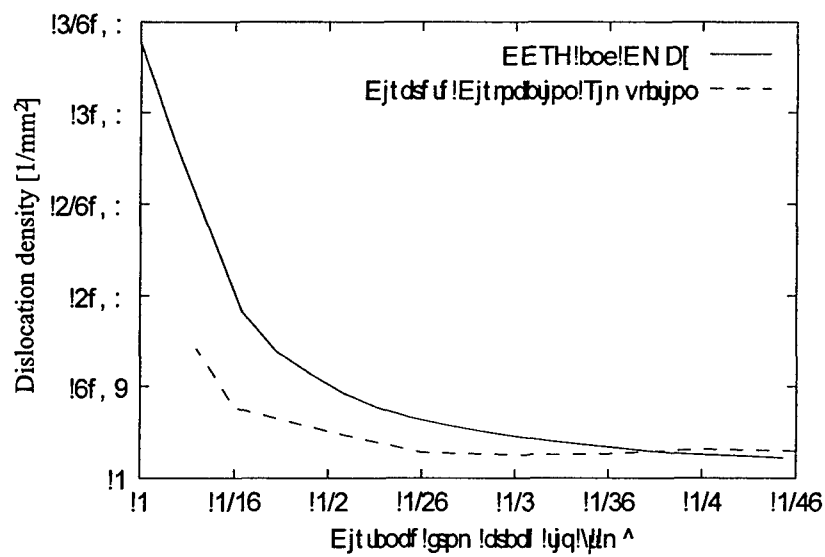
Figure 8.5: Dislocation density perpendicular to crack growth direction predicted by the present model for fatigue loading compared to discrete dislocation dynamic results for monotonic loading.
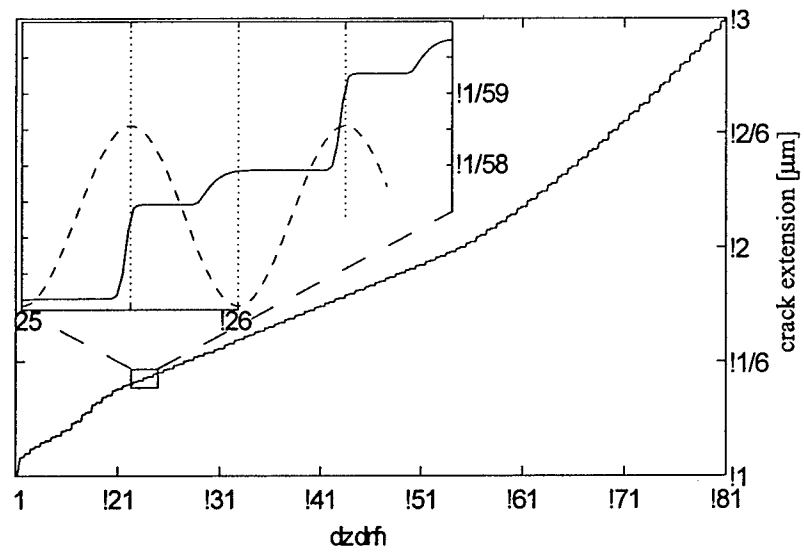
Figure 8.6: Crack extension as a function of load cycle for an applied stress intensity factor range $\Delta K = 0.904\,\mathrm{MPa}\sqrt{\mathrm{m}}$. The insert depicts a zoom of the crack propagation during the 14th and 15th cycle.
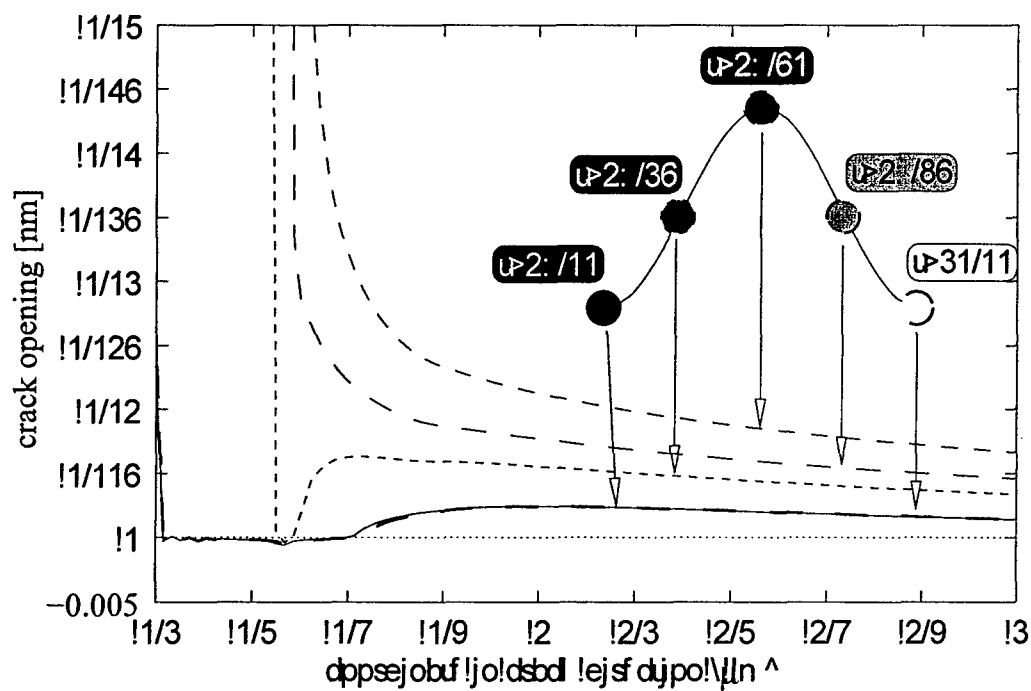
Figure 8.7: Profiles of crack surface at five instances (minimum AERR (t=18.00 cycle), median AERR during loading (t=18.25 cycle), maximum AERR (t=18.50 cycle), median AERR during unloading (t=18.75 cycle), minimum AERR (t=19.00 cycle)). The average crack extension from the initial crack tip is $0.54\mu m$ during the 19th cycle. The stress intensity factor range is $\Delta K = 0.904 MPa\sqrt{m}$ and $R = 0.1$. [AERR = applied energy release rate.]
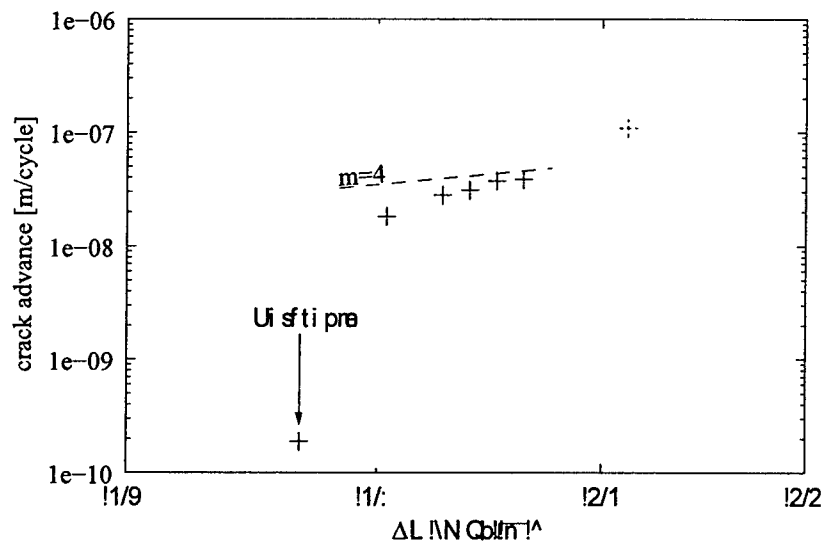
Figure 8.8: Steady state crack growth rate depending on the applied stress intensity factor range in a double-logarithmic plot. The data point at $\Delta K = 1.01 \mathrm{MPa}\sqrt{\mathrm{m}}$ was obtained from an unstable simulation.
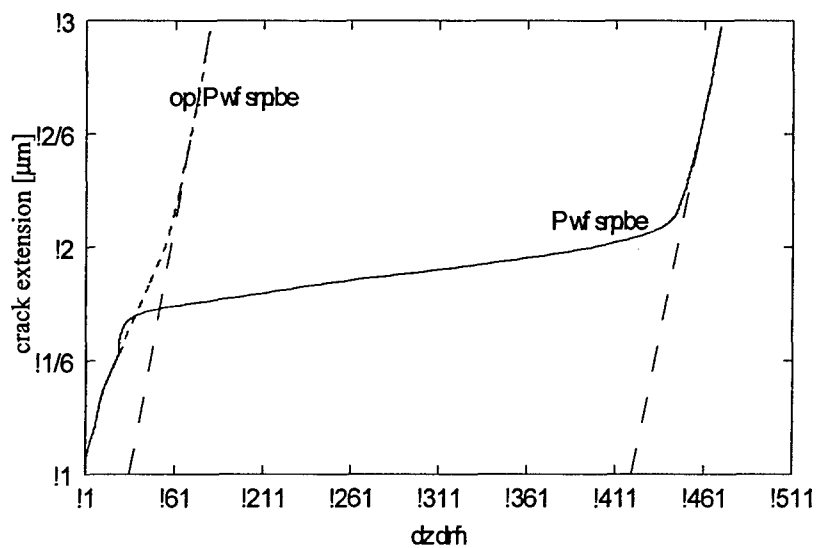
Figure 8.9: Simulation with $\Delta K = 0.904\mathrm{MPa}\sqrt{m}$ applied stress intensity factor range and a 5% overload during the 18th cycle. The crack extension for the case without overload is shown with dashed lines.
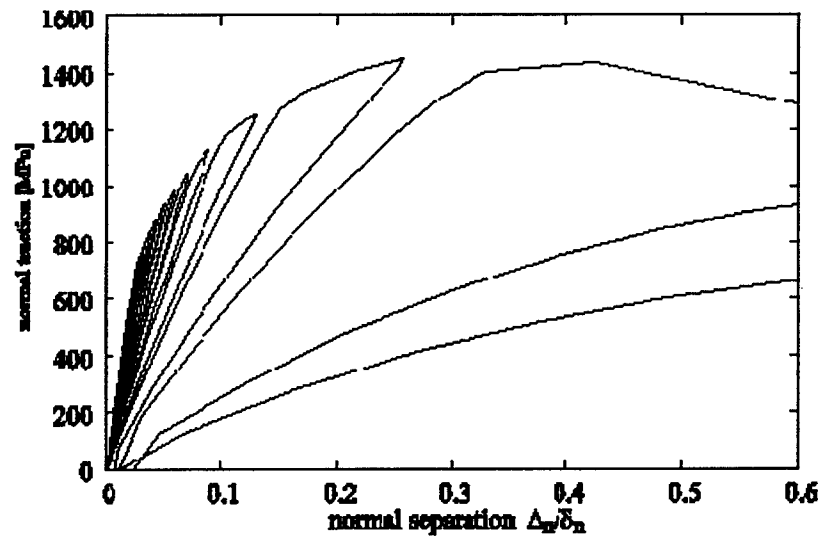
(a)
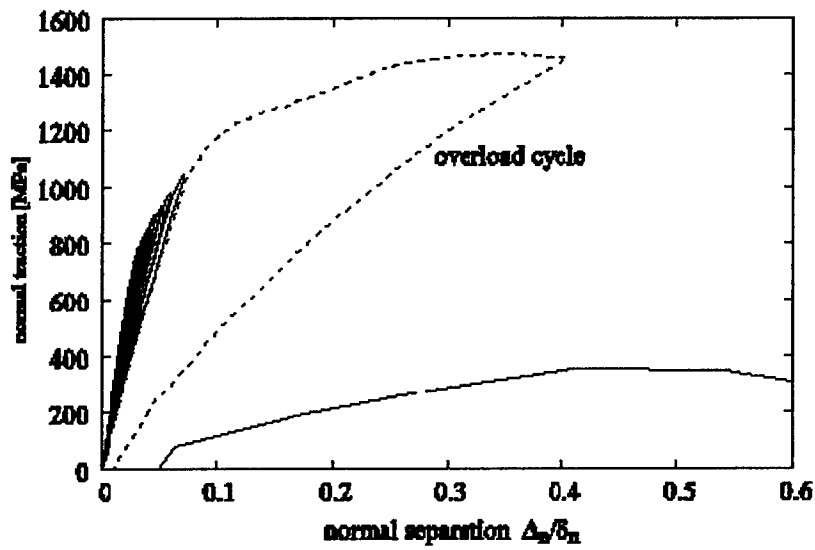
(b)

Figure 8.10: Evolution of traction – separation curve as the stress enhancement accumulates for cohesive surface in the steady state regime (a) and with the influence of the overload (b).
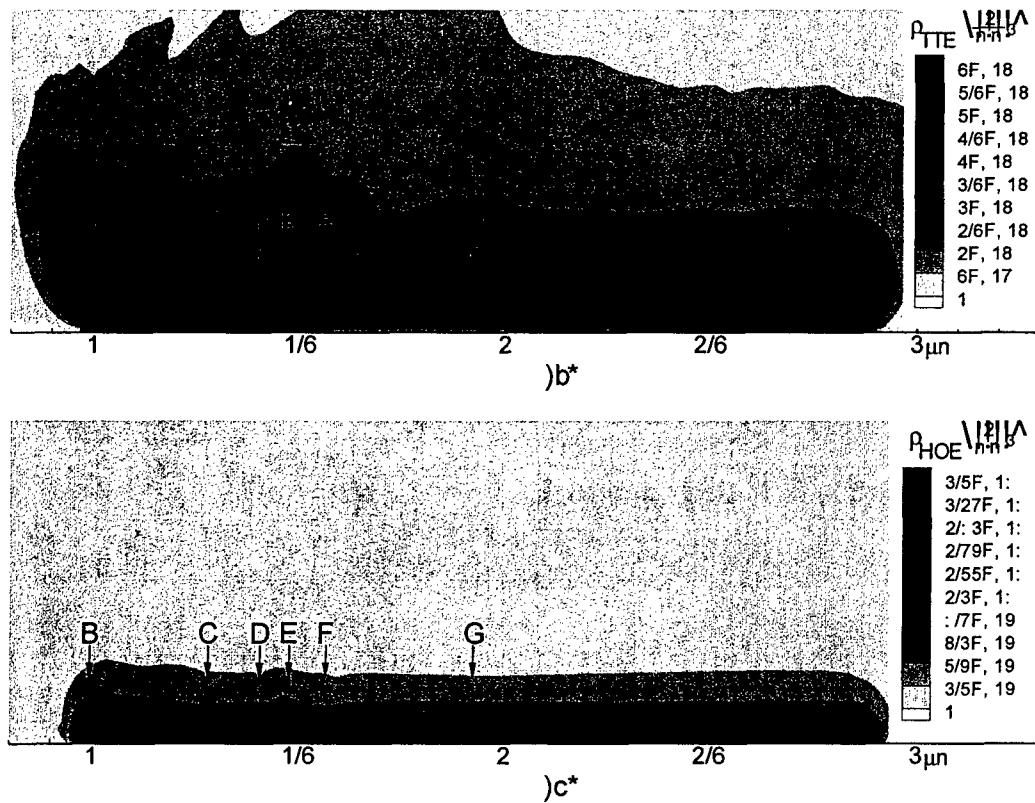
Figure 8.11: Dislocation density distribution of statistically stored dislocations (a) and geometrically necessary dislocations (b) after 359 cycles at an applied stress intensity factor range $\Delta K = 0.904 \text{MPa}\sqrt{m}$ with an overload at 18 cycles. The current crack tip in the initial position A, at the beginning of the steady state regime B, the end of the steady state regime C, at the overload D, at the beginning of the slow growth regime E and end of the slow growth regime F.

LIST OF REFERENCES

Brinckmann, S., Siegmund, T., Huang, Y., 2006. A Dislocation Density based Strain Gradient Model. *Int. J. Plasticity* 22, 1784-1797.

Brinckmann, S. and Siegmund, T., 2006. On the influence of strain gradients on fatigue crack propagation predictions. (submitted).

Chen, J.Y., Wei, Y., Huang, Y., Hutchinson, J.W., Hwang, K.C., 1999. The crack tip fields in strain gradient plasticity: the asymptotic and numerical analyses. *Eng. Fract. Mech.* 64, 625-648.

Clayton, J.D., McDowell, D.L., Bammann, D.J., 2004. A multiscale gradient theory for elastovisco-plasticity of single crystals. *Int. J. Eng. Sci.* 42, 427-457.

Cleveringa, H.H.M., Van der Giessen, E., Needleman, A., 2000. A discrete dislocation analysis of mode I crack growth. *J. Mech. Phys. Solids* 48, 1133-1157. .

Deshpande, V.S., Needleman, A., Van der Giessen, E., 2002. Discrete dislocation modelling of fatigue crack propagation. *Acta Mater.* 50, 831-846.

Deshpande, V.S., Needleman, A., Van der Giessen, E., 2001. A discrete dislocation analysis of near-threshold fatigue crack growth. *Acta Mater.* 49, 3189-3203.

Dillon, O.W., Kratochvil, J., 1970. A strain gradient theory of plasticity. *Int. J. Solid Struct.* 6, 1513-1533.

Elber, W., 1971. The significance of fatigue crack closure. in: Damage tolerance in aircraft structures. ASTM STP 486, 230-242 .

Fleck, N.A., Hutchinson, J.W., 1993. A phenomenological theory for strain gradient effects in plasticity. *J. Mech. Phys. Solids* 41, 1825-1857.

Gao, H., Huang, Y., Nix, W.D., Hutchinson, J.W., 1999. Mechanism-based strain gradient plasticity– I. Theory. *J. Mech. Phys. Solids* 47, 1239-1263.

Garikipati, K., 2003. Couple stresses in crystalline solids: origins from plastic slip gradients, dislocation core distortions, and three-body interatomic potentials. *J. Mech. Phys. Solids 51*, 1189-1214.

Gurtin, M.E., 2000. On the plasticity of single crystals: free energy, microforces, plastic strain gradients. *J. Mech. Phys. Solids* 48, 989-1036.

Gurtin, M.E., 2002. A gradient theory of single-crystal viscoplasticity that accounts for geometrically necessary dislocations. *J. Mech. Phys. Solids* 50, 5-32.

Gurtin, M.E., 2004. On a framework for small-deformation viscoplasticity: free energy, microforces, strain gradients. Int. J. Plasticity 19, 47-90.

Hirth, J.P. and Lothe, J., 1968. Theory of dislocations. New York: McGraw-Hill.

Huang, Y., Chen, J.Y., Guo, T.F., Zhang, L., Hwang, K.C., 1999. Analytic and numerical studies on mode I and mode II fracture in elastic-plastic materials with strain gradient effects. *Int. J. Fracture* 100, 1-27.

Huang, Y., Qu, S., Hwang, K.C., Li, M., Gao, H., 2004. A conventional theory of mechanism-based strain gradient plasticity. *Int. J. Plasticity* 20, 753-782.

Menzel, A., Steinmann, P., 2000. On the continuum formulation of higher gradient plasticity for single and polycrystals. *J. Mech. Phys. Solids* 48, 1777-1796.

Mughrabi, H., 1983. Dislocation wall and cell structures and long-range internal stresses in deformed metal crystals. *Acta Metall.* 31, 1367-1379.

Mughrabi, H., 2004. On the current understanding of strain gradient plasticity. *Mater. Sci. Eng.* A 387-389, 209-213.

Nguyen, O., Repetto, E.A., Ortiz, M., Radovitzky, R.A., 2001. A cohesive model of fatigue crack growth. *Int. J. Fract.* 110, 351-369.

Rice, J.R., 1967. The Mechanics of Crack Tip Deformation and Extension by Fatigue. Special Technical Publication 415, ASTM 247-311.

Ritchie, R.O., Dauskardt, R.H., 1991. Cyclic fatigue of Ceramics: A fracture mechanics approach to subcritical crack growth and life prediction. *J. Ceramic Society of Japan* 99; 1047-1062.

Roe, K.L., Siegmund, T., 2003. An irreversible cohesive zone model for interface fatigue crack growth simulation. *Eng. Frac. Mech.* 70, 209-232.

Rose, J.H., Ferrante, J. and Smith, J.R., 1981. Universal binding energy curves for metals and bimetallic interfaces. *Phys. Rev. Lett.* 47, 675 - 678,

Shu, J.Y., Fleck, N.A., 1998. The prediction of a size effect in micro-indentation. *Int. J. Solids Structures* 35, 1363-1383.

Shu, J.Y., Fleck, N.A., 1999. Strain gradient crystal plasticity: size-dependent deformation of bicrystals. *J. Mech. Phys. Solids* 47, 297-324.

Stolken, J.S., Evans A.G., 1998. A microbend test method for measuring the plasticity length scale. *Acta Mater.* 46, 5109-5115.

Tvergaard, V., Hutchinson, J.W., 1996. Effect of Strain-dependent Cohesive Zone Model on Predictions of Crack Growth Resistance, *Int. J. Solids Structures* 33, 3297-3308.

Wang, B., Siegmund, T., 2005. A numerical analysis of constraint effects in fatigue crack growth by use of an irreversible cohesive zone model. Int. J. Fract. 132, 175-196.

Wen, J., Huang, Y., Hwang, K.C., Liu, C., Li, M., 2005. The modified Gurson model accounting for the void size effect. Int. J. Plasticity 21, 381-395.

Xu, X.P. and Needleman, A., 1994. Numerical simulations of fast crack growth in

brittle solids. *J. Mech. Phys. Solids* 42, 1397-1434.

9. A MODIFIED 4-POINT BEND DELAMINATION TEST

The 4-point bend delamination test has been used as the preferred method to measure interface properties of semiconductor devices. Since Charalambides et al. (1989, 1990) initially proposed the 4-point bend delamination test, it has been widely used to determine the mixed mode fracture resistance of bimaterial interfaces (e.g., Charalambides 1989, 1990; Ma et al., 1995, 1997; Klingbeil and Beuth, 1997; Zou et al., 2004). It was also used to investigate the time dependent subcritical debonding of multi-layer interconnect structures (Ma et al., 1997). Recently, the 4-point bend delamination test was used to quantitatively measure the interfacial fracture resistance and crack velocity of interfaces in thin film structures under the consideration of different metal layer thickness values (Phillipps et al., 1993; Ma, 1997; Dauskardt et al., 1998; Lane et al., 2000a, 2000b; Hugh et al., 2004).

In a conventional 4-point bend delamination test, interface cracks are assumed to propagate along both sides symmetrically, or only the first growing crack is considered. The steady-state strain energy release rate is then calculated based on the assumptions of symmetrical crack propagation. Experimental results indicate, however, that cracks rarely grow symmetrically along the interface, due to slight asymmetry in specimen or loading condition. In most of the cases, this asymmetry is inevitable. While this is acceptable for fracture toughness testing – with the information of the second crack lost – such a situation is no longer acceptable for fatigue testing.

In order to use the second crack information for fracture toughness testing and to obtain symmetrical crack growth for fatigue testing, a modified 4-point bend delamination test is reported. The goal of this chapter is to provide a methodology for fracture toughness and fatigue testing by using a modified 4-point bend delamination test.

At first, equations for the steady-state strain energy release rate for asymmetrical crack configuration are derived based on classical beam theory. Then, designs for an articulated 4-point bend fixture are provided. Fracture toughness and fatigue tests conducted with the articulated fixture are described and analyzed.

9.1 Theory

Generally, the equation used to calculate the strain energy release rate in the conventional 4-point bend delamination test are based on assumption of a symmetrical crack configuration. Experimental results, see e.g. (Ma, 1997) and also the experiments presented in this work, however, indicate that crack rarely grow symmetrically along the interface. One of the possible reasons is that, at least for very stiff specimens, even very small shape distortions (~100µm) can cause significant loading asymmetries, which in turn affect the load at which crack propagation occurs (Phillipps et al., 1993). The presence of imperfect precracks can also result in the asymmetrical crack propagation. In fracture toughness test conducted by use of the conventional 4-point bend delamination test, one crack will propagate first and arrest at the inner roller. In a rigid fixture, due to the subsequent unbalanced load condition, the other crack will not propagate even after a further load increase. In an articulated fixture that compensates the unbalanced load makes it possible to propagate the second crack along the interface. To be able to use this approach equations for the calculation of the strain energy release rate under the asymmetrical crack configuration need to be derived.

Figure 9.1(a) shows loading conditions and dimensions of the 4-point bend delamination sample with crack lengths of a_1 and a_2. In general $a_1 \neq a_2$ with the left and right crack tip located at point G and F, respectively. Following Euler-Bernoulli beam analysis of this 4-point bend sample, the energy release rate under this asymmetrical crack configuration can be calculated by using the equation given by Hutchinson and Suo (1992). There, in section III. B. 4, an interfacial crack in a bilayer was analyzed. The

energy release rate for both side cracks need to be calculated. Here, as an example, the loading situation for the right hand side crack was enlarged and shown in Figure 9.1(b). When the crack length exceeds the thickness of the top layer by a factor of two, it can be considered as semi-infinite beam. The strain energy release rate is calculated in close form:

$$G = \frac{1}{2E_2}\left(12\frac{M_1^2}{h_2^3} - \frac{M_2^2}{Ih_1^3}\right) \tag{9.1}$$

where M_1 and M_2 are the internal bending moments per unit width. The dimensionless moment of inertia I is given by the following equation.

$$I = \Sigma\left[\left(\Delta - \frac{1}{\eta}\right)^2 - \left(\Delta - \frac{1}{\eta}\right) + \frac{1}{3}\right] + \frac{\Delta}{\eta}\left(\Delta - \frac{1}{\eta}\right) + \frac{1}{3\eta^3} \tag{9.2}$$

where $\eta = \dfrac{h_1}{h_2}$, $\Sigma = \dfrac{E_1(1-v_2^2)}{E_2(1-v_1^2)}$, $\Delta = \dfrac{1+2\Sigma\eta+\Sigma\eta^2}{2\eta(1+\Sigma\eta)}$

The following beam analysis is carried out to calculate the internal moments M_1 and M_2. At first, the beam is divided into 6 regions which are indicated in Figure 9.1(a). For each region, the functions for internal shear force and bending moment are derived by free body diagram analysis. Then, the deflection curve equations are derived for each region as follows:

$$
\begin{aligned}
E_c I_c v_1''(x) &= -F_3 x \quad (0 \le x \le L) \\
E_c I_c v_2''(x) &= (F_1 - F_3)x - F_1 L \quad (L \le x \le L_2/2 - a_1) \\
E_2 I_2 v_3''(x) &= (F_1 - F_3)x - F_1 L \quad (L_2/2 - a_1 \le x \le L_2/2) \\
E_2 I_2 v_4''(x) &= (F_1 - F_3)x - F_1 L \quad (L_2/2 \le x \le L_2/2 + a_2) \\
E_c I_c v_5''(x) &= (F_1 - F_3)x - F_1 L \quad (L_2/2 + a_2 \le x \le L_2 - L) \\
E_c I_c v_6''(x) &= (F_1 + F_2 - F_3)x - F_1 L - F_2(L + L_1) \quad (L_2 - L \le x \le L_2)
\end{aligned} \tag{9.3}
$$

where E_c and I_c are the Young's modulus and moment of inertia of composite beam. E_2 and I_2 are the Young's modulus and moment of inertia of the bottom layer. $v_i(x)$ represents the deflection of the ith region. The boundary conditions and continuity conditions are:

At point A: $v_1'(L) = v_2'(L), v_1(L) = v_2(L), v_1(L) = v_2(L) = 0$

At point G: $v_2'(L_2/2 - a_1) = v_3'(L_2/2 - a_1), v_2(L_2/2 - a_1) = v_3(L_2/2 - a_1)$

At point E: $v_3'(L_2/2) = v_4'(L_2/2), v_3(L_2/2) = v_4(L_2/2), v_3(L_2/2) = v_4(L_2/2) = 0$

At point F: $v_4'(L_2/2 + a_2) = v_5'(L_2/2 + a_2), v_4(L_2/2 + a_2) = v_5(L_2/2 + a_2)$

At point B: $v_5'(L_2 - L) = v_6'(L_2 - L), v_5(L_2 - L) = v_6(L_2 - L), v_5(L_2 - L) = v_6(L_2 - L) = 0$

Also, based on the free body diagram of the whole beam, we have

$$F_1 + F_2 = F_3 + F_4$$

$$F_1 + F_2 = P$$

$$F_3 L + F_2 L_1 = F_4(L_2 - L)$$

Based on the above beam deflection curve equations and boundary conditions, totally, we have 16 unknowns and 16 equations. By solving these equations, the internal bending moments for the calculation of strain energy release rate can be determined as function of crack lengths a_1 and a_2. The internal bending moments for right side crack (tip at F) can be derived as

$$M_1^R = -\frac{PL}{2b}$$

$$M_2^R = -\frac{PL}{2b}\left(\frac{512\xi + 24(1-\xi)a_2^2 + 192(\xi-1)(a_2 - a_1) + (\xi-1)(a_1^3 + a_2^3)}{512\xi + 12(1-\xi)(a_1^2 + a_2^2) + (\xi-1)(a_1^3 + a_2^3)}\right) \tag{9.4}$$

while for left side crack (tip at G), the internal bending moments are given as

$$M_1^L = -\frac{PL}{2b}$$

$$M_2^L = -\frac{PL}{2b}\left[\frac{512\xi + 24(1-\xi)a_1^2 + 192(\xi-1)(a_1 - a_2) + (\xi-1)(a_1^3 + a_2^3)}{512\xi + 12(1-\xi)(a_1^2 + a_2^2) + (\xi-1)(a_1^3 + a_2^3)}\right] \tag{9.5}$$

where b is the sample width and $\xi = (E_2 I_2)/(E_c I_c)$. Substituting calculated moments into equation (9.1), the strain energy release rate for two crack tips G and F can be calculated.

If the crack propagated along both sides symmetrically, the crack lengths are identical. Substituting $a_1 = a_2$ into the equation (9.4) and (9.5), the sample is subjected to constant moment conditions between the inner roller lines. The strain energy release rate is independent on the crack length. By using equation (9.1), the strain energy release rate can be calculated by using the following equation:

$$G^s = \frac{P^2 L^2}{2E_2 b^2}\left(\frac{3}{h_2^3} - \frac{1}{4Ih_1^3}\right) \tag{9.6}$$

here, G^s represent the strain energy release rate for the symmetrical crack configuration.

Under the asymmetrical crack configuration, i.e., the general case of $a_1 \neq a_2$, the following equations can be used to calculate the strain energy release rate for two crack tips at point of F and G, G^F and G^G.

$$G^F = \frac{P^2 L^2}{2E_2 b^2}\left[\frac{3}{h_2^3} - \frac{1}{4Ih_1^3}\left(\frac{512\xi + 24(1-\xi)a_2^2 + 192(\xi-1)(a_2-a_1) + (\xi-1)(a_1^3+a_2^3)}{512\xi + 12(1-\xi)(a_1^2+a_2^2) + (\xi-1)(a_1^3+a_2^3)}\right)^2\right] \tag{9.7}$$

$$G^G = \frac{P^2 L^2}{2E_2 b^2}\left[\frac{3}{h_2^3} - \frac{1}{4Ih_1^3}\left(\frac{512\xi + 24(1-\xi)a_1^2 + 192(\xi-1)(a_1-a_2) + (\xi-1)(a_1^3+a_2^3)}{512\xi + 12(1-\xi)(a_1^2+a_2^2) + (\xi-1)(a_1^3+a_2^3)}\right)^2\right] \tag{9.8}$$

For fracture toughness testing, the following situations are considered: (a) Initial cracks are symmetrical ($a_1 = a_2$) and both cracks propagated at the same situation. Then, equation (9.6) provides the fracture toughness, provided that the load P is substituted with the critical load P_c; (b) Initial cracks are symmetrical. One crack propagates and arrests at the roller and a first critical load $P_{c,1}$ is recorded. Subsequently, as the load is increased the second crack propagates and a second critical load $P_{c,2}$ is recorded. Two values of the critical strain energy release rate are obtained. One is calculated from equation (9.6) with the load P replaced by the first critical load $P_{c,1}$. The second one is obtained from equation (9.7) with the simplification by use of $a_1 = L_1/2$; (c) If precracking results in two initial crack of different length then the load $P_{c,1}$ inserted into equation (9.8) yields the first value of the critical strain energy release rate and the second one is obtained as described in situation (b).

In Charalambides et al., (1989) the symmetrical crack configuration was assumed and the critical strain energy release rate was expressed in terms of the applied moment M as

$$G = \frac{M^2(1-\nu_2^2)}{2E_2}\left(\frac{1}{I_2} - \frac{\lambda}{I_c}\right) \tag{9.9}$$

223

where $\lambda = \dfrac{E_2\left(1-v_1^2\right)}{E_1\left(1-v_2^2\right)}$, $M = PL/2b$. The moment of inertia I_c and I_2 can be calculated by

$$I_c = \frac{h_1^3}{12} + \frac{\lambda h_2^3}{12} + \frac{\lambda h_1 h_2 \left(h_1 + h_2\right)^2}{4\left(h_1 + \lambda h_2\right)}$$

$$I_2 = \frac{h_2^3}{12}$$

(9.10)

Simplifing equations (9.9) and (9.6) by using the same dimensions as shown in Figure 9.1, the same results for the critical strain energy release rate under symmetrical crack configuration are obtained. The solution provided by Charalambides et al., (1989) is the special case of the general solution of our analysis.

9.2 Experimental Method

9.2.1 Articulated Fixture Design

In a fully articulated 4-point bend fixture both the top and bottom support structures for the rollers are to be free to pivot. This allows the fixture to compensate for any unevenness on the specimen surface. This "floating platen" approach can also correct the unsymmetrical crack propagation by maintaining the symmetrical loading situation. In this study, one such articulated structure is designed. Figure 9.2(a) shows the schematic picture of the assembled articulated 4-point bend fixture. Figure 9.2(b) shows the fixture in use.

Considering the small dimensions of samples of interest in microelectronics and MEMS, a 4-point bending fixture with relatively small dimensions was manufactured. The four steel rollers with diameter of 3mm sit in the slot of bottom and top fixture to support and load the sample. In order to make the rollers to contact the surfaces of the slot without gap, springs were used to hold the rollers in position. The nominal span between the inner and outer roller lines, L_2 and L_1, is equal to 22mm and 16mm,

respectively. It provides longer distance between the inner rollers for the crack propagation under the constant moment. Figure 9.3 show the detail design for this rigid 4-point bending fixture. The corresponding design for articulated structures is shown in Figure 9.4. The designed structure can be called semi-articulated 4-point bend fixtures since only the bottom rollers attached to the rotating pin are free to articulate. It compensates the unevenness on the specimen surface and unbalanced load under asymmetrical crack configuration. The semi-articulated fixture is convenient in the test set-up. Generally, the center of the top and bottom rollers should be aligned. However, in actual situation there is a very small distance (~200μm) between them. This design can minimize such misalignment by adjusting the left and right position screws attached to the bottom fixture. Moreover, the flange is designed on the articulated structure to fix the bottom fixture in position and reduce the misalignment.

9.2.2 Test Set-up and Samples

Experiments were performed using a low-force electrodynamically actuated test-frame (ELF 3200, EnduraTec Inc., Minnetonka, MN, USA). A load cell (Model F717-01, SenSoTec) with the capacity of 450 N was used for the toughness test. A high resolution displacement gauge (Model 3540, Epsilon Technology Corp.) was used to monitor the displacement. Function generation and data acquisition were accomplished by using the WinTest Software (Version 2.50, EnduraTec Inc., Minnetonka, MN, USA). A traveling microscope was used to observe the interface at the location of the initial crack tip during monotonic mechanical loading. A Mitutoyo infinity-corrected long working distance objective with 50x magnification (M plan Apo SL 50x) was used. It provides the resolution power of 0.7μm and the field of view of 180μm x 130μm. An Infinitube[TM] in-line assembly connects this objective to a CCD camera. By utilizing an in-path beam splitter and side-port illumination tube with collimating optics, the Infinitube[TM] in-line assembly provides incident illumination parallel to the optical axis (coaxial). The higher magnification and coaxial illumination allow the visual observation of the crack length. The imaging system is fixed on top of a micro-stage which can provide the movement along X and Y direction with the resolution of 1μm (see Figure 9.5). The light is

provided by the fiber optic illuminator (Stocker & Yale Model 20) and fiber optic light guide (1/4"OD x 72", Edmund Industrial Optics, Barrington, NJ, USA).

The samples used in this study are MEMS relevant multi-layer structure manufactured by standard integrated circuit fabrication processes. Multi-layer thin films were deposited on top of 3 inch <100> silicon wafers. Silicon wafers are $1000 \pm 25 \mu m$ thick, single-side polished, n-type silicon with native SiO_2 of $6000 \overset{o}{A} \pm 5\%$. The Young's modulus of the <100> Si wafer was measured as 112GPa. The Poisson's ratio is 0.28. Figure 9.6 shows a schematic picture of the sample with multi-layer structures. A thin gold layer was deposited as a patch of width 1 mm onto SiO_2. Subsequently TiN is deposited onto the entire wafer, followed by an aluminum layer (0.5 μm or 1.0 μm) and a SiO_2 layer. The Au patch at the center of the sample serves as a weak interface to ensure the deflection of a vertical precrack into the interface. After thin film deposition onto the silicon wafer, a glass wafer was anodically bonded to the silicon wafer. Pyrex #7740 glass wafer of diameter 3 inch and thickness $1000 \mu m$ was used for the anodic bonding. This borosilicate glass possesses a Young's modulus of 60GPa and Poisson's ratio of 0.20. After bonding, specimens were obtained by wafer dicing (nominal dimension of 25.0mm x 2mm x 2mm). A vertical prenotch of $200 \mu m$ width and $940 \mu m$ depth was carefully machined in glass layer.

Three-point bend loading was used to precrack the samples under a concentrated load at the center of the sample. The sample was loaded monotonically under displacement control ($0.3 \mu m/s$) until a vertical precrack occurred starting from the tip of the machined notch. Once the vertical precrack occurred and kinked into the interface, the test was aborted and the sample anloaded to avoid the sample breakage.

After the precracking procedures, the specimens were placed into the articulated 4-point bend fixture to conduct the fracture toughness test. Such test were conducted under displacement control (0.05 $\mu m/s$), with displacement controlled by the internal displacement transducer of the test system. The reading of the displacement from the actuator was verified using the high resolution displacement gauge and was then taken as the measurement.

For fatigue testing, the same set up as the fracture toughness test was used. Due to the small displacement applied during the cyclic loading, typically, the maximum displacement is less than 20 μm, the high resolution displacement gauge was used as the feedback signal. Cyclic loading was conducted under a frequency of 2.0 Hz.

9.3 Results and Analysis

9.3.1 Fracture Toughness

During the fracture toughness test, the applied displacement and the corresponding load values were recorded. Figure 9.7 shows a typical relationship between the load P and displacement u. Figure 9.8 shows images taken at the left and right initial crack tip and the center of the specimen Several regimes are indicated in Figure 9.7 and described as follows: (a) The load increased proportionally to displacement. Figure 9.8 (a) shows that there is no crack propagation in this stage and that the crack opening at the center is very small; (b) Interface delamination occurred along one side and a load plateau is obtained. The crack arrests at the inner roller line. In Figure 9.8 (b), the right side crack propagated while the left side crack did not propagate. This asymmetrical crack growth situation was clearly visible at the specimen center with the right side crack showing a larger opening than the left side; (c) The load again increases proportional to the displacement. Compared to region (a), the compliance of the sample increased due to the previous crack growth event. (d) A second load plateau occurred with corresponds to crack growth along the left side. Figure 9.8 (c) indicates that now the opening of both crack is similar. Both cracks have reached the corresponding inner roller; (e) Under further loading the crack tips either remain stable at the inner roller line or passed the inner roller lines under increasing load. The sample compliance has increased further due to the additional crack growth along the left side. In comparison to the common results from 4-point bend delamination test, Figure 9.7 clearly shows two load plateaus which can be used to calculated two corresponding values of the

fracture toughness values. Two test results can be obtained by using this modified 4-point bend delamination test instead of one test result due to one side interface delamination.

With the articulated fixture, it is also possible to observe symmetric crack growth. This, however, remained a rare event. Among sixteen samples tested, only two samples provided such a scenario. Figure 9.9 shows the recorded the load and displacement for one of such samples (aluminum layer thickness 1 μm). Figure 9.10 shows the interface delamination at the initial crack tip for left, right and center of the prenotch. In Figure 9.9, three data regions are identified as follows: (a) The load increased proportionally to displacement with no crack propagation in this region as indicated by Figure 9.10 (a). (b) Plateau region indicated the steady-state crack growth of the interface. This is also verified by Figure 9.10 (b) where the left and right side crack propagated with the same crack opening. At the center, symmetrical crack opening was clearly shown.

9.3.2 Fatigue Crack Growth

Samples were also tested under cyclic loading to verify there the articulated fixture allows one to obtain symmetrical crack propagation. Transparency of the glass allowed direct observation of the interface through the top of glass. Interface delamination was observed using an optical microscope (Labphot-2, Nikon, Inc.) and a Moticam 2000 digital camera with Advance 3.2 Imaging Software (Motic Instruments, Inc). Before the fatigue test, the initial crack front was observed and the initial crack length was measured. Cyclic loading was conducted with $P_{min} = 3.5$ N, $P_{max} = 10.9$ N for $N = 5.1 \times 10^5$ cycles, and with $P_{min} = 2.9$ N, $P_{max} = 9.2$ N for $N = 5.1 \times 10^5$ cycles. These loads ensure a load ratio of $R = 0.1$ such that $\Delta G = (1 - R)G_{max}$. Crack lengths were measured at $N = 5.1 \times 10^5$ and $N = 1.2 \times 10^6$ cycles. A sample with aluminum film thickness 0.5 μm was considered. An optical micrograph of the fatigue loaded sample shown in Figure 9.11. The dash lines represented the crack front after $N = 5.1 \times 10^5$ cycles.

Figure 9.11 (a) shows that the crack front developed during fatigue was not straight. The crack length was thus measured at seven equally separated positions along

the sample width. The average value was taken as the measured crack length. The center of the prenotch was selected as the original point for the crack length measurement. Figure 9.11 (a) provides evidence that there is crack propagation along both sides. Crack length vs. cyclic numbers is shown in Figure 9.11 (b). Although the initial crack length for both sides is not the same $a_{1,0} = 1.343\,$mm and $a_{2,0} = 1.0$ both cracks grew and $\Delta a_1 = 921$ µm, $\Delta a_2 = 895$ µm in the first stage of the experiment. Assuming a symmetrical configuration the loads $P_{min} = 3.5$ N, $P_{max} = 10.9$ N lead to the following energy release rate range value, equation 9.6, $G_{max}^S = 2.85$ J/m^2. Considering these loads and the actual asymmetric initial crack lengths, the energy release rate ranges at the two crack tips are calculated from equations 9.7 and 9.8 as $G_{max}^G = 2.93$ J/m^2 and $G_{max}^F = 2.77$ J/m^2, i.e. relative to G_{max}^S a difference of $\pm 3\%$. Considering the actual crack lengths at the end of the first loading stage $G_{max}^G = 2.92$ J/m^2 and $G_{max}^F = 2.78$ J/m^2, i.e. relative to G_{max}^S a difference of $\pm 2\%$. At the end of the experiment $\Delta a_1 = 953$ µm, $\Delta a_2 = 925$ µm Considering the actual crack lengths at the end of the experiment and the loads $P_{min} = 2.9$ N, $P_{max} = 9.2$ N, $G_{max}^G = 2.08$ J/m^2 and $G_{max}^F = 1.98$ J/m^2, i.e. relative to $G_{max}^S = 2.03$ J/m^2 a difference of $\pm 2\%$.

The fatigue crack growth rate were similar for both cracks. In the first stage $da_1 / dN = 1.79 \times 10^{-9}$ m/cycle and $da_2 / dN = 1.74 \times 10^{-9}$ m/cycle, and for the second stage $da_1 / dN = 6.24 \times 10^{-11}$ m/cycle and $da_2 / dN = 5.85 \times 10^{-11}$ m/cycle, indicating that the two cracks indeed propagated symmetrically under fatigue loading.

9.4 Conclusions

A modified 4-point bend delamination test methodology was provided in this study. This methodology was used and verified by fracture toughness tests and fatigue

loading tests on samples with a weak interface sandwiched between a glass and a silicon wafer.

Instead of considering one crack as it is commonly the case in 4-point bend delamination test, our modified 4-point bend delamination can produce symmetric crack propagation. The equation used to calculate the steady-state strain energy release rate based on two load plateaus under an asymmetrical crack growth situation was derived. Thus two test results for the fracture toughness can be obtained from a single test.

Also, by using the articulated 4-point bend fixture, symmetrical crack propagation was obtained for fracture toughness tests. Albeit a rare event, such findings are uncommon in regular 4-point bend delamination test (Ma, 1997).

This methodology also provided the capability to conduct the fatigue test. Test results indicated that there was symmetrical fatigue crack growth despite a difference in the initial crack length. It solved the problem that crack only propagated along one side of prenotch under cyclic loading.

In summary, this methodology established here provides a capability to conduct the fracture toughness and fatigue loading test on the sample with multi-layer structure. Incorporating the articulated 4-point bend fixture and theory for the asymmetrical crack propagation, more reasonable and precise results were obtained by generating the double crack and symmetrical crack propagation in fracture toughness and fatigue loading test, respectively.
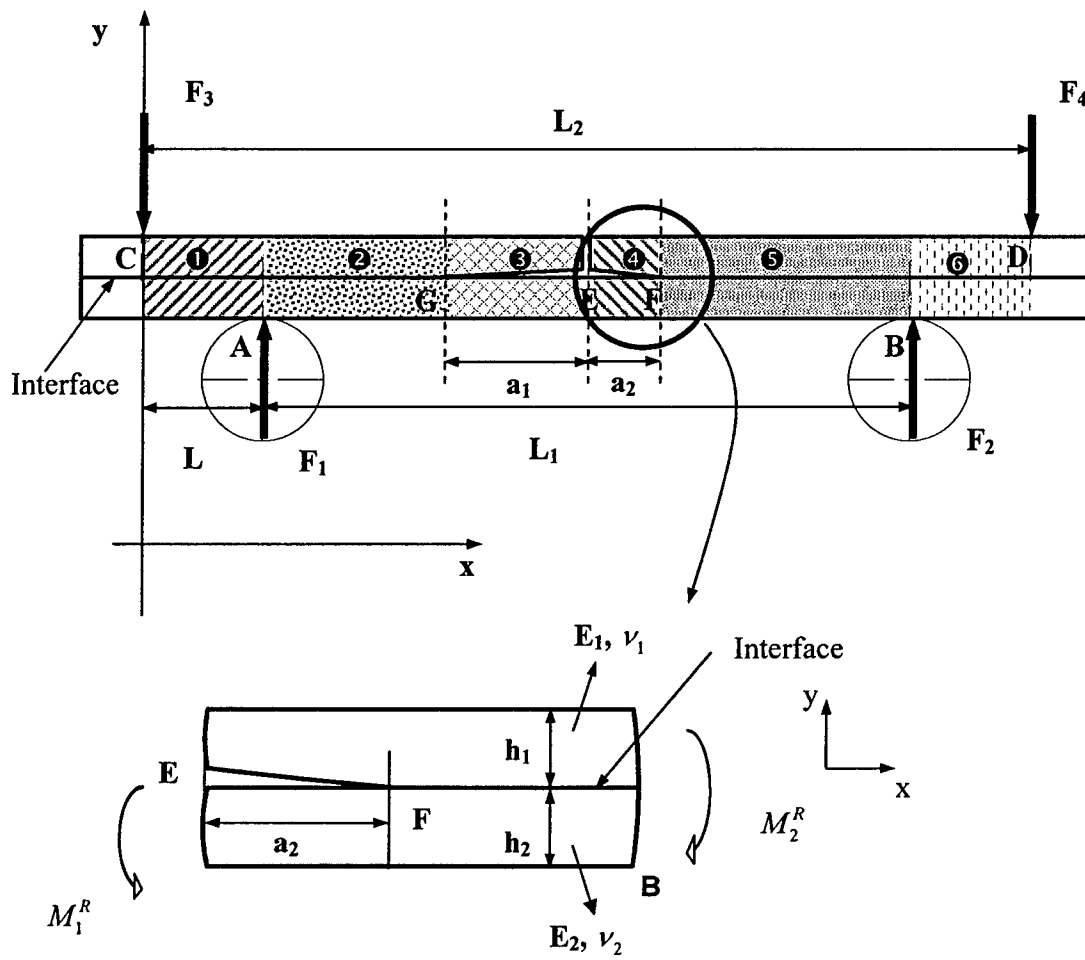
Figure 9.1: (a) Schematic picture for the loading conditions and dimensions of the 4-point bend delamination specimen with interface crack length of $a_1 \neq a_2$. (b) Enlarged picture to show the loading situation of right side crack.
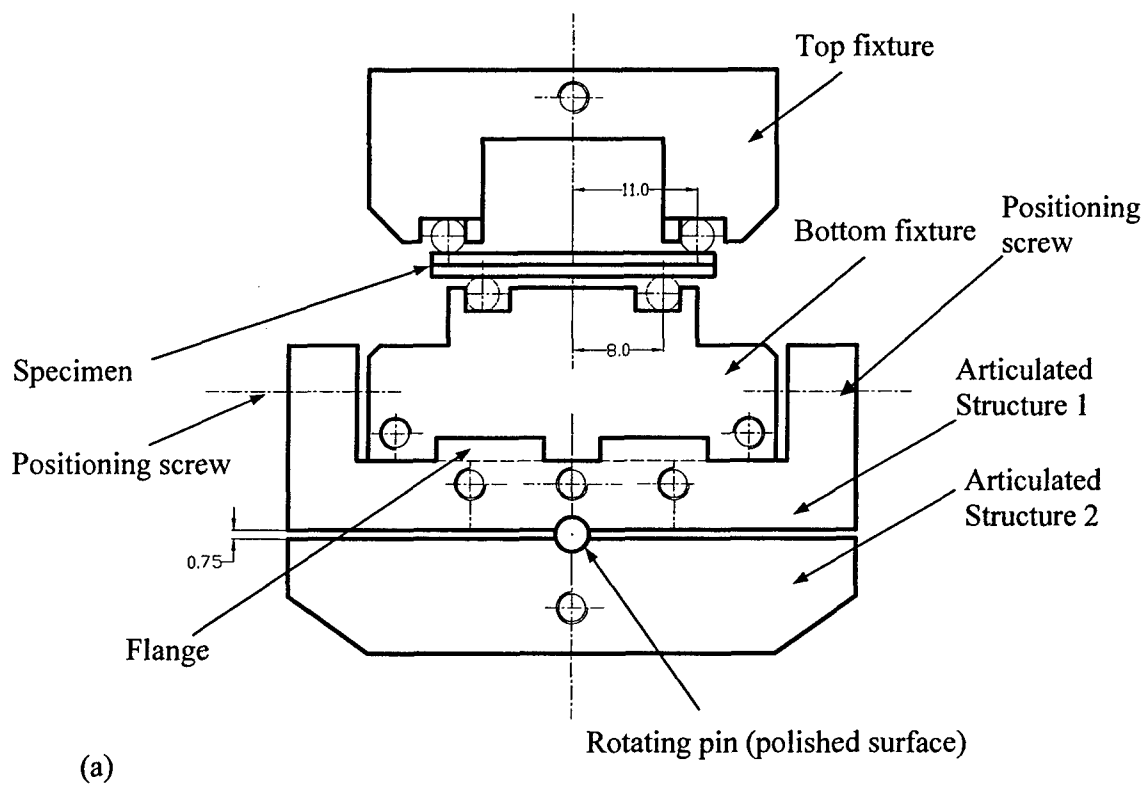
Figure 9.2: The semi-articulated 4-point bend fixture, (a) Schematic drawing; (b) Fixture in use. Unit is in mm.
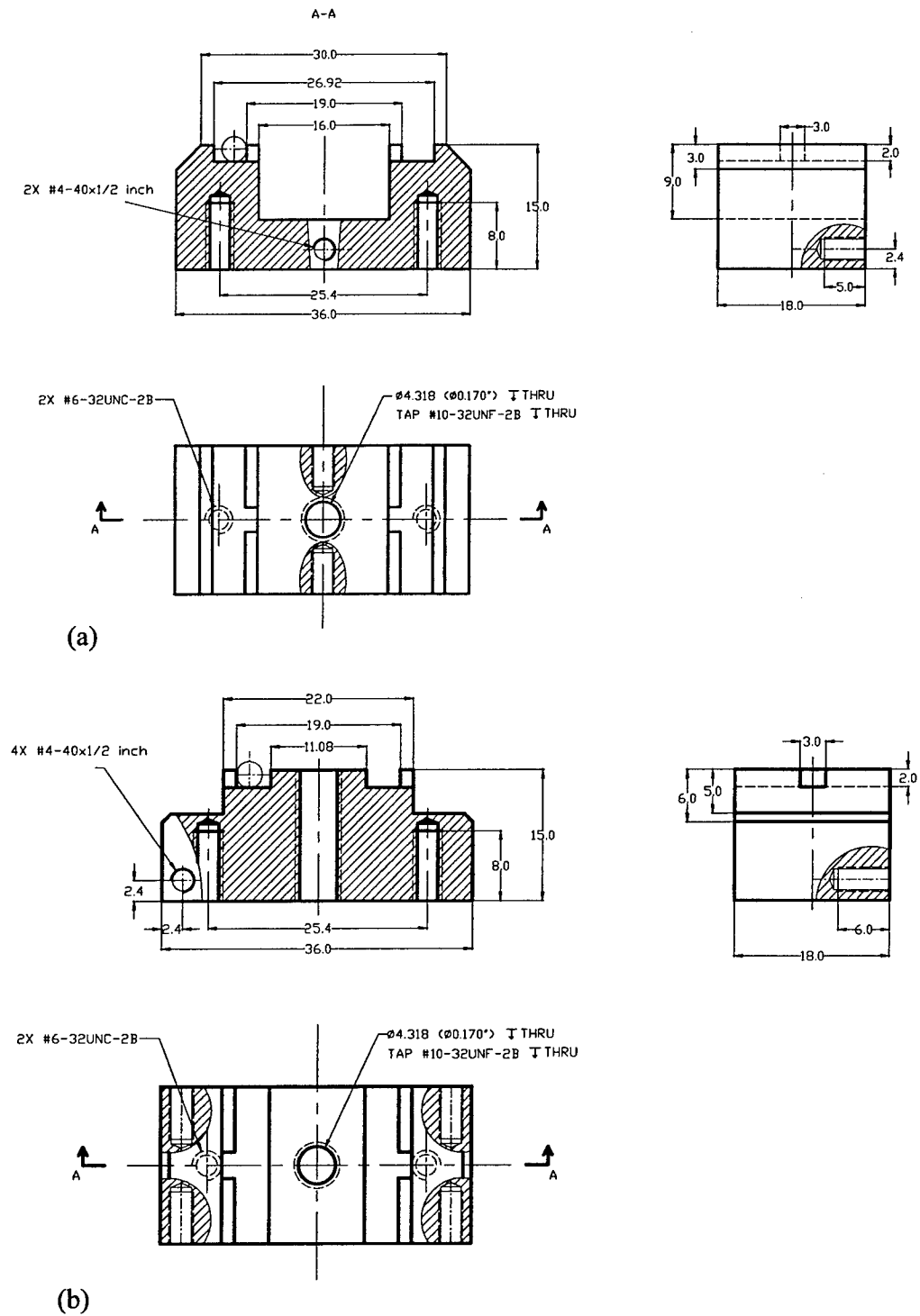
A-A

(a)

(b)

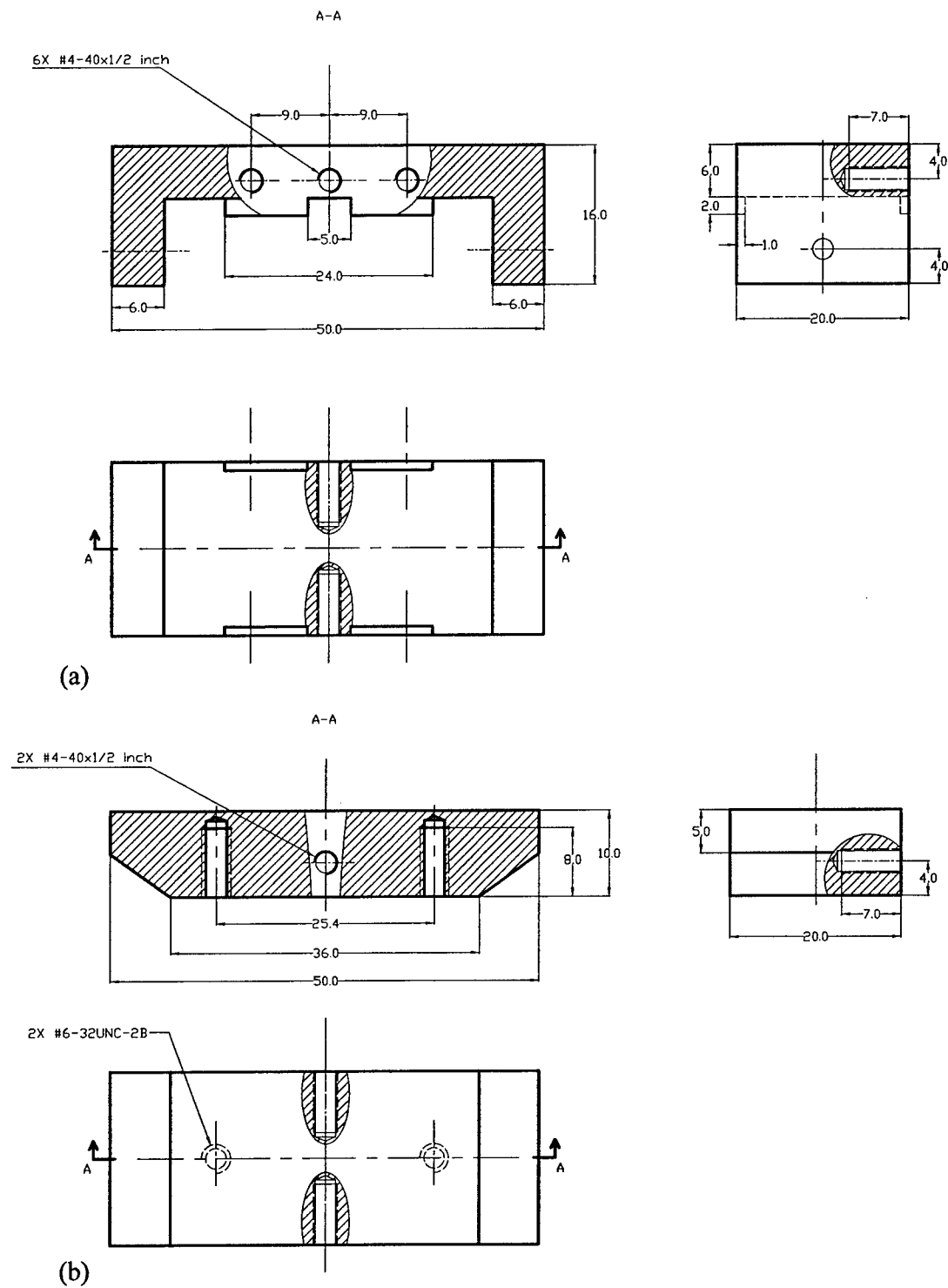Figure 9.3: Design of rigid 4-point bend fixture, (a) Top fixture (b) Bottom fixture. Unit is in mm.

6X #4-40x1/2 inch

9.0 — 9.0

16.0

5.0

24.0

6.0 — 6.0

50.0

7.0

6.0

2.0

1.0

4.0

4.0

20.0

(a)

2X #4-40x1/2 inch

10.0

8.0

25.4

36.0

50.0

5.0

4.0

7.0

20.0

2X #6-32UNC-2B

(b)

Figure 9.4: Design of articulated structure used as carrier for the 4-point bend fixture. (a) Structure 1. (b) Structure 2. Unit is in mm.
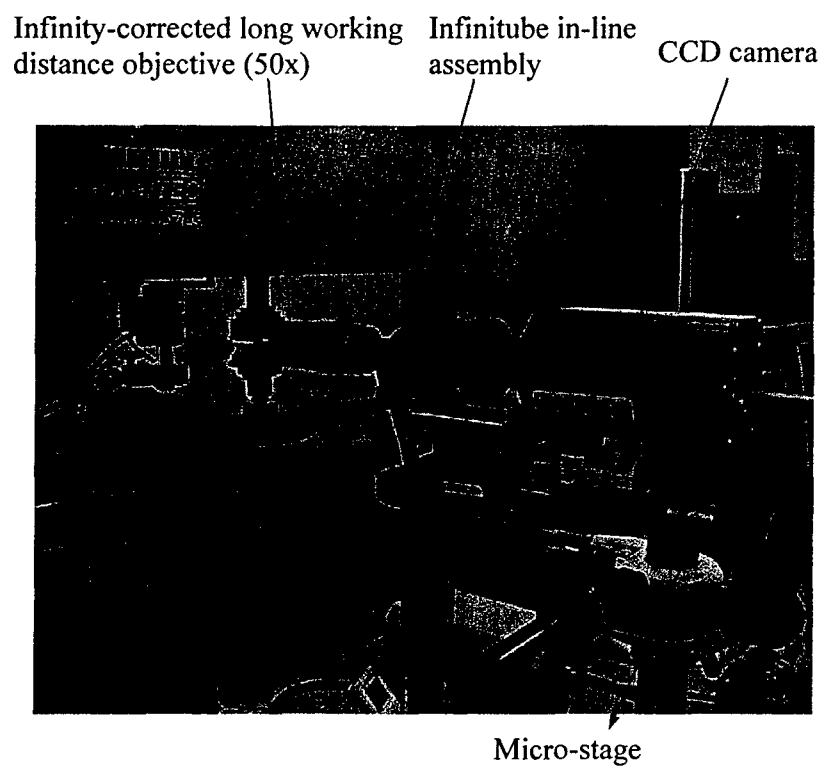
Figure 9.5: Optically imaging system used in the 4-point bend delamination test.

Au: 2mm

Glass: 1000μm
SiO$_2$: 0.6μm
Au/TiN: 0.025μm/0.02μm
Al: 0.05-2μm
SiO$_2$: 0.6μm
Si: 1000μm
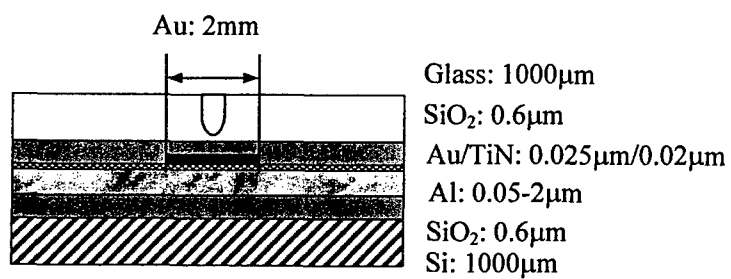
Figure 9.6: Schematic drawing of the multi-layer structure.

10. FATIGUE CRACK GROWTH IN A MEMS MULTILAYER STRUCTURE

With the widespread use of multi-layer structures in MEMS and microelectronic devices, experimental studies which focus on the reliability in multi-layer structures have been performed. Although there was considerable experimental work to characterize the fracture toughness of a variety of ceramic-metal systems under the different loading-mode configurations (e.g., Reimanis et al., 1990, 1991; Ritchie et al., 1993; Phillipps et al., 1993; Ma et al., 1995, 1997; Klingbeil and Beuth, 1997; Dauskardt, et al., 1998; Lane, et al., 2000a, 2000b; Hasegawa, et al., 2003; Hughey, et al., 2004; Shaviv, et al., 2005), corresponding investigations and experimental results on subcritical crack growth properties are extremely limited (Oh et al., 1988; Cannon et al., 1991; Shaw et al., 1994; McNaney et al., 1996; Hasegawa and Kagawa, 2006; Hirakata, et al., 2006). In this chapter, the dependence of FCG on metal layer thickness in a multi-layer thin film stack is studied. In the case of a metal layer sandwiched between two elastic substrates, constraint of the monotonic and cyclic plastic zone may occur when plasticity extends across the metal layer and impinges on the elastic substrates. These constraint effects are significantly determined by the metal layer thickness. Consequently, FCG may be influenced by the metal layer thickness. Few experimental studies have been reported on how FCG properties in multi-layer structures are affected by the constraint effects through variations in the metal layer thickness. McNaney et al. (1996) experimentally studied the fatigue and fracture toughness behavior of a metal/ceramic sandwich geometry based on the Al/Al_2O_3 system. The monotonic test and cyclic loading test under nominal mode I conditions were conducted to investigate the effect of the metal layer thickness on the fracture toughness and FCG by loading the sample in 4-point bend test. For the values of metal layer thickness considered ($100\mu m$, $200\mu m$ and $500\mu m$) no effect

of constraint on FCG rate was observed. Interfacial crack-advance mechanisms under cyclic loading were found to be similar to that in ductile metals. Hasegawa, et al. (2003) and Hasegawa and Kagawa (2006) investigated the effects of metal layer thickness on the fracture toughness and FCG rates of the Cu/Al_2O_3 interface by using double cleavage drilled compressive specimens. Hasegawa, et al. (2003) studied the effect of metal layer thickness (from 10 to 100μm) on the fracture resistance of the sapphire-Cu-sapphire interface. Their results showed that the initiation and steady-state toughness were substantially larger for systems with the thicker Cu layer. The difference in fracture toughness between the thin and thicker layers was mainly attributable to the constraint effects in the metal layer. Hasegawa and Kagawa (2006) studied the effects of the metal layer thickness (60μm and 100μm) on FCG rates. The measured FCG rates were independent on the thickness of the Cu layer. Kruzic, et al. (2004) carried out another experimental study using a ceramic-metal $Al_2O_3/Al/Al_2O_3$ system with the metal layer thickness of 5-100μm. FCG restuls for interfacial cracks showed an increase in crack-growth resistance with decreasing layer thickness in the near-threshold regime. For larger values of applied load, the crack growth resistance was observed as essentially independent of the metal layer thickness.

Under constant amplitude cyclic loading condition, the retardation of the FCG may be caused by the effects such as (i) periodic deflections in the path of the crack due to microstructural impediments to fracture or changes in local stress state and mode mixity, (ii) the bridging of the faces of the crack by fibers, particles, intact grains or corrosion products (Suresh, 1998). These extrinsic mechanisms of fatigue fracture can lead to an apparent retardation of the fatigue crack growth in brittle and ductile solids (Ritchie, 1999). Hence, FCG rates may also be influenced by the crack deflection and bridging. For example, Suresh (1983, 1985) indicated that methods by which the path of a crack can be periodically deflected from its nominal growth plane offered one possible way of enhancing the fatigue crack growth resistance. Cannon et al., (1991) investigated the fatigue crack growth in Cu/SiO_2 material system using double-cantilever-beam sandwich test specimens. Cyclic crack growth rates along glass-copper interfaces were reduced by many orders of magnitude due to crack tip shielding induced by crack

bridging. Experimental results of Kruzic et al. (2004) also revealed a crack path deflection during fatigue crack growth in a ceramic-metal $Al_2O_3/Al/Al_2O_3$ system with h_{Al}=5μm. This crack path deflection contributed to higher fatigue threshold and lower crack growth rates at comparable driving forces in the near-threshold regime.

FCG studies so far are in range of metal film thickness larger than 5μm. However, in many microelectronic devices much lower values of film thickness are of concern. For example, Dauskardt et al. (1998) have studied fracture toughness of such thin films. No previous studies of FCG for such small values of film thickness have been reported.

In this chapter, experimental studies and analysis of FCG were performed on a MEMS relevant material system where an aluminum thin film was sandwiched between two elastic substrates. The aluminum layer thickness varies from 0.05μm to 2μm. Monotonic and cyclic tests were conducted to investigate the constraint or size effects determined by the different metal layer thickness on the fracture toughness and FCG. This chapter is organized as follows. At first, the experimental methods which include preparations of samples, 4-point bend delamination testing and procedures used in fracture toughness and FCG test are discussed. The experiment results of fracture toughness and FCG test are reported in the second part. In the third part, the analysis of calibration of cohesive zone model under monotonic and cyclic loading is performed. Then, the experimental results are discussed. Finally, some conclusions are drawn.

10.1 Experimental Methods

10.1.1 Sample Manufacturing Process

Figure 10.1 shows SEM micrographs of a MEMS relevant sample with multi-layer thin film structure. The multi-layer structure was manufactured by using the standard integrated circuit fabrication processes. Using the E-beam evaporation, an aluminum layer (Al, thickness: 0.05μm~2μm) was deposited on a silicon wafer (Si, thickness: 1000μm, 3 inch <100>) with native layer of silicon dioxide (SiO$_2$, thickness:

0.6μm). Then, a layer of titanium nitride (TiN, thickness: 0.02μm) was reactively sputtered on top of aluminum layer. A thin gold layer was deposited on the TiN film by E-beam evaporation. The mask used for the Au deposition is shown in Figure 10.2(a). The mask was made by using the stainless steel shim disc (3" in diameter and 0.01" thick). The slots with the different width were carefully machined on the shim disc. Gold strips of 2.0 mm, 3.0 mm and 4.0 mm width are deposited (Figure 10.2(b)) on the wafer. Finally, one layer of silicon dioxide (SiO$_2$, thickness: 0.6μm) was formed on the TiN film by Plasma Enhanced Chemical Vapor Deposition (PECVD). After the thin film deposition, silicon wafers were diced into 25mm in square for the subsequent bonding process. Another glass wafer (Pyrex, thickness: 1000μm) was also diced into 25mm in square and anodically bonded to the top of the silicon wafer with the multi-layer structure. After bonding, squares are diced into strips with nominal dimension of 25mm x 2mm x 2mm (length x width x thickness). A prenotch of width 200μm and depth 940μm was carefully machined into the glass wafer by a diamond saw. Figure 10.3 (a) shows the process flow used to manufacture samples and Figure 10.3 (b) shows an anodically bonded square sample which was partially diced into 4-point bend samples.

For the 4-point bend delamination sample used here, a thin gold layer was deposited between SiO$_2$ and TiN films at the center of the diced strip sample to serve as a weak interface to ensure the deflection of the vertical precrack to the direction parallel to the interface. At the end of the gold layer, the crack seeks out a new weak path for further growth. Following (Ma et al., 1995), the interface between SiO$_2$ and TiN was to be expected as the weak link in the system and crack propagation is expected to be confined to the weak TiN/SiO$_2$ interface.

The Young's modulus of the <100> Si wafer was measured as 112GPa. The Poisson's ratio is 0.28. The Young's modulus of Pyrex #7740 glass wafer was measured as 60GPa and Poisson's ratio is 0.20.

10.1.2 Anodic Bonding Process

A second load carrying substrate needs to be bonded onto the top of the silicon wafer with multi-layer structure. Generally, it can be achieved by diffusion bonding a metal layer such as copper. In this study, two wafer bonding processes were explored. One is the silicon-to-glass anodic bonding process. This technology was widely used for the hermetic sealing and encapsulation in various areas of MEMS and microelectronics devices (Huang and Yang, 2002; Wei et al., 2003). The second bonding process considered was microwave bonding. Microwave bonding is a novel technology for bonding two metallized dielectric or semiconductor wafers to each other (Lei et al., 2004; Yussuf et al., 2005). However, in this study, the bonding results demonstrated that the microwave bonding was not reliable for the present material system and the sample bonded by microwave bonding had weak bond strength. Therefore, microwave bonding was not further considered.

The anodic bonding process was initially developed by Wallis and Pomerantz (1969). It has been extensively used in the vacuum packaging, hermetic sealing and encapsulation of the areas of MEMS and microelectronics. The main mechanism of this bonding process is to utilize the application of an electric filed to join a silicon and glass wafer (Figure 10.4(a)). The glass wafer must possess mobile ions such as sodium. Pyrex #7740 glass wafer is the most popular glass used for anodic bonding due to its rich sodium content, and its coefficient of thermal expansion (CTE) which is similar to silicon. During the anodic bonding process, the stack of silicon and glass wafers is placed on a hot plate and a high DC voltage is applied to the wafer pair with the negative electrode contacting the Pyrex. The presence of the resulting electric filed causes the Na^+ ions in the Pyrex to migrate to the negative electrode. A sodium depletion layer is created at the silicon-glass interface. The high electric field at the interface pulls the wafers together, and the O_2^- ions from the glass can oxidize the silicon, forming a SiO_2 layer, creating a strong, permanent bond between the glass and the silicon (Palensky, et al., 2002). In addition to silicon, other materials are possible such as SiO_2, polysilicon, Silicon nitride (Si_3N_4) and metals of Al, Ti, Ta, Cr, etc. For the samples in this study, the

248

anodic bonding process was used to bond the SiO$_2$ layer of 0.6μm thick and Pyrex #7740 glass. Instead of bonding entire wafer, the bonding process was applied to the 25mm square samples. The set-up[1] is shown in Figure 10.4(b).

Generally, the key parameters for the anodic bonding include the DC voltage values, temperature and bonding time. A typical temperature and voltage for anodic bonding is 400-500°C and 400-1200V (Wei, et al., 2003). Factors such as bonding area and bonding environment can also play some roles. A lot of research work has been done to investigate the effects of bonding parameters on the final strength (Nese and Hanneborg, 1993; Rogers and Kowal, 1995; Cozma and Puers, 1995; Cozma et al., 1998; Go and Cho, 1999; Lee et al., 2000; Dunn et al., 2000; Huang and Yang, 2002; Wei et al., 2003). The bond strength generally increases with the increase in applied voltage and temperature. It is found that bonding was performed easily and the number of non-bonded regions is smaller under high temperature compared to a low bonding temperature. However, the induced residual thermal stresses are larger with increasing bonding temperature due to the CTE mismatch. The applied voltage must be high enough to provide strong electrostatic forces able to bring the two surfaces into intimate contact. Also the higher voltages allow successful bonding with lower temperature. Several parametric studies were conducted to determine a set of reasonable bonding parameters. The temperature and voltage were selected as 540°C and 1200V, respectively. It took 50 minutes for an anodic bond to be achieved in the environment of N$_2$ gas without the use of bonding pressure or load. After bonding, it was found that contact area between the electrode and glass surface was damaged. When observing it under the microscope, needle-like material was observed in this small area. Based on Terazaki (2005), this is sodium spread on the glass surface due to the high bonding temperature and voltage. Placing a dummy glass between the cathode electrode and the Pyrex glass can reduce the amount of sodium found on the surface. One piece of dummy glass wafer was placed between the electrode and Pyrex glass. The bonding cannot be totally achieved by using the previous parameters due to this dummy glass wafer. To achieve the bonding, the

---

[1] The anodic bonding experiments were conducted in Prof. Bashir's laboratory in School of Electrical and Computer Engineering, Purdue University.

voltage was increased. After several tries, the bonding parameters were determined as 1800V for the bonding voltage, 540°C for the temperature, and 50 minutes for bonding time. Bonding was completely achieved by using these bonding parameters and the small area with the needle-like material on top of glass wafer disappeared.

In summary, based on the anodic bonding process developed, it shows that the reliable anodic bonding has been achieved between the Pyrex #7740 glass and SiO_2 thin film deposited by PECVD. A set of the bonding parameters with 540°C, 1800V, 50 minutes, no bonding load and N_2 gas environment are determined and used as the suitable bonding parameters for the samples developed in this study.

10.1.3 Initial Crack Preparation

The 3-point bend fixture was used to precrack the samples due to the concentrate critical load at the center of the sample. The sample was loaded monotonically under the displacement control with the displacement rate of 0.3μm/s until the vertical precrack occurred. The precrack was monitored using the optically imaging system. Once the vertical precrack occurred and kinked into the interface, the sample was unloaded to avoid the sample breakage. The photomicrograph of the interface delamination after the pre-cracking process is shown in Figure 10.5. It clearly shows that the vertical precrack deflected in the direction parallel to the interfaces due to the weak bonding of gold layer.

10.1.4 The Modified 4-point Bend Delamination Test

A modified 4-point bend delamination test developed in Chapter 6 was used here to conduct the fracture toughness test and FCG test on the samples with the different aluminum layer thickness. The 4-point bend delamination sample with symmetrical crack growth was schematically shown in Figure 10.6. Equation (9.6) is used to calculate the strain energy release rate under this symmetrical crack configuration.

10.1.5 Fracture Toughness Test and FCG Test

In fracture toughness test, the sample was loaded in the modified 4-point bend fixture under the monotonic loading condition. The displacement control with slow displacement rate of 0.05μm was used. The displacement applied and the corresponding load values were recorded during the test. The monotonic loading test was repeated for the samples with different aluminum layer thicknesses.

Fatigue crack growth rates were determined in the modified 4-point bend delamination test using a computer-controlled, low-force electrodynamically actuated testing frame. Experiments were conducted in room air (25°C, 40% relative humidity) at a test frequency of 2Hz and a load ratio (G_{min}/G_{max})of $R=0.1$. Based on the ASTM standard (ASTM E647-91, 1991) for conducting the fatigue crack growth test, specific information about the test procedures was considered.

When determining the FCG rates under the load control by 4-point bend test, it is preferred that each specimen be tested at a constant load range and a fixed set of loading variables (stress ratio and frequency). However, this may not be feasible when it is necessary to generate a wide range of information with a limited number of specimens. When the loading ranges or variables are changed during the test, potential problems arise from several types of transient phenomenon. In order to minimize or eliminate such effects, the following procedures were used.

- When changing the load range applied on one sample to get the FCG rates under the different load levels, the resulting P_{max} is increased rather than decreased to preclude retardation of crack growth rates caused by overload effects.
- Sufficient crack extension is needed following changes in load ranges to enable the growth rate to establish a steady-state value.
- If the crack growth rates following an interruption are less than those before interruption under the same load range, the crack growth rate data should be discarded.

After fracture toughness test and fatigue crack growth test, samples were put into the Field Emission Scan Electron Microscope (FESEM) and side surfaces of samples were observed to identify the thin film stack up and crack path.

10.2 Experimental Results

10.2.1 Fracture Toughness

Measured fracture toughness values represented by critical strain energy release rates G_c and critical stress intensity factors K_c were plotted with respect to the aluminum layer thickness h_{Al} in Figure 10.7 (a) and (b), respectively. The results indicate that the range of the average critical strain energy release rate measured is 2~4J/m^2. The corresponding stress intensity factor is in range of 0.4~0.6 MPa(m)$^{1/2}$. The measured fracture toughness valves were found to show a weak trend of increasing toughness with the increase of aluminum layer thickness over the range of 0.05~1μm. Samples with aluminum layer thickness of 2μm do not follow this trend. Low fracture toughness values were obtained for this sample.

Figure 10.8 shows the interface crack path at a distance away from the crack tip and near the crack tip for the sample with h_{Al}=0.05μm, 0.5μm, 1μm and 2μm. For the 0.05μm thick sample, the thinnest aluminum layer thickness considered, there are two crack paths observed at the crack tip. One is along the interface of Glass/SiO$_2$ and the other is inside the glass. For the sample with h_{Al}=0.5μm, the crack path deflection was observed at a distance away from the crack tip. Crack deflected from the interface of SiO$_2$/TiN to Glass/SiO$_2$. For the sample with h_{Al}=1μm, Crack path deflection is also observed near the crack tip as shown in Figure 10.8 (e). One crack path is along the Glass/SiO$_2$ and the other is inside the glass. For the sample with h_{Al}=2μm, there was a single crack path along the interface of Glass/SiO$_2$ and no crack deflection was observed.

10.2.2 Fatigue Crack Growth

Figure 10.9 shows the measured crack extension vs. the cyclic numbers for the sample with h_{Al}=1µm under G_{max}/G_c=31%. A linear relationship was found between the crack length and cyclic numbers. Based on this curve, the corresponding FCG rates can be determined. Calculated FCG rates da/dN for the samples with h_{Al}=0.05µm, 0.5µm and 1µm are plotted in Figure 10.10 as a function of both the range of applied strain energy release rate ΔG and the stress-intensity factor range ΔK. The measured FCG rates were mainly characterized over a range between 10^{-9} and 10^{-6} m/cycle. In this range, the measured FCG rates increase with an increase in ΔG or ΔK and show the linear relationship. In terms of the Paris law formulation (Paris, et al., 1961), the relationship can be described by da/dN=$3.69\times10^{-4}(\Delta K)^{5.6}$ for h_{Al}=1µm and da/dN=$4.56\times10^{-7}(\Delta K)^{3.2}$ for h_{Al}=0.5µm, respectively. Over the range of applied ΔK or ΔG, a trend of increasing crack-growth rate with increasing aluminum layer thickness is obtained (Figure 10.11). Under the same load level of G_{max}/G_c=90%, the FCG rates of the sample with h_{Al}=0.05µm and 0.5µm are equal to 2E-08m/cycle and 2.5E-08m/cycle, respectively. The FCG rate of the sample with thicker aluminum layer of h_{Al}=1µm is around 2 orders of magnitude faster than that of the sample with h_{Al}=0.05µm. In Figure 10.12, the measured FCG rates da/dN as the function of the stress intensity factor range ΔK was plotted with the test results of FCG rates for metals, intermetallics and ceramics provided by Ritchie (1999). Compared to the FCG rates of other structural materials, the measured FCG rates for the sample with h_{Al}=1µm are more like the brittle material whose crack growth rate behavior displays a higher sensitivity to the applied stress intensity factor range than is observed in most metals. Also Figure 10.12 indicates that multi-layer structures considered here possess the lower FCG resistance.

Figure 10.13 compares the crack path of the samples with h_{Al}=0.05µm, 0.5µm, 1µm after fracture toughness test and FCG test. Based on Figure 10.13, material separation process in fracture is not equal to that in FCG. Examination of the crack path

of sample with $h_{Al}=0.05\mu m$ after fracture and fatigue test revealed multiple cracks and crack bridging near the crack tip. However, the crack path is not exactly the same in fracture and fatigue. In fatigue test, crack bridging occurred when crack deflected from Glass/SiO$_2$ to SiO$_2$/TiN interface. In fracture test, crack propagated along the interface of Glass/SiO$_2$ or inside the glass. For the sample with $h_{Al}=0.5\mu m$, Figure 10.13 (b) indicates that crack path deflection during crack growth. At first, the crack propagated along the interface of Glass/SiO$_2$. Then, the crack kinked into the interface between Al and SiO$_2$ layer. After a small crack propagation, the crack kinked back into the interface of Glass/SiO$_2$. In fracture test, one flat path along the interface of Glass/SiO$_2$ was observed near the crack tip. For the sample with $h_{Al}=1\mu m$, no crack deflection was observed during crack growth and crack propagated along Glass/SiO$_2$ interface. In fracture test, Figure 10.13 (c) shows a flat path along the interface of Glass/SiO$_2$ at a location away from the crack tip. Figure 10.8 (e) shows a crack deflection near the crack tip.

10.3 Analysis

10.3.1 CZM - Under Monotonic Loading

The cohesive zone model is used to simulate the interface delamination and crack propagation in this study. The traction-separation law for the cohesive surface is taken to describe the relationship between the traction and displacement jump across the surface. The traction-separation law is very important for the cohesive zone model to well capture and simulate the material separation behaviors. Here, the traction-separation law is determined by measuring the crack opening displacement at the initial crack tip under the monotonic loading condition. When monotonically loading the sample, the images at the initial crack tip were captured. Figure 10.14 shows the captured images for the calculations of the crack tip opening displacement. Based on coordinates of the points on the images, the crack opening displacement at the initial crack tip was determined as the

crack propagated. The strain energy release rate G was calculated based on the recoded load values and equation (9.6). After the test, the curve of G vs. Δ_n was plotted and curve fitting was used to get the function of $G(\Delta_n)$ by use of equation (2.5) with $\phi_n = G_c$. Figure 10.15 (a) depicts the strain energy release rate vs. the crack tip opening displacement at the initial crack tip based on the test results and curve fitting. In Figure 10.15 (a), G values increase as the crack propagates until the steady state is reached. After the function of $G(\Delta_n)$ was determined by curve fitting, the cohesive traction-separation law can be derived by $T_n = \partial G(\Delta_n)/\partial \Delta_n$. Following the above process the cohesive zone parameters were calibrated as $\phi_n = 3.59 \mathrm{J/m}^2$, $\delta_n = 0.236 \mu\mathrm{m}$ and $\sigma_{\mathrm{max},0} = 5.6 \mathrm{MPa}$. The determined traction-separation law under monotonic loading is shown in Figure 10.15(b).

After the calibration of CZM under monotonic loading, it was then used to simulate the crack bridging observed during the fracture toughness test. For monotonic loading we simulate crack bridging behavior, i.e. the crack arrives on a given plane and continues to a neighboring weaker interface. In this study we employ the cohesive surface law of Xu and Needleman (1994) but do not take the fatigue damage evolution rule of Roe and Siegmund (2003) into account.

When introducing multiple planes of cohesive surfaces into a solid special attention has to be paid to the points at which these planes end. Under normal circumstances, these points lead to stress singularities since they are geometric singularities. These stress singularities then lead to strong, unphysical mesh distortions in the proximity of these singular points, which are amplified by neighboring planes of cohesive surfaces. To eliminate these problems, starting ten cohesive surfaces from the singular points, the cohesive strength increases exponentially to the singular points. This increase leads to an exponential increase in the stiffness and thereby a considerable reduction of the stress singularity.

The material system of a bi-material of silicon and glass is studied. The crack arrives on the glass-silicon interface and the probability of crack bridging across different widths of glass layer is studied. The material properties of glass and silicon are those as specified before. Also, the initial crack plane has the material properties as specified

255

before. The weaker plane, i.e. the plane to which the crack bridges, has a 100 times reduced strength than the initial plane, for example, due to some manufacturing error. The thick and thin layer have a thickness of 120 and 60 μm, respectively. The opening of both layers is shown in Figure 10.16(a) and (b). Both show no mesh distortions at the endpoints of the cohesive planes, proving our method of stress singularity elimination successful. Secondly, the crack bridging is more significant for the thin layer than for the thick layer at the same applied stress intensity factor. Therefore, the probability of crack bridging across a thin layer is greater than across a thick layer. This generic study proves the concept of simulation of crack bridging using CZM. In the future extended research has to be carried out to determine the fracture properties of the weak interface.

10.3.2 CZM – Under Fatigue Loading

Roe and Siegmund (2003) introduces fatigue failure into cohesive surfaces. The model includes three material parameters, which we fit to the experiments discussed earlier.

- The characteristic fatigue separation δ_Σ scales the amount of damage accumulation.

- The fatigue threshold σ_f defines that stress below which no damage accumulates.

- The Heaviside function could be included or excluded.

These three parameters were used to non-linearly fit the model to the Paris-type plot obtained in the FCG test as shown in Figure 10.10 (a).

The Heaviside function shifts the onset of damage accumulation for all cohesive surfaces identically. It thereby leads to the same crack growth rate as without the Heaviside function. Therefore, the Heaviside function has no influence on the Paris-type plot. The fatigue threshold and the characteristic fatigue separation shift the curve in the vertical direction, i.e. they increase/decrease the crack growth rate, while maintaining the same slope. The results of the fit are shown in Figure 10.17 for the characteristic fatigue separation $\delta_\Sigma = 10\,\delta_0$ and the fatigue threshold $\sigma_f = 0.25\,\sigma_Y$. Figure 10.17 shows that the

crack growth rates are comparable to those measured in experiments. The slope of the Paris-law curve, however, is smaller than that found in experiments. Additionally, the simulations do not predict a Paris-type power-law behavior as evident from the kink in the graph. The simulations for the mixed mode failure fit much better the experimental values than those for mode I failure. Therefore it has to be concluded that mode mixity plays an important role in the Paris-type behavior.

10.4 Discussions

The measured fracture toughness values are in the range of 2~4J/m^2 which are smaller than the interface toughness of TiN/SiO$_2$, 10J/m^2, measured by Lane, et al. (2000a). But they are in the range of 0.03~6.12J/m^2 measured for the interface of anodically bonded Glass/SiO$_2$ by Go and Cho (1999). Based on Figure 10.8, the crack path is not always confined to the interface of SiO$_2$/TiN. Indeed, most of the crack path is along the bonding interface of Glass/SiO$_2$. It results in the measured values fall into the range of the fracture toughness measured for the anodically bonded Glass/SiO$_2$ interface.

According to the lower cohesive strength obtained in the calibration of CZM under monotonic loading, little plasticity was generated and the constraint plasticity effects on fracture toughness should be small. Besides constraint plasticity effects, other mechanisms such as crack deflection also affect fracture toughness. Actually, crack deflection from one interface to the other has often been observed for ceramic/metal sandwich geometries (Oh, et al., 1988; Cannon, et al., 1991; Reimanis, 1991; Howard and Clyne, 1993; McNaney, et al., 1996). By introducing crack bridging due to crack deflection at particles or interfaces, factors of 3 increases in toughness can be obtained (Ritchie, 1999). Many methods by which the crack path can be periodically deflected from its nominal growth plane have been used to develop high toughness interfaces. For example, significant toughing was achieved for the glass/Cu interfaces through crack bridging by use of photolithography to implant microdefects near the interface (Oh, et al., 1988). In the present study, crack deflection was also commonly observed in the fracture

toughness test for the sample with h_{Al}=0.05µm, 0.5µm and 1µm. For the sample with h_{Al}=2µm, no crack deflection occurred along the entire interface. The crack bridging resulted from these crack deflection may explain why the fracture toughness of the sample with h_{Al}=2µm is smaller than those of the samples with thinner aluminum layer. The effect of crack deflection on fracture toughness can be assessed using estimates for an idealized two-dimensional crack with repeated kinked segments (Figure 10.18(a)). In this segment, θ is the kink angle, D is a deflected length, and S is an undeflected length. Based on Suresh (1983), the decrease in energy release rate due solely to deflection is estimated as

$$G^* = G_0 \left[\left(\frac{D+S}{D\cos^2(\theta/2)+S} \right)^2 - 1 \right]$$
(10.1)

whereas,

$$G^* = G_0 \left(\cos^{-4}(\theta/2) - 1 \right)$$
(10.2)

provides an estimate neglecting stress relaxation for extension between obstacles. Here, G_0 is the energy release rate for a straight crack. As an example, the effect of crack deflection on the fracture toughness is analyzed for the sample with h_{Al}=0.5µm. Figure 10.18 (b) shows SEM image of crack deflection observed in fracture toughness test. Based on the measured values of $\theta \approx 60°$, $D \approx 1.46$µm, and $S \approx 6.46$µm, the toughness increases from equation (10.1) and (10.2) are 10% and 78% of G_0, respectively.

Figure 10.8 also indicates that the probability of crack bridging across a thin layer is greater than across a thick layer. When the thickness of metal layer sandwiched between two elastic substrates was decreased, the local stress would increase substantially due to the constraint effects (Varias, et al., 1991; Wang and Siegmund, 2005). Thus, at the same applied driving force, samples with thinner and more constrained layers experience higher local stresses ahead of the crack tip (Kruzic, 2004). This higher local stress ahead of the crack tip greatly enhance tendency to crack bridging across the thinner layer. The simulation of crack bridging under monotonic loading

conducted in this study also indicated that the crack bridging was more significant for the thin layer than for the thick layer at the same applied stress intensity factor.

Generally, deflections in the crack path are ignored in the characterization of fatigue behavior because of the difficulties in estimating the effective crack-tip driving force. However, it is found that even small deflections in the path of a fatigue crack can lead to a reduction in crack growth rates by several orders of magnitude (Suresh, 1998). In the present study, crack deflections were also observed for the sample with h_{Al}=0.05μm and 0.5μm during crack growth. The corresponding FCG rates were retarded due to crack path deflection compared to the FCG rate of the sample with h_{Al}=1μm. To study effects of crack path deflection on the fatigue crack growth, a case of periodic two-dimensional deflections in the path of a fatigue crack is examined. The same segment of a deflected crack depicted in Figure 10.18 (a) is used. When the crack tip is deflected from its nominal growth direction, the overall fatigue crack growth rate is determined by the effective stress intensity factor range ΔK_{eff} which is defined as $\Delta K_{eff} = \Delta K_a - \Delta K_b$. Here, ΔK_a is the applied stress intensity factor range and ΔK_b is the reduction due to the bridging tractions (Cox and Rose, 1994). Based on the analysis of Suresh (1998), the effective stress intensity factor range ΔK_{eff} for the periodically deflected crack is written as

$$\Delta K_{eff} = \left[\frac{D\cos^2{(\theta/2)}+S}{D+S} \right] \Delta K_I \tag{10.3}$$

whereas,

$$\Delta K_{eff} = \cos^2{(\theta/2)} \Delta K_I \tag{10.4}$$

provides an estimate of effective stress intensity factor range with neglecting stress relaxation for extension between obstacles. Here, ΔK_I is the nominal far-field stress intensity factor range. Based on measurements of crack deflection for the sample with h_{Al}=0.5μm (Figure 10.19), a set of values with $\theta \approx 45°$, $D \approx 0.82$μm, and $d \approx 7.53$μm is substituted into equation (10.3) and (10.4). The calculated results of the effective stress intensity factor range are equal to 98% and 85% of ΔK_I. Hence, the effective stress

intensity factor range for crack growth of a deflected crack is typically smaller than that of a straight crack which is subjected to the same far-field ΔK_a. The corresponding FCG rates for a deflected crack are slower than a straight crack.

10.5 Conclusions

Based on the experimental studies and analysis to investigate the effects of changing aluminum layer thickness (over the range from 0.05μm to 2μm) on the fracture toughness and FCG of a MEMS relevant multi-layer structure, the following conclusions can be made:

The measured fracture toughness valves were found to show a weak trend of increasing toughness with the increase of aluminum layer thickness over the range of 0.05~1μm. Samples with h_{Al}=2μm do not follow this trend. Low fracture toughness values were obtained. Based on the SEM images of crack path, multiple crack path and crack deflections were observed for the sample with h_{Al}=0.05~1μm and no crack deflection was found for the sample with h_{Al}=2μm. With considering the lower values of fracture toughness of the sample with h_{Al}=2μm, the source of interface toughing for the thinner aluminum layer samples may arise from the crack bridging generated by crack deflection. The toughing contribution from crack deflection was estimated to be in the range of 10% -78% of the fracture toughness of the straight crack. Both experimental and simulation results indicate that the probability of crack bridging across a thin layer is greater than across a thick layer under the same load levels.

Fatigue crack growth rates, measured over the range between 10^{-9} and 10^{-6} m/cycle, were found to increase with increasing aluminum layer thickness. The samples with thinner aluminum layer showed pronounced crack bridging which results in the lower FCG rates. It is concluded that the sample with thinner films is shown to be more reliable due to crack bridging effects. Constraint plasticity effects on FCG in thin films are small due to the small plasticity under cyclic loading.

Based on SEM observations, material separation process in fracture toughness test is not equal to FCG test. Crack paths are highly constraint dependent. For the sample with thinner aluminum layer of h_{Al}=0.05μm and 0.5μm, multiple crack paths and crack defections occurred in the fracture and fatigue test. But the crack paths are not the same. For the sample with h_{Al}=1μm, crack deflection was observed in fracture toughness test. But in fracture test, no crack deflection occurred along the interface and a straight crack was observed.

The Cohesive Zone Model for the characterization of fracture and fatigue response was calibrated under the monotonic and cyclic loading conditions. A set of cohesive zone parameters were determined for both monotonic and fatigue loading. The simulations for the mixed mode failure fit much better the measured FCG rates than those for mode I failure.
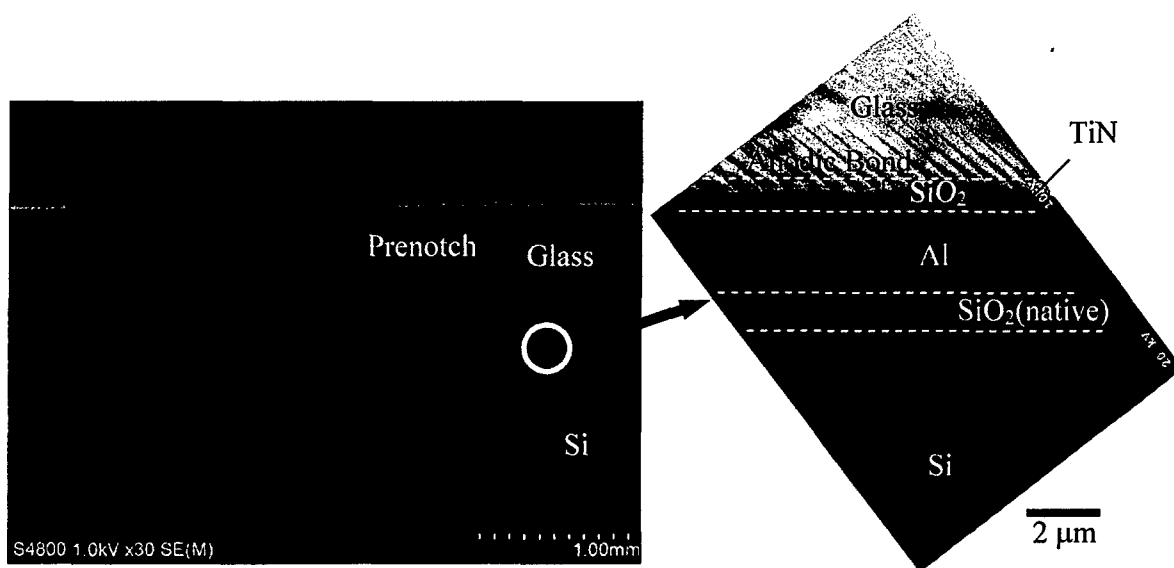
Figure 10.1: SEM micrographs of a MEMS relevant sample with multi-layer structure.

(a)

(b)
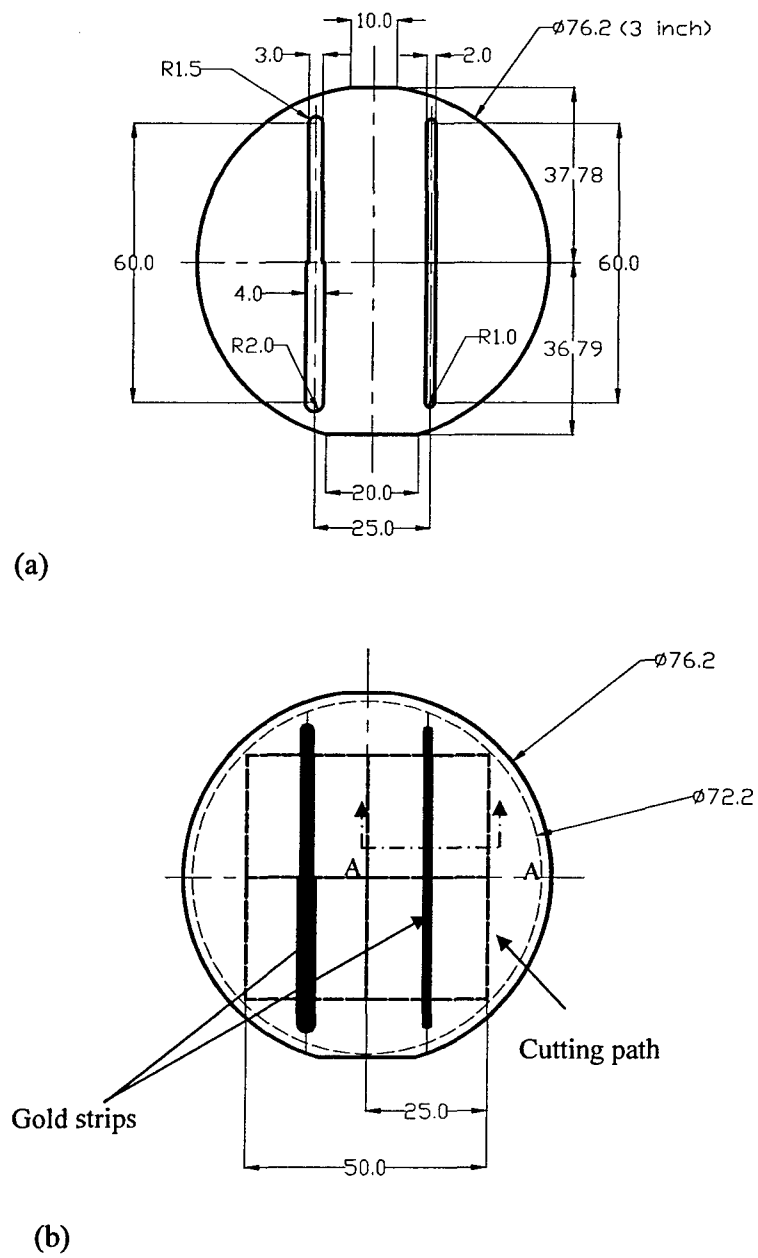
Figure 10.2: (a) Mask used for gold strip deposition; (b) Silicon wafer after gold deposition. Unit is in mm.

Bottom Stack:

Initial Silicon Wafer
SiO₂ — 0.6µm
Si — 1000µm

Al Deposition
Al — 0.05-2µm
SiO₂
Si

Reactive Sputtering TiN
TiN — 0.02µm
Al
SiO₂
Si

Au Deposition
Au — 0.025µm
TiN
Al
SiO₂
Si

SiO₂ PECVD
SiO₂ — 0.6µm
Au/TiN
Al
SiO₂
Si

Wafer Dicing
25mm
25mm

Solvent Clean + Plasma Clean

Top stack:

Initial Pyrex #7740 Wafer
Glass — 1000µm

Glass Wafer Dicing into 25mm square

Solvent Clean + Plasma Clean

Anodic bonding top and bottom stack

Diced into strips and machine notch
Glass: 1000µm
SiO₂: 0.6µm
Au/TiN: 0.025µm/0.02µm
Al: 0.05-2µm
SiO₂: 0.6µm
Si: 1000µm

Interface of interest

Prenotch: 940µm deep
200µm wide

(a)

5mm

(b)

Figure 10.3: (a) Process flow (Drawing is not to scale.) (b) An anodically bonded square sample, partially diced into 4-point bend specimens.

(a)

(b)
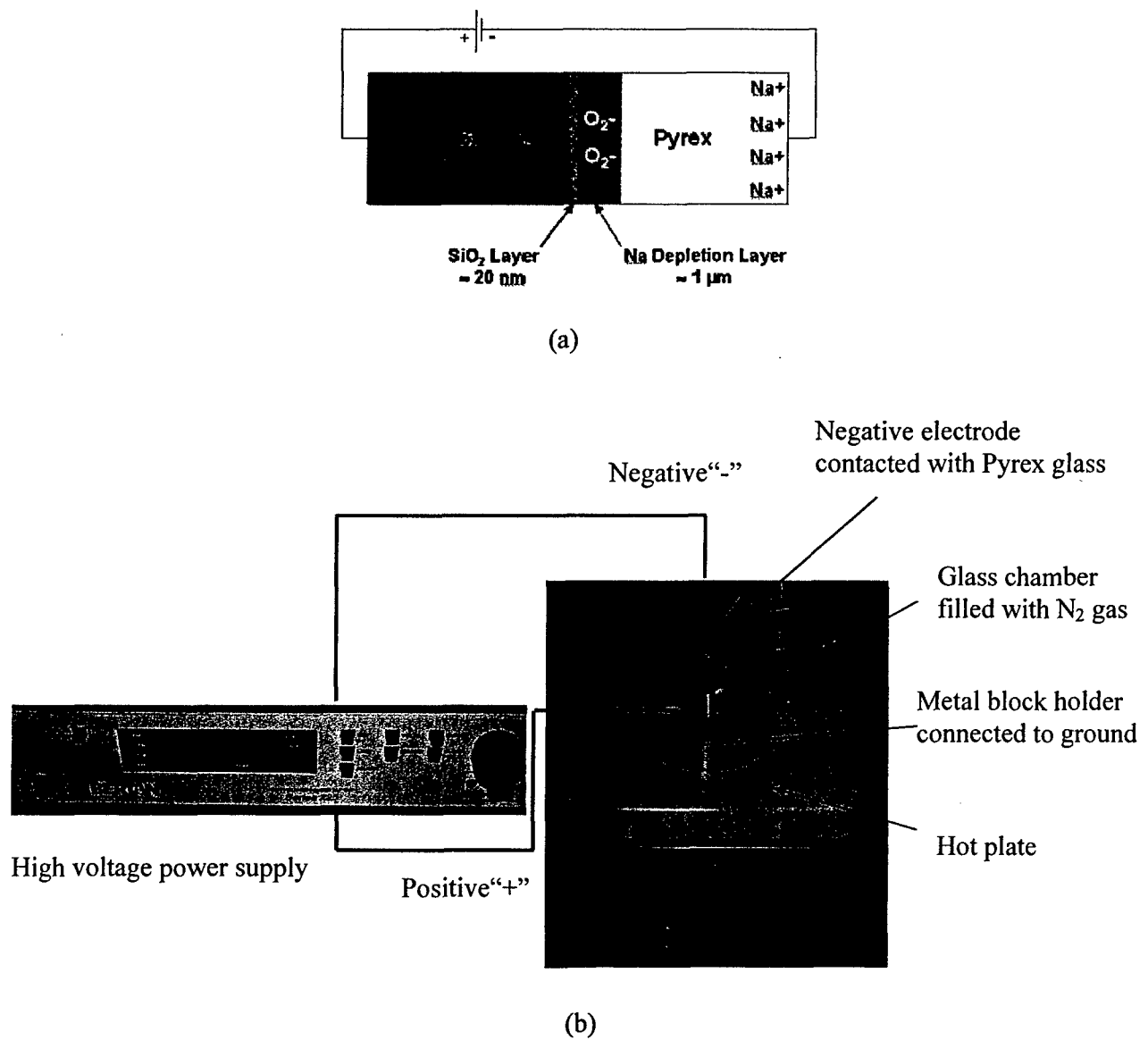
Figure 10.4: Anodically bonding process (a) Bonding mechanism (Palensky, et al., 2002); (b) Test set-up.
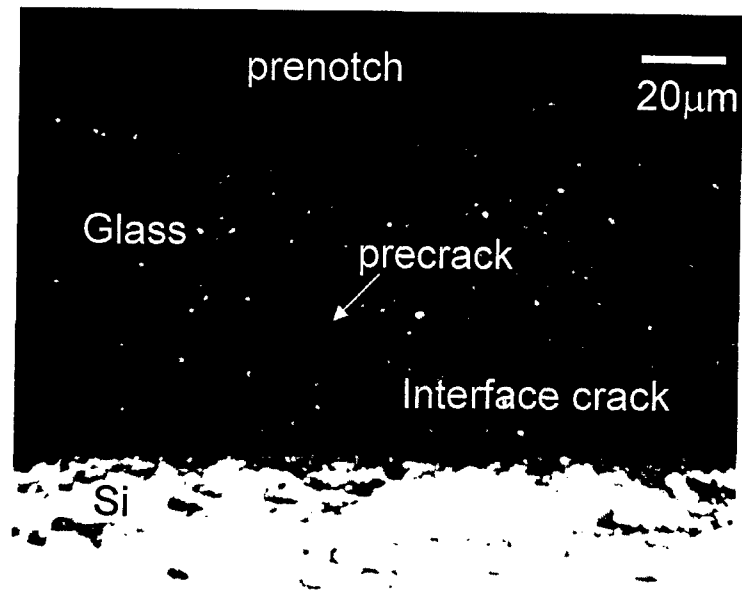
Figure 10.5: Photomicrograph of the interface delamination after the pre-cracking process.
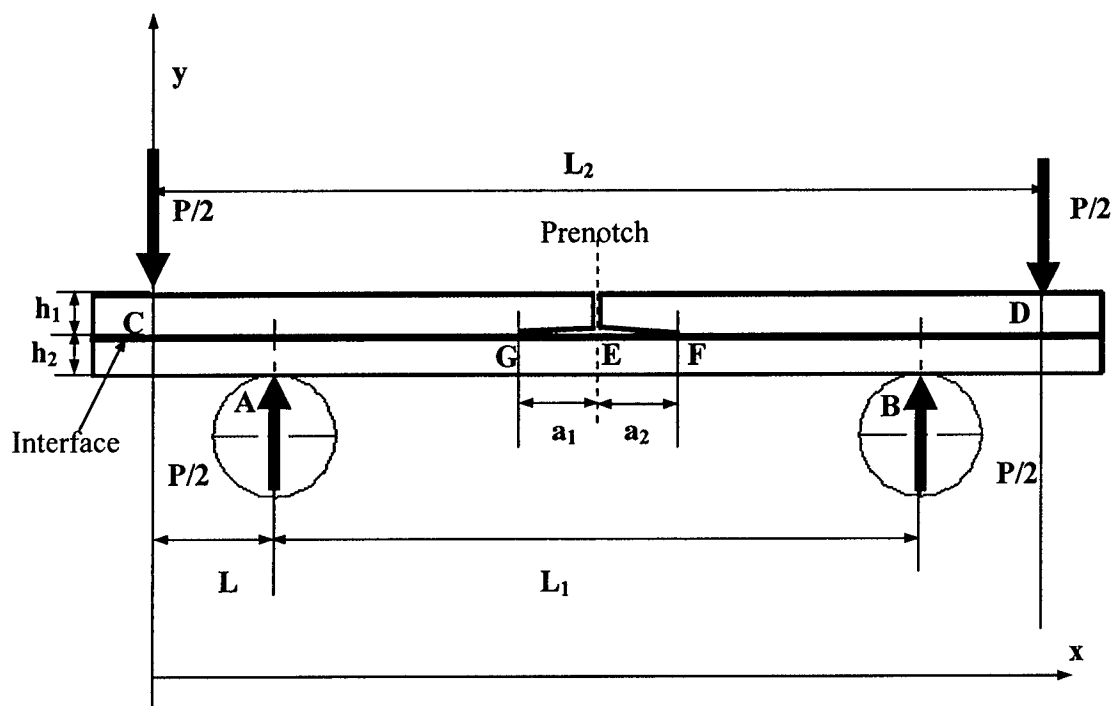
Figure 10.6: Schematic illustration of the specimen used in the modified 4-point bend delamination test.
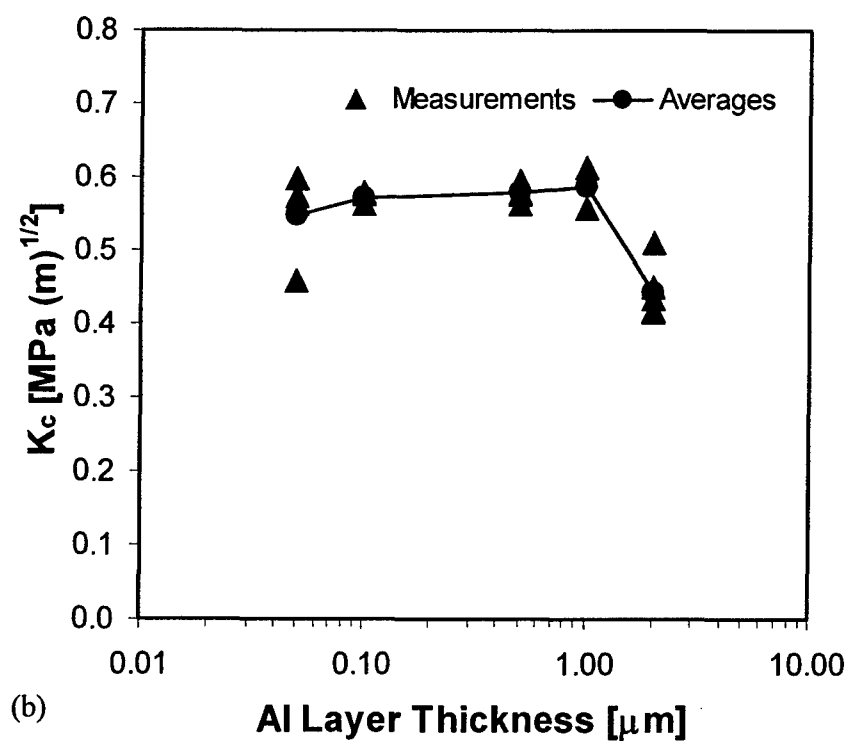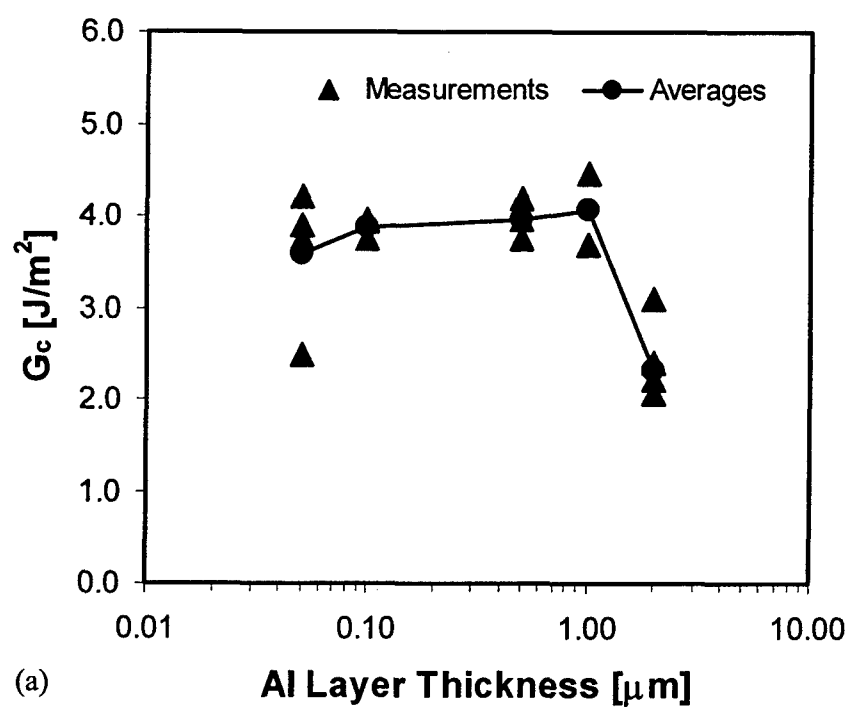
Figure 10.7: The dependence of (a) the critical strain energy release rate; (b) the critical stress intensity factor on the aluminum layer thickness.

Away from the crack tip   Near the crack tip

(a)

(b)

(c)

(d)

Crack propagation direction
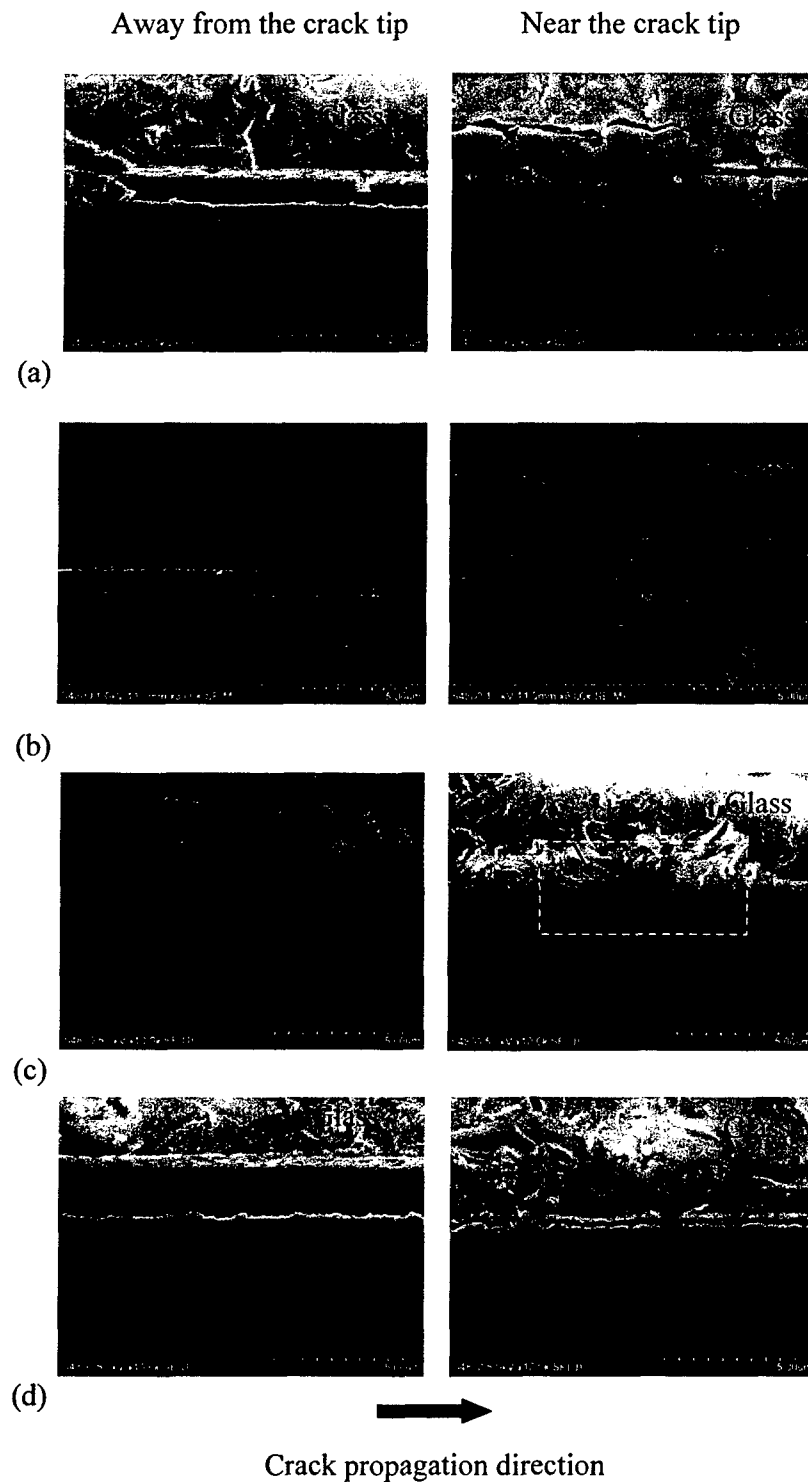
Figure 10.8: Comparison of crack path in fracture toughness test. Aluminum layer thickness: (a) 0.05μm; (b) 0.5μm; (c) 1μm; (d) 2μm; (e) Enlarged image of crack path near the crack tip.

269
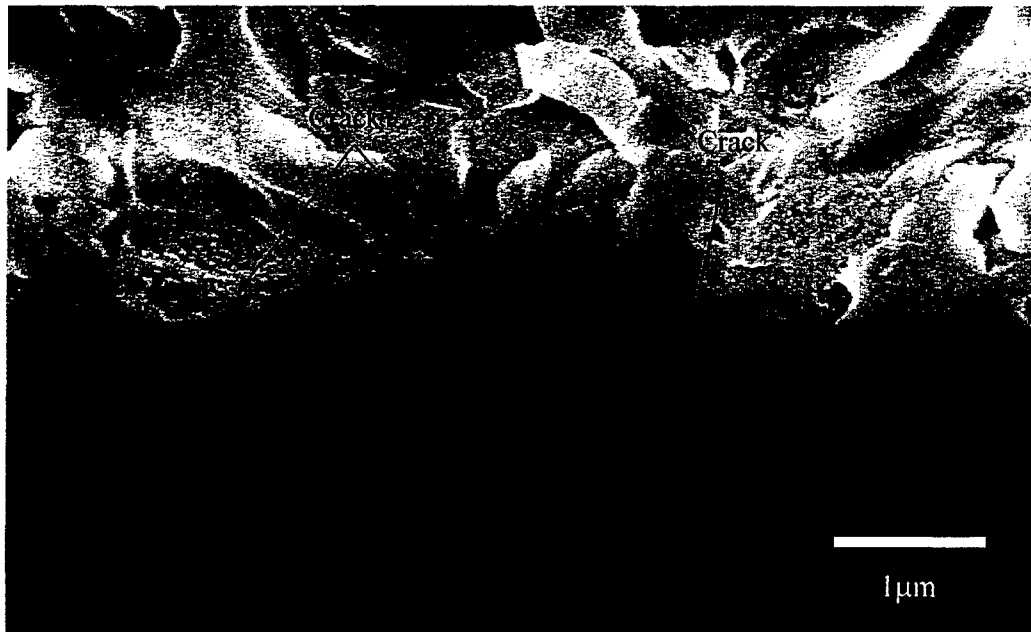
(e)

Figure 10.8: continued
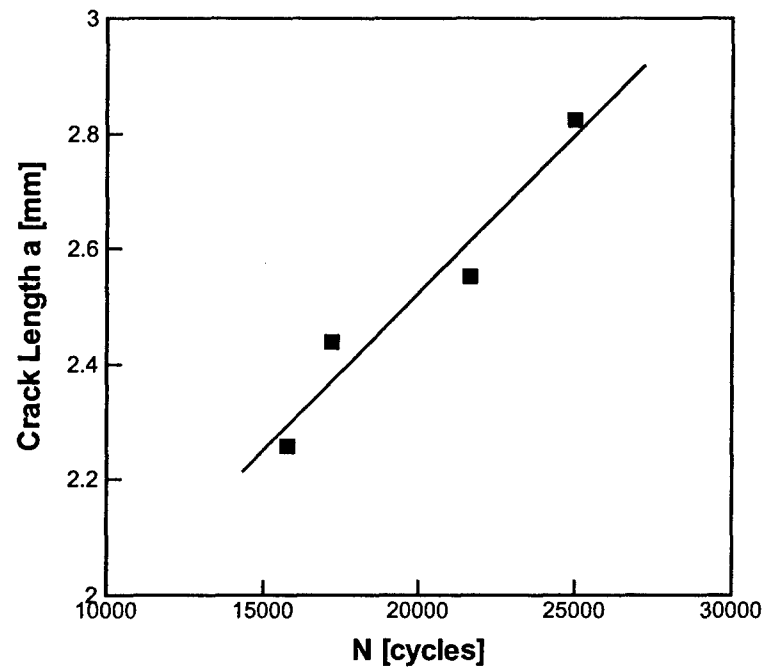
Figure 10.9: Crack length vs. numbers of cycles. $h_{Al}=1\mu m$, $G_{max}/G_c=31\%$.
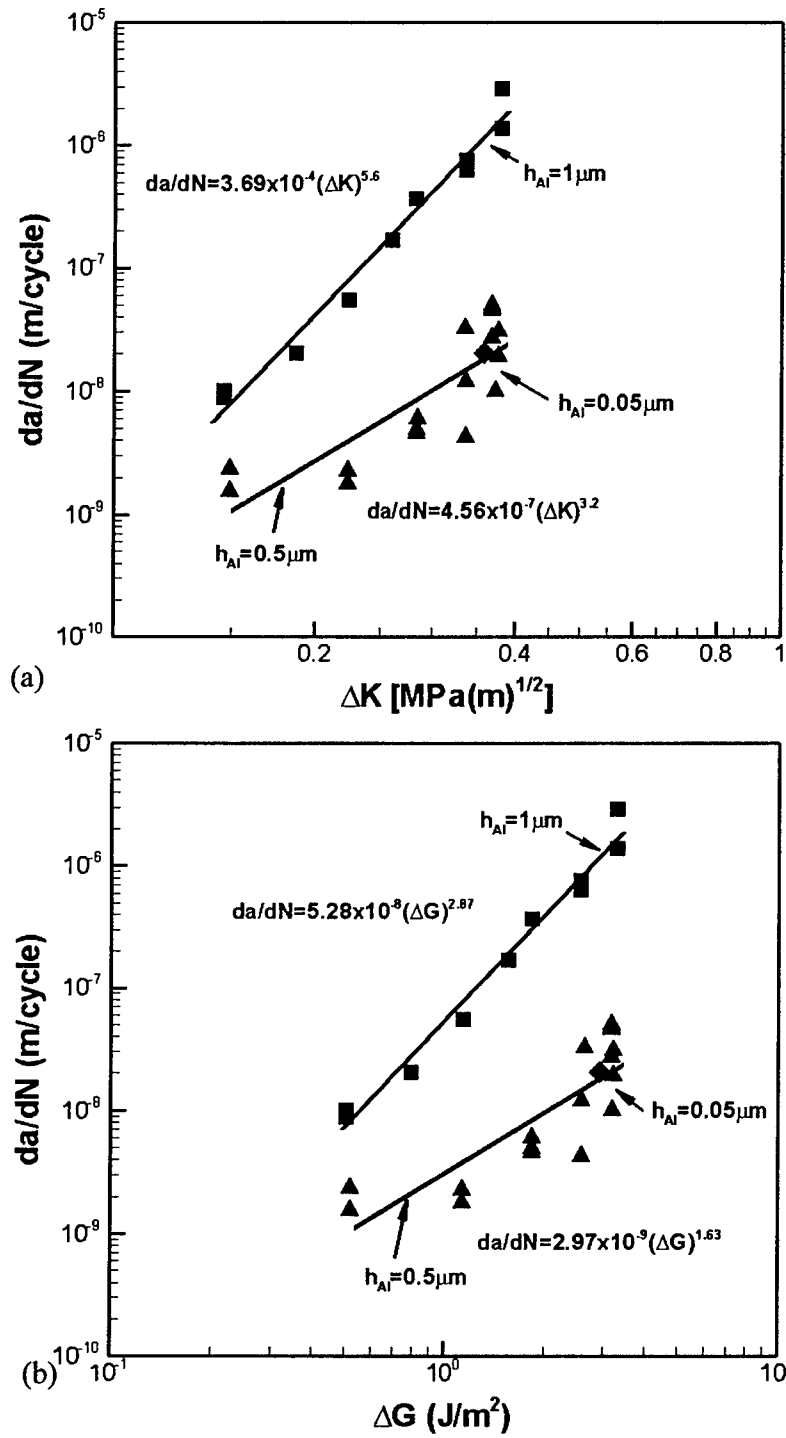
Figure 10.10: FCG rates in dependence on the applied driving force expressed in terms of (a) ΔK; (b) ΔG. h_{Al}=0.05µm, 0.5µm and 1µm.
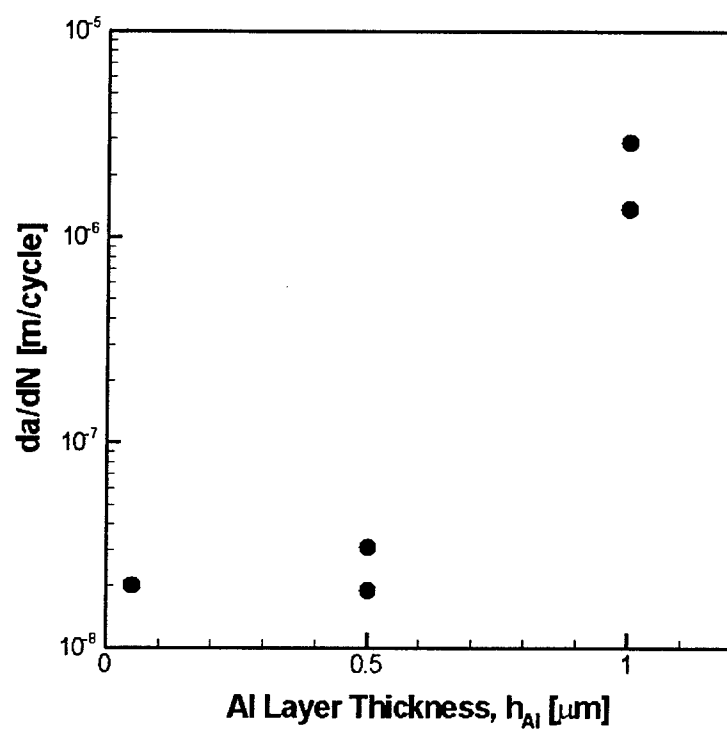
Figure 10.11: The dependence of FCG rates on the aluminum layer thickness. $G_{max}/G_c = 90\%$.
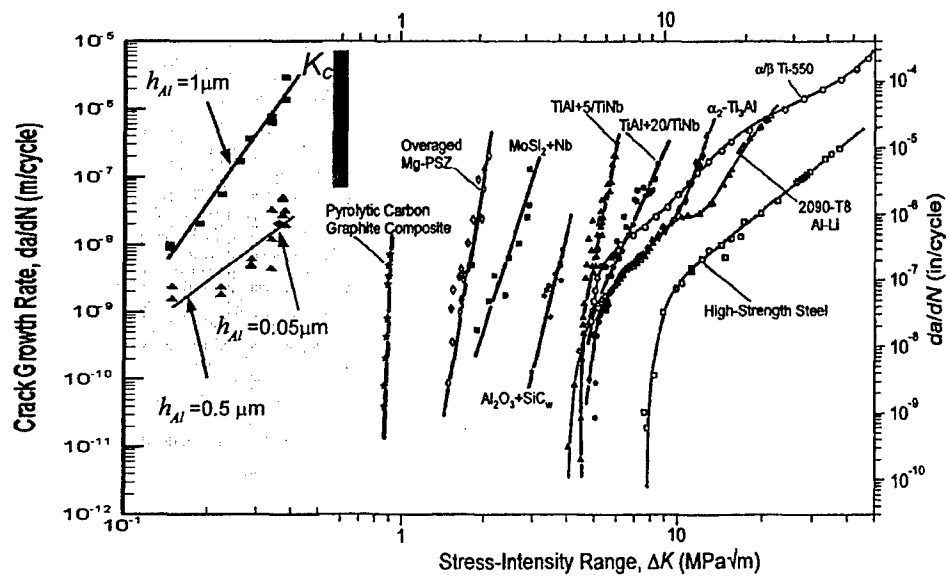
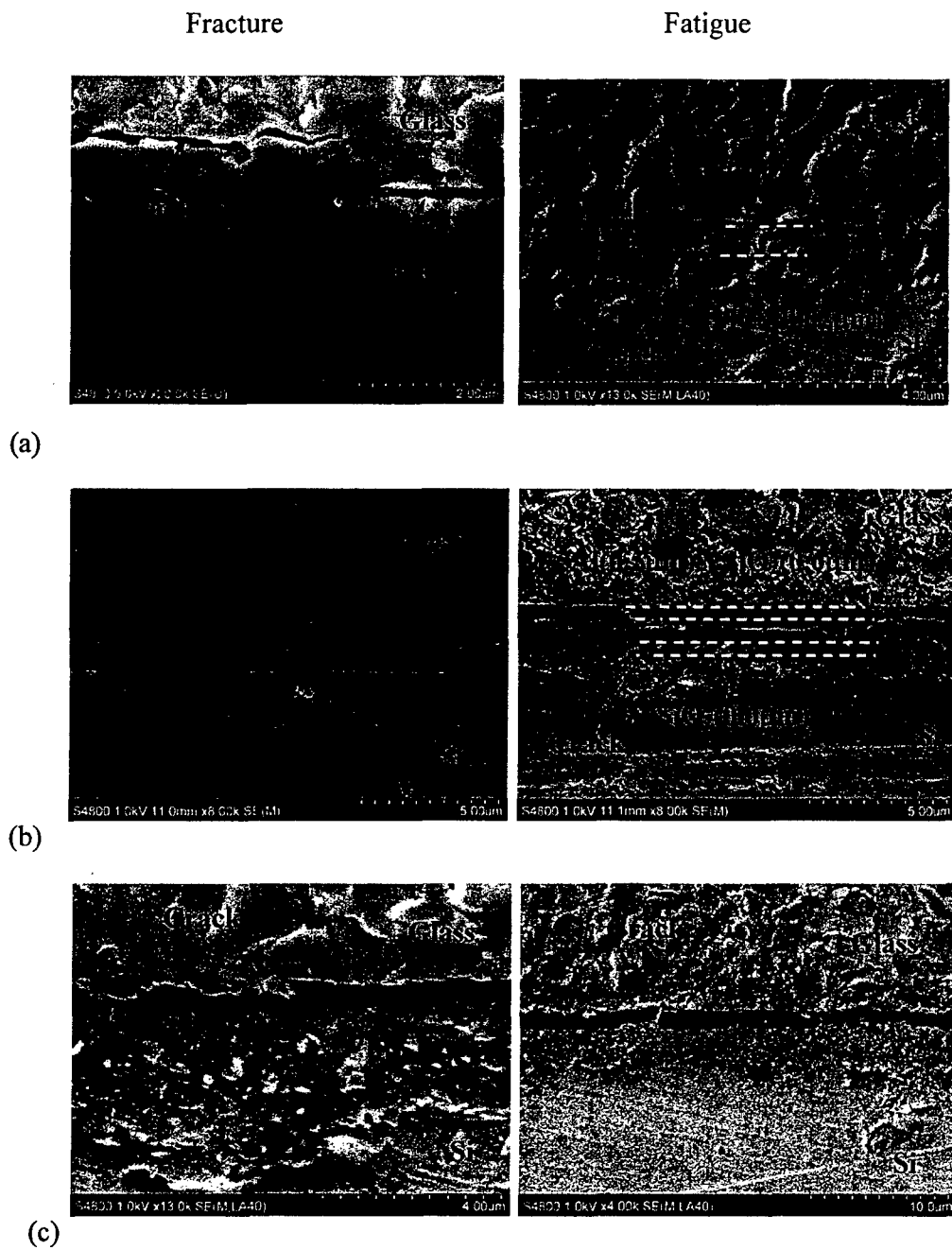Figure 10.12: Comparison of FCG rates obtained in this study to other structure materials (Ritchie, 1999).

Fracture   Fatigue

(a)

(b)

(c)

Figure 10.13: Comparison of crack path in fracture toughness test and FCG test.
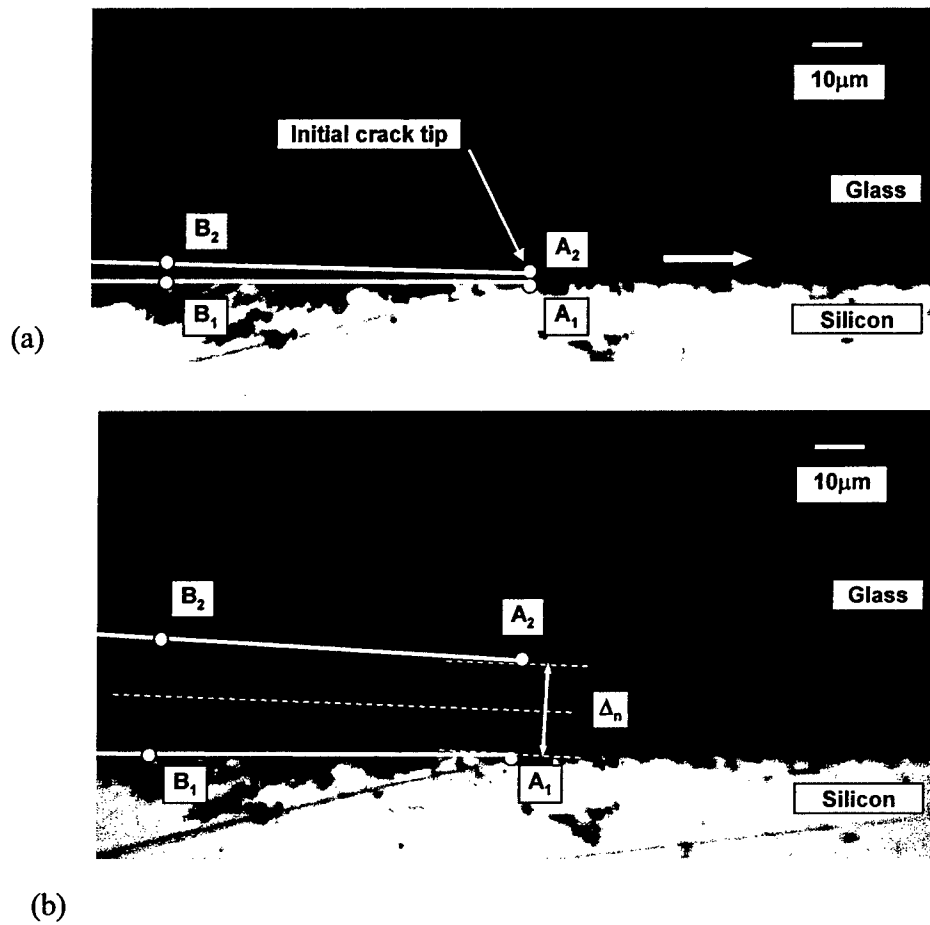Aluminum layer thickness: (a) 0.05μm; (b) 0.5μm; (c) 1μm.

Figure 10.14: Images of interface delamination for calculations of the crack tip opening displacement at the initial crack tip under monotonic loading. (a) Before crack propagation; (b) After crack propagation.
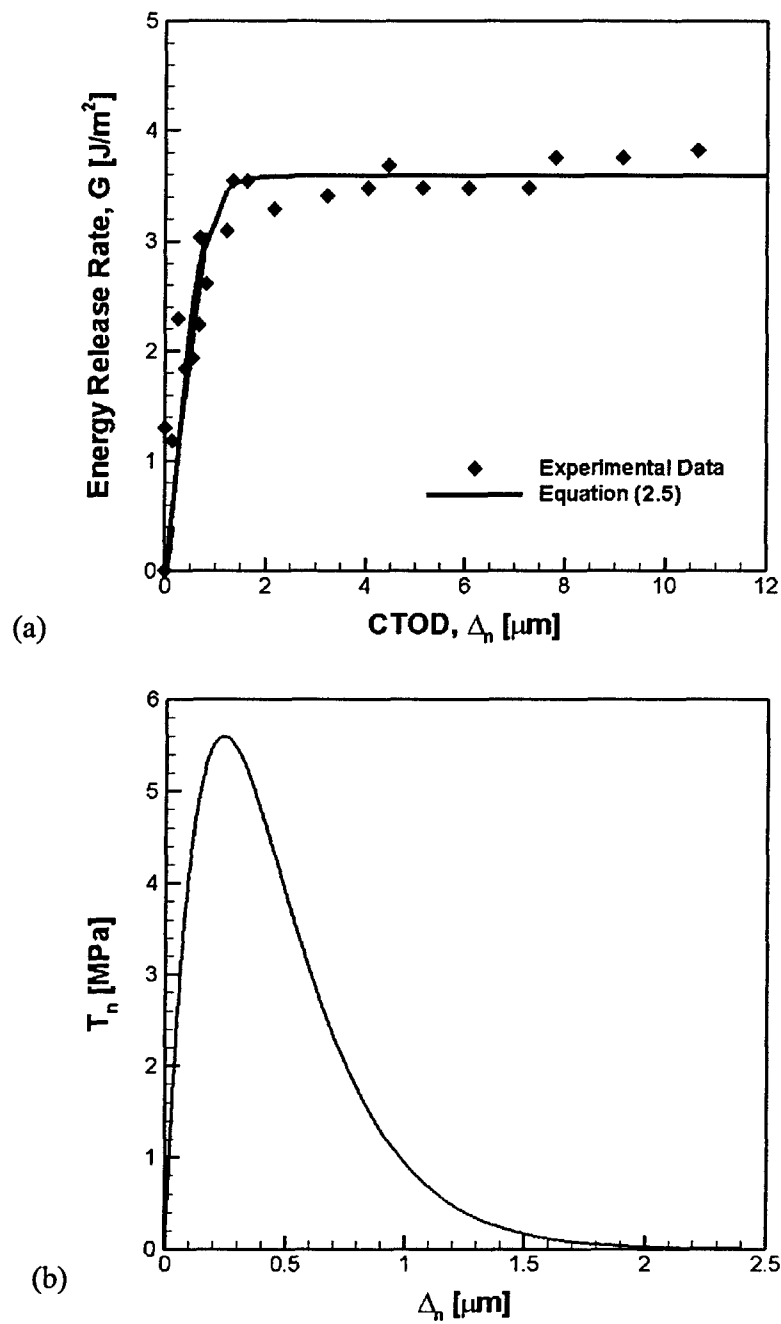
(a)

(b)

Figure 10.15: (a) The strain energy release rate vs. the crack tip opening displacement at the initial crack tip; (b) The traction-separation law.

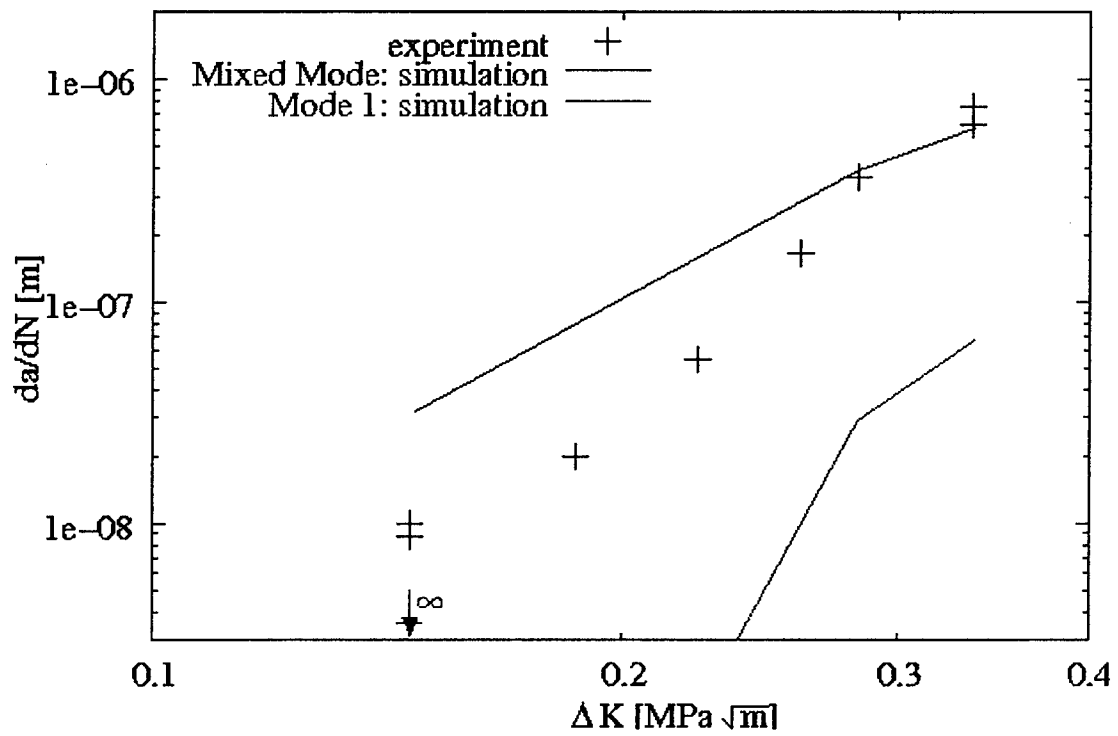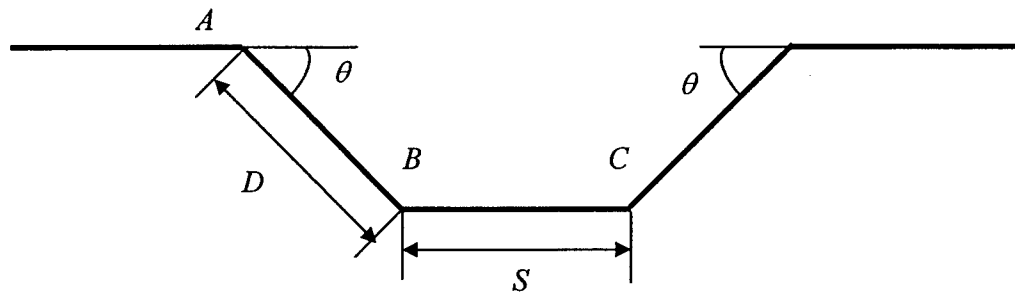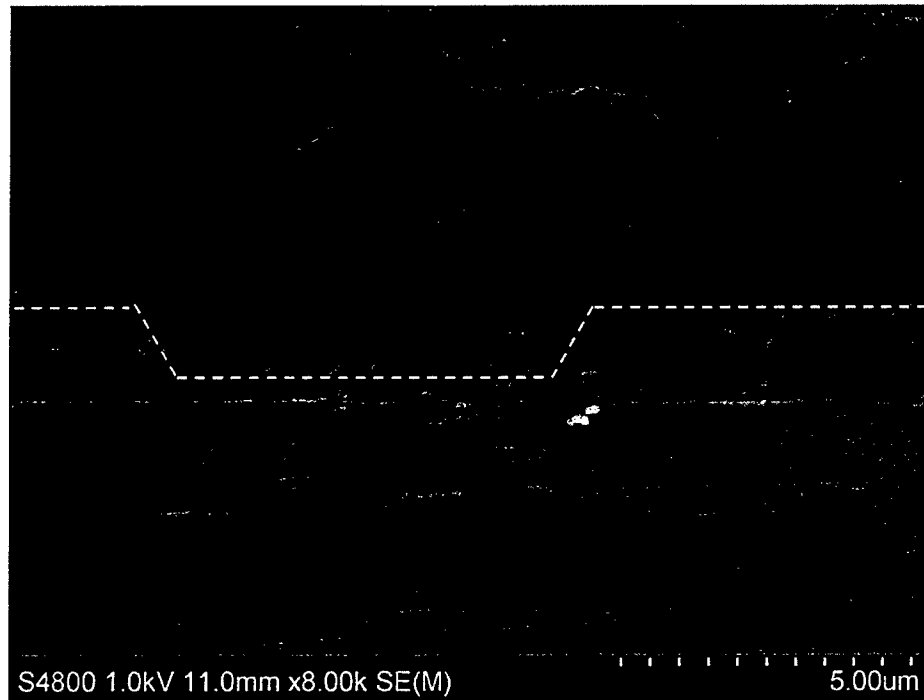Figure 10.16: Simulated crack bridging across different widths of glass layer. (a) 120μm; (b) 60μm.

278

Figure 10.17: Comparison of simulated FCG rates in dependence on the stress intensity factor range to the experimental results. h_{Al}=1μm.

(a)

S4800 1.0kV 11.0mm x8.00k SE(M)   5.00um

(b)

Figure 10.18: (a) Schematic illustration of a segment of a deflected crack. (b) SEM image of crack deflection for the sample with h_{Al}=0.5µm in fracture toughness test.

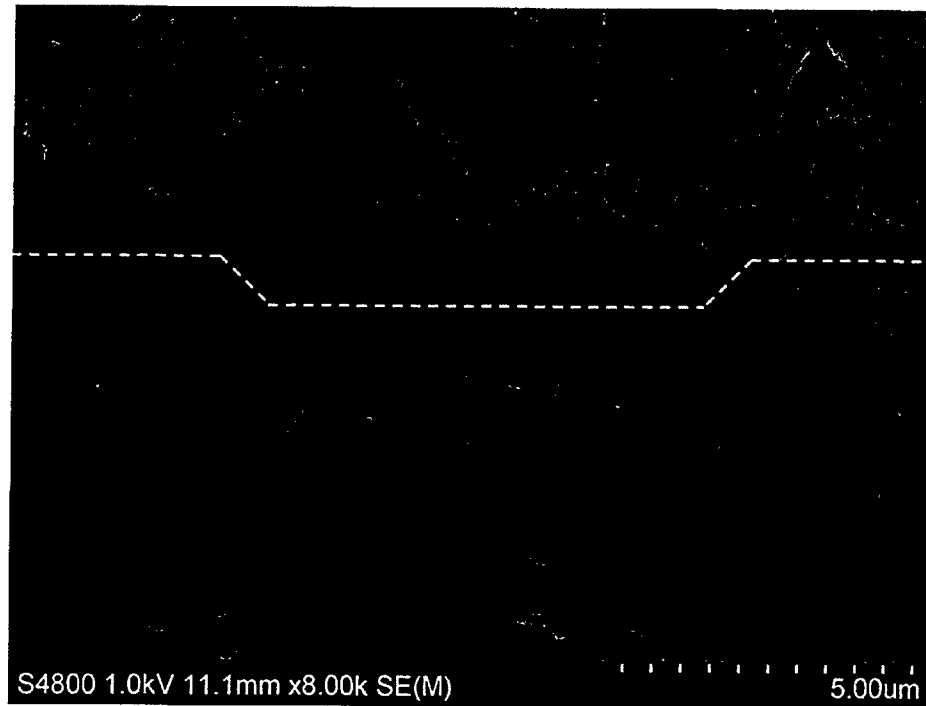Figure 10.19: SEM image of crack deflection for the sample with h_{Al}=0.5μm in fatigue crack growth test.

LIST OF REFERENCES

ASTM Standard E647-91, 1991, "Standard Test Method for Measurement of Fatigue Crack Growth Rates," *Annual Book of ASTM Standards*, Vol. 3.01, pp. 674-701.

Cannon R.M., Dalgleish, B.J., Dauskardt, R.H., Oh, T.S., Ritchie, R.O., 1991, "Cyclic fatigue-crack propagation along ceramic/metal interfaces," *Acta Metallurgica et Materialia*, Vol. 39(9), pp. 2145-2156.

Cox, B.N., Rose, L.R.F., 1994, "Time- or cycle-dependent crack bridging," *Mechanics of Materials*, Vol. 19, pp. 39-57.

Cozma, A., Puers, B., 1995, "Characterization of the electrostatic bonding of silicon and Pyrex glass," *Journal of Micromechanics and Microengineering*, Vol. 5, pp. 98-102.

Cozma, A., Jakobsen, H., Puers, B., 1998, "Electrical characterization of anodically bonded wafers," *Journal of Micromechanics and Microengineering*, Vol. 8, pp. 69-73.

Dauskardt, R.H., Lane, M., Ma, Q., and Krishna, N., 1998, "Adhesion and debonding of multi-layer thin film structures," *Engineering Fracture Mechanics*, Vol. 61, pp.141-162.

Dunn, M.L., Cunningham, S.J., Labossiere, P.E.W., 2000, "Initiation toughness of silicon/glass anodic bonds," *Acta Metallurgica*, Vol. 48, pp. 735-744.

Go, J.S., Cho, Y.H., 1999, "Experimental evaluation of anodic bonding process based on the Taguchi analysis of interfacial fracture toughness," *Sensors and Actuators*, Vol. 73, pp. 52-57.

Hasegawa, M., Zhu, S.J., Kagawa, Y., Evans, A.G. 2003, "Effect of metal layer thickness on the decohesion of high purity copper-sapphire interfaces," *Acta Materialia*, Vol. 51, pp. 5113-5121.

Hasegawa, M. and Kagawa, Y., 2006, "Decohesion Behavior in Copper-sapphire Interface under Mode I Cyclic Loading," *Materials Science and Engineering A*, Vol. 417, pp. 158-165.

Howard, S.J., Clyne, T.W., 1993, Surface preparation of titanium for vacuum plasma spraying and its effect on substrate/coating interfacial fracture toughness," Composites, Vol. 24(8), pp. 603-610.

Hirakata, H., Kitazawa, M., Kitamura, T., 2006, "Fatigue Crack Growth Along Interface Between Metal and Ceramics Submicron-thick films in Inert Environment," *Acta Materialia*, Vol. 54, pp. 89-97.

Huang, J.T., Yang, H.A., 2002, "Improvement of bonding time and quality of anodic bonding using the spiral arrangement of multiple point electrodes," *Sensors and Actuators A*, Vol. 102, pp. 1-5.

Hughey, M.P., Morris, D.J., Cook, R.F., Bozeman, S.P., Kelly, B.L., Chakravarty, S.L.N., Harkens, D.P., Stearns, L.C., 2004, "Four-point bend adhesion measurements of copper and permalloy systems," *Engineering Fracture Mechanics*, Vol. 71, pp. 245-261.

Klingbeil, N.W., Beuth, J.L., 1997, "Interfacial fracture testing of deposited metal layers under four-point bending," *Engineering Fracture Mechanics*, Vol. 56(1), pp. 113-126.

Kruzic, J.J., McNaney, J.M., Cannon, R.M., and Ritchie, R.O., 2004, "Effects of plastic constraint on the cyclic and static fatigue behavior of metal/ceramic layered structures," *Mechanics of Materials*, Vol. 36, pp. 57-72.

Lane, M., Dauskardt, R.H., Vainchtein, A., and Gao, H. 2000a, "Plasticity contributions to interface adhesion in thin-film interconnect structures," *Journal of Materials Research*, Vol. 15, pp. 2758-2769.

Lane, M., Dauskardt, R.H., Krishna, N., Hashim, I., 2000b, "Adhesion and reliability of copper interconnects with Ta and TaN barrier layers," *Journal of Materials Reviews*, Vol. 15(1), pp. 203-211.

Lee, T.M.H., Lee, D.H.Y., Liaw, C.Y.N., Lao, A.I.K., Hsing, I.M., 2000, "Detailed characterization of anodic bonding process between glass and thin-film coated silicon substrates," *Sensors and Actuators*, Vol. 86, pp. 103-107.

Lei, K.F., Ahsan, S., Budraa, N., Li, W.J., Mai, J.D., 2004, "Microwave bonding of polymer-based substrates for potential encapsulated micro/nanofluidic device fabrication," *Sensors and Actuators A*, Vol. 114, pp. 340-346.

Ma, Q., Fujimoto, H., Flinn, P., Jain, V., Adibi-rizi, F., Moghadam, F., Dauskardt, R.H., 1995, "Quantitative measurement of interface feature energy in multi-layer thin film structures," *Materials Research Society*, Vol. 391, pp. 91-96.

Ma, Q., Bumgarner, J., Fujimoto, H., Lane, M, Dauskardt, R.H., 1997, "Adhesion measurement of interfaces in multilayer interconnect structures," *Materials Research Society*, Vol. 473, pp. 3-14.

Ma, Q., 1997, "A four-point bending technique for studying subcritical crack growth in thin films and at interfaces," *Journal of Materials Research*, Vol. 12(3), pp. 840-845.

McNaney, J.M., Cannon, R.M., and Ritchie, R.O., 1996, "Fracture and fatigue-crack growth along aluminum-alumina interfaces," *Acta Metallurgica*, Vol.12, pp. 4713-4728.

Nese, M., Hanneborg, A., 1993, Anodic bonding of silicon to silicon wafers coated with aluminum, silicon oxide, polysilicon or silicon nitride," *Sensors and Actuators A*, Vol. 37-38, pp. 61-67.

Oh, T. S., Rödel, J., Cannon R. M., Ritchie, R. O., 1988, "Ceramic/metal interfacial crack growth: Toughening by controlled microcracks and interfacial geometries," *Acta Metallurgica* , Vol. 36(8), pp. 2083-2093.

Palensky, J., Wieder, B., Schaefer, C., Lindner, P., 2002, "Wafer bonding for sensors," *Sensors Expo*, pp. 1-4.

Paris, P.C., Gomez M.P., Anderson W.P., 1961, "A rational analytic theory of fatigue," *The Trend in Engineering*, Vol. 13, pp. 9–14.

Phillipps, A.J., Clegg, W.J., Clyne, T.W., 1993, "Fracture behavior of ceramic laminates in bending-II. Comparison of model predictions with experimental data," *Acta Metallurgica et Materialia*, Vol. 41(3), pp. 819-827.

Reimanis, I.E., Dalgleish, B.J., Brahy, M., Rühle, M., Evans, A.G., 1990, "Effects of plasticity on the crack propagation resistance of a metal/ceramic interface," *Acta Metallurgica et Materialia*, Vol. 38(12), pp. 2645-2652.

Reimanis, I.E., Dalgleish, B. J., Evans, A. G.,1991, "The fracture resistance of a model metal/ceramic interface ," *Acta Metallurgica et Materialia* , Vol. 39(12), pp. 3133-3141.

Ritchie, R. O., Cannon R. M., Dalgleish, B. J., Dauskardt, R. H., McNaney J. M., 1993, "Mechanics and mechanisms of crack growth at or near ceramic-metal interfaces: interface engineering strategies for promoting toughness," *Materials Science and Engineering A* . Vol.166(1-2), pp. 221-235.

Ritchie, R.O., 1999, Mechanisms of fatigue-crack propagation in ductile and brittle solids, *International Journal of Fracture*, Vol. 100, pp. 55-83.

Roe, K.L. and Siegmund, T., 2003, "An irreversible cohesive zone model for interface fatigue crack growth simulation," *Engineering Fracture Mechanics*, Vol.70, pp. 209-232.

Rogers, T., Kowal, J., 1995, "Selection of glass, anodic bonding conditions and material compatibility for silicon-glass capacitive sensors," *Sensors and Actuators A*, Vol. 46-47, pp. 113-120.

Shaviv, R., Roham, S., Woytowitz, P., 2005, "Optimizing the Precision of the Four-point Bend Test for the measurement of Thin Film Adhesion," *Microelectronic Engineering*, Vol. 82, pp. 99-112.

Shaw, M. C., Marshall, D. B., Dalgleish, B. J., Dadkhah, M. S., He, M. Y., Evans, A. G., 1994, "Fatigue crack growth and stress redistribution at interfaces", *Acta Metallurgica et Materialia*, Vol. 42(12), pp. 4091-4099.

Suresh, S., 1983, "Crack deflection: implications for the growth of long and short fatigue cracks," *Metallurgical Transactions*, Vol. 14A, pp. 2375-2385.

Suresh, S., 1985, "Crack initiation in cyclic compression and its applications," *Engineering Fracture Mechanics*, Vol. 21, pp. 453-463.

Suresh, S., 1998, *Fatigue of Materials*. Cambridge University Press.

Terazaki, T., Nomura, M., Takeyama, K., Nakamura, O., Yamamoto, T., 2005, "Development of multi-layered microreactor with methanol reformer for small PEMFC," *Journal of Power Sources*, Vol. 145, pp.691-696.

Varias, A.G., Suo, Z. and Shih, C.F., 1991, "Ductile Failure of a Constrained Metal Foil," *Journal of the Mechanics and Physics of Solids*, Vol. 39(7), pp. 963-986.

Wang, B., Siegmund, T., 2005, "A numerical analysis of constraint effects in fatigue crack growth by use of an Irreversible Cohesive Zone Model," *International Journal of Fracture* Vol. 132, pp.175-196.

Wallis, G., Pomerantz, D.I., 1969, "Field assisted glass-metal sealing," *Journal of Applied Physics*, Vol. 40(10), pp.3946-3949.

Wei, J., Xie, H., Nai, M.L., Wong, C.K., Lee, L.C., 2003, "Low temperature wafer anodic bonding," *Journal of Micromechanics and Microengineering*, Vol. 13, pp. 217-222.

Xu, X.P., Needleman, A., 1994, "Numerical Simulations of Fast Crack Growth in Brittle Solids", *J. Mech. Phys. Solids*, Vol. 42, pp. 1397-1434.

Yussuf, A.A., Sbarski, I., Hayes, J.P., Solomon, M., Tran, N., 2005, "Microwave welding ofpolymeric-microfluidic devices," *Journal of Micromechanics and Microengineering*, Vol. 15, pp. 1692-1699.